TECHNISCHE UNIVERSITÄT WIEN
Vienna University of Technology

x-ray center

Diplomarbeit

Synthesis and symmetry relationships of octahedral fluorophosphates and fluoroantimonates

ausgeführt am

Fachbereich Röntgenzentrum
der Technischen Universität Wien

betreut durch

Privatdoz. Dipl.-Ing. Dr.techn. Berthold Stöger

durchgeführt
von

Martin Nastran, BSc

Wien, am 30. September 2021 Martin Nastran

Abstract

The symmetry of a solid is crucial for the existence of its physical properties. In "crystal engineering", for example, an attempt is made to enable desired properties through targeted symmetry descent. Symmetry relationships are also used to classify crystal structures. In the simplest case, two crystal symmetries are related via a group/subgroup relation. However, some symmetry relationships (e.g. different stacking sequences) are more complex and not yet fully investigated. In order to investigate such complex symmetry relationships, octahedral fluorophosphates and fluorophosphonates were synthesised and structurally characterised by means of single crystal diffraction. These systems are suitable because the cubic symmetry of the anions can be specifically reduced by partial hydrolysis. Furthermore, hydroxyl groups are structure-determining due to the hydrogen bonds and thus provide for a complex crystal chemistry through the formation of periodic hydrogen bond networks. Complementary to the X-ray methods, NMR measurements were carried out. The reason for this is the tricky distinction between F^- and OH^- using X-ray diffraction methods. The mono- to tetramethylammonium salts of the superacid $HSbF_6$ crystallise at high-temperatures in cubic CsCl-like structures. The K, Rb and Cs salts of $HSbF_5(OH)$ and $HSbF_4(OH)_2$ have an even more complex behaviour. Superstructures form on cooling and the point symmetry or crystal class is, in extreme cases, reduced to triclinic. Here, both the statistical incorporation of OH (resulting in isotypic disordered structures) and various polytypes (stacking sequences) have been observed, whose relationship cannot be described by group/subgroup relationships. In the case of $RbSbF_4(OH)_2$, oriented intergrowth of different polytypes occurred in the same crystal (allotwinning). Furthermore, a synthesis strategy of the $[H_2PF_4]^-$ ion was developed and pursued, which previously could only be prepared in a complex manner in an anhydrous, strongly fluoride-containing environment. In contrast to $[SbF_4(OH)_2]^-$, this anion adopts *trans*-configuration of the non-F substituents. During the preparations for this, new phosphinates could be produced and characterised by single crystal X-ray diffraction.

Zusammenfassung

Die Symmetrie eines Festkörpers ist maßgeblich für das Vorhandensein von physikalischen Eigenschaften verantwortlich. Im „Crystal Engineering“ beispielsweise wird versucht durch gezielten Symmetrieabstieg gewünschte Eigenschaften zu ermöglichen. Symmetriebeziehungen dienen auch zur Klassifikation von Kristallstrukturen. Im einfachsten Fall handelt es sich um Gruppe/Untergruppe-Beziehungen. Manche Symmetriebeziehungen (z.B. verschiedene Stapelfolgen) sind allerdings komplexer und noch nicht vollständig untersucht. Um solche komplexen Symmetriebeziehungen zu Untersuchen, wurden in dieser Arbeit oktaedrische Fluorophosphate und -antimonate synthetisiert und strukturell mittels Einkristalldiffraktion charakterisiert. Diese Systeme bieten sich an, da durch partielle Hydrolyse die kubische Symmetrie der Anionen gezielt reduziert werden kann. Des Weiteren sind Hydroxylgruppen aufgrund der Wasserstoffbindungen strukturbestimmend und sorgen somit für eine komplexe Kristallchemie durch Ausbildung von periodischen Wasserstoffbrückennetzwerken. Komplementär zu den röntgenographischen Methoden wurden NMR-Messungen durchgeführt. Der Grund hierfür liegt in der schwierigen Unterscheidung zwischen F^- und OH^- mittels Röntgenbeugungsmethoden. Die Mono- bis Tetramethylammoniumsalze der Supersäure $HSbF_6$ kristallisieren bei hohen Temperaturen in kubischen CsCl-artigen Strukturen. Die K, Rb und Cs-Salze von $HSbF_5(OH)$ und $HSbF_4(OH)_2$ besitzen ein noch komplexeres Verhalten. Es bilden sich beim Abkühlen Überstrukturen aus und die Punktsymmetrie oder Kristallklasse ist, im Extremfall, bis zum triklinen reduziert. Hier wurde einerseits der statistische Einbau von OH beobachtet (resultierend in isotypen fehlgeordneten Strukturen), sowie andererseits verschiedene Polytype (Stapelfolgen), deren Verwandtschaft nicht durch Gruppe/Untergruppe-Beziehungen beschrieben werden können. Im Fall von $RbSbF_4(OH)_2$ kam es zur orientierten Verwachsung von verschiedenen Polytypen im gleichen Kristall (Allozwilling). Des weiteren wurde eine Synthesestrategie des $[H_2PF_4]^-$-Ions entwickelt und verfolgt, welches zuvor nur umständlich in einer wasserfreien, stark fluoridhaltigen Umgebung hergestellt werden konnte. Im Gegensatz zu $[SbF_4(OH)_2]^-$ nimmt dieses Anion *trans*-Konfiguration ein. Während der Vorbereitungen für dieses konnten neue Phosphinate hergestellt und mittels Einkristall Röntgenbeugung charakterisiert werden.

Danksagung:

An dieser Stelle möchte ich mich bei all denjenigen bedanken, die mich während dieser Arbeit direkt unterstützt haben. Alle zu nennen, die auch indirekt involviert waren, würde den Rahmen sprengen. Dennoch hoffe ich, dass sich diese Personen an dieser Stelle auch ohne direkte Erwähnung angesprochen fühlen.
Vor allem gebührt mein Dank Herrn Dr. Berthold Stöger, der meine Masterarbeit engagiert betreut und begutachtet hat. Die zuverlässigen Ratschläge und die hilfreiche Kritik waren immer Gold wert. Vor allem sein umfangreiches Fachwissen, selbst in Gebieten außerhalb seiner Expertise und sein Ehrgeiz, komplizierte Problemstellungen zu lösen, haben mir oft viel Aufwand erspart. Ich bin unglaublich dankbar für die großartige Zeit und möchte mich aus ganzen Herzen bedanken.
Herrn DI Werner Artner möchte ich als Nächstes für seine umfangreiche Hilfsbereitschaft danken. Er war immer zur Stelle, wenn physische Dinge benötigt wurden und dank ihm hatte es nie an funktionstüchtigem Werkzeug oder Reagenzien gemangelt. Darüber hinaus gebührt mein Dank allen Mitgliedern des XRC, Frau Dr. Klaudia Hradil, Herrn Dr. Erich Halwax und Herrn DI Erik Lübke, die mich fachlich immer wieder in ihren jeweiligen Fachbereichen unterstützten. Dazu gehören für mich auch Herr Dr. Markus Sauer und Frau Annette Foelske, die auch immer wieder der Runde beiwohnten.
Ebenso für die professionelle und vor allem zuverlässige Hilfe bei NMR-Messungen möchte ich mich bei Herrn Dr. Christian Hametner bedanken. Vor allem, dass er sich die Zeit genommen hat, auch noch spät am Abend die empfindlichen Proben zu messen.
Herrn DI Felix Eder, welcher neben meinem Betreuer mir bei Fragen immer mit Rat und Tat zur Seite stand, möchte ich hier ebenso noch meine Dankbarkeit aussprechen. Gerade bei Herausforderungen bei der Datenauswertung war ein zweites Paar Augen viel wert.
Abschließend geht mein Dank noch an meine großartige Familie. Gerade meine Eltern Edeltraud und Stefan bin ich unendlich dankbar. Sie haben mich während meines gesamten Studiums bedingungslos, trotz der großen Entfernung, mit allem was in ihrer Macht stand, unterstützt. Danke auch an meine Geschwister, meine Schwester Manuela und meinem Bruder Stefan. Dank den beiden wurde mir nie langweilig, vor allem nicht, wenn ich in Kärnten auf Besuch war.

Contents

1. Introduction

1.1 Motivation

The symmetry of a crystal is technologically and theoretically essential. For example, a crucial part of *crystal engineering* is to control the symmetry to allow or prohibit certain physical properties [1]. Moreover, symmetry relationships are of theoretical interest. Not all symmetry relationships can be described by simple group/subgroup relations [2]. For example, the symmetry of stacking arrangements (polytypes) is described by space groupoids [3]. Up to now there is no comprehensive theory of the relationship of such groupoids. In this work, the focus was placed on the study of symmetry descents generated by replacing chemically related groups in octahedral ions, in particular fluoroantimonates(V) and fluorophosphates(V).
The symmetry of a crystal determines whether physical properties can occur and also their directionality with respect to the orientation of the crystal. Many physical properties are described by tensors [4]. The tensor elements are limited by the existing point symmetry of the crystal. For example, a prerequisite for a single crystal to generate piezoelectricity/ferroelectricity and/or pyro electricity is to not possess inversion symmetry. Compressibility, shearability and a multitude of other mechanical, optical and magnetic properties are also influenced differently by the crystal class [4]. It is gaining importance and is far from being fully understood. Another crucial point in this respect is the investigation of crystallisation properties [5]. This work attempts to shed light on all these topics by introducing structure directing hydrogen bonds into highly symmetric structures.

1.2 Symmetry

1.2.1 Symmetry operations

Symmetry is the property of an object to be mapped onto itself by a *motion*. A motion is a distance preserving transformation of Euclidean space onto itself. Such mapping of an object onto itself is called a symmetry operation of the object. The motions of three-dimensional Euclidean space are: rotations, inversion, reflections, higher rotoinversions, translations, screw rotations and glide reflections.

1.2.2 Symmetry elements

The geometric element of a symmetry operation is a point, a line and/or a plane about which a symmetry operation is performed. The element here unambiguously determines the orientation of the symmetry operation. The symmetry element is an axis for rotations, a point for inversions, a plane for reflections, and an axis *and* a plane for higher rotoinversions. A symmetry element is a geometric element and all the symmetry operations that share this element. For example, a sixfold rotation axis is an axis and the respective rotations by -120°, -60°, 60°, 120° and 180° about the axis.

1.2.3 Symmetry in crystals

The set of all symmetry operations of an object forms a group with the composition operation. This group is called the symmetry group of the object or, for short, the symmetry of the object. A crystal is (discretely) periodic in three dimensions, which means that translations exist in three linearly independent directions, but there are no vanishingly small translation vectors different from the zero vector.
The symmetry group of a crystal is called a *space group*. The translations of a crystal form the translation lattice. According to the *crystallographic restriction theorem*, a lattice, and therefore a periodic crystal, can only have 1, 2, 3, 4 and 6-fold rotations, inversions, rotoinversions (including the reflection), screw rotations and glide reflections derived from them. Nevertheless, there are an infinity of distinct space groups that differ in the metric of the lattice. If one abstracts from the metric, one obtains 230 crystallographic space group types [6].
Certain helical screw rotation axes exist in enantiomorphic pairs: $3_1/3_2$, $4_1/4_3$, $6_1/6_5$ and $6_2/6_3$. Ignoring this handedness, the 230 space types are reduced to the 219 affine space group types. If non-lattice intrinsic translations of the screw rotations and glide reflections are also ignored, the 73 arithmetic crystal classes are obtained, which are the possible, unique combinations of the 32 crystal classes (point group types) and the 14 Bravais lattices. All these symmetry groups are uniquely labelled via the Hermann-Mauguin notation [6].
The Bravais lattices and crystal classes can be classified into seven lattice systems or seven crystal systems on the basis of their point symmetry. The fundamental difference is that one describes the point symmetry of the lattice and the other the point symmetry of the crystal. A hexagonal (sixfold axis) as well as a trigonal (threefold axis) crystal can exist in the hexagonal lattice system. A trigonal crystal, in contrast to a hexagonal crystal, can also exist in the rhombohedral lattice system, since the rhombohedral lattice has only the trigonal point group $\bar{3}m$.

1.2.4 Layer symmetry

In the context of polytypes (structures built of layers), it is useful to consider the symmetry of layers periodic in two dimensions. Their symmetry groups are designated as *layer groups* [7]. These layer groups represent a three-dimensional extension of a wallpaper group. There are 80 layer group types that abstract from the metrics, like the space groups. In 17 of them, there is no operation that inverts the orientation of the layer (with respect to the stacking direction). These 17 types correspond to the „wallpaper groups“, the two-dimensional space groups. Layer group types are likewise named using the Hermann-Mauguin notation, but in contrast to the space groups, a lower case letter is used for the centring. It will be necessary in this work to describe layers not parallel to (001). Unfortunately, in the International tables of Crystallography Vol.E, a stacking direction [001] is presupposed. Therefore, the stacking direction will be given here in the subscript of the centring, as for example in $p_y\bar{1}$. This symbol designates a layer group with the two lattice basis vectors parallel to (010) and featuring only inversion and translation symmetry.

1.2.5 Point groups

Finite objects do not possess translation symmetry. This means that at least one point is mapped onto itself by all symmetry operations of the object. Symmetry operations can be grouped into a group of symmetry operations. The corresponding symmetry groups are called *point groups*. There are infinite types of point groups (e.g. the groups generated by the rotation about an arbitrary angle), but due to the crystallographic restriction theorem, only 32 of them are possible in three-dimensional crystals.

1.2.6 Site symmetry

The site symmetry (group) or point symmetry of a point (and its surroundings) in a crystal is its finite symmetry group formed by the set of all symmetry operations of the space group of the crystal. It is determined by the symmetry of the whole crystal (or molecule) and by the location of the point in the crystal (or molecule) and it is isomorphic to a subgroup of the point group to which the space group of the crystal belongs. It maps the point onto itself and therefore in three-dimensional space, the site symmetry must be one of the 32 point groups.

1.2.7 Group-subgroup relationships

According to Hermann's theorem [8], maximum subgroups must arise from a *klassengleich* or *translationengleich* symmetry descent from the minimum supergroup. A *translationengleich* symmetry descent is given if the symmetry of the point group changes, but the translation lattice remains the same. The lost symmetry operations are thereby often retained as twinning operations.
A *klassengleiche* symmetry descent, on the other hand, preserves the point group (crystal class) and reduces the translation lattice. This can lead to a phenomenon called antiphase domains [9]. If the type of the space group is preserved after a *klassengleiche* symmetry descent, it is called an *isomorphic* symmetry descent, since space groups of the same type are isomorphic [10].

t (***translationsgleich***)	k (***klassengleich***)	i (***isomorph***)
Complete translational lattice of the space group is preserved	Subgroup belongs to the same crystal class	Special case of the *klassengleiche* subgroup
Volume of the primitive unit cell remains unchanged	Enlarged unit cell, loss of centring	Subgroup belongs to the same space group type (same HM symbol) or enantiomorphic space group type

The extreme case of a *klassengleiche* symmetry descent is incommensurable modulation. Here, (at least) one cell axis becomes infinitely long, since the object is never again perfectly mapped onto itself by simple translation in this direction. Incommensurable modulated structures are quasi-periodic in this direction, since they can achieve arbitrarily small, but never complete, mapping onto itself by translation by a vector not equal to **0**. The better the match, the longer the translation must be. Incommensurably modulated structures with d modulation directions can be embedded in (3+d)-dimensional space. In this so-called *superspace*, the structure is periodic, and the symmetry can be described by a (3+d)-dimensional superspace group. The real space can be derived by a three-dimensional section through superspace.

As described by U. Müller in the International Tables for Crystallography [11]:

> The relations between crystal structures that are related by symmetry can be set forth in a concise manner with a tree of group–subgroup relations of their space groups, called a *Bärnighausen family tree*. From a mathematical point of view, trees are always cycle-free, which means that individual branches can no longer be brought together. For this reason, *Bärnighausen family trees* are not *trees* in the graph-theoretical sense.
> At its top, the tree starts from the space-group symbol of an *aristotype*, i.e. a simple, highly symmetrical crystal structure. Arrows pointing downwards depict symmetry reductions that result from structural distortions or partial substitutions of atoms; each arrow represents the relation from a space group to a maximal

subgroup. In the middle of each arrow the kind of the subgroup is marked by a t (*translationengleiche*), k (*klassengleiche*) or i (*isomorphic*) followed by the index of the symmetry reduction. In addition, changes of the basis vectors and origin shifts are marked if not clear. Each step of the symmetry reduction may involve changes of the atomic coordinates that have to be monitored. From the kinds of subgroups it can be deduced which and how many kinds of domains can result at a phase transition or topotactic reaction involving a symmetry reduction [12].

1.2.8 Polytypes

Polytypes are a special type of polymorphs [13]. Polytypes are built of layers, which can be arranged in different ways [14]. It is a common, multi-faceted phenomenon and can lead to a variety of crystallographic phenomenons:

- twinning [15]: an inter- or overgrowth of the same polytype in different crystallographic orientations
- allotwinning [16]: an inter- or overgrowth of different polytypes
- antiphase domains [9]: an inter- or overgrowth of the same polytype with the same orientation
- disordered stacking arrangements, which may result in diffuse scattering
- Systematic non-space group absences
- Diffraction enhancement of symmetry

1.3 Crystal chemistry of the employed building blocks

1.3.1 Fluoro- and oxo-coordination of the pnictogens(V)

To deal with this chapter exhaustively would go beyond the scope of this thesis. For this reason, the following discussion is limited to the points relevant to this work. Basically, the work dealt with compounds of pnictogens(V). However, in contrast to $[PF_6{-}]$ (P(V)), $[H_2PF_4]^-$ is formally a P(I) compound (as are the phosphinates). Nevertheless, $[H_2PF_4]^-$ will be summarised with the As(V) and Sb(V) compounds in the following, due to its octahedral coordination.
Hexafluoroantimonates $[SbF_6]^-$ and hexafluorophosphates $[PF_6]^-$ ideally possess octahedral coordination, which corresponds to a point symmetry of $m\bar{3}m$. This is likewise the symmetry of the dual Platonic solid, namely the cube. This maximum symmetry exists of the anions is realized in the solid state, for example, in cubic hexafluoroantimonates. Concerning hydrolysis of the fluoro-compound, octahedrally coordinated $[AsF_5(OH)]^-$ and $[AsF_4(OH)]^-$ were described in the literature [17, 18]. For the phosphates however, only the tetrahedral mono- and diphosphates $[PFO_3]_2^-$ and $[PF_2O_2]^-$ are known [19–21]. The corresponding tetrahedral monofluoroarsenates have likewise been described. In general, the oxo-phosphates and oxo-arsenates are also tetrahedral, though in the case of condensed oxo-arsenates, octahedral coordination has been described [22].

Note that in the literature, both the prefixes "hydroxo-" and "hydroxy-" are used for compounds of the type $[SbF_{6-x}(OH)_x]^-$ (x = 0–6) [23–25]. In the context of this work, fluorohydroxoantimonate is used uniformly.

1.3.2 Symmetry of the anions

It is expected that the substitution of one to three F groups of $[SbF_6]^-$ leads to a decrease in point symmetry of the anions (Figure 1.1). If a high-symmetry group is replaced by a low-symmetry one and the site symmetry in the crystal can no longer be fulfilled the symmetry of the crystal may be reduced. Another possibility is that the low-symmetry group is disordered about the symmetry element and thus the space group symmetry is maintained.

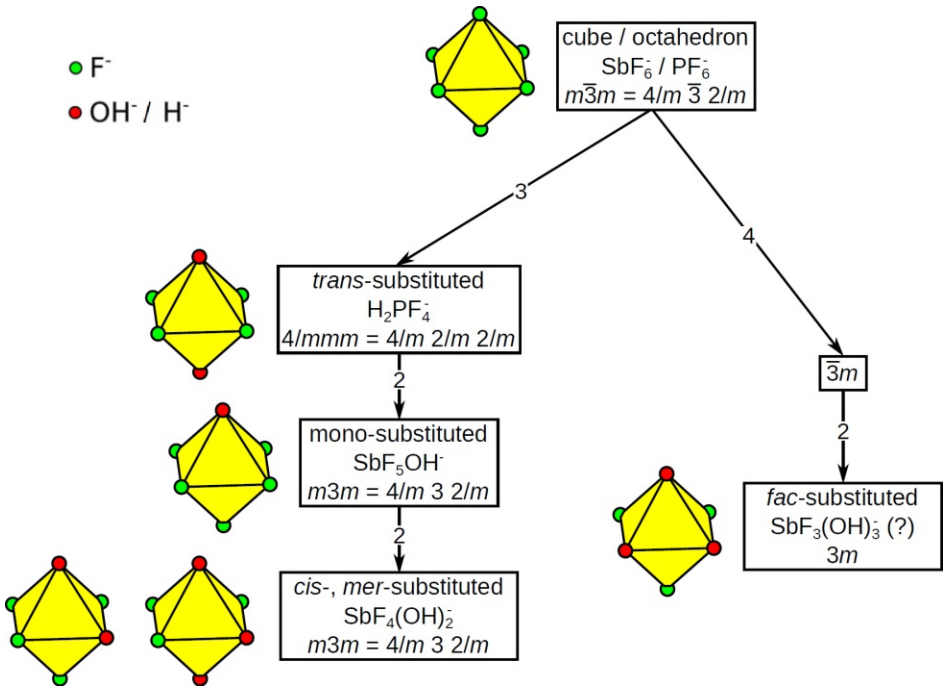

Figure 1.1: Point group scheme of different idealised octahedral fluoroantimonate anions and dihydridotetrafluorophosphate anion ($[SbF_3(OH)_3]^-$ only theoretical, H of OH is ignored).

Although this exchange is not completely isoelectronic, similar structures are expected owing to a very similar radial electron distribution. However, this also makes their distinction difficult with X-ray-based methods.
For fluoroantimonates, the one- and twofold substitution by OH is known, whereby the OH groups are always located in *cis* position [26]. A similar substitution exists for $[PF_6]^-$, but with H or OH in a *trans* configuration [27, 28].
With respect to hydrogen bonds, OH can act as an acceptor and a donor, the latter is not possible for F. F can only act as an acceptor of hydrogen bonds, whereby O and OH are stronger acceptors. Because of these different H-bond properties, it is hoped that the groups will not simply disorder, and that new structures will be formed.

1.3.3 Symmetry of the cations

Besides inducing symmetry descent by variation of the cations, the influence of the symmetry of the monovalent cations was likewise investigated. The alkali metals can be considered to possess spherical symmetry (point group $\overline{\infty}\overline{\infty}$) and can therefore in principle be located on sites of any symmetry, even though their coordination chemistry may show preference for certain sites.
To vary the symmetry of the cations, simple organic amines were employed to balance the negative charge of the hexafluoroantimonate. They are summarised in Table 1.1 as well as

their individual point symmetries.

Table 1.1: Cations used in combination with the $[SbF_6]^-$ anion and their highest possible point symmetries (different point symmetries depending on conformation).

Used cations	**Idealised point symmetry**
K^+	$\bar{4}3m$
Rb^+	$\bar{4}3m$
Cs^+	$\bar{4}3m$
$[NH_4]^+$	$\bar{4}3m$
$[H_5O_2]^+$	mmm or $2/m$
$[(CH_3)NH_3]^+$	$3m$ or 3
$[(CH_3)_2NH_2]^+$	$mm2$
$[(CH_3)_3NH]^+$	$3m$ or 3
$[(CH_3)_4N]^+$	$\bar{4}3m$

1.4 Previous investigations

The synthesis of fluorinated antimonates has mostly been realised via the reaction of superacids or SbF_5 with MF (M = alkali metals) [29, 30]. More recent syntheses of simple hexafluoroantomonates were mainly carried out starting from the corresponding oxides or hydroxides ($MSbO_3$, $MSb(OH)_6$), which were subsequently reacted with HF [31]. This led to many studies in the field of alkali hexafluoroantimonates [25, 26, 32–35] however, single crystal structure analyses of the pentafluorohydroxo as well as tetrafluorodihydroxoantimonates have been lacking so far, even though compounds of this type are already known as solids and in solution [25, 26, 36]. Only for $NaSbF_4(OH)_2$ structural data were published [32]. However, the structure is dubious, as probably only a higher symmetric basic structure was determined here. In contrast, analogous pentafluorohydroxoarsenates $[AsF_5(OH)]^-$ and tetrafluorodihydroxoarsenates $[AsF_4(OH)_2]^-$ are already known in literature and have already been structurally characterized on the basis of their single crystal structure data [18, 37].
During the work on fluorinated phosphorus (I) compounds, a comparatively simple synthesis was found for the dihydridotetrafluorophosphate ($[H_2PF_4]^-$), which likewise features an octahedral coordination of the central P atom and which could only be prepared by complex synthesis [27, 38].

1.4.1 Stability and formation rate of the fluoropnictogens(V)

It has been shown that there is a clear trend concerning the stability of the fluorophosphate, -arsenate and -antimonate cations. In the case of phosphates, the fluorination in aqueous environment is rather sluggish. Starting from phosphates ($[H_2PO_4]^-$), 40 $\%_{wt}$ only lead to PO_3F^- [37]. The hexafluorophosphate anion ($[PF_6]^-$) itself is relatively stable against hydrolysis [39].
In the case of the arsenates, starting from arsenates ($[H_2AsO_4]^-$), various fluoroarsenates can be prepared depending on the concentration of the hydrofluoric acid, but under the used aqueous conditions the fluorination can only yield up to pentafluorinated ($[AsF_5(OH)]^-$) salts [37]. An analogue of the hexafluorophosphate anion, the hexafluoroarsenate anion ($[AsF_6]^-$) is relatively stable against hydrolysis [39].

As will be shown in this work, the antimonates can easily be fluorinated up to the hexafluoroantimonate ($[SbF_6]^-$). Accordingly, the fluorinated ions are significantly harder to hydrolyse than their As and P counterparts.

1.4.2 Hydrogen bonding topology

As mentioned above, hydrogen bonds are crucial in this work because they are meant to provide ordered structures. Therefore, special attention will be paid to the H-bond topologies.
The topology of a hydrogen-bonding network can be represented by a graph, where vertices represent molecules and edges hydrogen bonds. Thereby, any geometric information, such as bond-lengths or angles, are ignored. Depending on the structure of the network, the hydrogen-bonding graph can range from simple one dimensional rods to quite intricate three-dimensional networks.
Hydrogen bond notations are directed from donor (atom connected to H by covalent bond) to acceptor, which can be represented by directed edges: $A \longrightarrow B$. The result is therefore a directed graph. More precisely, since there may be multiple connections between two molecules, these are directed *multigraphs*. The connectivity of a node is the sum of the incoming and outgoing edges. For the sake of clarity, the symbols of the ions will be reduced to their central atom.
Formally, in a directed graph, an edge is represented by an ordered pair of vertices. If the hydrogen bond is disordered in a 1:1 manner or in the rare case of a symmetrical hydrogen bond, it is represented as a bi-directed edge: $A \longleftrightarrow B$. In such an undirected graph, edges correspond to unordered pairs of vertices.
To simplify infinite connectivity graphs, translationally equivalent molecules are merged to obtain voltage graphs [40]. The edges passing the unit cell boundary are labelled. The corresponding label indicates that the molecule in the unit cell is connected via a hydrogen bond to a molecule outside the unit cell and shows the translational component needed to map the molecule outside back onto the unit cell when crossing unit-cell boundaries [41]. The labelled voltage graph is a unique representation of a connectivity network in contrast to a quotient graph, which is missing the labels.

1.4.2.1 Two-dimensional hydrogen bond networks

Many structures presented here form two-dimensional hydrogen bonding networks. Graphs of such a network (i.e. ignoring directionality of the hydrogen bonding) are called Platonic nets, if all edges (and therefore all nodes) are topologically equivalent. Formally, a net is Platonic, if the automorphism group of the graph acts transitively on the edges. If all nodes (but not necessarily all edges) are equivalent, one speaks of an Archimedean net (the automorphism group acts transitively on the nodes) [42, 43]. The eleven Archimedean (including the three Platonic) nets are represented in Figure 1.2.
The Archimedean nets can be named unambiguously by specifying the polygons located about a node (representative for all nodes of an Archimedean net). The number of sides of the adjacent polygons is in the base, the exponent gives the number of subsequent equivalent polygons.

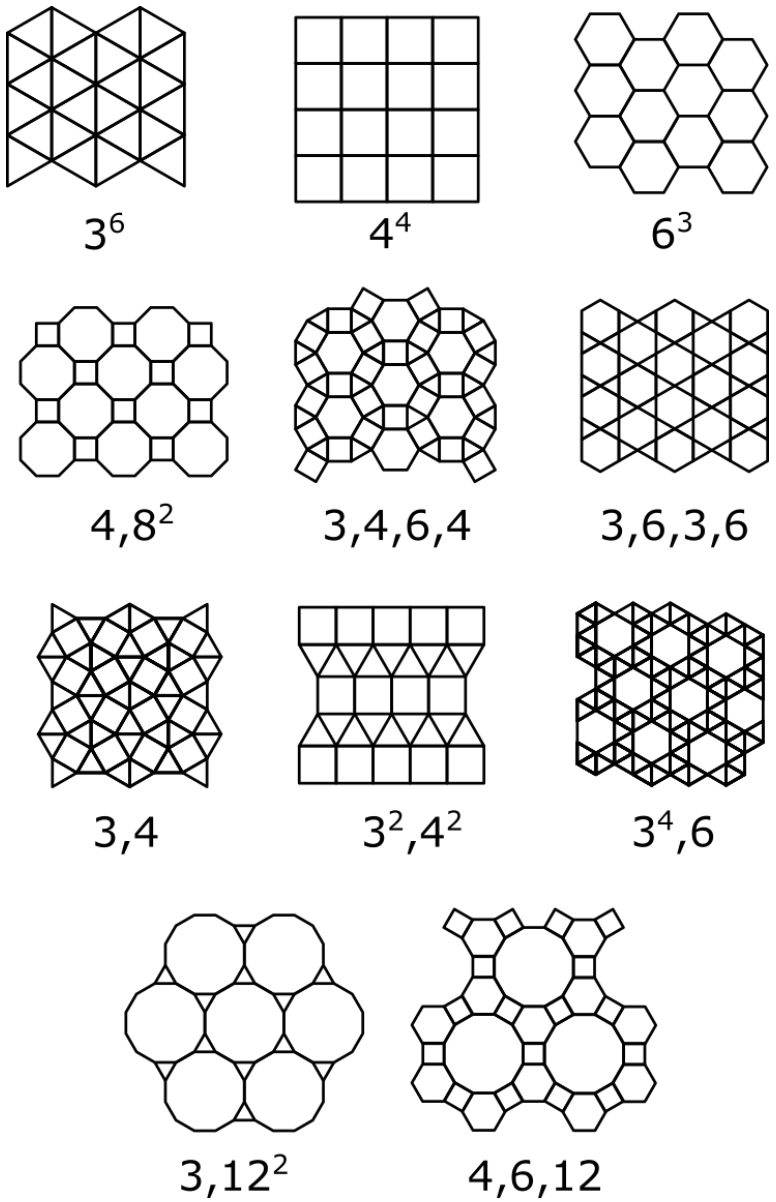

Figure 1.2: The eleven planar Archimedean nets, including the three Platonic nets [42].

2. Experimental

2.1 Characterisation

2.1.1 X-ray Powder diffraction (XPRD)

Preparation: PXRD measurements of fluorinated compounds turned out to be challenging. When the crystals were ground into a fine powder using a mortar and pestle (made from agate), fluorosilicates formed and were present in the powder diffraction pattern. On the flip side, crushing dry crystals in a plastic dish resulted in a preferred orientation of the crystallites, as well a relatively large crystallite size, leading to a bad statistic.
For this reason, whenever fluorides or free hydrofluoric acid were present, the contact to glass, stone and ceramics was avoided. Before measurement, the dry, fluoride containing crystals were crushed in the plastic container using a spatula. For measurement the samples were placed on cropped PMMA microscope slides, which resulted in a distinct continuous background signal.

Measurements at ambient conditions: All measurements were carried out on a PANalytical X´Pert Pro type PW 3040/60 with Cu-K$\alpha_{1,2}$-radiation. The instrument had a Bragg-Brentano geometry with a BBHD mirror and a 0.04° soller slit. The detector – a PIXCel 3D – was in a distance of 220 mm from the sample. In each case, the measurements were recorded from $2\vartheta = 5 to 80°$ with a recording speed of 0.1028°/s (overall measurement time about 12 min). The data collection was controlled by PANalytical DataCollector software.
For evaluation of the data, PANalytical Data Viewer and Highscore+ [44] were used. Rietveld refinements of the measurements were also performed in Highscore+.

Non-ambient, Temperature-dependent PXRD above room temperautre: For the high-temperature measurements, an Anton Paar TTK450 chamber was mounted on the diffractometer. The sample was heated in 5°C steps, at every temperature step, a measurement was recorded from $2\vartheta = 6$ to 60° within 9 minutes. The height adjustment correction was calibrated in advance. During the measurements and heating processes, a nitrogen flow of 0.5 L/min was maintained.

Non-ambient, Temperature-dependent PXRD below room temperature: Low-temperature (LT) measurements were performed in the Oxford Cryosystems Oxford PheniX chamber. Since no automatic height adjustment correction was undertaken, height errors resulting in a shift of reflections within a degree occurred. During the measurement, a nitrogen flow of 0,5 L/min was maintained.

Rietveld refinements: For all powder measurements, a Rietveld refinement with Highscore-Plus[44] was performed. The models obtained by single crystal diffraction were used and showed reasonable result and accuracy considering the circumstances and difference temperatures of powder and single-crystal X-ray diffraction. Only lattice parameters, crystallite size and orientation have been refined, but *not* atomic coordinates.

2.2 Crystal growth and single crystal selection

Crystallisation of most of the crystals was performed by slow evaporation of an aqueous solution of the product. $[H_5O_2]SbF_6$, $[(CH_3)_2NH_2]SbF_6 \cdot H_2O$, $[(CH_3)NH_3]H_2PO_2$, $[(CH_3)_2NH_2]H_2PO_2$ and $[(CH_3)_4N]H_2PO_2 \cdot {}_2H_2O$ were crystallised at 260 K after drying for 6 h *in vacuo*.
For the anhydrous phosphinic acid an aqueous H_3PO_2 solution (commercial, ca. 50 $\%_{wt}$) was held under vacuum (10^{-4} mbar) in a round bottom flask using a rotary vane vacuum pump for three days at 278 K while protected from light via Al foil. The colourless crystals were stored at 260 K.

2.2.1 X-ray single crystal diffraction (SC-XRD)

Single crystal selection process: Small amounts (40 mg) of the sample were suspended in Fomblin oil (Perfluoropolyether YR-1800, high-viscosity perfluoropolyether fluid; kinematic viscosity 1850 cSt at 20 °C) on a PMMA microscope slide under a transmission light Microscope at room temperature. After a proper single crystal was selected under the microscope using polarised light, the crystal was placed on the Kapton® micromounts sample holder. Excess oil was removed and the crystal immersed into the cold dry nitrogen stream of the diffractometer. In the case of highly hygroscopic samples or compounds with a melting point near or below room temperature, the selection of single crystals was conducted on a previously chilled plastic microscope slide under cool nitrogen stream generated by boiling liquid nitrogen.
This procedure was repeated until the quality of collected data was satisfying, or no suitable crystals were observed any more in the used batch. In such case, a new batch of single crystals was immersed in pefluorinated oil and the whole procedure repeated.

Measurement and data processing: The single crystal diffraction measurements were performed on a Bruker KAPPA APEX II single crystal diffractometer with a graphite-monochromatized Mo-$K\alpha$ -radiation (λ = 0.71073 Å) using fine sliced ω and ϕ scans. The measurements were carried out under a stream of dry nitrogen.
Data reduction was performed using the SAINT [45] software, the absorption correction by SADABS [45]. The structure solution and refinement against F^2 were done using SHELXT [46] and SHELXL [47], respectively. Non-H atoms were refined with anisotropic displacement parameters. Hydrogen atoms were located mostly from difference Fourier maps. The O–H distances of non-hydric Hs were restrained to 0.90 (4) Å, whereas the hydridic H atoms attached to P were refined freely. In order to confirm the symmetry of some refined structures the ADDSYM routine of the PLATON [48] software was applied. All crystal structures pictures were created with DIAMOND [49]. Measurements of distances and angles not directly derivable from the .cif files were determined in Diamond or JANA [50]. Super structures were transformed into the basic structure using JANA. If possible unit cell settings and origins were chosen in accordance with the literature. In the case of simple fluoroantimonates the Sb atom was placed in the origin $(0, 0, 0)^T$.

2.2.2 Nuclear magnetic resonance spectroscopy (NMR)

All spectra were recorded in dry deuterated solvents and using standard borosilicate glass tubes sealed with polyethylene caps. ^{1}H and ^{19}F- NMR spectra were recorded on a Bruker AVANCE-250 spectrometer and on a Bruker 200 FS FT-NMR. All NMR chemical shifts are reported in ppm. Shifts in ^{1}H-NMR are calibrated based on residual solvent resonance. Since many products obtained were hygroscopic or contained residual moisture from the reaction

solution, all substances were vacuum-dried for at least 6 h in the desiccator before measurement.

2.3 Synthesis

2.3.1 General techniques

Fluoride-free experiments used laboratory grade glass vessels. In contrast, the main vessel for growing crystals and storing the fluorinated compounds were small polystyrene vessels with volumes of 20 ml. The cups were sealed with screw on, air tight caps. If a slow evaporation was needed, two holes with a diameter of 3 mm were cut into the caps using a knife.
For heating samples or storing them at certain temperatures, two types of drying furnaces were used in combination with a platinum crucible: a Binder FD23 and a Heratherm OGH60 by Thermo Fischer scientific.
Two types of scales were used. For very precise weighting a Mettler Toledo AB 184-A3 was used, in all other situations a Mettler Toledo ME1002.
The centrifuge used for this work was a Rotofix 32 A table centrifuge by Hettich. It was operated with 3000 rpm usually for a time of 2 min.

Fluorination reactions and hydrolyses of fluorinated compounds were carried out in glassy carbon crucibles (18 ml) shown in Figure 2.1 with a matching cover. Solid-state reactions at temperatures above 300 °C were carried out in a platinum crucible.

Figure 2.1: Glassy carbon crucible.

For vacuum-drying of fluorinated compounds, a poly-carbonate desiccator was used with H_2SO_4 as desiccant, contained in a PTFE dish, as any glassware present in the desiccator led to the formation of fluorosilicates.
Hydrothermal experiments were performed in steel autoclaves with PTFE containers (inner volume of ca. 2 mL) at 220°C.

If not stated otherwise, the chemicals were used as supplied.

2.3.2 Antimonates

According to the literature, the synthesis of fluorinated antimonates can be realised via the reaction of super acids (SbF_5) [27, 29, 51]. In this thesis the conversion of antimony hydroxides and antimony oxides with HF_{aq} (48 $\%_{wt}$) was chosen. The precursors and reagents are easier to handle and comparably stable to moisture.

2.3.2.1 „Antimonic (V) acid“

An undefined, amorphous form of antimonic(V) acid in solution is obtained by hydrolysis of $SbCl_5$ in cold water. The compound is separated by centrifugation and decantation of the water and by-product HCl, resulting in a white, seemingly solid residue. The „solid“ liquefies when agitated, which is why filtration was not feasible. The product is immediately processed further to prevent conversion to Sb_2O_5 which reacts only very sluggishly. The exact stoichiometry of the product is unknown.

$$SbCl_5 + (6 + x)H_2O \xrightarrow{-5HCl} HSb(OH)_6 \cdot xH_2O \tag{2.1}$$

2.3.2.2 „Ammonium antimony oxide-hydroxide“ ($(NH_4)Sb(OH)_6 \cdot xH_2O$)

To the antimonic acid of the previous section an excess of aqueous NH_3 (25 $\%_{wt}$) is added. The resulting amorphous white solid is washed two times with distilled water, once with MeOH, separated by centrifugation and dried at room temperature. The exact stoichiometry of the product is unknown.

$$HSb(OH)_6 \cdot xH_2O + NH_3 \longrightarrow (NH_4)Sb(OH)_6 \cdot xH_2O \tag{2.2}$$

2.3.2.3 „Methylammonium antimony oxide-hydroxide“ ($[(CH_3)NH_3]Sb(OH)_6 \cdot xH_2O$)

To the antimonic acid an excess of ethanolic $MeNH_2$ (33 $\%_{wt}$) is added. The resulting amorphous white solid is washed two times with distilled water, once with MeOH, separated by centrifugation and dried at room temperature. The exact stoichiometry of the product is unknown.

$$HSb(OH)_6 \cdot xH_2O + (CH_3)NH_2 \longrightarrow [(CH_3)NH_3]Sb(OH)_6 \cdot xH_2O \tag{2.3}$$

2.3.2.4 „Dimethylammonium antimony oxide-hydroxide“ ($[(CH_3)_2NH_2]Sb(OH)_6 \cdot xH_2O$)

To the antimonic acid an excess of ethanolic $(CH_3)_2NH$ (40 $\%_{wt}$) is added. The product was precipitated from solution using acetone and dried without further purification, yielding an amorphous white solid of unknown stoichiometry.

$$HSb(OH)_6 \cdot xH_2O + (CH_3)_2NH \longrightarrow [(CH_3)_2NH_2]Sb(OH)_6 \cdot xH_2O \tag{2.4}$$

2.3.2.5 „Trimethylammonium antimony oxide-hydroxide“ ($[(CH_3)_3NH]Sb(OH)_6 \cdot xH_2O$)

To the antimonic acid an excess of ethanolic $(CH_3)_3N$ (33 $\%_{wt}$) is added. The product was precipitated from solution using acetone and dried without further purification, yielding an amorphous white solid of unknown stoichiometry.

$$HSb(OH)_6 \cdot xH_2O + (CH_3)_3N \longrightarrow [(CH_3)_3NH]Sb(OH)_6 \cdot xH_2O \tag{2.5}$$

2.3.2.6 „Tetramethylammonium antimony oxide-hydroxide“ ($[(CH_3)_4N]Sb(OH)_6 \cdot xH_2O$)

To the antimonic acid a solution of $(CH_3)_4NOH \cdot 5\,H_2O$ in H_2O (ca. 20 $\%_{wt}$) is added. The product was precipitated from solution using acetone and dried without further purification yielding an amorphous white solid of unknown stoichiometry.

$$HSb(OH)_6 \cdot xH_2O + (CH_3)_4NOH \cdot 5\,H_2O \longrightarrow [(CH_3)_4N]Sb(OH)_6 \cdot xH_2O + 6\,H_2O \tag{2.6}$$

2.3.2.7 „Antimony(V) oxide hydrate“ ($Sb_2O_5 \cdot xH_2O$)

An antimony(V) oxide hydrate of unknown stoichiometry was obtained by decomposition of $(NH_4)Sb(OH)_6 \cdot xH_2O$ at 220 °C for 3 days. The resulting glass-like solid was ground, yielding a yellow powder.

2.3.2.8 Rubidium antimony oxide(V) ($RbSbO_3$)

Finely powdered $Sb_2O_5 \cdot xH_2O$ (1.00 g) and Rb_2CO_3 (713.86 mg, 3.09 mmol) were mixed and the homogeneous powder placed in an alumina crucible. The crucible was heated to 720 °C for 15 h yielding the product as a white powder.

$$Sb_2O_5 \cdot xH_2O + Rb_2CO_3 \longrightarrow 2\,RbSbO_3 + xH_2O\uparrow + CO_2\uparrow \tag{2.7}$$

2.3.2.9 Caesium antimony oxide(V) ($CsSbO_3$)

Caesium antimony oxide(V) could not be produced similarly. At 600, 650 and 700 °C the reaction always resulted in a mixture of different oxides ($Cs_xSb_yO_z$) as indicated by PXRD. At higher temperatures above 700 °C potential product decomposes [52].

2.3.2.10 Alkali hexahydroxyantimonate(V) ($MSb(OH)_6$, M = Rb, Cs)

The corresponding alkali hexahydroxyantimonates were synthesised via displacement of the ammonium cation ($[NH_4]^+$) using corresponding alkali hydroxide solutions.
To a suspension of solid $(NH_4)Sb(OH)_6$ in water, alkali hydroxide solution (50 $\%_{wt}$) was added and heated until all solids dissolved. Displacement and expulsion of ammonia was observed using a wet pH-paper above the solution. The liquid was evaporated at room temperature, yielding the product as colourless mostly amorphous solid. The hydroxides are unstable in acidic solution and decompose to the respective salt and Sb_2O_5.

Rubidium hexahydroxoantimonate(V) ($RbSb(OH)_6$)

$$[NH_4]Sb(OH)_6 + RbOH \longrightarrow RbSb(OH)_6 + H_2O + NH_3\uparrow \tag{2.8}$$

Caesium hexahydroxoantimonate(V) ($CsSb(OH)_6$)

$$[NH_4]Sb(OH)_6 + CsOH \longrightarrow CsSb(OH)_6 + H_2O + NH_3\uparrow \tag{2.9}$$

2.3.3 Hexafluoroantimonate (V) ($[SbF_6]^-$)

All hexafluoroantimonates ($(CH3)_xNH_{4-x}$ (x = 0–4), Rb^+, Cs^+) were prepared using the same procedure with aqueous HF (45 $\%_{wt}$, 8 mL) in a glassy carbon crucible.

The precursors are fluorinated to the hexafluoroantimonate using aq. HF (40 $\%_{wt}$, 8 mL). The corresponding hexahydroxoantimonate(V) (1 g) was dissolved in an excess of HF. The solution was heated (80 °C) under stirring until crystals started to form. The solution was left to cool to room temperature, the remaining liquid was removed using a plastic pipette. The crude product was recrystallised from aq. HF (6 ml) and dried in a vacuum desiccator. Recrystallisation from water was not feasible, as it results in a partial hydrolysis of the product [26].

$$[Sb(OH)_6]^- + 6\,HF \longrightarrow [SbF_6]^- + 6\,H_2O \tag{2.10}$$

Alternately, $RbSbF_6$ was prepared using $RbSbO_3$, employing the method described by Kolditz and Rehak [53]. This method can also be used to create the Cs compound, if oxide with Cs:Sb = 1:1 is available.

$$MSbO_3 + 6\,HF \longrightarrow MSbF_6 + 3\,H_2O \tag{2.11}$$

Crystallisation of $[(CH_3)_2NH_2]SbF_6$ was problematic. The compound crystallises in the cubic, strongly disordered high-temperature modification, of which only the unit cell could be determined due to high disorder and poor quality of the crystals. Cooling below the phase transition temperature resulted in fracturing of the crystals. For this reason, crystallisation at -20 °C was attempted, but first crystals of $[H_5O_2]SbF_6$ precipitated, which were subsequently characterised and also prepared directly using the strategy described next. Then, crystals of the hydrate were obtained instead of the target compound.

2.3.3.1 Hydroniumhydrate hexafluoroantimonate (V) ($[H_5O_2]SbF_6$)

The hexafluoroantimonate of the Zundel-ion [54] ($[H_5O_2]^+$) is is already known and studied [55]. However, the new synthesis presented here is significantly simpler. Instead of using super acids, starting from SbF_5 and using an anhydrous pathway, the Zundel-salt is obtained by simple aqueous fluorination of the antimonic (V) acid.

$$HSb(OH)_6 \cdot H_2O + 6\,HF \longrightarrow [H_5O_2]Sb(OH)_6 \tag{2.12}$$

The compound is crystallised after removal of the excess of HF and water by crystallisation at -20 °C. Compared with the synthesis from Minkwitz[55], this crystallisation from aqueous solution also prevents dehydration on the surface of the crystals during removal of HF.

The reaction was not successful using $Sb_2O_5 \cdot xH_2O$ instead of $HSb(OH)_6 \cdot H_2O$ because of the low solubility of the oxide in HF under the described conditions.

2.3.3.2 Pentafluorohydroxoantimonate (V) ($[SbF_5(OH)]^-$)

The pentafluorohydroxoantimonates are obtained from the hexafluoroantimonate by recrystallization from water after application of heat (75 °C, 30 min). This was performed with 350 mg of $MSbF_6$ (M = K, Rb, Cs) in 5 mL of water.

$$[SbF_6]^- \xrightarrow{90\,^\circ C} [SbF_5(OH)]^- + HF \tag{2.13}$$

2.3.3.3 Tetrafluorodihydroxoantimonate (V) ($[SbF_4(OH)_2]^-$)

Potassium tetrafluorodihydroxoantimonate (V) ($KSbF_4(OH)_2$) For $KSbF_4(OH)_2$ the synthesis was successful when hydrolysing $KSbF_6$ (200 mg in 1.5 mL water) under hydrothermal conditions at 220 °C for 10 days. This resulted in a phase mixture of $KSbF_5(OH)$ and $KSbF_4(OH)_2$, where both of the products could be unambiguously determined using SC-XRD measurements.

$$KSbF_6 \xrightarrow{\text{HT } 220\,^\circ\text{C}} KSbF_4(OH)_2 + 2\,HF \tag{2.14}$$

Rubidium and caesium tetrafluorodihydroxoantimonate (V) (Rb and $CsSbF_4(OH)_2$) For the Rb and Cs compounds, the equilibrium is on the pentafluorohydroxoantimonate side. The tetrafluorodihydroxoantimonates could not be produced by simple hydrolysis.

$$MSbF_6 \xrightleftharpoons{\text{HT } 220\,^\circ\text{C}} MSbF_4(OH)_2 + 2\,HF \tag{2.15}$$

Instead, the products are obtained by stoichiometric reaction with the corresponding hexahydroxoantimonate.
In an PTFE autoclave inlay, 200 mg of the $M SbF_6$ were combined with 100 mg of the $M Sb(OH)_6$ (M = Rb, Cs) in 0.5 mL of water. The reaction was carried out at 220 °C for 2 months, yielding a clear solution. Crystallisation was performed by slow evaporation of the liquid.

$$2\,RbSbF_6 + RbSb(OH)_6 \xrightarrow{\text{HT } 220\,^\circ\text{C}} 3\,RbSbF_4(OH)_2 \tag{2.16}$$

$$2\,CsSbF_6 + CsSb(OH)_6 \xrightarrow{\text{HT } 220\,^\circ\text{C}} 3\,CsSbF_4(OH)_2 \tag{2.17}$$

2.3.4 Phosphinates

Because phosphinic acid and all phosphinates are sensitive to oxidation and spontaneous combustion above 100 °C, the contact to oxygen was minimised and all compounds stored at -20 °C under argon.

2.3.4.1 Anhydrous hypophosphorous acid (H_3PO_2)

A solution of aqueous H_3PO_2 (10 g, 50 $\%_{wt}$) was dried under vacuum in a round bottom-flask using a rotary vane vacuum pump for three days at room temperature protected from light. The colourless crystals were stored at 260 K. At room temperature or under light the anhydrous acid yellows readily.

2.3.4.2 Methyl-substituted ammonium phosphinates ($[(CH_3)_xNH_{4-x}]H_2PO_2$, $x = 1 - 4$)

To dried crystals of phosphinic acid (1.00 g, 15.15 mmol), ethanolic methyl-substituted amine solution was added and stirred at RT for 10 min. The solution was dried under vacuum and used without further purification. The exact ratios are summarised in Table 2.1.

Table 2.1: Reaction ratios of acid base reactions between H_3PO_2 and methyl-substituted amines.

	H_2PO_2		amine sulution		
	m (g)	**n (mmol)**		**V (mL)**	**n (mmol)**
$[(CH_3)NH_3]H_2PO_2$	1.00	15.15	33% in ethanol	5	32.12
$[(CH_3)_2NH_2]H_2PO_2$	1.00	15.15	40% in ethanol	4	31.80
$[(CH_3)_3NH]H_2PO_2$	1.00	15.15	33% in ethanol	5	20.91

$$H_3PO_2 + (CH_3)NH_2 \longrightarrow [(CH_3)NH_3]H_2PO_2 \tag{2.18}$$

$$H_3PO_2 + (CH_3)_2NH \longrightarrow [(CH_3)_2NH_2]H_2PO_2 \tag{2.19}$$

$$H_3PO_2 + (CH_3)_3N \longrightarrow [(CH_3)_3NH]H_2PO_2 \tag{2.20}$$

Tetramethylammonium phosphinate ($[(CH_3)_4N]H_2PO_2$) To aqueous H_3PO_2 (2 g, 50 $\%_{wt}$, 15.15 mmol) solid $(CH_3)_4NOH$ (1.38 g, 15.15 mmol) was added and stirred at RT for 10 min. The solution was dried under vacuum and used without further purification.

$$H_3PO_2 + (CH_3)_4NOH \longrightarrow [(CH_3)_4N]H_2PO_2 + H_2O \tag{2.21}$$

2.3.4.3 Guanidinium phosphinate (GuH_2PO_2)

To a stirred solution of phosphinic acid (50 $\%_{wt}$, 8.94 g) guanidinium carbonate (6.10 g) was added. After the gas evolution ceased, the solution was heated to 60 °C until crystals started to form. The cooled crystals were dried under vacuum overnight.
The remaining liquid was filtered off, the crystals washed with cold absolute ethanol, yielding colourless needle-like crystals (3.93 g, 46 %).

$$2\,H_3PO_2 + (Gu)_2CO_3 \longrightarrow 2\,GuH_2PO_2 + CO_2 + H_2O \tag{2.22}$$

2.3.5 Dihydridotetrafluorophosphate(V) anion trans-$[H_2PF_4]^-$)

The use of cations other than $[(CH_3)_3NH]^+$ for the preparation of the $[H_2PO_2]^-$ ion led to solutions that did not crystallise even at low temperatures.
Attempts were made with: K^+, Rb^+, Cs^+, $[(CH)NH_3]^+$, $[(CH)_2NH_2]^+$, $[(CH)_4N]^+$, Gu^+.

$$[H_2PO_2]^- + 4\,HF \rightleftharpoons [H_2PF_4]^- + 2\,H_2O \tag{2.23}$$

2.3.5.1 Trimethylammonium dihydridotetrafluorophosphate(V) ($[(CH_3)_3NH][H_2PF_4]$)

To liquid tetramethylammonium phosphinate (600 mg) an excess of HF (45 $\%_{wt}$, 5 mL) was added. The solution was stirred under heating at 120 °C for 30 min. The solution was dried in vacuum for two days until colourless crystals started to form. The product was stored under argon at -20 °C. The obtained colourless crystals were characterised by SC-XRD and NMR.

$$[(CH_3)_3NH][H_2PO_2] + 4\,HF \xrightleftharpoons{80\ °C,\ water} [(CH_3)_3NH][H_2PF_4] + 2\,H_2O \tag{2.24}$$

Alternatively, the reaction was also carried out by using anhydrous HF in the form of Olah's reagent (HF in pyridine) [56, 57]. Due to no heating equipment being available in inert, glass free conditions, this reaction could only be carried out at room temperature. In the argon-purged plastic desiccator using the glassy carbon crucible $[(CH_3)_3NH][H_2PO_2]$ (1 g) was dissolved in an excess of HF (in pyridine) and then stirred for 3 days. Water and pyridine were then removed *in vacuo* until crystals formed. The product was stored under argon at -20 °C.

$$[(CH_3)_3NH][H_2PO_2] + 4\,HF \xrightleftharpoons{RT,\ pyridine} [(CH_3)_3NH][H_2PF_4] + 2\,H_2O \tag{2.25}$$

3. Results

3.1 Chemistry

3.1.1 Using antimony(V) oxides as precursor versus SbF_5

The use of antimony(V) oxides or hydroxides as precursors for fluoroantimonates has been described before. However, up to now it has seen only few applications.[24, 31]. In contrast to the production of $[SbF_6]^-$ salts using SbF_5, the syntheses are simpler, cheaper, faster and less complicated. Since all the reactants are solid or liquid, the syntheses could be easily carried out on a laboratory scale, under the common safety regulation. The problem that many of the reaction solutions attack glass due to the properties of fluorides still exists, but no inert conditions had to be maintained. This meant that all the syntheses could be carried out faster and more conveniently as lengthy cooling and heating times were no longer necessary.

3.1.2 Synthesis overview

$SbCl_5$ was used as the ultimate precursor to all reaction paths, as it is cheaply available, even in high purity. Via hydrolysis and acid-base reaction, $[NH_4]Sb(OH)_6 \cdot xH_2O$ was prepared in one step. The intermediate hydrolysis product with putative stoichiometry was never isolated, owing to its undefined and unstable nature.
From the ammonium salt, the stoichiometric alkali hexahydroxo salts could simply be formed, since they displace the ammonia from the salt, which subsequently escapes from the solution in gaseous form. The difficulty here was that the reactant's $[NH_4]Sb(OH)_6 \cdot xH_2O$ molecular mass was not precisely known. An excess of the hydroxides (RbOH or CsOH) could not be easily separated afterwards. In addition, the hygroscopic properties of the hydroxides resulted in the product being present as a viscous paste. For this reason, the addition had to be done carefully and slowly. The addition was stopped as soon as the reactant had completely dissolved. For particularly clean products, $[NH_4]Sb(OH)_6 \cdot xH_2O$ was added in excess and unreacted portions separated by filtration after complete reaction.
This method could not be applied to the synthesis of the methylammonium precursors, since the corresponding methylamines possess a volatility comparable to that of ammonia. For this reason, they were prepared using the amines instead of ammonia during the acid-base reaction in the previous step. The corresponding methylammonium hexahydroxoantimonates have a rather high solubility and a low melting point, which led to a more difficult separation from the reaction solution.

A summary of the syntheses of the reactants, which were then further reacted with HF to give the hexafluoroantimonates, is given in Figure 3.1.

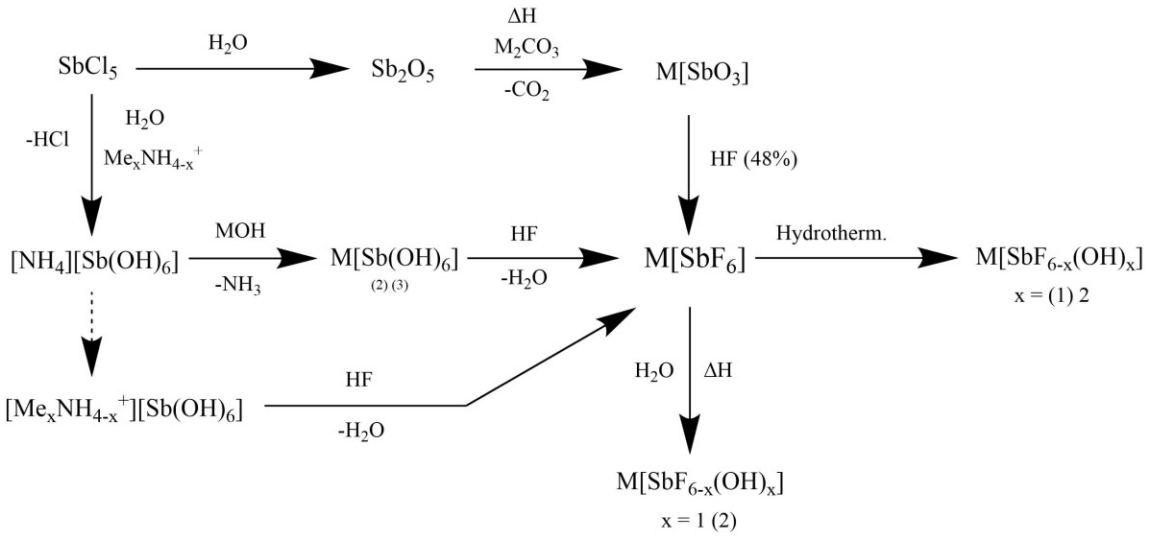

Figure 3.1: Overview of the synthesis of oxo- and fluoroantimonates(V).

The syntheses worked out can also be applied to the synthesis of other antimonates. Starting from the hydroxides, many of the oxides can be prepared as already described in 1938 [32]. For example, the synthesis of the Ag antimonates would also be easy, $AgSb(OH)_6$ has a low solubility [58] and can afterwards easily be separated from a soluble precursor like $KSb(OH)_6$.

3.1.2.1 Hydrolysis of $SbCl_5$

Conflicting and erroneous information on the hydrolysis of $SbCl_5$ in water is found in the literature [24]. This involves the addition of ammonia, which supposedly merely leads to a "second hydrolysis" in aqueous solution, further hydrolysing the oxides to hydroxides after the first one only substituting Cl^- with OH^-. However, as has been found out in this work, this is not correct. The addition of ammonia to the precursor in suspension certainly leads to the formation of the corresponding ammonium salt (Reaction 2.2). This product can be handled much more easily, since it forms a physically stable precipitate in contrast to the intermediate product. The existence of ammonium impurities is proved by the formation of $[NH_4]SbF_6$ after fluorination when using precursors obtained via the addition of ammonia. When no ammonia was used, $[H_5O_2]SbF_6$ was yielded after fluorination of the hydrolysis product.
Moreover, when $HSb(OH)_6 \cdot xH_2O$ that has been prepared with NH_3 is added to an alkaline solution, free NH_3 can be detected with wet universal pH paper. This suggests that NH_3 acts as a counter cation and not just as free ammonia to form a basic solution. Nevertheless, the $[NH_4]Sb(OH)_6$ intermediate is a good starting material for further syntheses since it is easy to purify, even though it is present with non-stoichiometric amounts of water of crystallisation and is amorphous according to PXRD measurements. Furthermore, it was observed that over time especially $HSb(OH)_6 \cdot xH_2O$ decomposes to $Sb_2O_5 \cdot xH_2O$, with significantly lowered reactivity and results in an insoluble off-white residue after further reactions.

3.1.2.2 Hydroxides versus oxides as precursor for fluorination

The fluoroantimonates were obtained via fluorination of antimony(V) hydroxides and oxides, whereby both behave in the same way during the reaction. The difference is that the hydroxoantimonates can be produced quickly and without much effort via the route described above, and they do not have to be precipitated for reaction with HF but can be reacted directly in solution. The oxides ($MSbO_3$), however, have to be produced at high-temperatures. For this

reason, the first option was mainly used during the work. Moreover, in the case of $M = \mathrm{Cs}$, the corresponding $CsSbO_3$ could not be prepared as a well-defined compound. This is due to the high volatility of Cs at the corresponding temperatures and the problem of the formation of various oxides in which Cs:Sb is not present in the desired 1:1 ratio [52]. This ratio is not necessarily needed, but as already described, surplus of Cs^+ leads to products being hygroscopic glass-like pastes instead of well-defined crystals.

3.1.3 Aqueous fluorination of Sb(V) compounds

Reaction of antimonate oxides and hydroxides with $40\%_{wt}$ HF invariably yielded fully fluorinated $[SbF_6]^-$, even under diluted conditions ($5\%_{wt}$ HF). This tendency towards complete fluorination when using aqueous HF was independent of the cations investigated (alkali metals and methylammonium compounds). After synthesis, the crystals are dissolved in aqueous hydrofluoric acid. Crystal growth must take place from aq. HF, as in water $[SbF_5(OH)]^-$ salts are formed as by-products.

3.1.4 Hydrolysis of Sb(V) compounds

Conversely, starting from the hexafluoroantimonate, even under harsh conditions (hydrothermal, 2 months at 220 °C), hydrolysis only yields the pentafluorohydroxo- or tetrafluorodihydroxoantimonate. These products still showed significant amount of $[SbF_5(OH)]^-$ and traces of $[SbF_6]^-$. Apparently, an equilibrium is established, which is difficult to influence due to the low volatility of HF in water. Probably the reverse reaction occurs during the evaporation of water when the crystals are grown.

$$[SbF_4(OH)_2]^- + 2\,HF \rightleftharpoons [SbF_5(OH)]^- + HF + H_2O\uparrow \rightleftharpoons [SbF_6]^- + 2\,H_2O\uparrow \tag{3.1}$$

The hydrolysis of the first F atom can easily be carried out by recrystallisation from boiling water. This is consistent via Raman studies, which showed that the compounds in solution exist almost exclusively as $[SbF_5(OH)]^-$ [34]. For the preparation of clean $[SbF_4(OH)_2]^-$, a stoichiometric 1:3 mixture of the hydroxide with the hexafluoroantimonate was chosen. Otherwise, no pure product could be obtained. During experiments, only up to two F atoms could be substituted by OH and crystallised successfully. In solution allegedly also trifluorotrihydroxy- and difluorotetrahydroxoantimonates are stable [26, 39].

3.1.5 Synthesis of dihydridotetrafluorophosphat $[H_2PF_4]^-$

The $[H_2PF_4]^-$-ion was already described as a K^+ and Cs^+ salts [59]. The compounds were created by forming adduct between H_2PF_3 and MF(M=K,Cs) using only well-passivated stainless steel or PTFE materials at temperatures well below 0°C [27].

$$H_2PF_3 + KF \xrightarrow{\text{-20 °C, 2 d}} KH_2PF_4 \tag{3.2}$$

$$H_2PF_3 + CsF \xrightarrow{\text{-20 °C, 2 d}} CsH_2PF_4 \tag{3.3}$$

During this work, a less involved synthesis was performed by fluorinating phosphinates.

3.1.5.1 Phosphinates

The starting point for the synthesis of $[H_2PF_4]^-$ salts was the preparation of RbH_2PO_2, CsH_2PO_2 and the four methyl-substituted ammonium phosphinates, which were obtained by simple acid-base reactions. The reactions with volatile amines are simpler than the analogous reaction of phosphoric acid (H_3PO_4) [37]. Since phosphinic acid has only one acidic proton, mixtures of salts (such as hydrogen and dihydrogen phosphates) are not obtained. For this reason, higher salts cannot be created. Therefore, the amines were used in a slight excess and the excess was evaporated before reaction with HF to prevent the formation of ammonium fluorides. From the clear solutions, hygroscopic crystals were obtained after evaporation for $[(CH_3)NH_3]H_2PO_2$, $[(CH_3)_2NH_2]H_2PO_2$ and $[(CH_3)_4N]H_2PO_2$. $[(CH_3)_3NH]H_2PO_2$ could not be isolated in crystalline form even after prolonged drying in vacuo over KOH. Heating above 100°C in air led to spontaneous decomposition with self-ignition, probably due to formed phosphane (PH_3) as decomposition product. Cooling to -20 °C resulted in a very viscous liquid and further cooling in liquid nitrogen only resulted in solidification to a glass-like solid.

3.1.5.2 Aqueous fluorination of P(I) salts

Crystalline product could only be obtained by fluorination of trimethylammonium phosphinate with aqueous HF (40 $\%_{wt}$) at elevated temperatures (75 °C). Due to the many variable parameters during the reaction, it has not yet been possible to work out an optimal strategy to obtain pure $[H_2PF_4]^-$ compound. The $[H_2PF_4]^-$ anion is highly sensitive to hydrolysis and reacts back to ($[H_2PO_2]^-$) in the presence of water.

$$[H_2PF_4]^- + 2\,H_2O \longrightarrow [H_2PO_2]^- + 4\,HF \tag{3.4}$$

The phosphinate anion ($[H_2PO_2]^-$) always cocrystallised to a variable degree with $[H_2PF_4]^-$, resulting in a mixed $[(CH_3)_3NH][H_2PF_2]_x[H_2PO_2]_{1-x}$ product. The phosphinate anion is able to form stronger hydrogen bonds with the cation ($[(CH_3)_3NH]^+$) compared to the $[H_2PF_4]^-$ anion, which probably favours the cocrystallisation. Using other methylammoniumphosphinates or alkaliphosphinates did not yield any crystalline product. An influence of basicity is unlikely, the employed methylammonium compounds have a similar basicity, whereby in aqueous solution the base strength of methylamine to trimethylamine decreases due to their solubility [60]. Increasing the amount of HF and excluding water by using hydrogen fluoride dissolved in pyridine (Olah's reagent) showed only incomplete conversion at room temperature. However, due to the difficult handling of the reaction mixture, it could not be fully clarified why this was the case. For this reason, the reaction conditions would still have to be optimized, which would however, only be possible by using more complex equipment.

3.2 Crystal structures

The crystal structures obtained by single crystal X-ray diffraction measurements will be discussed in the following chapters. Attention will be paid to the symmetry relationship of the structures. In particular, it will be shown that many structures can be derived from simple cubic structure types. The symmetry of the produced hexafluoroantimonates can all be derived from the cubic caesium chloride $Pm\bar{3}m$ base structure, where the fluoroantimonate is located on the Cl^--position and the cation on the Cs^+-position. However, especially for the hydroxylated fluoroantimonates, a very strong deviation from the cubic metrics can be observed owing to formation of hydrogen bonding. The structures of polymorphic compounds will be discussed in order of decreasing symmetry, if not specified otherwise.
The alkali hexafluoroantimonates can all be derived from a basic cubic structure. $KSbF_6$ has originally been described as crystallising in a cubic structure with space group $Ia3$. However, conflicting information about actual symmetry and phase transition temperature are found in the literature [33, 61, 62]. All the four investigated methylammonium hexafluoroantimonates, adopt a CsCl-like cubic structure at high-temperatures and form various superstructures on cooling.
As expected, partial hydrolysis of the $[SbF_6]^-$ anion generally leads to a lowering of the crystal symmetry. Likewise, in general, lower temperature structures are lower in symmetry. However, as discussed below, exceptions exist. For example, in some cases, the $[SbF_5(OH)]^-$ ion can appear in a disordered fashion on a higher-symmetry position. Some low-temperature phases are not in group/subgroup relation with respect to the corresponding high-temperature phases.

The crystallographic differentiation of F and O for the determination of the crystal structures was not trivial in many cases. It is especially difficult when no hydrogens can be localised. In this case, the differentiation took place via crystallographic and chemical considerations. A differentiation on the basis of the Sb—F/O distances was not feasible, as their distances often did not differ significantly. This is especially the case, when F's act as hydrogen bonds acceptors. Then the distance to the central atom increases.

3.3 „Cubic hexafluoroantimonate“

As already mentioned, all octahedral fluoroantimonates can be derived from the aristotype discussed in this chapter, that can be considered as isotypic with CsCl with the space group $Pm\bar{3}m$. In this theoretical structure, both the cation (M) and the central atom of the octahedral anion (Sb) are located on a position with the site symmetry of $m\bar{3}m$. The six symmetrically equivalent F are located along the fourfold axes, which aligns the octahedra along ⟨100⟩.
It is implied that the octahedral anion must be aligned in the case of a cubic structure due to the $m\bar{3}m$ site symmetry. If this is not the case, the point symmetry of this position and thus the symmetry of the crystal is reduced. Examples of this are the following real structures. Because of the other possible symmetries of the octahedral anion, the other possible site symmetries for the central atom Sb are as follows: $4/m$ (e.g. $[(CH_3)_4N]SbF_6$), $\bar{3}/3$ (e.g. $[NH_4]SbF_6$), 2 (e.g. $RbSbF_4(OH)_2$) and 1.
The hypothetical primitive cubic cell is shown in Figure 3.2. The unit cell boundaries are marked in red. In the following chapters, the primitive pseudo-cubic cell of the different crystal structures will also be highlighted in red.

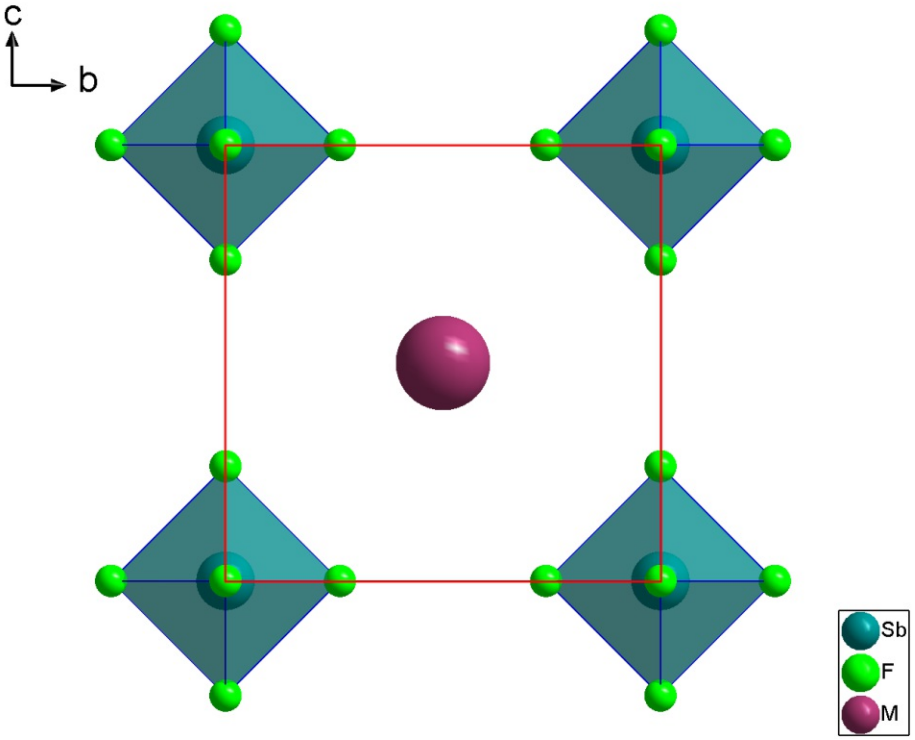

Figure 3.2: Crystal structure of a hypothetical cubic hexafluoroantimonate viewed down in [001].

Based on this simple structure, the symmetry descents can be deduced easily. In the case of a symmetry descent, the octahedral anions rotate from the ⟨100⟩ directions, so that the F are no longer located on a fourfold axis. This leads to a loss of point symmetry or the generation of superstructures.

3.4 Hydroniumhydrate hexafluoroantimonate ($[H_5O_2]SbF_6$)

The hydroniumhydrate cation ($[H_5O_2]^+$), also known as "Zundel" cation [54], is formally a hydrate of the hydronium ion ($[H_3O]^+ \cdot H_2O$). The three possibilities of how the $[H_5O_2]^+$ ion can be present within the crystal structure are shown in Figure 3.3.

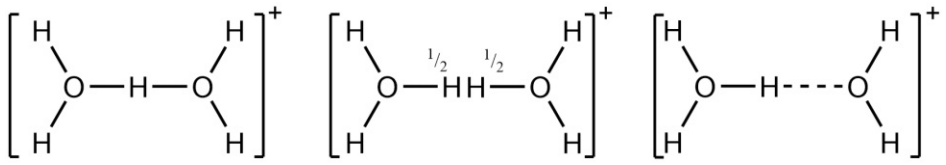

Figure 3.3: From left: symmetrical, disordered and ordered asymmetrical hydroniumhydrate ion.

$[H_5O_2]SbF_6$ has already been described in literature [55] as well as numerous other $[H_5O_2]^+$ compounds [63]. There, it was formed during the reaction of phosphorous acid with HF/SbF_5 at low-temperatures under inert gas. In contrast to the synthesis presented here, the reaction was performed under exclusion of water and the water molecule of $[H_5O_2]^+$ was formed via a side reaction. In their case, the bridging hydrogen positions were not split, resulting in a symmetrical cation.
In our case, the reaction used aq. HF ($40\%_{wt}$) as solvent, which means that during the reaction and crystallisation a stoichiometric excess of water is present. Still, only crystals of the $[H_5O_2]^+$ salt formed and no higher hydrates, such as $[H_7O_3]^+$ were obtained in single crystalline form. Powder measurements were not possible due to the low melting point (below 0 °C) of the reaction product.
The non-hydrated hydronium salt ($[H_3O]SbF_6$) has been described and can be obtained via removal of water from the hydrate ($[H_5O_2]SbF_6$) [55]. The highest known hydrate that has been described for $HSbF_6$ is the dihydrate, not counting $HSbF_6 \cdot 5\,H_2O$, which is better described as a clathrate hydrate [64].

$[H_5O_2]SbF_6$ crystallises below 0 °C in small colourless crystals in the triclinic crystal class in the space group $P\bar{1}$ (No. 2).

Cell (200 K): $a = 6.5088(6)$ Å, $b = 7.4912(6)$ Å, $c = 8.1258(7)$ Å, $\alpha = 116.384(2)°$, $\beta = 93.548(2)°$, $\gamma = 112.078(2)°$, $V = 316.16(5)$ Å^3, $Z = 2$

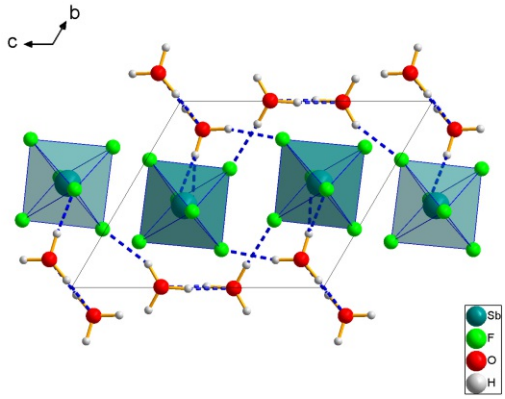

Figure 3.4: Crystal structure of $[H_5O_2]SbF_6$) viewed down [100].

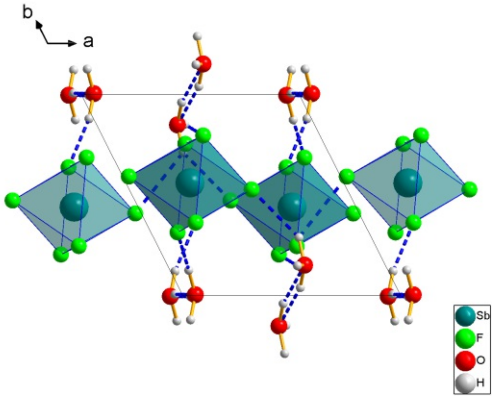

Figure 3.5: Crystal structure of $[H_5O_2]SbF_6$) viewed down [001].

According to the difference Fourier maps, the bridging H atom was clearly disordered. This is in contrast to the findings of Minkwitz[55]. The bridging H atoms of both $[H_5O_2]^+$ ions are disordered about centres of inversion (occupancy $\frac{1}{2}$). The terminal H atoms form a three-dimensional hydrogen bond network with the neighbouring anions. The hydrogen bonding network can be decomposed into layers parallel to (101), as shown of Figure 3.6. The terminal H atoms of $[H_5O_2]^+$ not involved in Figure 3.6 connect adjacent layers forming the 3D network.

The Sb—F bond lengths and F—Sb—F angles deviate only marginally from regular octahedral geometry and match well with the known hexafluoroantimonates [65]. The unit cell contains two symmetrically independent $[H_5O_2]^+$ cations located on centres of inversion with similar O—O(a) distances (2.4088(26) and 2.4014(17) Å). The F—M—F angles deviate by a maximum of 1.5° from the right angle.

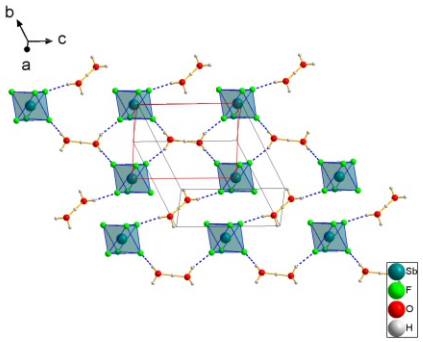

Figure 3.6: Structure of one layer of the hydrogen bond network of $[H_5O_2]SbF_6$ viewed down [211].

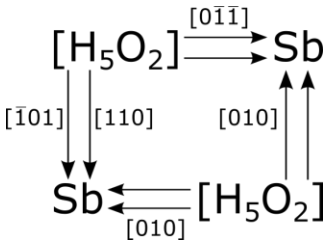

Figure 3.7: Voltage graph of the three-dimensional periodic hydrogen bonding network of $[H_5O_2]SbF_6$.

Table 3.1: Atomic parameters of $[H_5O_2]SbF_6$.

Atom	Wyck.	Site	occ.	x/a	y/b	z/c	U_{eq}/U_{iso} (Å^2)
Sb1	2i	1	1	0.29375(2)	0.56008(2)	0.25725(1)	0.01612(4)
F1	2i	1	1	0.3629(2)	0.7544(2)	0.1619(2)	0.0312(3)
F2	2i	1	1	0.4643(2)	0.7962(2)	0.50674(18)	0.0313(2)
F3	2i	1	1	0.2273(2)	0.3623(2)	0.3521(2)	0.0357(3)
F4	2i	1	1	0.1222(2)	0.3140(2)	0.01305(19)	0.0348(3)
F5	2i	1	1	0.5611(2)	0.5275(2)	0.2164(2)	0.0326(3)
F6	2i	1	1	0.0279(2)	0.5918(2)	0.3022(2)	0.0353(3)
O1	2i	1	1	0.3707(3)	0.8486(3)	0.8464(2)	0.0329(3)
O2	2i	1	1	-0.0593(3)	-0.0039(3)	0.3543(2)	0.0306(3)
H6	2i	1	1	0.333(5)	0.7115(16)	0.817(4)	0.057(8)
H3	2i	1	1	0.405(5)	0.852(5)	0.746(3)	0.051(8)
H4	2i	1	1	0.021(4)	0.121(3)	0.358(5)	0.054(9)
H5	2i	1	1	-0.086(5)	-0.126(3)	0.250(2)	0.050(8)
H2	2i	1	0.5	0.442(8)	0.960(6)	0.963(3)	0.028(13)
H1	2i	1	0.5	-0.033(10)	0.006(11)	0.465(4)	0.030(13)

Deviation from the cubic metrics: Event though the structure of $[H_5O_2]SbF_6$ can be related to the CsCl structure, the deviation from cubic metrics are pronounced owing to the cation being elongated. This becomes particularly clear from the metric parameters of the basic structure, where the axes deviate very strongly from each other and the angles are far from 90°.
The transformation matrix from the triclinic into the primitive cubic setting is $\begin{pmatrix} 0.5 & 0.5 & -0.5 \\ 0 & 1 & 0 \\ 0.5 & 0.5 & 0.5 \end{pmatrix}$. Here, the volume of the actual cell is twice as large as the volume of the pseudo-cubic basic structure. This is due to the two orientations of the elongated cations in the crystal. Furthermore, a 24-fold symmetry descent of the point symmetry takes place. Of the symmetry elements of the regular cubic cell, only the inversion centres remain.

Table 3.2: Pseudo-cubic metrics of $[H_5O_2]SbF_6$ after transformation into the pseudo-cubic primitive cell.

Compound **$[H_5O_2]SbF_6$**	**a** (Å)	**b** (Å)	**c** (Å)	α (°)	β (°)	γ (°)
pseudo-cubic metrics:	6.0168(5)	5.0460(3)	5.3605(4)	102.634(1)	87.238(1)	84.760(1)

3.5 Rhombohedral hexafluoroantimonates (MSbF$_6$, M = Rb, Cs, [NH$_4$])

After fluorination the hexafluoroantimonates crystallise at room temperature in large, colourless crystals with trigonal symmetry in the space group $R\bar{3}$ (No. 148). The structures are isotypic to KAsF$_6$ [18] in contrast to KSbF$_6$ which is reported as being cubic ($P\bar{4}2m$) or tetragonal ($P4_2/mcm$) [61].

The Sb atom occupies the special position $(0,0,0)^T$ with $\bar{3}$ symmetry and is octahedrally coordinated by six F atoms. The [SbF$_6$]$^-$ ion is located on a $\bar{3}$ position and forms a practically regular octahedron. The Rb—F and Cs—F distances, range from 3.1563(11) Å (RbSbF$_6$) to 3.3279(9) Å (CsSbF$_6$). In contrast to the arsenates [31], these are not the shortest M—F bonds, the shortest ones being the three M—F bonds the (001) plane of three separate octahedra: 2.9603(11) Å (RbSbF$_6$) and 3.1082(9) Å (CsSbF$_6$). Summary of geometric parameters in compiled in Table 3.3.

Table 3.3: Interatomic distances and angle of RbSbF$_6$, CsSbF$_6$ and [NH$_4$]SbF$_6$ at 100 K.

	Sb(1)—F(1) (Å)	M—**F** (Å)	**Sb(1)—M(1) in [001]** (Å)	**∠F(1)—Sb(1)—F(1)** (°)
RbSbF$_6$	1.8921(8)	3.1563(11)	3.879(1)	91.30(4)
CsSbF$_6$	1.8895(8)	3.3279(9)	4.0627(8)	90.89(3)
[NH$_4$]SbF$_6$	1.8902(9)	3.1594(11)	3.8795(8)	91.19(5)

Deviation from the cubic structure: To compare the metrics to the metrics of the putative $Pm\bar{3}m$ CsCl type structure, the primitive setting of the $R\bar{3}$ space group is used. In the space group $R\bar{3}$, only one of the four $\bar{3}$ axes remains from the cubic $Pm\bar{3}m$ beside the centres of inversion, due to the different orientation of the octahedral anion decreasing the site symmetry $m\bar{3}m$ by a factor of eight.
The MSbF$_6$ (M = Rb, Cs, [NH$_4$]) show only a small distortion compared to the cubic structure. The transformation matrices from the obverse rhombohedral into the primitive cubic setting is $\begin{pmatrix} 2/3 & -1/3 & 1/3 \\ 1/3 & 1/3 & 2/3 \\ 1/3 & 1/3 & 2/3 \end{pmatrix}$ and the parameters obtained are listed in Table 3.4. Owing to one threefold axis being preserved from the cubic structure, the condition $a = b = c$ remains. Because of the very different orientation of the octahedral cations, the angles undergo a significant change from 90° to 96.12(1)° for Cs, 96.64(1)° for [NH$_4$] and 96.68(2)° for the Rb structure respectively.

The individual structures will be described in more detail in the next sections.

Table 3.4: Pseudo-cubic metrics of MSbF$_6$ (M = Rb, Cs, [NH$_4$]) after transformation into the pseudo-cubic primitive cell.

Pseudo-cubic metrics of	**a** (Å)	**b** (Å)	**c** (Å)	α (°)	β (°)	γ (°)
RbSbF$_6$	5.1131(14)	5.1131(6)	5.1131(14)	96.6794(192)	96.679(25)	96.679(19)
CsSbF$_6$	5.2894(8)	5.2894(4)	5.2894(8)	96.1242(111)	96.1242(139)	96.1242(111)
[NH$_4$]SbF$_6$	5.1098(8)	5.1098(4)	5.1098(8)	96.6449(115)	96.6449(144)	96.6449(115)

3.5.1 Rubidium hexafluoroantimonate ($RbSbF_6$)

Cell (100 K): $a = 7.640(2)$ Å, $c = 7.758(2)$ Å, $V = 392.16(23)$ Å^3, $Z = 3$

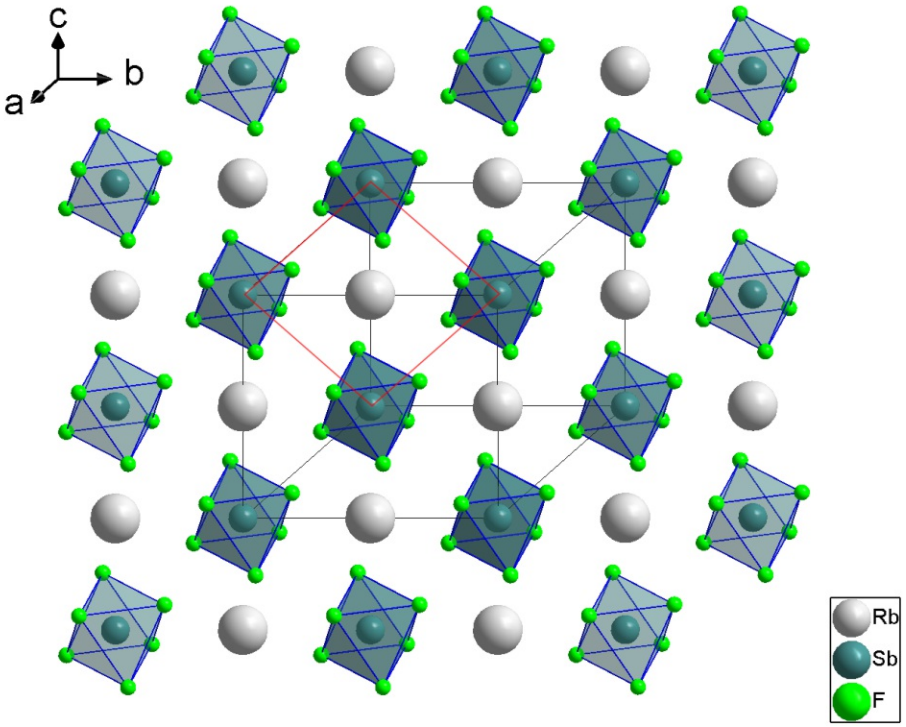

Figure 3.8: Crystal structure of $RbSbF_6$ viewed down [302] showing the distorted cubic structure with the primitive pseudo-cubic cell highlighted in red.

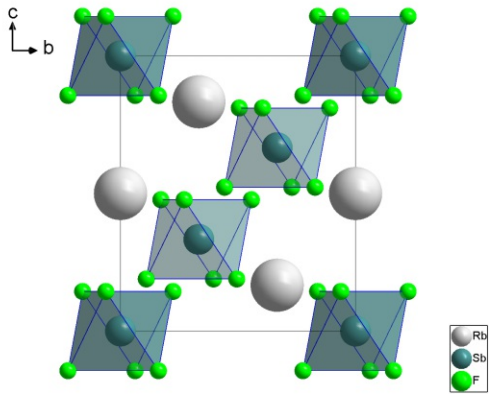

Figure 3.9: Crystal structure of $RbSbF_6$ viewed down [100].

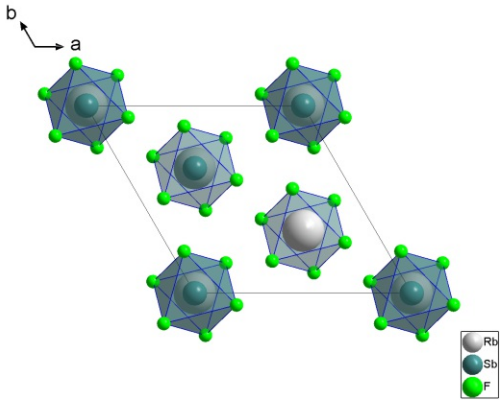

Figure 3.10: Crystal structure of $RbSbF_6$ viewed down [001].

Table 3.5: Atomic parameters of $RbSbF_6$.

Atom	Wyck.	Site	x/a	y/b	z/c	U_{eq}/U_{iso} (Å^2)
Rb1	3b	$\bar{3}$	0	0	1/2	0.00895(6)
Sb1	3a	$\bar{3}$	0	0	0	0.00615(6)
F1	18f	1	0.22368(12)	0.16129(12)	-0.14396(11)	0.01334(15)

3.5.2 Caesium hexafluoroantimonate ($CsSbF_6$)

Cell (100 K): $a = 7.8692(11)$ Å, $c = 8.1255(16)$ Å, $V = 435.75(15)$ Å^3; $Z = 3$

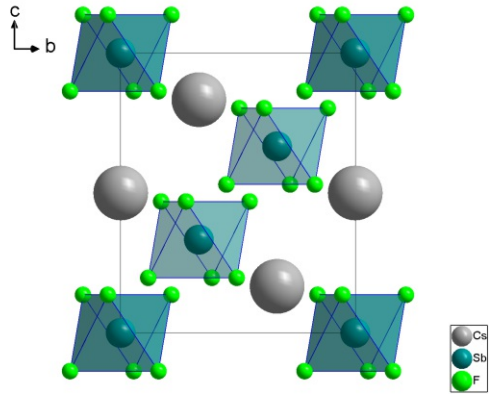

Figure 3.11: Crystal structure of $CsSbF_6$ viewed down [100].

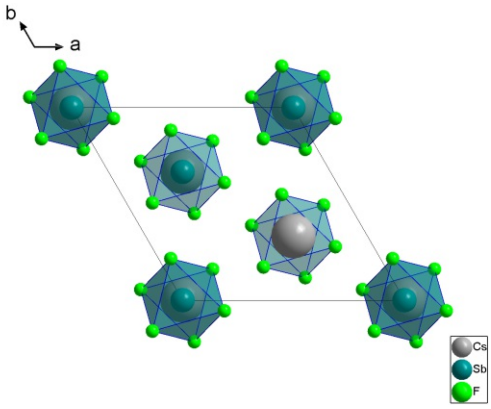

Figure 3.12: Crystal structure of $CsSbF_6$ viewed down [001].

Compared to $RbSbF_6$, owing to the additional space required by the Cs^+ cation, the substitution results in an increase of the unit cell volume by 11.1 %. The factor c/a increases from 1.026 (Rb) to 1.051 (Cs), which means that the cell is 2.4 % more elongated in the direction of the threefold axis when compared to the $RbSbF_6$.

Table 3.6: Atomic parameters of $CsSbF_6$.

Atom	Wyck.	Site	x/a	y/b	z/c	U_{eq}/U_{iso} (Å^2)
Cs1	3b	$\bar{3}$	0	0	1/2	0.00941(5)
Sb1	3a	$\bar{3}$	0	0	0	0.00737(5)
F1	18f	1	0.21614(11)	0.16099(11)	-0.13633(10)	0.01563(15)

3.5.3 Ammonium hexafluoroantimonate ($[NH_4]SbF_6$)

Although various nitrogen containing salts of the $[SbF_6]^-$ anion such as hydrazinium [66, 67] and monofluorammonium salts [35] have been structurally characterised, to our knowledge the crystal structure of $[NH_4]SbF_6$ has not been described up to now.

3.5.3.1 Single crystal structure analysis $[NH_4]SbF_6$

The low-temperature phase of the compound crystallises with trigonal symmetry in the space group $R\bar{3}$ (No. 148) or $R3$ (No. 146). Owing to the small contribution of H to the X-ray diffraction pattern it is not possible to tell whether the hydrogens of the ammonium ion are really disordered (resulting in the centrosymmetric space group $R\bar{3}$), which corresponds to a completely random arrangement in the crystal, or there exist distinct twinned domains (resulting in the Sohncke space group $R3$). It should be noted that the difference between a disordered and a twinned structure is merely a matter of domain size.
The ammonium salt is in principle isotypic to the previous alkali compounds, if the space group $R\bar{3}$ is applicable. In case of $R3$ the centre of inversion would be lost. This direct group-subgroup relationship could be described by a *translationengleiche* symmetry descent $t2$ (Figure 3.13).

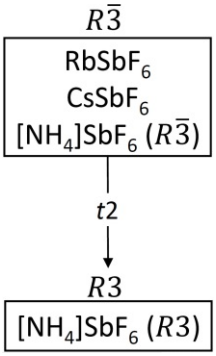

Figure 3.13: Bärnighausen family tree of rhombohedral hexafluoroantimonates.

Cell (100 K): $a = 7.6330(11)$ Å, $c = 7.7590(16)$ Å, $V = 391.50(14)$ Å^3, $Z = 3$
The interatomic distances of $[NH_4]SbF_6$ are nearly identical compared to $RbSbF_6$. The distance N—F is just slightly lager, due to the different sizes of the cations, and the Sb—F distance is slightly shortened. Compared to $RbSbF_6$, the exchange of the cation results in a decrease of the unit cell by only 0.2 % and c/a is just 0.9 % smaller compared to the $RbSbF_6$.

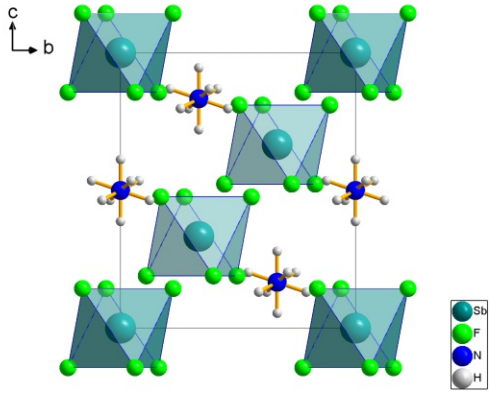

Figure 3.14: Crystal structure of $R\bar{3}$-$[NH_4]SbF_6$ viewed down [100].

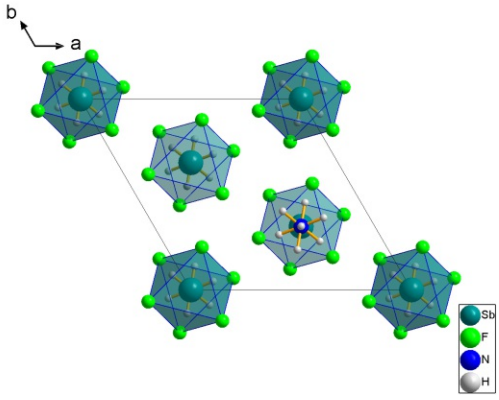

Figure 3.15: Crystal structure of $R\bar{3}$-$[NH_4]SbF_6$ viewed down [001].

Table 3.7: Atomic parameters of $R\bar{3}$-$[NH_4]SbF_6$.

Atom	Wyck.	Site	occ.	x/a	y/b	z/c	U_{eq}/U_{iso} (Å^2)
Sb1	3a	$\bar{3}$	1	1/3	2/3	2/3	0.01091(5)
F1	18f	1	1	0.55699(14)	0.72833(14)	0.52312(12)	0.01962(14)
N1	3b	$\bar{3}$	1	2/3	1/3	5/6	0.0161(4)
H1	6c	3	0.5	2/3	1/3	0.721(3)	0.07(5)
H2	18f	1	0.5	0.622(17)	0.412(15)	0.869(12)	0.05(2)

3.5.4 PXRD analysis of rhombohedral hexafluoroantimonates

For examination of the bulk crystals at room temperature, a Rietveld refinement of the single-crystal model was performed. The resulting patterns are in good agreement and are shown in Figures 3.16, 3.17 and 3.18. The resulting cell parameters at room temperature are listed below for $RbSbF_6$, $CsSbF_6$ and $[NH_4]SbF_6$ in Table 3.8. As expected, all cell parameters at

room temperature are increased when compared to 100 K, whereby in [001] the expansion is clearly more pronounced.

Table 3.8: Overview of cell parameters of $RbSbF_6$ at 100 K from SC-XRD Data and 300 K from Rietveld refinement.

	a (Å)	b (Å)	c (Å)	α (°)	β (°)	γ (°)	V (Å^3)	**T (K)**
$RbSbF_6$	7.66129	7.66129	7.85342	90	90	120	399.2023	300
	7.640(2)	7.640(2)	7.758(2)	90	90	120	392.16(23)	100
increase (%)	0.28	0.28	1.23			1.80		
$CsSbF_6$	7.90781	7.90781	8.25910	90	90	120	447.2761	300
	7.8692(11)	7.8692(11)	8.1255(16)	90	90	120	435.75(15)	100
increase (%)	0.49	0.49	1.64			2.65		
$[NH_4]SbF_6$	7.67886	7.67886	7.86433	90	90	120	401.5926	300
	7.6330(11)	7.6330(11)	7.7590(16)	90	90	120	391.50(14)	100
increase (%)	0.60	0.60	1.36				2.85	

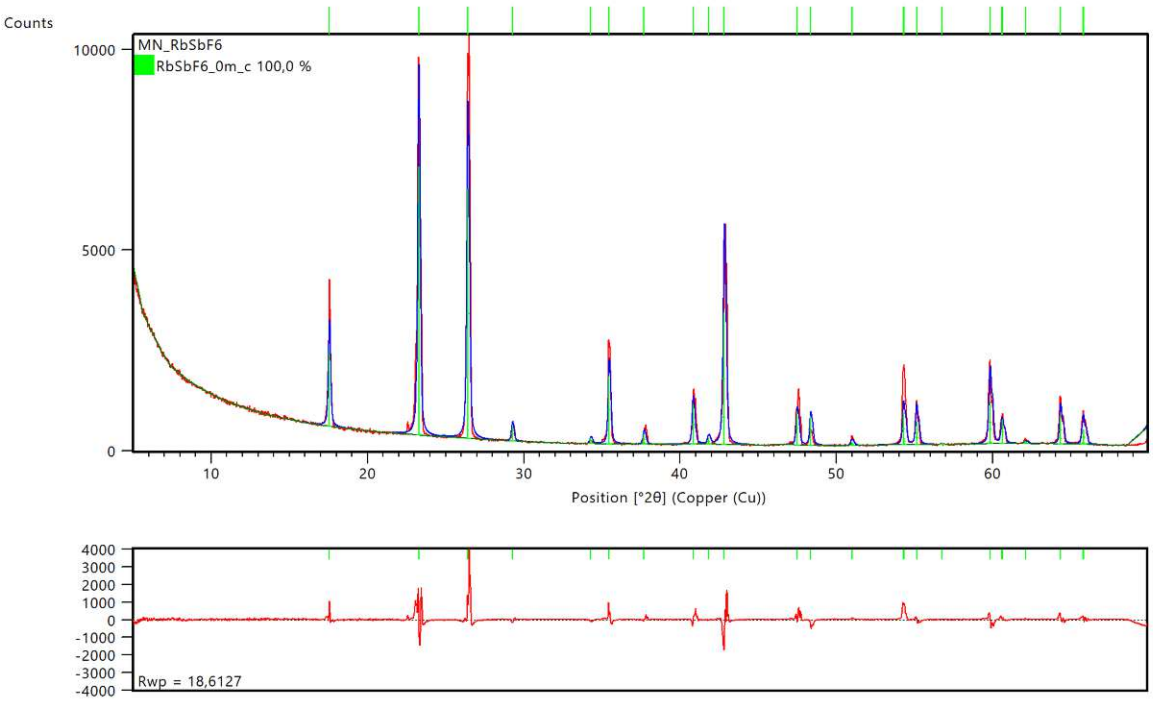

Figure 3.16: PXRD of $RbSbF_6$ at 300 K (red) with Rietveld refinement of a model derived from single crystal diffraction (blue) with difference plot (in red) below.

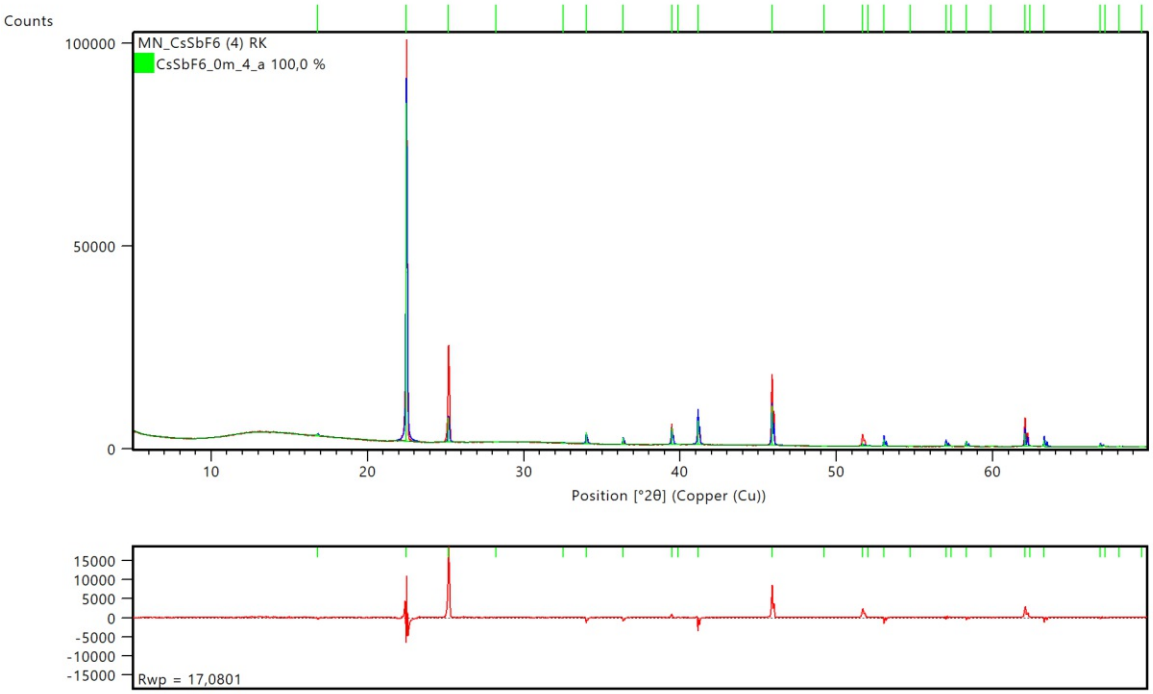

Figure 3.17: PXRD of $CsSbF_6$ at 300 K (red) with Rietveld refinement of a model derived from single crystal diffraction (blue) with difference plot (in red) below.

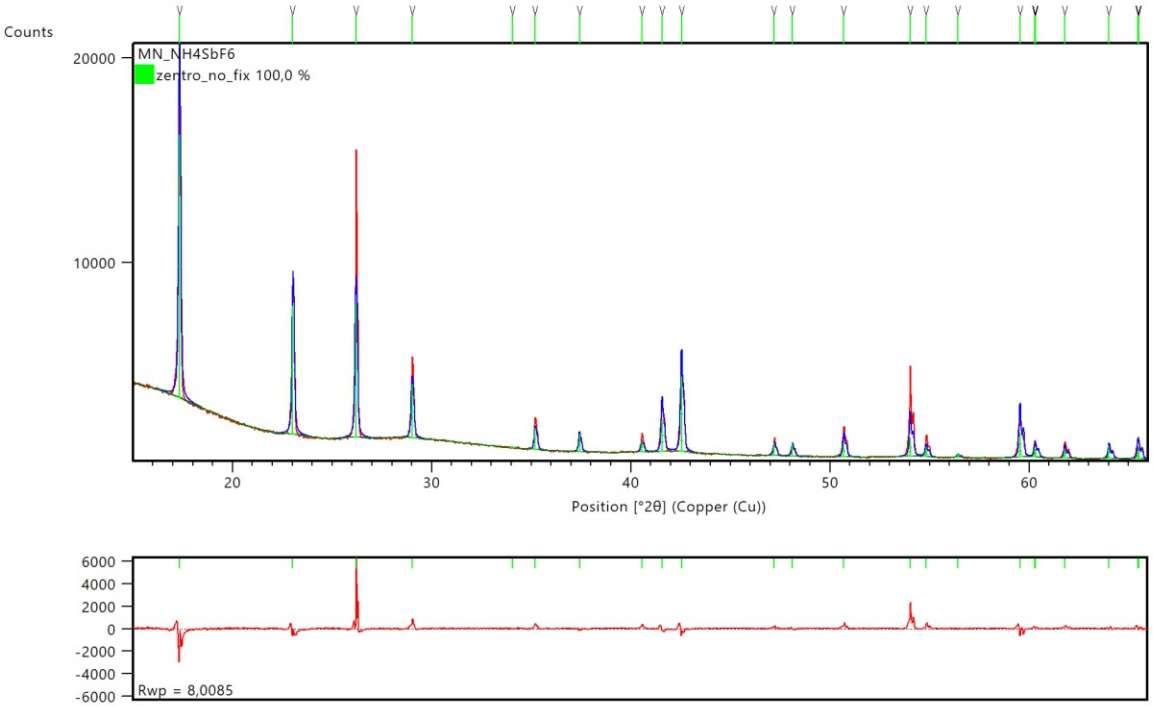

Figure 3.18: PXRD of $[NH_4]SbF_6$ at 300 K (red) with Rietveld refinement of a model derived from single crystal diffraction (blue) with difference plot (in red) below.

3.6 Pentafluorohydroxoantimonates (V) ($[SbF_5(OH)]^-$)

Even though the OH groups could not be unambiguously evidenced by X-ray diffraction of Rb, Cs and $[NH_4]SbF_5(OH)$, the nature of the anion was proved by NMR spectroscopy, which is described in more detail in the corresponding chapter. Only negligible amounts of $[SbF_6]^-$ were evidenced in NMR spectra. When $RbSbF_5(OH)$ was crystallised, also crystals of $RbSbF_5(OH) \cdot (RbF_2H)_2$ precipitated.
The crystals of Rb, Cs and NH_4 produced in this way were all isotypic with the unhydrolysed compounds. Even though the point symmetry of the $[SbF_5(OH)]^-$ anion of $4/mmm$ not compatible with the site symmetry $\bar{3}$ of $[SbF_6]^-$ in the hydrolysed compounds, overall space group symmetry is retained owing to disorder. Formally, every F position in the $[SbF_5(OH)]^-$ compound corresponds to a 5:1 occupationally disordered F/OH position, resulting in a „$[Sb(F_{5/6}/OH_{1/6})_6]^-$ "-anion. Potential superstructures could not be evidenced due to the small difference of F and OH in X-ray diffraction experiments. Likewise, no diffuse scattering indicative of the nature of the disorder was observed for the same reason. Neutron diffraction could provide additional information (location of the H atom). However, in contrast to the hexafluoroantimonates, the crystals of the pentafluorohydroxoantimonates were all tiny and thus not suitable for neutron diffraction.
The cell parameters are only slightly changed with respect to the unhydrolysed compounds (Table 3.9).
Two effects must be taken into account in this deviation: on the one hand, the incorporation of OH instead of F leads to an expansion of the structure, since the H atom needs space. On the other hand as O in the structure can now act as a hydrogen bond donor, the hydrogen bonding of OH$\cdots$F leads to a contraction of the structure. The second effect is dominant at 100 K, resulting in a small reduction of the cell parameters. Comparison of known cell parameters at room temperature ($CsSbF_5(OH)$ [25]) and the results from Rietveld refinement shows that at this temperature the cell occupies a larger volume compared to the hexafluoroantimonate ($CsSbF_6$ [36]), which means that at room temperature the first effect is predominant.

Table 3.9: Overview of pentafluorohydroxoantimonate cell parameters at 100 K, all isotypic and crystallizing in the $R\bar{3}$ space group.

Compound	a **(Å)**	c **(Å)**	V **(Å^3)**	**T (K)**
$RbSbF_6$	7.640(2)	7.758(2)	392.16(23)	100
$RbSbF_5(OH)$	7.6421(10)	7.7335(11)	391.14(12)	100
$CsSbF_6$	7.8692(11)	8.1255(16)	435.75(15)	100
$CsSbF_5(OH)$	7.8626(5)	8.1138(5)	434.40(6)	100
$[NH_4]SbF_6$	7.6330(11)	7.7590(16)	391.50(14)	100
$[NH_4]SbF_5(OH)$	7.6128(8)	7.7282(9)	387.88(9)	100

3.6.1 Potassium pentafluorohydroxoantimonate $KSbF_5(OH)$

Among the studied pentafluorohydroxoantimonates, the potassium salt is particular. Although the cation K^+ differs only in size from Rb^+ and Cs^+, crystallisation results in a novel crystal structure (Figure 3.19), which is not isotypic to the unhydrolysed compound.
This result is also very interestingly, because $[KSbF_5(OH)]^-$ is closely related in symmetry to the corresponding fluoroarsenate compound ($KAsF_5(OH)$), both crystallise in seemingly closely related orthorhombic space groups, viz *Pbca* (Sb) and *Pnab* (As) [18]. Nevertheless, both are structurally surprisingly unrelated. Whereas the H-bonding of $KSbF_5(OH)$ forms tetramers, in $KAsF_5(OH)$ it forms infinite chains and thus a completely different crystal structure, with a coincidentally closely related symmetry.

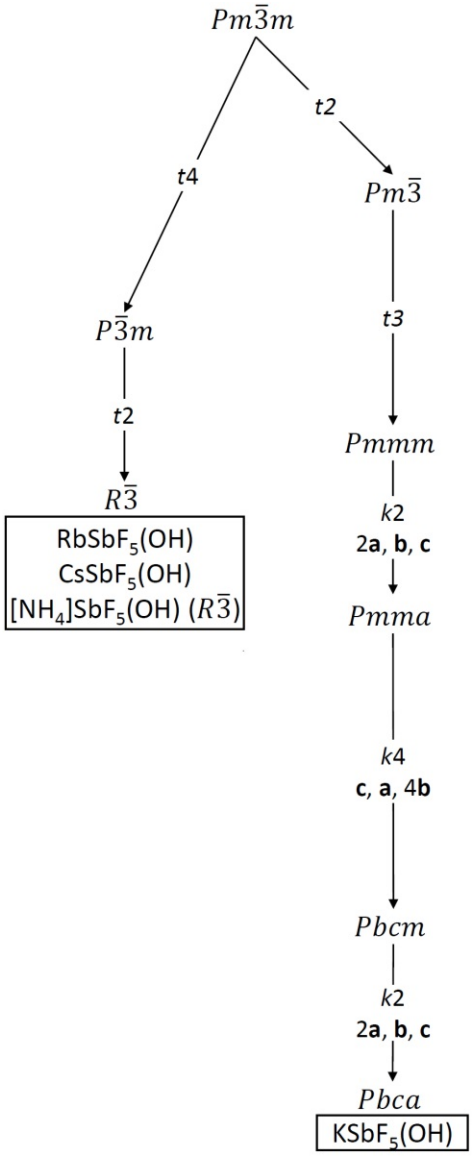

Figure 3.19: Bärnighausen family tree of the pentafluorohydroxoantimonates.

Single crystal structure analysis $KSbF_5(OH)$ The phase of the compound crystallises with orthorhombic symmetry in the space group *Pbca* (No. 61).

Cell (100 K): $a = 10.189(2)$ Å, $b = 10.372(2)$ Å, $c = 19.985(4)$ Å, $V = 2112.02(72)$ Å^3, $Z = 16$

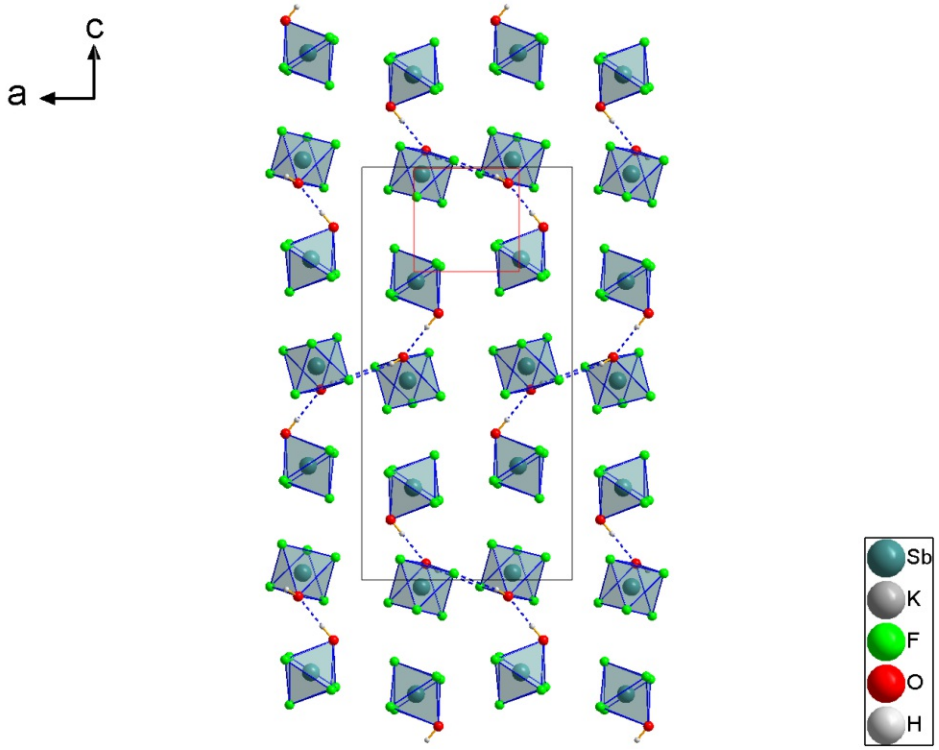

Figure 3.20: One slab of the crystal structure of $KSbF_5(OH)$ viewed down [010] $y \in [0.3, 0.8]$ with the primitive pseudo-cubic cell highlighted in red.

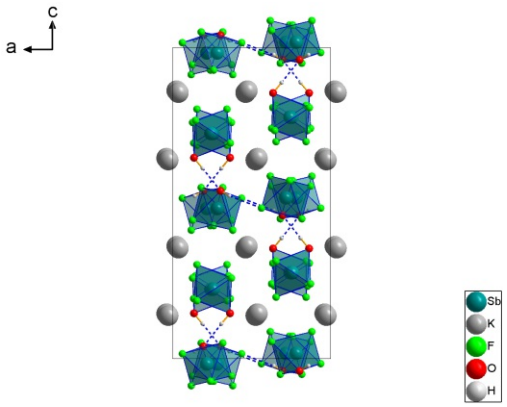

Figure 3.21: Crystal structure of $KSbF_5(OH)$ viewed down [010].

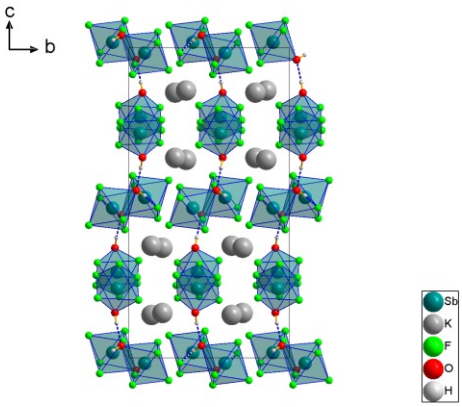

Figure 3.22: Crystal structure of $KSbF_5(OH)$ viewed down [100].

Table 3.10: Atomic parameters of $KSbF_5(OH)$.

Atom	Wyck.	Site	x/a	y/b	z/c	U_{eq}/U_{iso} (Å^2)
Sb1	8c	1	0.75663(2)	0.92846(2)	0.72338(2)	0.00877(4)
Sb2	8c	1	0.71673(2)	1.09959(2)	0.48274(2)	0.01062(4)
K1	8c	1	0.47329(6)	0.64215(6)	0.63854(3)	0.01486(12)
K2	8c	1	0.46221(6)	1.21091(6)	0.64530(3)	0.01589(12)
F1	8c	1	0.63389(17)	0.80578(17)	0.69309(10)	0.0240(4)
F2	8c	1	0.65296(17)	1.06149(17)	0.68649(10)	0.0203(4)
F3	8c	1	0.65472(18)	0.94151(19)	0.80225(9)	0.0242(4)
F4	8c	1	0.85421(17)	0.79673(17)	0.76623(9)	0.0204(4)
F5	8c	1	0.87257(16)	1.05360(17)	0.75909(9)	0.0200(4)
F6	8c	1	0.87353(18)	1.03582(19)	0.44482(10)	0.0243(4)
F7	8c	1	0.61804(19)	1.0244(2)	0.41295(10)	0.0290(5)
F8	8c	1	0.81751(18)	1.18065(17)	0.55003(9)	0.0217(4)
F9	8c	1	0.56224(18)	1.17952(19)	0.51577(11)	0.0293(5)
F10	8c	1	0.73947(16)	1.24804(17)	0.42776(9)	0.0191(4)
O1	8c	1	0.8635(2)	0.9140(2)	0.64540(11)	0.0159(4)
O2	8c	1	0.6964(2)	0.9533(2)	0.53938(11)	0.0178(4)
H1	8c	1	0.813(5)	0.926(5)	0.612(2)	0.09(2)
H2	8c	1	0.647(5)	0.901(4)	0.521(3)	0.09(2)

Hydrogen bond topology: In the crystal structure of $KSbF_5(OH)$, four octahedral $[SbF_5(OH)]^-$ anions each are connected via hydrogen bonds, forming a centrosymmetric tetramer (Figure 3.23). There are four tetramers per unit cell. At the centre of the group, two Sb2 octahedra are connected to each other respectively in [100] (Sb2—Sb2: 4,9249(3) Å) via a OH$\cdots$F interaction. Moreover, each Sb2 anion is acceptor of a Sb1 anion via O—H...O hydrogen bonding, connected in [001] direction (Sb2—Sb1: 5.1424(11) Å), resulting in the following graph:

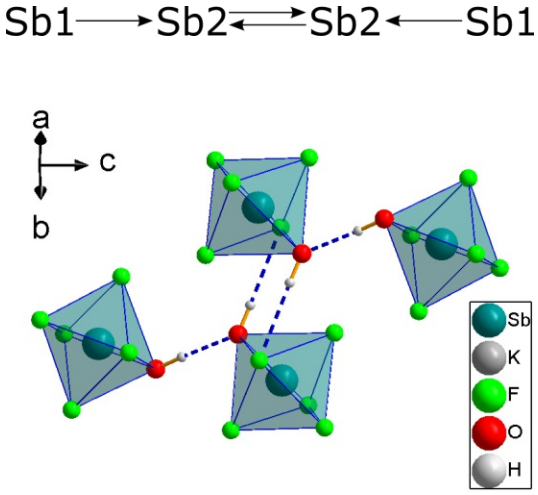

Figure 3.23: Hydrogen-bonded tetramer of $KSbF_5(OH)$ viewed down [110].

The hydrogen bond length H$\cdots$O is 1.897(45) Å with an O-H$\cdots$O angle of 178.3(42)°. This anion distance is longer than that observed for the packing of Rb and $CsSbF_5(OH)$ compounds. This crystal structure, which is not isotypical of $[SbF_6]^-$ and represents a unique structure type, is probably possible here due to the smaller cations.
In the $[SbF_5(OH)]^-$ octahedra, the Sb—F distances are only slightly shorter than the Sb—O1

distances. An exception to this is F10, which like F5, acts as a hydrogen bond acceptor, resulting in an increase in the distance to the central atom. This shows, as has been discussed above, the difficulties of the O/F assignment using bond-lengths. A comparison of all Sb—F/O distances is given in Table 3.11.

Table 3.11: Octahedral bond parameters of $KSbF_5(OH)$.

Atoms	distance (Å)	Atoms	distance (Å)
Sb1—F1	1.8840(17)	Sb2—F6	1.8879(18)
Sb1—F2	1.8876(17)	Sb2—F7	1.888(2)
Sb1—F3	1.8924(18)	Sb2—F8	1.8893(17)
Sb1—F4	1.8944(17)	Sb2—F9	1.8974(18)
Sb1—F5	1.8946(17)	Sb2—O2	1.904(2)
Sb1—O1	1.907(2)	Sb2—F10	1.9058(17)

Deviation from the cubic metrics: The lattice of the basic structure of $KSbF_5(OH)$ features a small distortion compared to the cubic structure (Table 3.12). The distortion is due to the influence of the hydrogen bonds, especially in [100] and [001] direction, as these are the directions in which the hydrogen bonds are aligned. Depending on the hydrogen bond interaction, this leads to a splitting of the Sb positions as already described above. Compared to the cubic primitive cell, **a** and **b** are approximately doubled and **c** quadrupled, introducing a distinct modulation in the [010] direction. Additionally, there is a *klassengleiche* symmetry descent of index eight. The transformation matrix to the pseudo-cubic lattice of the basic structure is: $\begin{pmatrix} 1/2 & 0 & 0 \\ 0 & 1/2 & 0 \\ 0 & 0 & 1/4 \end{pmatrix}$.

Table 3.12: Pseudo-cubic metrics of $KSbF_5(OH)$ after transformation into the pseudo-cubic primitive cell.

Compound	a	b	c	α	β	γ
pseudo-cubic metrics:	**(Å)**	**(Å)**	**(Å)**	**(°)**	**(°)**	**(°)**
$KSbF_5(OH)$	5.0945(10)	5.1860(10)	4.9962(10)	90	90	90

3.6.1.1 PXRD analysis $KSbF_5(OH)$

For examination of the bulk crystals at room temperature, a Rietveld refinement of the single-crystal model was performed. The resulting pattern are shown in Figure 3.18, the resulting cell parameters at room temperature are listed below in Table 3.13. A single reflection could not be explained. The reflection is not in agreement with either the $KSbF_6$ or the $KSbF_4OH_2$ structure. Therefore it was assumed that it was due to an unknown contamination.

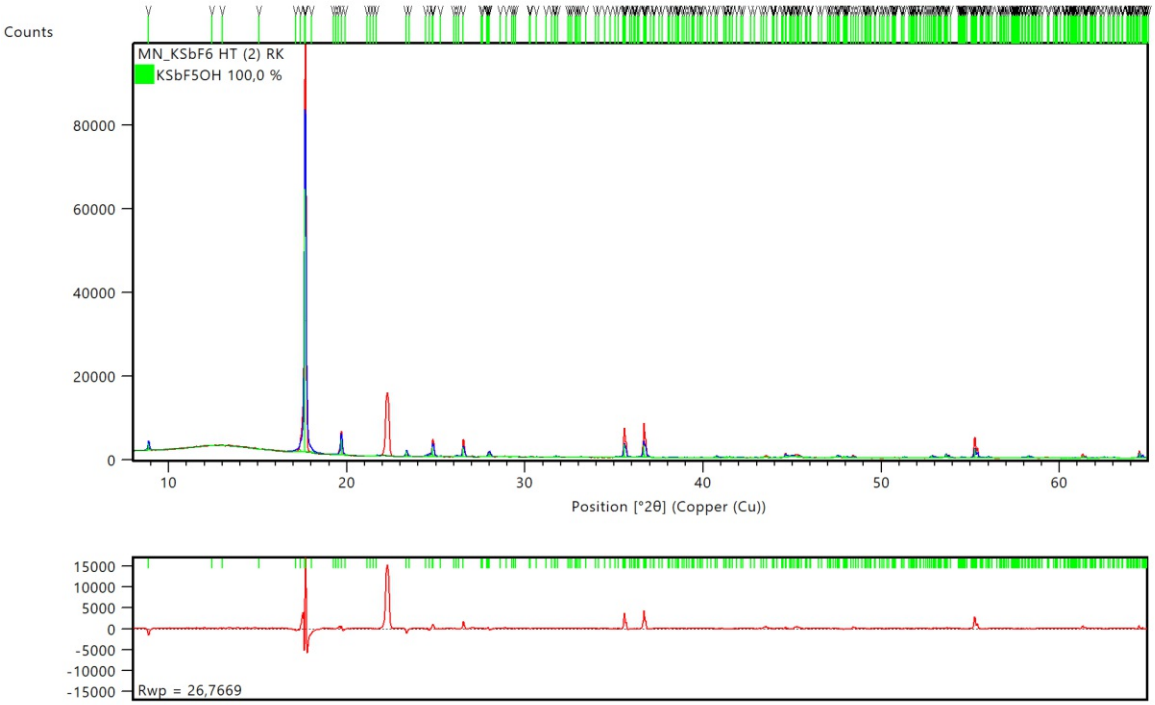

Figure 3.24: PXRD of $KSbF_5(OH)$ at 300 K (red) with Rietveld refinement of a model derived from single crystal diffraction (blue) with difference plot (in red) below.

Table 3.13: Overview of cell parameters of $KSbF_5(OH)$ at 100 K from SC-XRD Data and 300 K from Rietveld refinement.

	a (Å)	b (Å)	c (Å)	α (°)	β (°)	γ (°)	**V** (Å³)	**T** (K)
$KSbF_5(OH)$	10.27278	10.43725	20.24794	90	90	90	2170.9755	300
	10.189(2)	10.372(2)	19.985(4)	90	90	90	2112.02(72)	100

3.6.1.2 Potassium pentafluorohydroxoarsenate (V) ($KAsF_5(OH)$)

Single crystal structure analysis $KAsF_5(OH)$ from Peterková [18]. The phase of the compound crystallises in the space group of *Pnab* (No. 60).
As seen in the crystal structure of $KAsF_5(OH)$ (Figure 3.25), the octahedral anions form chain-like H-bonds in the [100] direction. It has no similarity to the crystal structure of $KSbF_5(OH)$.

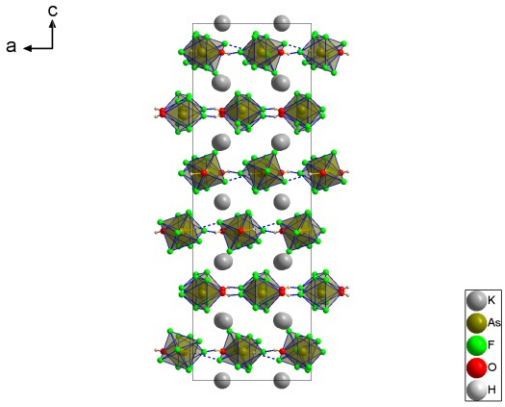

Figure 3.25: Crystal structure of $KAsF_5(OH)$ viewed down [010].

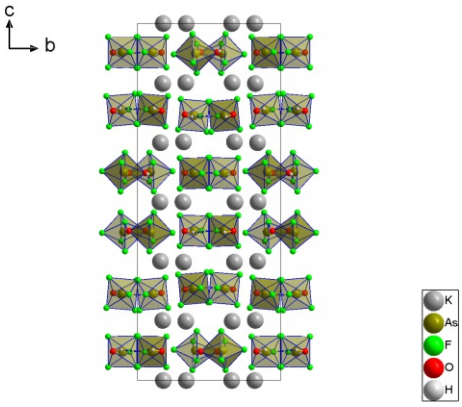

Figure 3.26: Crystal structure of $KAsF_5(OH)$ viewed down [100].

3.7 Alkali tetrafluorodihydroxoantimonate (MSbF$_4$(OH)$_2$, M = K, Rb, Cs)

Similar to the fluorodihydroxoarsenates, the fluorodihydroxoantimonates tend to form more complex structures (compared to the monohydroxo compounds) due to an increased number of hydroxyl groups that participate in hydrogen bonding. The structural richness is due to two opposing effects. The hydrogen bonds connect the $[SbF_4(OH)_2]^-$ anions, resulting in shorter Sb—Sb distances. On the flip side, the hydrogen bonding prevents an ideal close packing of the structures owing to the constraints resulting from this interaction.

All $[SbF_4(OH)_2]^-$ compounds discussed in this work show a layered structure. The layers extend in the (010)-plane and are formed by $[SbF_4(OH)_2]^-$ octahedra, which are linked by O—H$\cdots$O hydrogen bonds. The hydrogen bonds are all located inside the layers, orientated along the $[10\bar{1}]$ direction. The layers are stacked in the [010]-direction.
The crystal structures resulting from the different cations can all be derived from an aristotype structure, which crystallises in $C2/c$ symmetry (Figure 3.27). The modulation with respect to the aristotype affects the position and the orientation of the $[SbF_6]^-$ octahedra. Moreover, the hydrogen bonds may be ordered or disordered.

3.7.1 Symmetry relationships of the $[SbF_4(OH)_2]^-$ compounds

While KSbF$_4$(OH)$_2$ and CsSbF$_4$(OH)$_2$ are each only present in a single polytype between 100 and 300 K, RbSbF$_4$(OH)$_2$ has four polytypes in this temperature range.

The symmetry relations of the different $[SbF_4(OH)_2]^-$ compounds are illustrated by a Bärnighausen family tree (Figure 3.27). The lowest common supergroup $C2/c$ forms the symmetry of the aristotype with four ions of each kind respectively per unit cell. In the aristotype structure, the hydrogens are disordered. Except for the aristotype structure, all $[SbF_4(OH)_2]^-$ anions and cations are located on general positions (site symmetry 1).
The two monoclinic and triclinic structures of RbSbF$_4$(OH)$_2$ are distinguished via the prefixes 's' for "short" ($C2/c$ at 300 K and $C\bar{1}$ 100 K) and 'l' for "long" (Cc at 300 K and $C\bar{1}$ at 150 K).

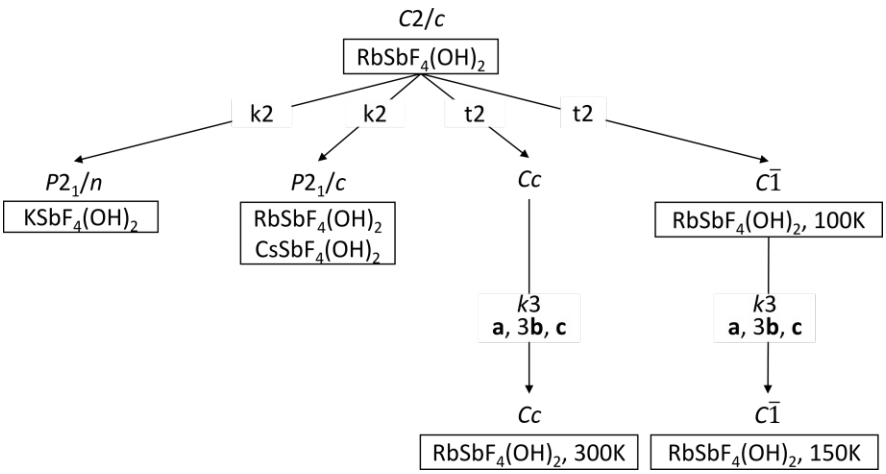

Figure 3.27: Bärnighausen family tree of tetrafluorodihydroxoantimonates; KSbF$_4$(OH)$_2$ and CsSbF$_4$(OH)$_2$ crystallize in the same space group type, but are not isotypic and therefore shown separately.

3.7.2 Hydrogen bond layers

The crystal structures of $KSbF_4(OH)_2$, $CsSbF_4(OH)_2$ and all $RbSbF_4(OH)_2$ can be distinguished by their ordering type and direction sequence of the hydrogen bonds in the layers (Figure 3.28). In the following, disordered hydrogen bond layers are designated as X. In the case of ordered bonds, they are designated as A or B, depending on whether the hydrogens are oriented in the $[10\bar{1}]$ (A) or in $[\bar{1}01]$ direction (B). Moreover, the layer symmetry of the layers varies can be determined for each layer. In simple structures, all layers are symmetrically equivalent. In the more complex structures, layers are not equivalent and sometimes even feature different layer symmetries.

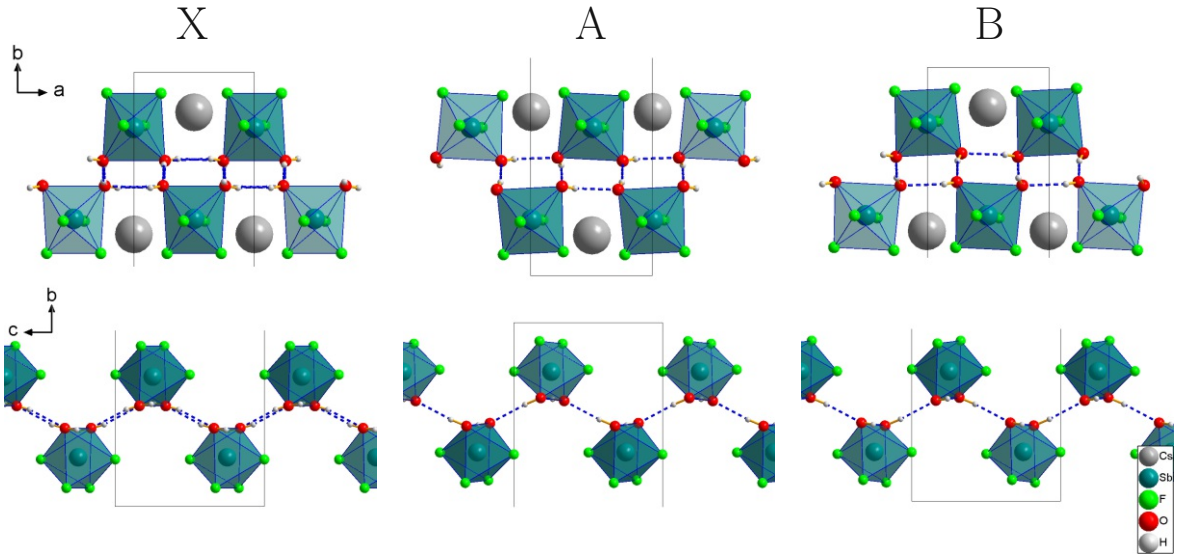

Figure 3.28: Disordered (X) and the two orientations of the ordered (A and B) hydrogen-bonding networks, viewed down [001] and [100].

3.7.2.1 Hydrogen bond networks

As stated above, the $[SbF_4(OH_2)]^-$ crystal structures under investigation show layered structures. Only the oxygen act as donors and acceptors, because F is a weaker hydrogen bond acceptor. This resulted in two-dimensional periodic networks whereby the layers are connected with each other exclusively by ion-ion interactions. Topologically, if the direction of the hydrogen bonds is ignored, all hydrogen bonding networks can be considered as square nets (4^4).
The voltage graph corresponding to an ordered and a disordered hydrogen-bonded layer are given in Figure 3.29. From A to B, only the direction of all the ordered hydrogen bonds are inverted.

Figure 3.29: Voltage graphs for an ordered A or B layer (left) and a disordered X (right) layer of $[SbF_4(OH)_2]^-$.

All $[SbF_4(OH)_2]^-$ compounds show a very strong distortion from a cubic arrangement due to the hydrogen bonds formed in the crystal. The relationship to the CsCl structure type is recognised in projection along the [001] direction. A comparison of the stackings of $KSbF_4(OH)_2$,

$CsSbF_4(OH)_2$ and all $RbSbF_4(OH)_2$ is given in Figure 3.31. The layer sequences are summarised in Table 3.14 and the symmetry relations of the layers are illustrated by a Bärnighausen family tree (Figure 3.30).

Table 3.14: Layer sequences of the $[SbF_4(OH)_2]^-$ compounds, a subscript is used to differentiate between symmetrically non-equivalent layer

Compound	**Space group**	**Layer sequence**	**Layer symmetry**
$KSbF_4(OH)_2$	$P2_1/c$	$\ldots X - X \ldots$	X: $p_y\bar{1}$
$CsSbF_4(OH)_2$	$P2_1/n$	$\ldots A - B \ldots$	A, B: p_yn
s-m-$RbSbF_4(OH)_2$	$C2/c$	$\ldots X - X \ldots$	X: p_y2/n
l-m-$RbSbF_4(OH)_2$	Cc	$\ldots B_1 - A - B_2 - B_2 - A - B_1 \ldots$	A: p_yn
			B: p_y1
l-tric-$RbSbF_4(OH)_2$	$C\bar{1}$	$\ldots X - B - A - X - B - A \ldots$	X: $p_y\bar{1}$
			A, B: p_y1
s-tric-$RbSbF_4(OH)_2$	$C\bar{1}$	$\ldots X - X \ldots$	X: $p_y\bar{1}$

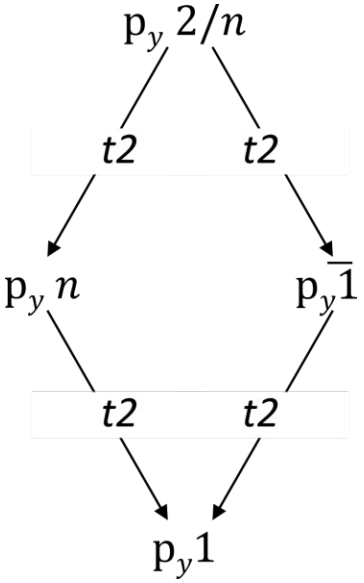

Figure 3.30: Bärnighausen family tree of layers of the tetrafluorodihydroxoantimonates.

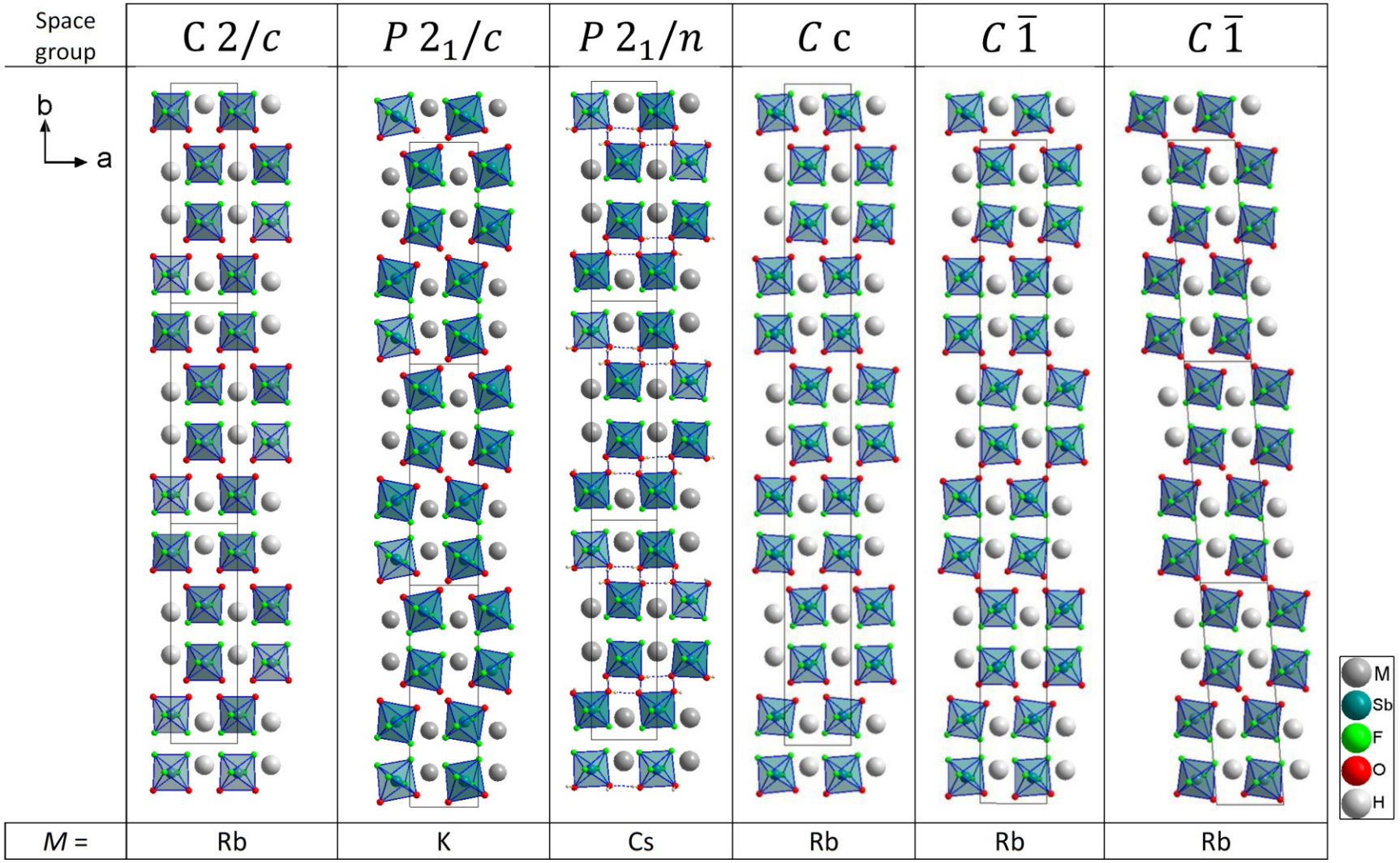

Figure 3.31: Overview of crystal structures of K, Cs and $RbSbF_4(OH)_2$.

To describe the modulation inside one layer, the absolute values of two torsion angles between the anions inside the unit cell connected by hydrogen bonds are listed for each compound and layer (Table 3.15). The angle between the axis of *trans*-F atoms (green lines) and the axes through the two *cis*-O atoms (red lines) are used (Figure 3.32).

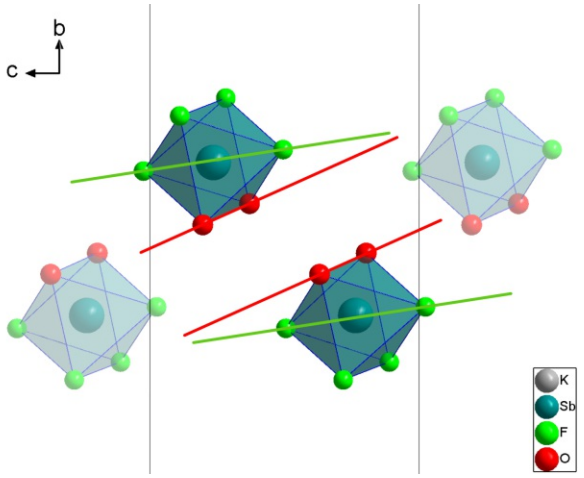

Figure 3.32: Description of the alignment of the octahedra to each other based on the angles between the axes through the atoms F1,F2 (green) and O1,O2 (red) within the unit cell.

Table 3.15: Torsion angles in tetrafluorodihydroxoantimonates of polyhedral $[SbF_4(OH)_2]^-$ anions connected by hydrogen bonds.

Compound	**Layer**	**Layer symmetry**	**∠ F1, F2 (°)**	**∠ O1, O2 (°)**
$KSbF_4(OH)_2$	X	$p_y\bar{1}$	0.00(6)	0.00(8)
$CsSbF_4(OH)_2$	A, B	p_yn	1.93(6)	7.7(1)
s-m-$RbSbF_4(OH)_2$	X	p_y2/n	0.00(9)	0.0(2)
l-m-$RbSbF_4(OH)_2$	B_1	p_y1	0.8(4)	8.7(7)
	A	p_yn	1.8(5)	8.6(9)
	B_2	p_y1	1.9(4)	7.3(6)
l-tric-$RbSbF_4(OH)_2$	X	$p_y\bar{1}$	0.0(1)	0.0(3)
	B	p_y1	0.1(2)	7.2(3)
	A	p_y1	3.2(2)	12.4(4)
s-tric-$RbSbF_4(OH)_2$	X	$p_y\bar{1}$	0.00(9)	0.0(3)

The layers in the aristotype have a symmetry of p_y2/n. Starting from this, all possible *translationengleiche* symmetry descents of the layers can be observed. IF inversion symmetry is present (p_y2/n and $p\bar{1}$), the hydrogen bonds are always disordered. In the absence of inversion symmetry (p_yn and p_y1) the hydrogen bonds are ordered.
In all layers with a layer symmetry of p_y2/n and $p_y\bar{1}$, the octahedral anions are aligned parallel to each other.
In contrast, if twofold rotation symmetry of the crystal is lost due to tilting of the anions, but a glide mirror plane is retained, an overall symmetry of Cc results, which allows for an ordered hydrogen bonding network.
If the twofold axis is lost, but the centres of inversion are retained, the space group $C\bar{1}$ is obtained. In this case, the octahedral anions are aligned parallel to each other. There are two possibilities in this case. Either the inversions are located between the layers or inside

the layers. The former case results in ordered, the latter in a disordered hydrogen-bonding network. In the case of superstructures in the [010] direction, as for example observed in l-m-$RbSbF_4(OH)_2$, some part of the layers maybe disordered whereas others aren't. A similar phenomenon is observed when the C-centring of the aristotype is lost (which in principle also corresponds to a superstructure). In this case the inversions may either persist in the layers (symmetry $P2_1/c$, $KSbF_4(OH)_2$) or between the layers (symmetry $P2_1/n$, $CsSbF_4(OH)_2$). Again, the former case features an ordered, the latter a disordered hydrogen bonding network. Thus, the structures are unrelated despite crystallizing in the same space group type.

3.7.3 Potassium tetrafluorodihydroxoantimonate (V) ($KSbF_4(OH)_2$)

$KSbF_4(OH)_2$ shows a similar crystal structure when compared with the analogue arsenate $KAsF_4(OH)_2$. Both crystal structures can be represented as modulated phases. The super space group is $C2/c(\sigma_1 0\sigma_3)00$. In case of the antimonate, $\mathbf{q} = \mathbf{a}^*$, which represents a double superstructure, or a commensurable modulation resulting in the three-dimensional space group $P2_1/c$. For the arsenate, an incommensurable structure results with $\mathbf{q} = 0.8607\mathbf{a}^* + 0.5585\mathbf{c}^*$ [68].
No powder with a significant phase fraction of $KSbF_4(OH)_2$ could be produced, and the compound could so far only be characterised on the basis of single crystal data. In contrast to the other $[SbF_4(OH)_2]^-$ salts, the preparation via stoichiometric use of $KSbF_6$ and $KSb(OH)_6$ has not yet been attempted.

Single crystal structure analysis $KSbF_4(OH)_2$ $KSbF_4(OH)_2$ crystallises with monoclinic symmetry in the space group $P2_1/c$ (No. 14).

Cell (100 K): $a = 4.9806(4)$ Å, $b = 16.0927(12)$ Å, $c = 6.6138(4)$ Å, $\beta = 96.533(3)°$, $V = 526.66(7)$ Å^3; $Z = 4$;

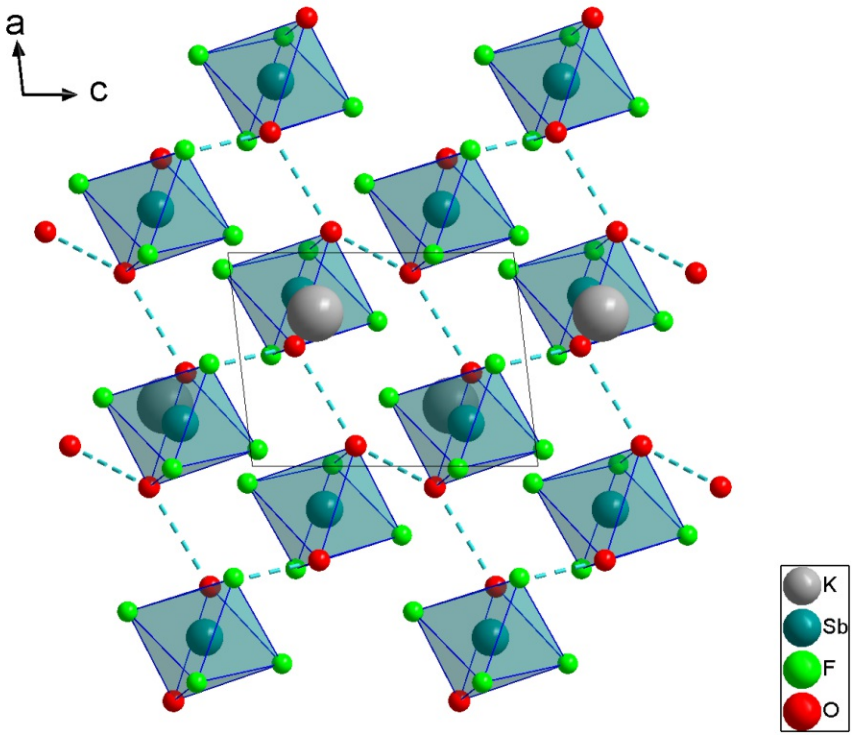

Figure 3.33: One layer of $KSbF_4(OH)_2$ viewed down [010] (one layer) with proposed H-bonds.

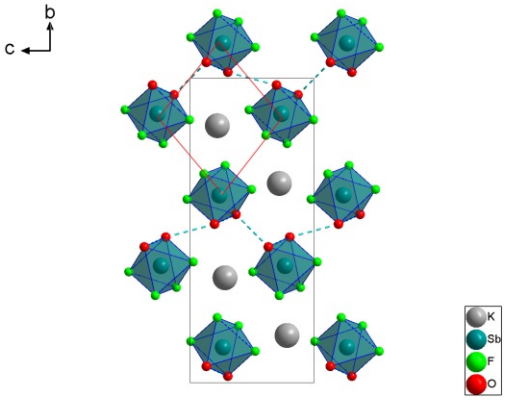

Figure 3.34: Crystal structure of $KSbF_4(OH)_2$ viewed down [100] with proposed H-bonds.

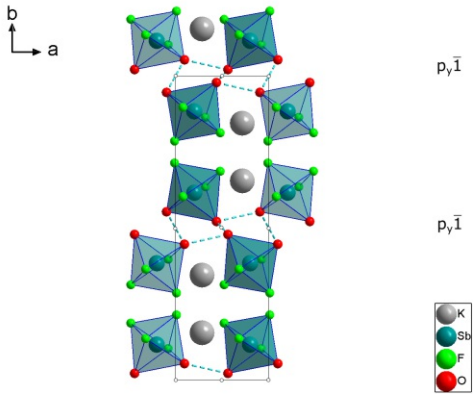

Figure 3.35: Crystal structure of $KSbF_4(OH)_2$ viewed down [001] with proposed H-bonds.

$KSbF_4(OH)_2$ has four octahedral $[SbF_4(OH)_2]^-$ units per unit cell on general positions. The two anions in a layer are related to each other via the centre of inversion. The layers are related to each other via the 2_1 screw axis along [010].
The O—H···O distances range from 2.6907(30) Å to 2.7505(30) Å. Within a layer, all octahedra are aligned parallel within the experimental resolution. Of the two layers, all X layers (centred at $y = 0, \frac{1}{2}$) are located on centres of inversion, resulting in a layer symmetry of $p_y\bar{1}$ and therefore they are necessarily disordered. The result is the following sequence of layers in the [010]-direction:

$$\cdots\cdots \text{X} \text{——} \text{X} \cdots\cdots \tag{3.5}$$

Table 3.16: Atomic parameters of $KSbF_4(OH)_2$.

Atom	Wyck.	Site	x/a	y/b	z/c	U_{eq}/U_{iso} (Å^2)
K1	4e	1	0.71556(14)	0.84492(4)	0.78084(10)	0.01656(14)
Sb1	4e	1	0.20105(4)	0.88392(1)	0.26461(3)	0.00900(7)
F1	4e	1	0.3212(4)	0.86435(12)	0.0052(3)	0.0184(4)
F2	4e	1	0.0783(4)	0.60299(12)	0.0245(3)	0.0201(4)
F3	4e	1	-0.0099(4)	0.78617(12)	0.2182(3)	0.0197(4)
F4	4e	1	0.5212(4)	0.18673(12)	0.6103(3)	0.0215(4)
O1	4e	1	0.4383(4)	0.97862(13)	0.3039(3)	0.0124(4)
O2	4e	1	-0.0963(4)	0.94643(14)	0.1303(3)	0.0159(4)

3.7.3.1 Potassium tetrafluorodihydroxoarsenate (V) ($KAsF_4(OH)_2$)

Single crystal structure analysis $KAsF_4(OH)_2$ from Peterková[18] Crystals of the compound are incommensurately modulated. Using the superspace approach, they can be described using the superspace group $C2/c(\sigma_1 0 \sigma_3)00$.

Cell (291 K): $a = 4.818(1)$ Å, $b = 16.001(4)$ Å, $c = 6.374(2)$ Å, $\beta = 99.36(2)°$, $V = 484.85(20)$ Å^3, $Z = 4$
The figures below represent an approximant structure with $\mathbf{q} = \frac{6}{7}\mathbf{a}^* + \frac{5}{9}\mathbf{c}^*$.

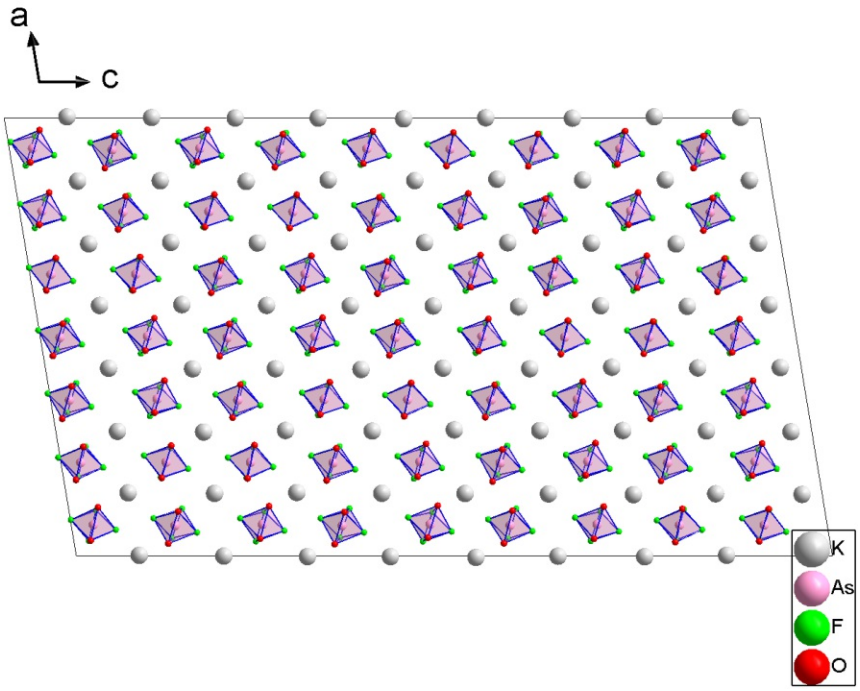

Figure 3.36: One layer of $KAsF_4(OH)_2$ viewed down [010] ($y \in [0, 0.1]$), data provided by Michal Dušek [68].

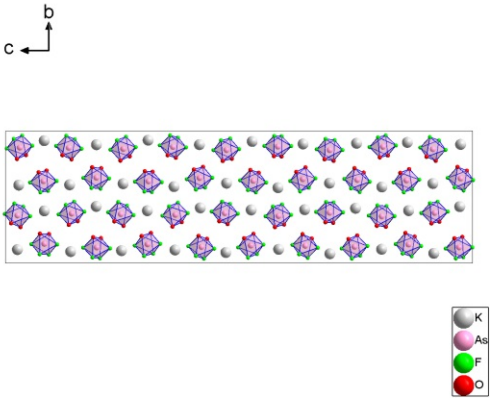

Figure 3.37: One slab of $KAsF_4(OH)_2$ viewed down [100] ($x \in [0, 0.2]$), data provided by Michal Dušek [68].

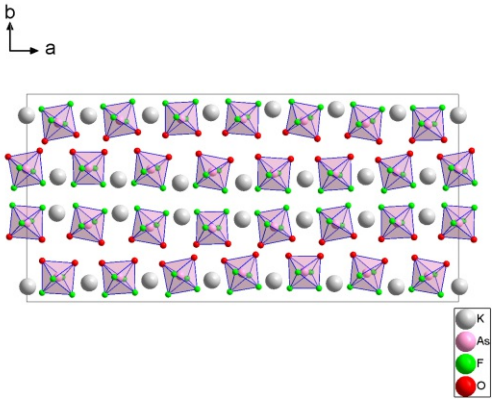

Figure 3.38: One slab of $KAsF_4(OH)_2$ viewed down [100] ($z \in [0, 0.5]$), data provided by Michal Dušek [68].

The rotational modulation of the anions is distinctly more pronounced in the arsenate than in the antimonate. Whereas the layers of $KAsF_4(OH)_2$ are incommensurable modulated in the [100] and [001] directions, the stacking of the layers in the [010] direction is periodic (the σ_2 component of the modulation vector is 0).
The distinctly different modulation of the arsenate and the antimonate is probably due to the bigger rotational freedom caused by the smaller size of the anions. Between F atoms in trans position, on average the distance is only 3.484(12) Å ($KAsF_4(OH)_2$) in contrast to F—F in $KSbF_4(OH)_2$ being 3.805(3) Å (9.5 % bigger).

3.7.4 Caesium tetrafluorodihydroxoantimonate (V) ($CsSbF_4(OH)_2$)

In principle, the same commensurate modulation vector $\mathbf{q}^* = \mathbf{a}^*$ can be used for $CsSbF_4(OH)_2$ as for $KSbF_4(OH)_2$, but the structures are still fundamentally different. This is because here the hydrogen-bonded layers are ordered, whereas in $KSbF_4(OH)_2$ the layers are disordered. This structure is stable in the 100–300 K range and so far no other polymorphs have been found in contrast to $RbSbF_4(OH)_2$.

Single crystal structure analysis $CsSbF_4(OH)_2$ The compound crystallises with monoclinic symmetry in the space group $P2_1/n$ (No. 14).

Cell (100 K): a=5.1208(10) Å, b=16.938(3) Å, c=7.1356(14) Å, β=98.612(4)°; V=611.94(20) Å^3; Z=4

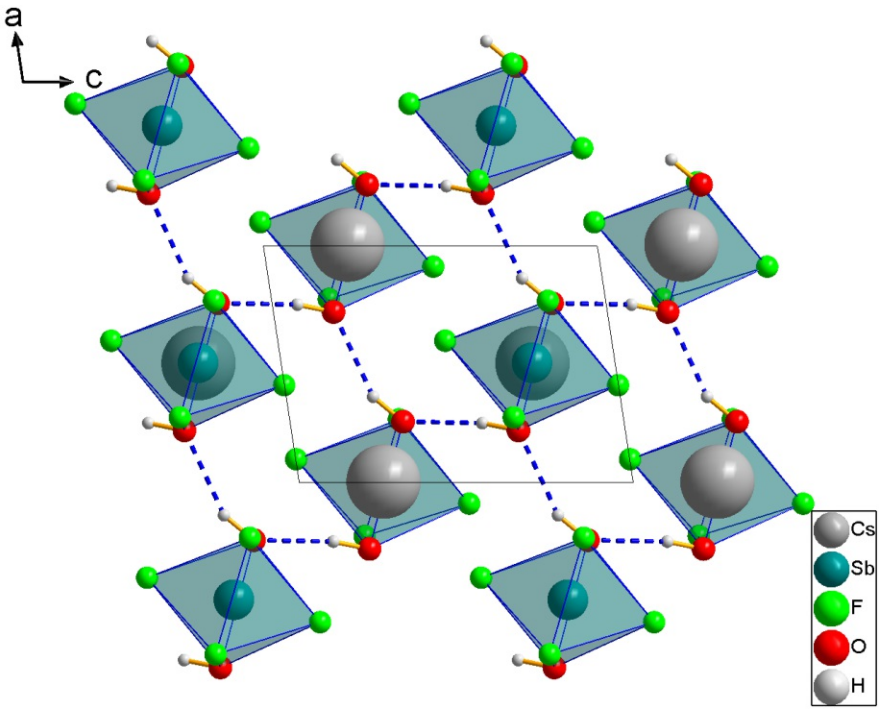

Figure 3.39: One layer of $CsSbF_4(OH)_2$ viewed down [010] ($y \in [0, 0.5]$).

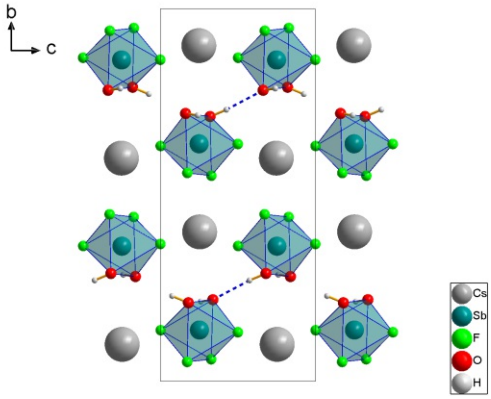

Figure 3.40: Crystal structure of $CsSbF_4(OH)_2$ viewed down [100].

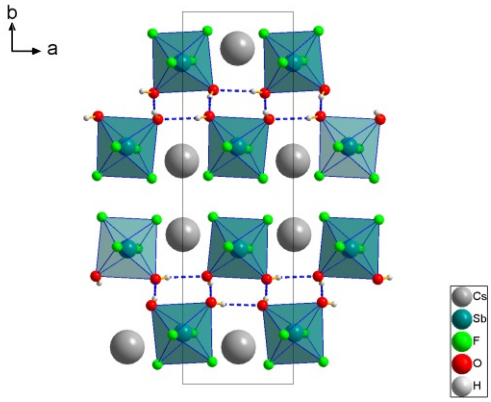

Figure 3.41: Crystal structure of $CsSbF_4(OH)_2$ viewed down [001].

$CsSbF_4(OH)_2$ has four octahedral $[SbF_4(OH)_2]^-$ units per unit cell on general positions. The two anions in a layer are related to each other via the 2_1 screw axis. The layers are related to each other via the centre of inversion.

The O—H···O distances range from 2.7479(31) Å to 2.7780(31) Å, forming the layered hydrogen network in the (010)-plane centred a $y = \frac{1}{4}, \frac{3}{4}$. One B layer is shown in Figure 3.39. Within a layer, the octahedra are not aligned parallel, with a large modulation present, with respect to the aristotype structure.
In contrast to $KSbF_4(OH)_2$, the centres of inversion are located between the layers. The inversions invert the orientation of the hydrogen bonding in adjacent layers, resulting in a stacking sequence in [010]-direction of

$$\cdots\cdots \text{A} \text{——} \text{B} \cdots\cdots \tag{3.6}$$

whereby each layer has a layer symmetry of $p_y\bar{1}$.

Table 3.17: Atomic parameters of $CsSbF_4(OH)_2$

Atom	Wyck.	Site	x/a	y/b	z/c	U_{eq}/U_{iso} (Å^2)
Cs1	4e	1	-0.00463(3)	0.59895(2)	0.74749(2)	0.01300(3)
Sb1	4e	1	0.49369(3)	0.63744(2)	0.24886(2)	0.00910(3)
F1	4e	1	0.5881(3)	0.63158(11)	0.0010(2)	0.0192(3)
F2	4e	1	0.4006(3)	0.63685(11)	0.4985(2)	0.0184(3)
F3	4e	1	0.7244(4)	0.55182(11)	0.3283(3)	0.0240(4)
F4	4e	1	0.2321(3)	0.55914(11)	0.1730(3)	0.0228(3)
O1	4e	1	0.2421(4)	0.71890(12)	0.1618(3)	0.0178(4)
O2	4e	1	0.7790(4)	0.71062(13)	0.3199(3)	0.0182(4)
H1	4e	1	0.137(7)	0.714(3)	0.240(5)	0.031(12)
H2	4e	1	0.748(7)	0.729(2)	0.425(3)	0.015(9)

3.7.4.1 PXRD analysis $CsSbF_4(OH)_2$

To check for possible phase transitions, PXRD-measurements in the temperature range between 30 and 290 K were performed (10 K steps). No other polytypes could be detected for this temperature range using the PXRD. Nevertheless, the existence of other polytypes cannot be completely ruled out, as superstructures reflexes are easily overlooked due to their weak intensities.

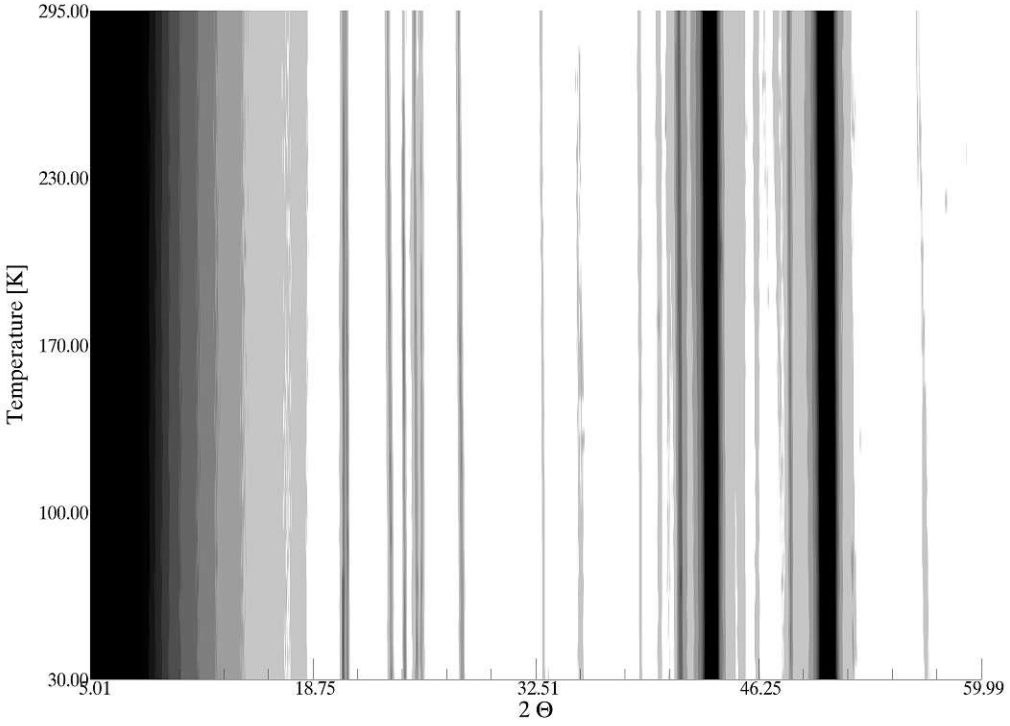

Figure 3.42: Temperature-dependent PXRD of $CsSbF_4(OH)_2$, in the range of 30-295 K on Pt.

For examination of the bulk crystals at room temperature, a Rietveld refinement of the single-crystal model was performed. The resulting simulations are in good agreement and are shown in Figure 3.43, the resulting cell parameters at room temperature are listed below in Table 3.18. The poor signal-to-noise ratio is due to the small sample size.

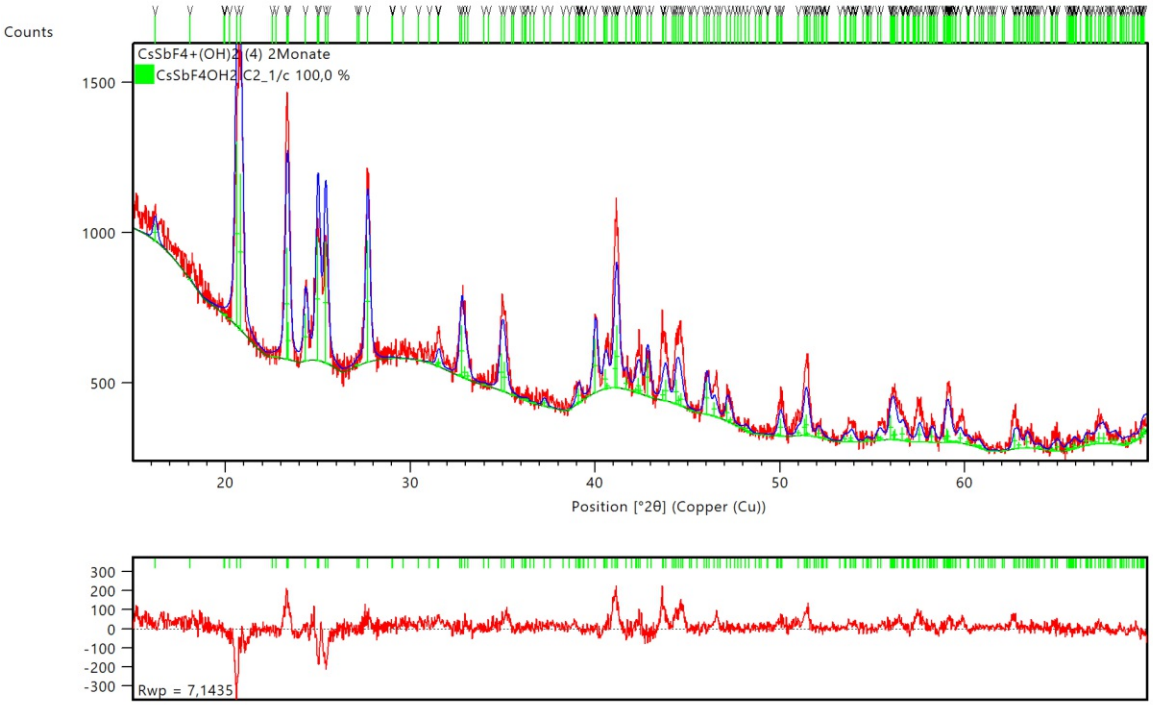

Figure 3.43: PXRD of $CsSbF_4(OH)_2$ at 300 K (red) with Rietveld refinement of a model derived from single crystal diffraction (blue) with difference plot (in red) below.

Table 3.18: Overview of cell parameters of $CsSbF_4(OH)_2$ at 100 K from SC-XRD Data and 300 K from Rietveld refinement.

	a (Å)	**b** (Å)	**c** (Å)	α (°)	β (°)	γ (°)	**V** (Å^3)	**T** (K)
$CsSbF_4(OH)_2$	10.27278	10.43725	20.24794	90	90	90	2170.9755	300
	10.189(2)	10.372(2)	19.985(4)	90	90	90	2112.0(7)	100

3.7.5 Rubidium tetrafluorodihydroxoantimonate (V) ($RbSbF_4(OH)_2$)

Based on SC-XRD measurements of different crystals at different temperatures, multiple polytypes of $RbSbF_4(OH)_2$ could be detected. Here, a complex crystallisation behaviour is present and, depending on the crystallisation conditions, different polytypes or also oriented intergrowths of different polytypes, also known as allotwins [16], are formed. A monoclinic $RbSbF_4(OH)_2$ polytype isotypic with $CsSbF_4(OH)_2$ was only observed in allotwins.
Single-phase crystals were observed for four polytypes, which will be described in more detail below.
Up to now, we were not able to elucidate the precise formation condition of the various polytypes. All crystals from the data presented were picked from a singe reaction vessel. Possible factors are length of reaction, speed of crystallisation as well as the ratio of product to traces of $RbSbF_5(OH)$ or RbF. Of particular interest is the presence of two stable phases at 300 K, where the $P2_1/c$ phase is stable down to 100 K, whereas the Cc phase undergoes two transformations upon cooling.
Apart from slight differences in the F-positions, the various polytypes of $RbSbF_4(OH)_2$ differ from each other and from the aristotype only in the sequence of the layers built up from hydrogen bonds.

The hydrogen bonds could not be located reliably using the single crystal measurements. However, crystal chemical reasoning and comparison with the Cs analogue makes assignment of the nature of the H-bonds possible. The structures will be discussed below in the order in which they occur with decreasing temperature. This deviates from the usual list, in which the highest to the lowest symmetry is considered. One of the symmetry changes is not described by a group/subgroup relationship, and the last transition is even described by an increase of symmetry.

The relationships of the $RbSbF_4(OH)_2$ polytypes are shown in Figure 3.27. In order to be able to distinguish the different crystal structures of a compound, their crystal system will be added as prefix.

Single crystal structure analysis s-m-$RbSbF_4(OH)_2$ $RbSbF_4(OH)_2$ crystallises in the monoclinic crystal system in the space group $C2/c$ (No. 15).

Cell (300 K): $a = 5.0697(3)$ Å, $b = 16.5935(9)$ Å, $c = 6.8649$ Å, $\beta = 97.961(1)°$, $V = 571.94(6)$ Å^3, $Z = 4$

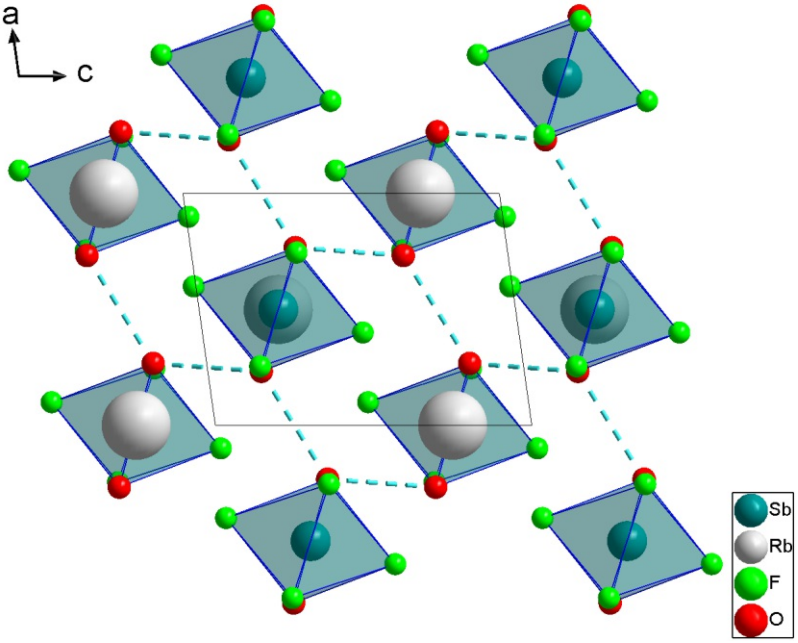

Figure 3.44: One layer of s-m-$RbSbF_4(OH)_2$ viewed down [010] (one layer) with proposed H-bonds.

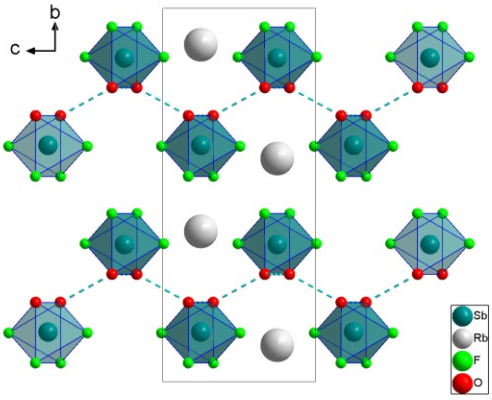

Figure 3.45: Crystal structure of s-m-$RbSbF_4(OH)_2$ viewed down [100] with proposed H-bonds.

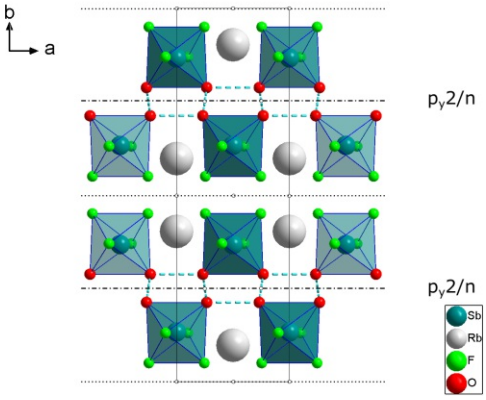

Figure 3.46: Crystal structure of s-m-$RbSbF_4(OH)_2$ viewed down [001] with proposed H-bonds.

s-m-$RbSbF_4(OH)_2$ forms the aristotype of all $[SbF_4(OH)_2]^-$ structures. One crystallographically unique $[SbF_4(OH)_2]^-$ unit is located on a twofold axis (four per unit cell). The two non-translationally equivalent anions in a layer are related to each other via the n glide reflection plane and the centre of inversion. The two layers are related to each other via the 2_1 screw axis in [010] direction as well as the centres of inversion (Figure 3.46).

The O—H···O distances are in the range of 2.666(5) Å. Within a layer, all octahedra are aligned parallel within the experimental resolution. Of the two layers, all X layers (centred at $y = \frac{1}{4}, \frac{3}{4}$) are located on centres of inversion, and therefore they are necessarily disordered. The result is the following sequence of layers in the [010]-direction:

$$\cdots\cdots \text{X} \text{——} \text{X} \cdots\cdots \tag{3.7}$$

Each layer has a layer symmetry of p_y2/n.

Table 3.19: Atomic parameters of s-m-$RbSbF_4(OH)_2$.

Atom	**Wyck.**	**Site**	x/a	y/b	z/c	U_{eq}/U_{iso} (Å^2)
Sb1	4e	2	1/2	0.63292(2)	3/4	0.02169(10)
Rb2	4e	2	1	0.59755(3)	1/4	0.03486(12)
F1	8f	1	0.5996(6)	0.63040(13)	0.4930(4)	0.0461(6)
F2	8f	1	0.2543(6)	0.54986(18)	0.6674(4)	0.0606(7)
O1	8f	1	0.7672(7)	0.7122(2)	0.8309(5)	0.0582(9)

Single crystal structure analysis l-m-$RbSbF_4(OH)_2$ $RbSbF_4(OH)_2$ crystallises in the monoclinic crystal system in the space group Cc (No. 9).

Cell (300 K): $a = 5.1075(10)$ Å, $b = 50.19(1)$ Å, $c = 6.9095(14)$ Å, $\beta = 97.87(3)°$; $V = 1754.54(62)$ Å^3, $Z = 12$
In the Cc structure of $RbSbF_4(OH)_2$, the cell is three times as long in the [010] direction and runs through six layers. The positions of the anions are split in the unit cell into three crystallographically independent positions.
Starting from the $C2/c$ aristotype, the inversions and the twofold axis are lost and only the c glide reflection remains. This corresponds to a *translationengleiche* symmetry descent of index 2 resulting in the crystal class of Cc. From this, only every third translation in the [010] direction is maintained, which corresponds to a *klassengleiche* symmetry descent of index 3.

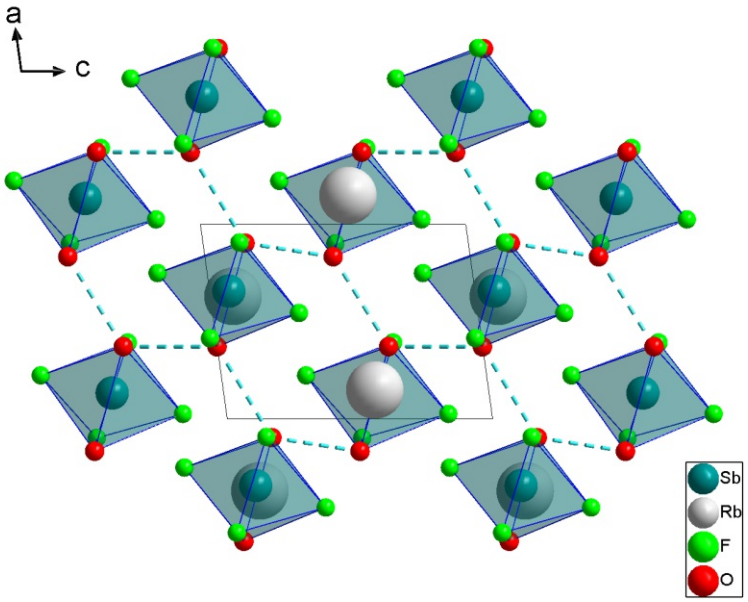

Figure 3.47: One layer of l-m-$RbSbF_4(OH)_2$ viewed down [010] (one layer) with proposed H-bonds.

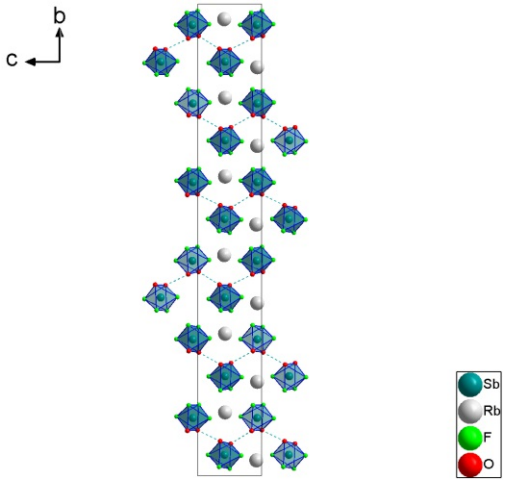

Figure 3.48: Crystal structure of l-m-$RbSbF_4(OH)_2$ viewed down [100].

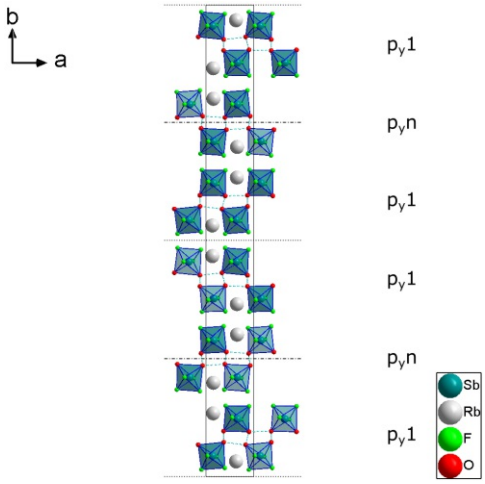

Figure 3.49: Crystal structure of l-m-$RbSbF_4(OH)_2$ viewed down [001].

The O-H···O distances range from 2.7118(183) Å to 2.7160(188) Å, forming the layered hydrogen network in the (010)-plane centred at $y = \frac{1}{12}, \frac{3}{12}, \frac{5}{12}, \frac{7}{12}, \frac{9}{12}, \frac{11}{12}$. Within the layers, all octahedra show a similar modulation.
Of the 6 layers, the A layers ($y = \frac{3}{12}, \frac{9}{12}$) are located on n glide planes. Due to a c-glide plane being located in the middle of the unit cell, it can be assumed that the two A layers are arranged opposite to the four remaining. Because these four layers are not equal, this results in the following sequence of layers in the [010]-direction:

$$\cdots\cdots \; B_1 \text{ —— } A \text{ —— } B_2 \text{ —— } B_2 \text{ —— } A \text{ —— } B_1 \; \cdots\cdots \tag{3.8}$$

Where A has a layer symmetry of $p_y n$ and B_1 and B_2 have a layer symmetry of $p_y 1$.

Table 3.20: Atomic parameters of l-m-$RbSbF_4(OH)_2$.

Atom	Wyck.	Site	x/a	y/b	z/c	U_{eq}/U_{iso} (Å^2)
Sb1	4a	1	0.63223(10)	0.45570(2)	1.07980(8)	0.01588(17)
Sb2	4a	1	0.15624(10)	0.37773(2)	0.57242(8)	0.0207(2)
Sb3	4a	1	0.15177(12)	0.28903(3)	0.07203(10)	0.0258(2)
Rb1	4a	1	1.1294(3)	0.46760(3)	0.5853(2)	0.0270(3)
Rb2	4a	1	0.6479(3)	0.36582(4)	0.0711(2)	0.0324(3)
Rb3	4a	1	0.6515(3)	0.30102(4)	0.5714(3)	0.0425(5)
F1	4a	1	0.723(2)	0.45727(19)	0.8199(16)	0.031(2)
O1	4a	1	0.871(2)	0.4269(2)	1.1457(17)	0.035(2)
F3	4a	1	0.892(2)	0.4813(3)	1.1648(19)	0.058(3)
F4	4a	1	0.525(2)	0.4558(2)	1.3353(17)	0.040(3)
F2	4a	1	0.401(2)	0.4850(2)	0.9985(15)	0.042(2)
O2	4a	1	0.3329(19)	0.4324(3)	0.9834(18)	0.040(3)
F5	4a	1	0.249(2)	0.37860(19)	0.3135(16)	0.037(3)
F6	4a	1	0.406(2)	0.3506(3)	0.6378(19)	0.058(3)
F7	4a	1	0.044(2)	0.3746(2)	0.8249(17)	0.043(3)
F8	4a	1	-0.086(2)	0.3498(2)	0.4768(15)	0.047(3)
O3	4a	1	0.403(2)	0.4048(3)	0.6583(18)	0.049(3)
O4	4a	1	-0.130(3)	0.4034(3)	0.499(2)	0.060(4)
F9	4a	1	0.241(3)	0.2912(3)	-0.1868(17)	0.048(3)
F10	4a	1	0.370(3)	0.3190(3)	0.144(2)	0.072(4)
F11	4a	1	0.046(3)	0.2895(3)	0.3275(18)	0.060(4)
F12	4a	1	-0.117(2)	0.3153(2)	-0.0134(17)	0.056(3)
O5	4a	1	-0.105(3)	0.2615(3)	-0.021(2)	0.063(4)
O6	4a	1	0.427(2)	0.2644(3)	0.1379(16)	0.047(3)

Single crystal structure analysis l-tric-$RbSbF_4(OH)_2$ At 150 K the l-m phase is transformed into a triclinic space group $C\bar{1}$ (No. 2).

Cell (150 K): $a = 5.0389(4)$ Å, $b = 49.472(4)$ Å, $c = 6.8273(5)$ Å, $\alpha = 89.729(3)°$, $\beta = 98.319(3)°$, $\gamma = 90.393(3)°$, $V = 1683.98(23)$ Å^3, $Z = 12$

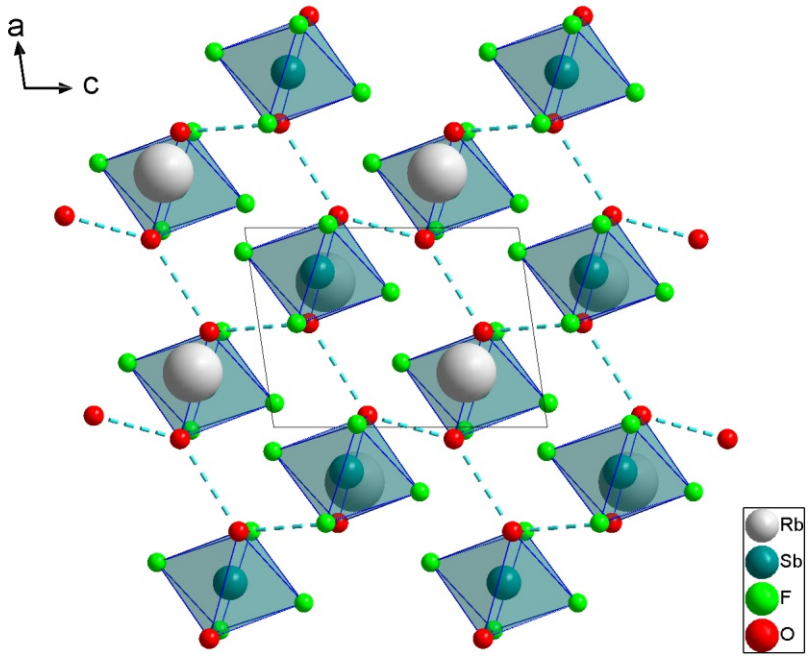

Figure 3.50: One layer of l-tric-$RbSbF_4(OH)_2$ viewed down [010] (one layer) with proposed H-bonds.

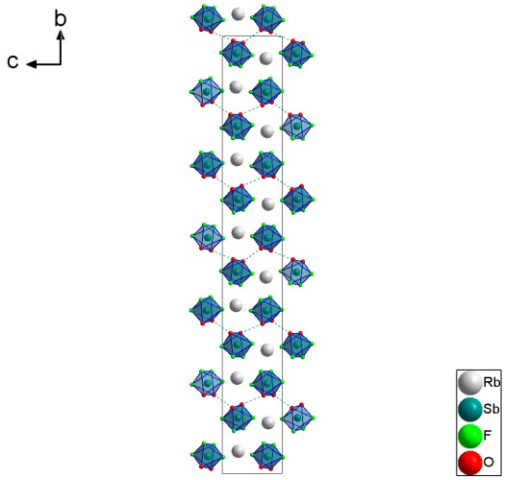

Figure 3.51: Crystal structure of l-tric-$RbSbF_4(OH)_2$ viewed down [100].

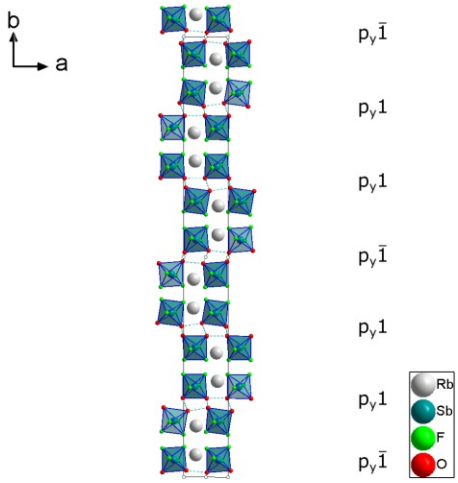

Figure 3.52: Crystal structure of l-tric-$RbSbF_4(OH)_2$ viewed down [001].

The O—H···O distances range from 2.6685(92) Å to 2.6851(83) Å, forming a layered hydrogen network in the (010)-plane centred at $y = 0, \frac{1}{6}, \frac{2}{6}, \frac{3}{6}, \frac{4}{6}, \frac{5}{6}$. Of all the polytypes, the $l-C\bar{1}$ crystal structure shows the greatest variation between its layers. Within an X layer, all octahedra are aligned parallel within the experimental resolution. The B layers show a modulation akin to the Cc structure. Within an A layer, the octahedra are not aligned parallel with the largest

modulation present of all layers of all members of the $[SbF_4(OH)_2]^-$ family.
Of the 6 layers, the X layers ($y = 0$ and $y = \frac{1}{2}$) are located on centres of inversion and based on this they are definitely disordered. It is unclear whether the four other layers feature ordered or disordered hydrogen bonding. Assuming an ordered hydrogen bonding, the layers centred at $y = \frac{1}{6}, \frac{4}{6}$ and at $y = \frac{2}{6}, \frac{5}{6}$ possess opposite orientation, since they are related by inversion. The result is the following sequence of layers in the [010]-direction:

$$\cdots\cdots \text{X} \text{——} \text{B} \text{——} \text{A} \text{——} \text{X} \text{——} \text{A} \text{——} \text{B} \cdots\cdots \tag{3.9}$$

Where X has a layer symmetry of $p_y\,\bar{1}$ and A, B have a layer symmetry of $p_y\,1$.

Table 3.21: Atomic parameters of l-C-1-$RbSbF_4(OH)_2$.

Atom	**Wyck.**	**Site**	x/a	y/b	z/c	U_{eq}/U_{iso} (Å^2)
Rb1	2i	1	0.76040(14)	0.21778(2)	0.75313(10)	0.01889(13)
Rb2	2i	1	0.28074(15)	0.11612(2)	0.23036(11)	0.01988(13)
Rb3	2i	1	0.27347(14)	0.05063(2)	0.73315(10)	0.01935(13)
Sb1	2i	1	0.24506(8)	0.20553(2)	0.24849(6)	0.01172(8)
Sb2	2i	1	0.78435(9)	0.12754(2)	0.73867(6)	0.01302(8)
Sb3	2i	1	0.77834(8)	0.03901(2)	0.24223(6)	0.01226(8)
F1	2i	1	0.3479(10)	0.20986(11)	-0.0066(7)	0.0243(9)
F2	2i	1	0.1418(11)	0.20299(10)	0.5054(7)	0.0259(10)
F3	2i	1	0.4838(11)	0.23341(11)	0.3492(8)	0.0314(11)
F4	2i	1	-0.0091(11)	0.23327(10)	0.1799(8)	0.0296(11)
O1	2i	1	-0.0194(12)	0.17942(13)	0.1376(10)	0.0312(14)
O2	2i	1	0.5201(12)	0.17902(13)	0.3078(9)	0.0277(12)
F5	2i	1	0.8809(10)	0.12756(11)	0.4802(7)	0.0267(10)
F6	2i	1	0.5024(11)	0.10307(10)	0.6430(8)	0.0292(11)
F7	2i	1	0.9988(11)	0.09678(10)	0.8065(8)	0.0292(11)
F8	2i	1	0.6867(10)	0.12493(10)	0.9992(6)	0.0231(9)
O3	2i	1	1.0883(11)	0.15021(11)	0.8314(9)	0.0220(10)
O4	2i	1	0.5479(11)	0.15749(11)	0.6719(8)	0.0220(10)
F9	2i	1	0.8790(11)	0.03727(11)	-0.0159(7)	0.0260(10)
F10	2i	1	0.6766(9)	0.04286(10)	0.4990(6)	0.0221(9)
F11	2i	1	1.0155(12)	0.06864(11)	0.3055(9)	0.0331(12)
F12	2i	1	0.5204(12)	0.06493(11)	0.1388(8)	0.0348(13)
O5	2i	1	0.5216(12)	0.01041(12)	0.1840(9)	0.0256(11)
O6	2i	1	1.0584(11)	0.01500(12)	0.3486(9)	0.0266(12)

Single crystal structure analysis s-tric-$RbSbF_4(OH)_2$ Between 150 and 100 K, an isomorphic phase transition occurs, increasing the symmetry to only one symmetrical independent anion and cation. This corresponds to a threefold symmetry ascent.

Cell (100 K): $a = 4.9994(5)$ Å, $b = 8.4021(7)$ Å, $c = 6.8666(6)$ Å, $\alpha = 89.884(3)°$, $\beta = 96.842(3)°$, $\gamma = 77.285(3)°$, $V = 279.24(4)$ Å^3, $Z = 2$

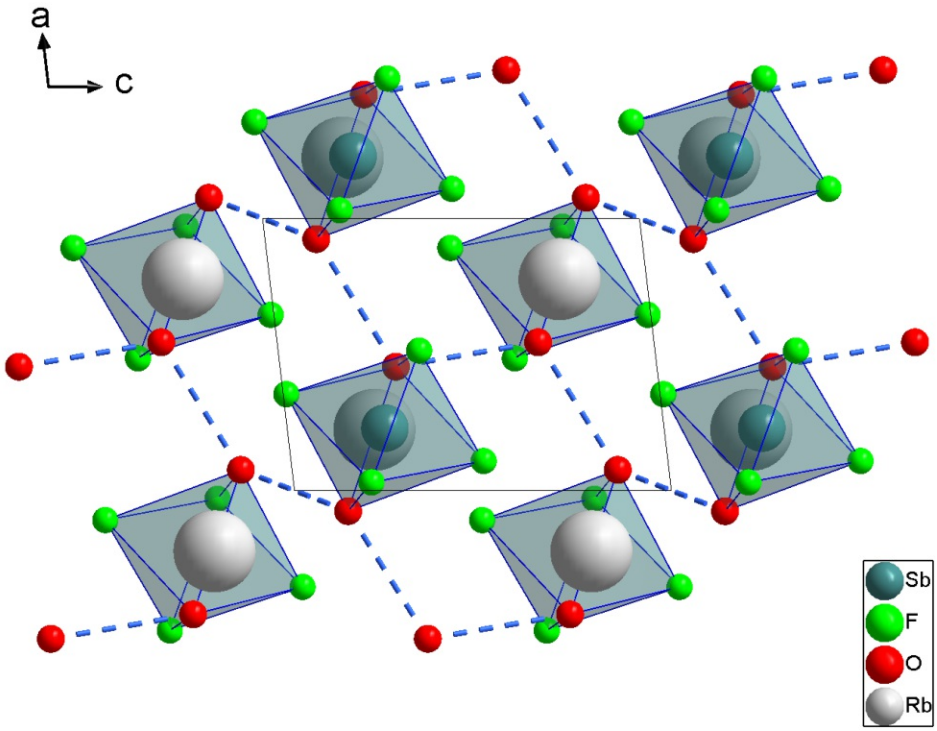

Figure 3.53: One layer of s-tric-$RbSbF_4(OH)_2$ viewed down [010] (one layer) with proposed H-bonds.

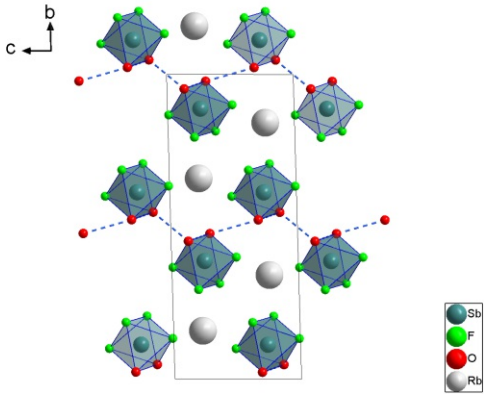

Figure 3.54: Crystal structure of s-tric-$RbSbF_4(OH)_2$ viewed down [100] with proposed H-bonds.

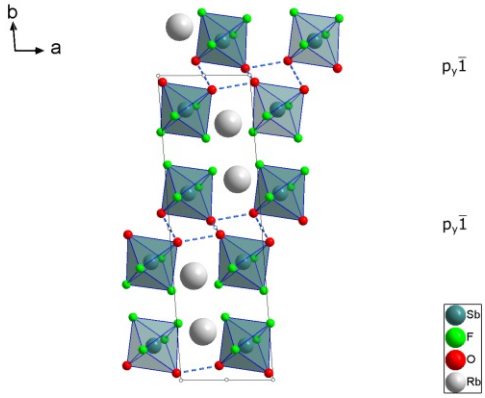

Figure 3.55: Crystal structure of s-tric-$RbSbF_4(OH)_2$ viewed down [001] with proposed H-bonds.

The O-H···O distances are in the range of 2.6658(49) Å, forming a layered hydrogen network in the (010)-plane centred at $y = 0, \frac{1}{2}$. Within a layer, all octahedra are aligned parallel

within the experimental resolution.
Of the two layers, all X layers ($y = 0$ and $y = \frac{1}{2}$) are located on centres of inversion, therefore they are necessarily disordered. The result is the following sequence of layers in the [010]-direction:

$$\cdots\cdots \text{X} \text{——} \text{X} \cdots\cdots \tag{3.10}$$

Each layer has a layer symmetry of $p_y\,\bar{1}$.

Table 3.22: Atomic parameters of s-C-1-$RbSbF_4(OH)_2$.

Atom	Wyck.	Site	x/a	y/b	z/c	U_{eq}/U_{iso} (Å^2)
Sb1	2i	1	0.72921(5)	0.11264(2)	0.25915(3)	0.01021(4)
F1	2i	1	0.6087(6)	0.09972(16)	0.5111(3)	0.0196(5)
F2	2i	1	0.8542(5)	0.13338(16)	0.0085(4)	0.0184(4)
F3	2i	1	0.5301(6)	0.20650(16)	0.2066(4)	0.0236(5)
F4	2i	1	1.0143(6)	0.18603(17)	0.3742(4)	0.0237(5)
O1	2i	1	0.4242(6)	0.04760(19)	0.1359(5)	0.0188(5)
O2	2i	1	0.9551(6)	0.02260(18)	0.3075(4)	0.0165(5)
Rb1	2i	1	0.27685(7)	0.15838(2)	0.76895(5)	0.01610(7)

3.7.5.1 Allotwinning of $RbSbF_4(OH)_2$

In Figure 3.56 is shown the diffraction pattern of a crystal which is an intergrowth of two polytypes, namely the $P2_1/c$ and the Cc (l-m-$RbSbF_4(OH)_2$) polytype. The crystal structure present in the allotwin has not yet been refined.
The corresponding reflection scheme with the assignment of the reflections to the corresponding crystal structures is shown below in Figure 3.57. Visible here are the shared $C2/c$ aristotype structure in black, the twofold superstructure of $P2_1/c$ in red and the threefold superstructure of the $C2/c$ phase in green.

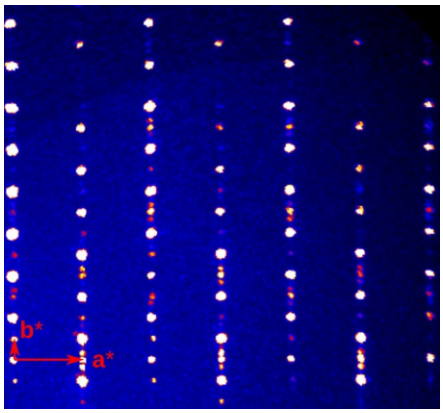

Figure 3.56: $(hk0)^*$ plane of reciprocal space of $RbSbF_4(OH)_2$ reconstructed from CCD data collected at 100 K.

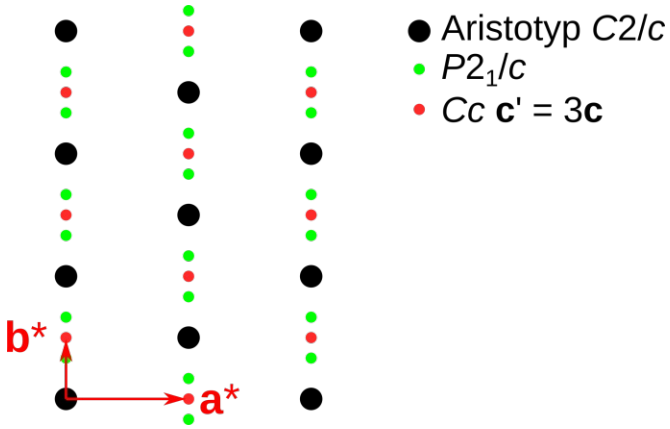

Figure 3.57: Scheme of $RbSbF_4(OH)_2$ $(hk0)^*$ plane precession image: Superposition of the $C2/c$ common structure in black, the double superstructure of $P2_1/c$ in red and the triple superstructure of the Cc phase.

3.7.5.2 PXRD analysis $RbSbF_4(OH)_2$

To check for possible phase transitions, PXRD-measurements in the temperature range between 30 and 290 K were performed (10 K steps). No other polytypes except for the $C2/c$ structure could be detected using the PXRD.

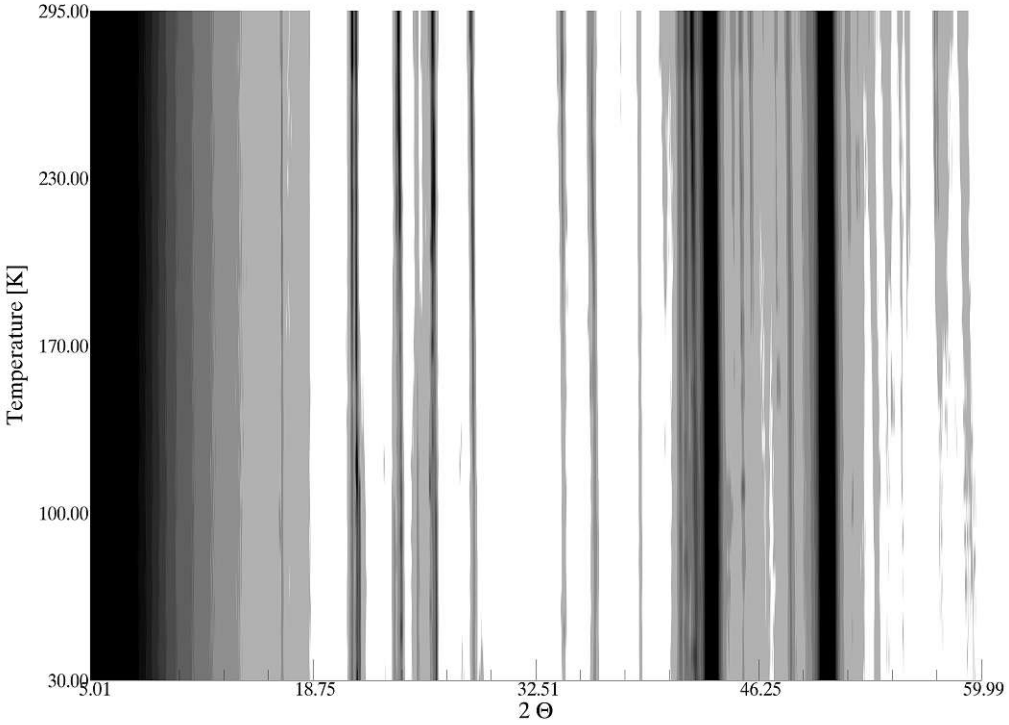

Figure 3.58: Temperature-dependent PXRD of $RbSbF_4(OH)_2$, in the range of 30-295 K on Pt.

For examination of the bulk crystals at room temperature, a Rietveld refinement of the single-crystal model was performed. The resulting simulations are in good agreement and are shown in Figure 3.59, the resulting cell parameters at room temperature are listed below in Table 3.23. Only the $C2/c$ structure, which is stable over the entire temperature range, can be seen in the measurement. Other possibly formed phases could not be evidenced owing to very weak superstructure reflections. The poor signal-to-noise ratio is due to the small sample size.

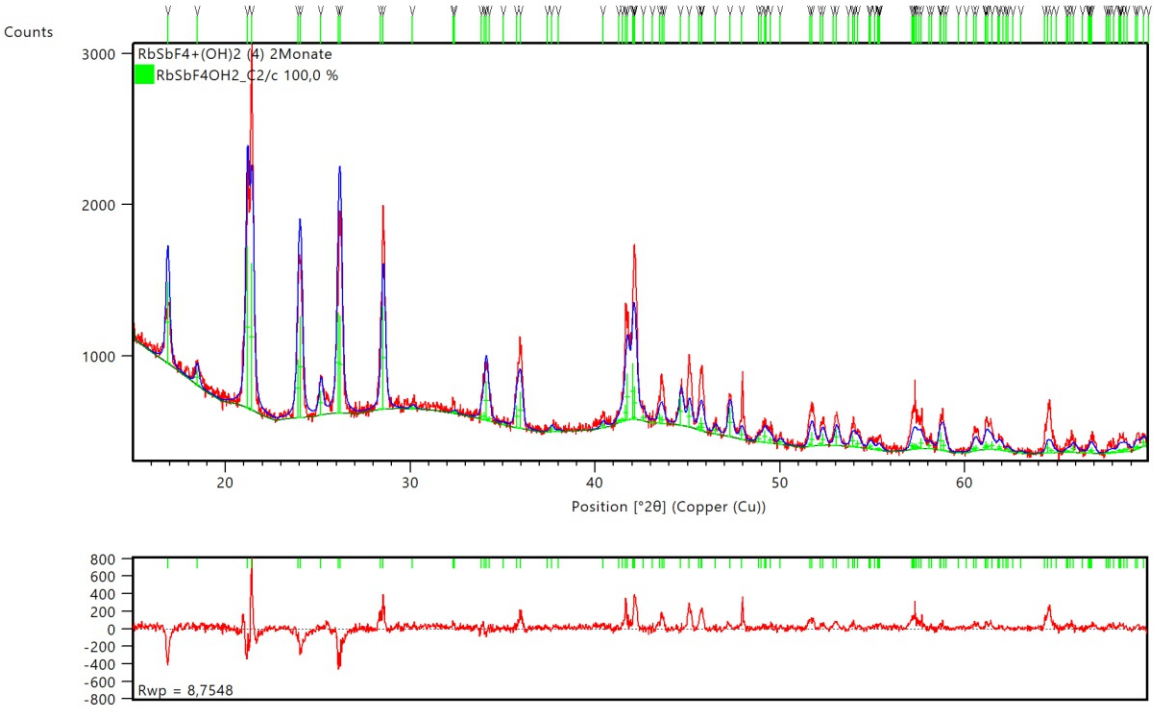

Figure 3.59: PXRD of $RbSbF_4(OH)_2$ at 300 K (red) with Rietveld refinement of a model derived from single crystal diffraction (blue) with difference plot (in red) below.

Table 3.23: Overview of cell parameters of $RbSbF_4(OH)_2$ at 100 K from SC-XRD Data and 300 K from Rietveld refinement.

	a (Å)	**b** (Å)	**c** (Å)	α (°)	β (°)	γ (°)	**V** (Å^3)	**T** (K)
$RbSbF_4(OH)_2$	5.07090	16.58757	6.86360	90	97.97325	90	571.7427	300
	5.0697(3)	16.5935(9)	6.8649(4)	90	97.961(1)	90	571.94(6)	300

3.8 Methyl-substituted ammonium hexafluoroantimonates ($[(CH_3)_xNH_{4-x}]SbF_6$)

As in the last chapter, likewise all $[(CH_3)_xNH_{4-x}]SbF_6$ crystal structures can be derived from a CsCl-like structure. In contrast to before, the cubic high-temperature phase is actually realized at or slightly above room temperature. This is clearly observed under a polarising microscope: the crystals lose birefringence either at room temperature or on heating. On cooling, the symmetry of the methyl-substituted ammonium salts then decreases via completely different symmetry paths, as shown in their respective chapters and summarised in Figure 3.60. The approximate transition temperatures for the methylammonium hexafluoroantimonates are summarised in Table 3.24 as determined by the non-ambient PXRD measurements. Except for $[(CH_3)_4N]SbF_6$, the transition temperatures are increasing with decreasing number of methyl groups. This is due to the energy needed to disorder the non-spherical cations in the respective crystal structures.

Only for the tetramethylammonium hexafluoroantimonate crystals, the atomic coordinates could be located reliably for the cubic high-temperature phases. This is due to the tetrahedral symmetry ($\bar{4}3m$) of the cation, which is a subgroup of index 2 of the site symmetry $m\bar{3}m$ in the CsCl structure type. It fits very well between the gaps of the anions and is thus well localised.

This is also the reason why the non-cubic phase of this compound in particular remains stable at higher temperatures compared to the other three compounds. In the cubic structure of the trimethylammonium salt for example, the cation is strongly dynamically disordered. The resulting average electron density is too smeared out to locate distinct maxima corresponding to individual atoms. Also, in contrast to the centrosymmetric $[(CH_3)_4N]^+$ ion, the barycenter of $[(CH_3)_3NH]^+$, $[(CH_3)_2NH_2]^+$ and $[(CH_3)NH_3]^+$ are not localised at the position of the N. The distance between the barycenter and the N gets bigger with decreasing methyl groups, distributing the electron density of the N over a wider space. For these cations, only a diffuse electron cloud was observed in SC-XRD measurements.

In all three of these cases, distinct electron density peaks could be localised corresponding to the Sb atom, which indicates that the barycenter of the $[SbF_6]^-$ anion is not affected by the disorder. The F atoms, on the other hand, were again too smeared out, which means that the $[SbF_6]^-$ ion has more or less full rotational freedom. The dynamic disorder of anions and cations is evidenced by intense three-dimensional diffuse scattering visible in the reconstructed reciprocal space sections in the next chapters.

Anothe notable effect in the diffraction patterns is that the cubic high-temperature phases scatter only to distinctly smaller angles owing to their less localised electron densities. After the phase transition and the symmetry descent, the cations are positioned at lower site symmetries (generally 1) with less freedom of movement. These well-ordered crystals accordingly diffract to distinctly higher diffraction angles.

Table 3.24: Approximate transition temperatures from the cubic to the non-cubic phases of the methylammonium hexafluoroantimonates determined via non-ambient PXRD measurements and the lattice parameter a of the cubic phases.

	cubic SG	trans. T (K)	a (Å)	T (K)	V (Å^3)
$\mathbf{[(CH_3)_4N]SbF_6}$	$P\bar{4}3m$ (215)	360	6.4490(13)	430	268.21(16)
$\mathbf{[(CH_3)_3NH]SbF_6}$	$Pm\bar{3}m$ (221)	225	6.144(6)	250	232.0(7)
$\mathbf{[(CH_3)_2NH_2]SbF_6}$	$Pm\bar{3}m$ (221)	270	5.916(3)	300	207.1(3)
$\mathbf{[(CH_3)NH_3]SbF_6}$	$Pm\bar{3}m$ (221)	380	5.658(9)	410	181.2(8)

The Table 3.24 shows that the volumes of the unit cells decrease relatively strongly as the number of methyl groups decreases. This is due to the fact that the cations rotate around a local centre at high-temperatures. In the case of tetramethylammonium, its barycenter is located at the centre of the N and moves further and further away as the number of methyl groups decreases. If the rotation or disordering would always happen around the N as the centre, the volume would have to remain approximately the same. When the methyl-substituted ammonium cations are disordered, the highest symmetry of $Pm\bar{3}m$ is assumed for all cubic methyl substituted ammonium hexafluoroantimonates. There was no indication of a lowering of the symmetry in either the diffraction pattern or during refinements. $[(CH_3)_4N]SbF_6$ is an exception, as here the cubic crystal structure with the space group $P\bar{4}3m$ could be clearly determined.
In order to be able to distinguish the different crystal structures of a compound, their crystal system will be added as prefix; for example, cub-$[(CH_3)_4N]SbF_6$ is the cubic crystal structure of $[(CH_3)_4N]SbF_6$.

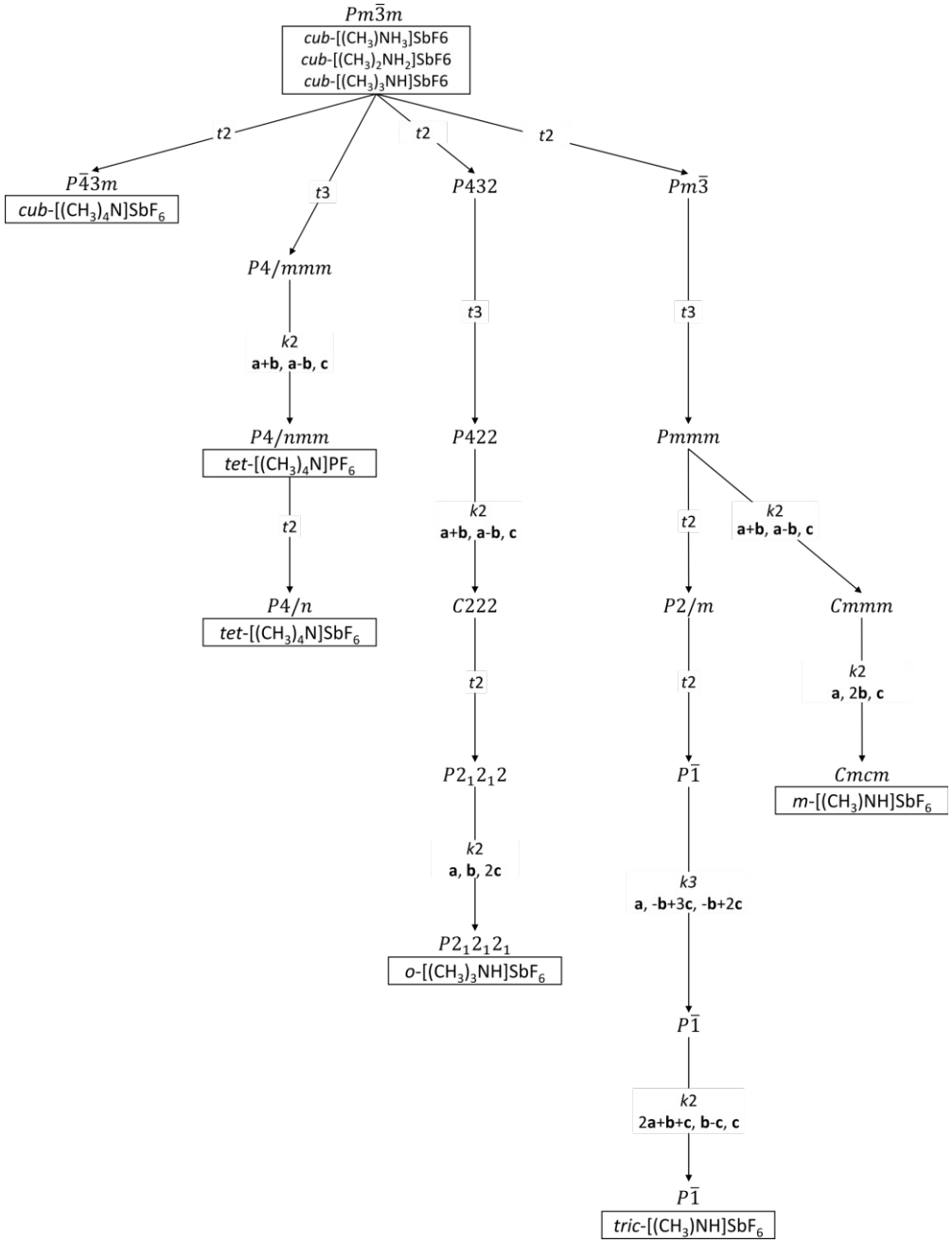

Figure 3.60: Bärnighausen family tree of the methylammonium hexafluoroantimonates.

3.8.1 Tetramethylammonium hexafluoroantimonate ($[(CH_3)_4N]SbF_6$)

$[(CH_3)_4N]SbF_6$ has two polymorphs between 100 and 430 K. The high-temperature phase is cubic, with the space group $P\bar{4}3m$. On cooling below 360 K, the crystal transforms into a tetragonal phase with the $P4/n$ symmetry. The phase is stable down to 100 K, the lowest temperature reached on the single crystal diffractometer.
Remarkably, the space groups of the cubic ($P\bar{4}3m$) and the tetragonal ($P4/n$) phases are not in a group-subgroup relation (Figure 3.61). This is due to the fact that the cubic $P\bar{4}3m$ structure, in contrast to the tetrahedral $P4/n$ structure, has no fourfold axis. However, these symmetry descents starting from the CsCl-like structure are also due to the tetrahedral symmetry of the cation and not just a twist of the octahedral anion. The related $[(CH_3)_4N]PF_6$ has a similar crystal structure to tet-$[(CH_3)_4N]SbF_6$, only with aligned anions, resulting in a higher symmetry and a direct group-subgroup relationship.

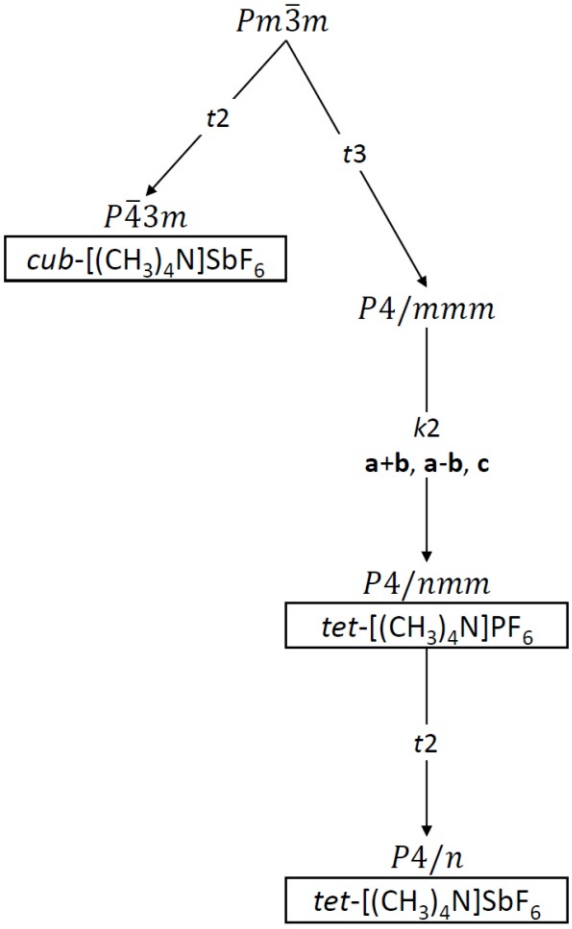

Figure 3.61: Bärnighausen family tree of $[(CH_3)_4N]SbF_6$.

Single crystal structure analysis cub-$[(CH_3)_4N]SbF_6$ The high-temperature phase of the compound crystallises with cubic symmetry in the space group $P\bar{4}3m$ (No. 215).

Cell (426 K): $a = 6.4490(13)$ Å, V= 268.21(16) Å^3, $Z = 1$

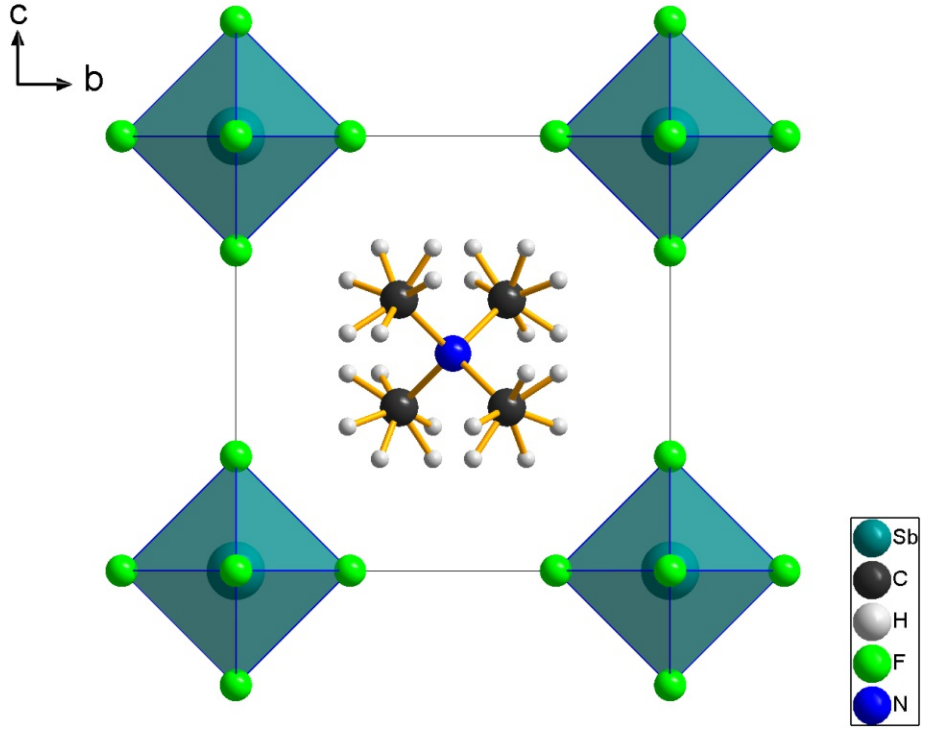

Figure 3.62: Crystal structure of cub−$[(CH_3)_4N]SbF_6$ viewed down [100].

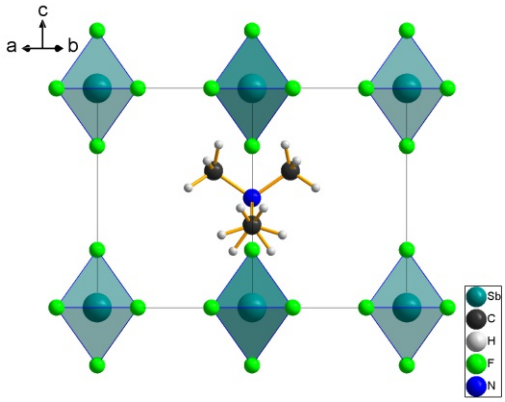

Figure 3.63: Crystal structure of cub−$[(CH_3)_4N]SbF_6$ viewed down [110].

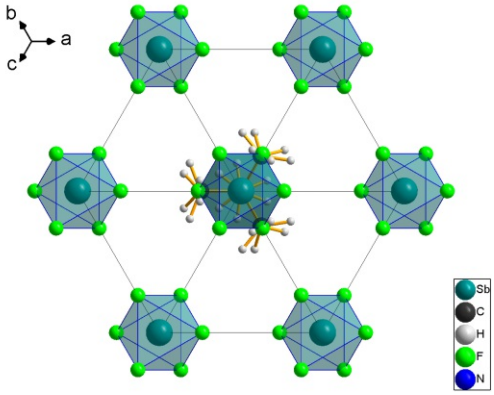

Figure 3.64: Crystal structure of cub−$[(CH_3)_4N]SbF_6$ viewed down [111].

In the cubic crystal structure, the anion with the site symmetry $\bar{4}3m$ forms a regular octahedron. Owing to the crystallographic orbit of Sb and F on the $1a$ ($\bar{4}3m$) and $6f$ ($2mm$) Wyckoff positions, the symmetry is increased to $m\bar{3}m$. The Sb—F bond length is 1.6961(3) Å. In the crystal structure, the tetrahedral methylammonium anion fits ideally into the gaps and adopts the $\bar{4}3m$ symmetry of a regular tetrahedron with a N—C distance of 1.40(13) Å. This comparatively poor standard deviation compared to the anion is due to the higher vibrational freedom of the cation.

Table 3.25: Atomic parameters of cub−$[(CH_3)_4N]SbF_6$.

Atom	**Wyck.**	**Site**	**occ.**	x/a	y/b	z/c	U_{eq}/U_{iso} (Å^2)
Sb1	1a	$\bar{4}3m$	1	0	0	0	0.133(3)
C1	4e	$.3m$	1	0.376(11)	0.624(11)	0.624(11)	0.37(12)
H1A	24j	1	0.50	0.33156	0.74275	0.54621	0.5560
H1B	24j	1	0.50	0.45379	0.66844	0.74275	0.5560
H1C	24j	1	0.50	0.25725	0.54621	0.66844	0.5560
F1	6f	$2.mm$	1	1	0.737(7)	1	0.48(7)
N1	1b	$\bar{4}3m$	1	1/2	1/2	1/2	0.127(16)

Single crystal structure analysis tet-$[(CH_3)_4N]SbF_6$ and comparison to $[(CH_3)_4N]PF_6$
The low-temperature phase of the compound crystallises with tetragonal symmetry in the space group $P4/n$ (No. 85).

Cell (298 K): $a = 8.8924(9)$ Å, $c = 6.5118(6)$ Å, $V = 514.92(11)$ Å^3, $Z = 2$
The symmetries of the HT- and LT-phases are not related by a group-subgroup relationship. Yet, both structures can be derived from a common aristotype, viz. a CsCl-like structure. During the rearrangement from the cubic into the tetrahedral structure, a realignment of the cations and $[SbF_6]^-$ anions takes place, caused by the alternating orientations of the tetrahedral cations (Figure 3.66). The $[SbF_6]^-$ anions are displaced along [001], by the four $[(CH_3)_4N]^+$ cations surrounding in the (001) plane. At the same time, the next anions are pushed in the [00$\bar{1}$] direction (Figure 3.66). This results in a modulation of the Sb position (Figure 3.65), arranging the $[SbF_6]^-$ anions on two different positions along [001]. The positions of the anions are symmetrical equivalent via a centre of inversion.

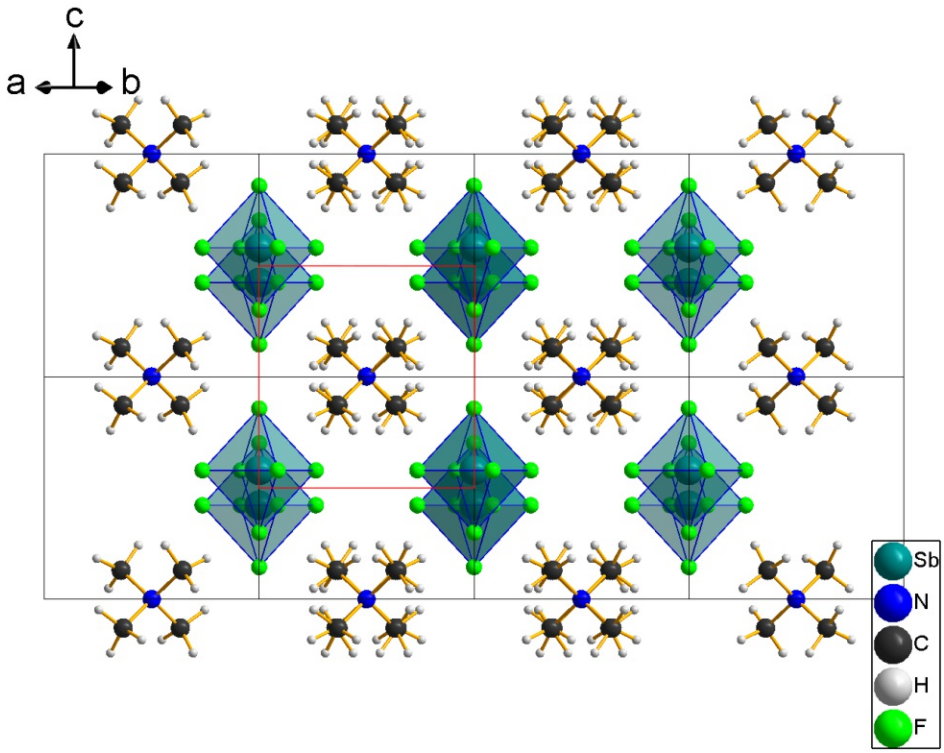

Figure 3.65: Crystal structure of tet-$[(CH_3)_4N]SbF_6$ viewed down [110] with the primitive pseudo-cubic cell highlighted in red.

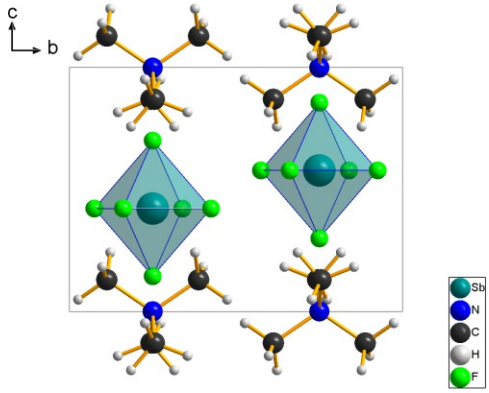

Figure 3.66: Crystal structure of tet$-[(CH_3)_4N]SbF_6$ viewed down [100].

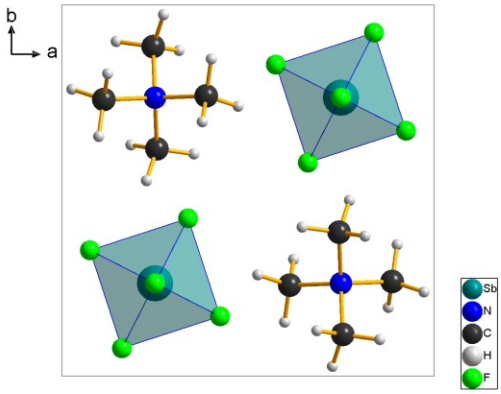

Figure 3.67: Crystal structure of tet$-[(CH_3)_4N]SbF_6$ viewed down [001].

After the transition, the local site symmetry at the positions $4\bar{3}m$ of the octahedral anions and the tetrahedral cations is reduced to 4 and $\bar{4}$, respectively. There is still a single crystallographically independent anion and a single cation. The $[SbF_6]^-$ anions, which were aligned along $\langle 100 \rangle$ are rotated about the tetragonal [001] axis by 12.5(12)° (Figure 3.67). Formally, the site of the $[SbF_6]^-$ anion even gains fourfold symmetry, since the $\bar{4}3m$ position of the HT phase does not possess a fourfold rotation. However, note that, as has been stated before, the anion possesses ideal $m\bar{3}m$ symmetry even in the HT phase owing to the special crystallographic orbits. In any case, this demonstrates that $P4/n$ and $P\bar{4}3m$ are not related by a group-subgroup relationship. Both groups possess symmetry operations that are only found in the $Pm\bar{3}m$ parent structure.
For the $[SbF_6]^-$ anions, this loss of the cubic symmetry is expressed by an elongation of the Sb—F bond along the fourfold axis to 1.815(13) Å and shortening of the equatorial Sb—

F distances to 1.749(13) Å. The cations are compressed along the 4-fold axis, whereby the previously ideal tetrahedral angle is then increased very slightly from 109.4(7)° to 110.9(11)°.

Table 3.26: Atomic parameters of tet−$[(CH_3)_4N]SbF_6$ (origin choice 2).

Atom	**Wyck.**	**Site**	x/a	y/b	z/c	U_{eq}/U_{iso} (Å^2)
Sb1	2c	4..	1/4	1/4	0.42184(9)	0.0592(3)
N1	2a	$\bar{4}$..	3/4	1/4	1	0.066(2)
C1	8g	1	0.6123(12)	0.245(4)	0.8704(18)	0.119(4)
H1A	8g	1	0.62280	0.31485	0.75834	0.1780
H1B	8g	1	0.52656	0.27298	0.95178	0.1780
H1C	8g	1	0.59857	0.14567	0.81738	0.1780
F1	2c	4..	1/4	1/4	0.7005(19)	0.236(11)
F2	2c	4..	1/4	1/4	0.144(2)	0.270(13)
F3	8g	1	0.339(3)	0.425(2)	0.4218(16)	0.31(2)

Comparison with $[(CH_3)_4N]PF_6$: When compared with the analogue hexafluorophosphate $[(CH_3)_4N]PF_6$ (Figure 3.68) with the space group $P4/nmm$ [69], the [tet−$(CH_3)_4N]SbF_6$ has lower symmetry. This can be explained by the $[PF_6]^-$ anions, which are all aligned along $\langle 110 \rangle$. They are therefore located on positions with $4mm$ symmetry.
In contrast, in $[(CH_3)_4N]SbF_6$ the $[SbF_6]^-$ anions are only aligned along the [001] and the other F are, as mentioned before, slightly rotated, thus breaking the mirror symmetry. Thus, the symmetries of $P4/nmm$ and $P4/n$ can be related by a *translationengleiche* symmetry descent of index 2.

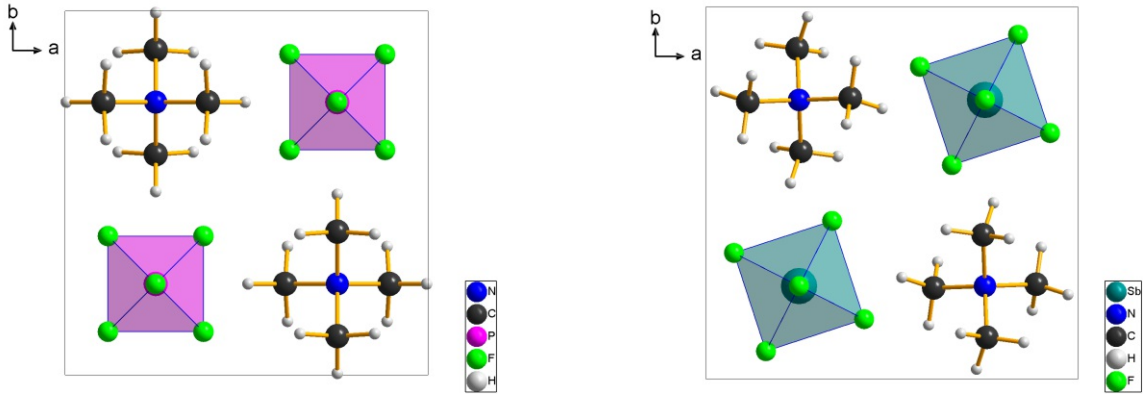

Figure 3.68: Crystal structures of $[(CH_3)_4N]PF_6$[69] (left) and tet−$[(CH_3)_4N]SbF_6$ (right) viewed down [001].

Deviation from the cubic metrics: tet-$[(CH_3)_4N]SbF_6$ shows the loss of the cubic structure owing to the realignment of the cations. The modulation of the two symmetrically equivalent Sb positions with different z coordinates causes an elongating the c parameter. The transformation matrix to obtain the skewed cubic primitive cell is $\begin{pmatrix} 1/2 & -1/2 & 0 \\ 1/2 & 1/2 & 0 \\ 0 & 0 & 1 \end{pmatrix}$, the resulting cubic parameters are listed in Table 3.27.

Table 3.27: Pseudo-cubic metrics of tet-$[(CH_3)_4N]SbF_6$ after transformation into the pseudo-cubic primitive cell.

Compound pseudo-cubic metrics:	**a (Å)**	**b (Å)**	**c (Å)**	α (°)	β (°)	γ (°)
tet-$[(CH_3)_4N]SbF_6$	6.2879(4)	6.2879(4)	6.5118(6)	90	90	90

Reciprocal space sections of $[(CH_3)_4N]SbF_6$ In contrast to the other methyl-substituted ammonium hexafluoroantimonates, comparatively little three-dimensional diffuse scattering is observed in the sections through the reciprocal space sections (Figure 3.69, 3.70). This is because, as already mentioned, the methyl groups of the $[(CH_3)_4N]^+$ cation are comparatively well localised in the crystal.

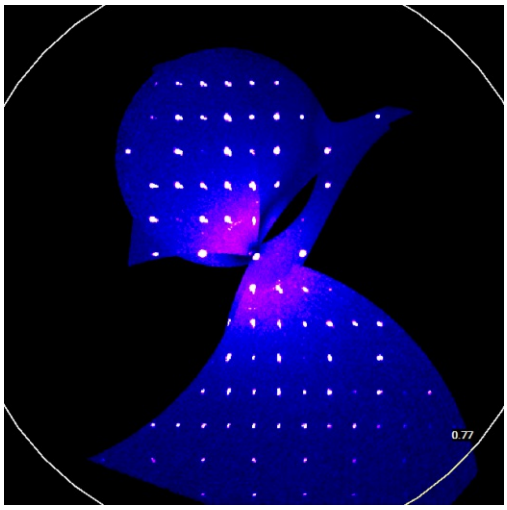

Figure 3.69: $(0kl)^*$ plane of reciprocal space of [tet$-(CH_3)_4N]SbF_6$ reconstructed from CCD data collected at 300 K.

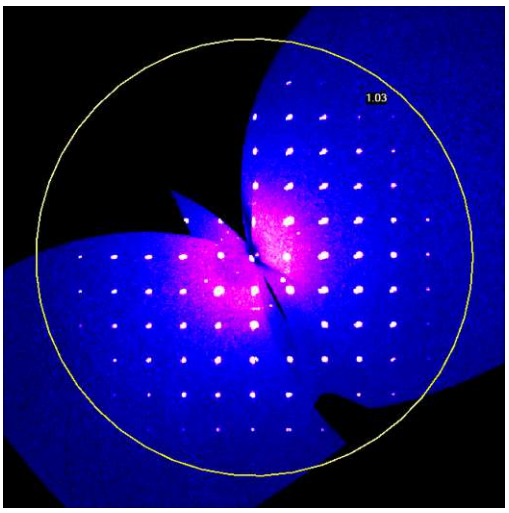

Figure 3.70: $(0kl)^*$ plane of reciprocal space of cub$-[(CH_3)_4N]SbF_6$ reconstructed from CCD data collected at 430 K.

3.8.1.1 PXRD analysis $[(CH_3)_4N]SbF_6$

The non-ambient measurements in the range from 310 K to 95 K show no phase transition. At room temperature, the tetragonal structure is still present which was confirmed by Rietveld refinement using a model derived from X-ray diffraction (Figure 3.71).

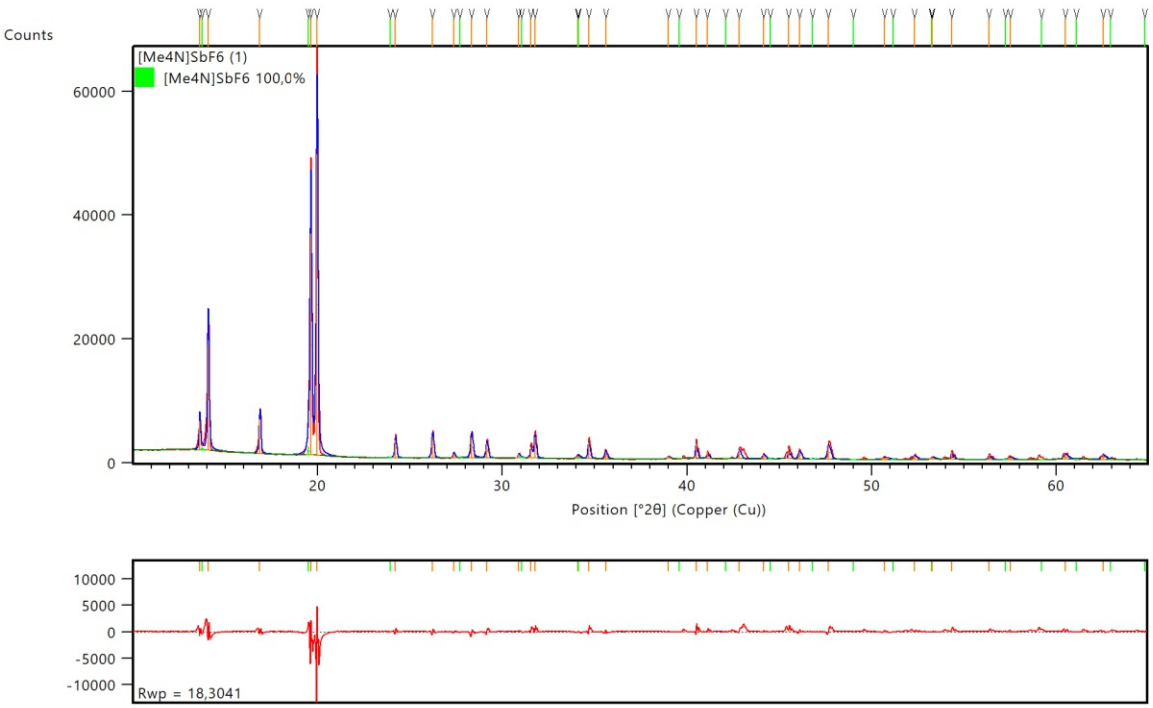

Figure 3.71: PXRD of $[(CH_3)_4N]SbF_6$ at 300 K (red) with Rietveld refinement of a model derived from single crystal diffraction (blue) with difference plot (in red) below.

3.8.2 Trimethylammonium hexafluoroantimonate ($[(CH_3)_3NH]SbF_6$)

Depending on the temperature, $[(CH_3)_3NH]SbF_6$ has two polymorphs, the cubic high-temperature crystal structure with the space group $Pm\bar{3}m$ and the orthorhombic low-temperature crystal structure with $P2_12_12_1$ symmetry. There are numerous possible series of maximal group/subgroup relations describing the symmetry descent. Here, only one possibility is listed in Figure 3.72.

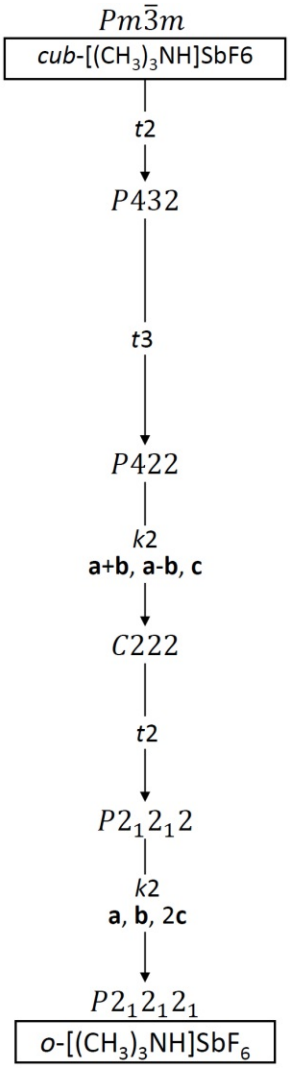

Figure 3.72: Bärnighausen family tree of $[(CH_3)_3NH]SbF_6$.

Single crystal structure analysis o−$[(CH_3)_3NH]SbF_6$ The low-temperature phase of the compound crystallises with orthorhombic symmetry in the space group $P2_12_12_1$ (No. 19).

Cell (100 K): $a = 8.2505(18)$ Å, $b = 8.929(2)$ Å, $c = 12.108(3)$ Å, $V = 891.98(36)$ Å^3, $Z = 4$

In the orthorhombic crystal structure of $[(CH_3)_3NH]SbF_6$, the distorted cubic structure can still be recognised in sheets parallel to 001 (Figure 3.74). In the [110] plane, the anions and cations are arranged in a chequerboard pattern, with the barycenters of the anions and cations located close to the screw axes in [001] direction. This is not the case for the other two directions, in the [100] and [010] directions the ions are located in between the screw axes. The octahedral $[SbF_6]^-$ anions are distinctly distorted. Geometric parameters are compiled

in Table 3.28.
In Figure 3.73 the two layers of the structure, related by the 2_1 screw axis are superimposed (Figure 3.74), and the distorted pseudo-cubic structure can be recognised. In contrast to the $[(CH_3)_4N]^+$ cation, which adopts the full symmetry in the crystal, the $3m$ symmetry of the $[(CH_3)_3NH]^+$ cation is reduced to 1, as the ion is located on a general position.

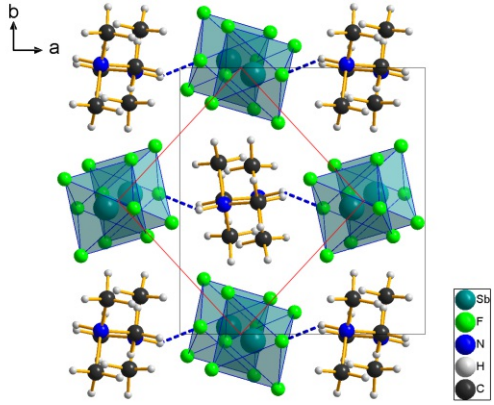

Figure 3.73: Crystal structure of o−$[(CH_3)_3NH]SbF_6$ viewed down [001].

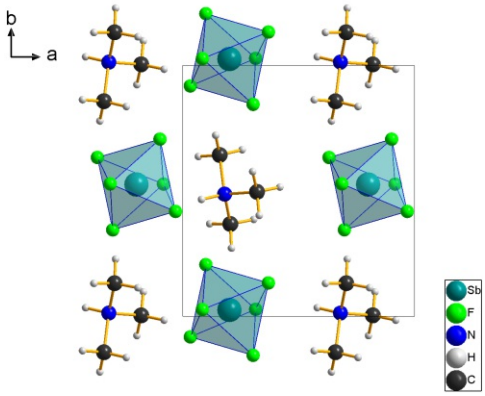

Figure 3.74: One layer of o−$[(CH_3)_3NH]SbF_6$ viewed down [001] ($y \in [0.5, 0.1]$).

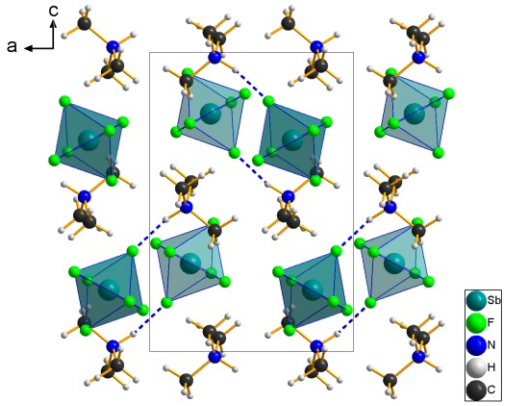

Figure 3.75: Crystal structure of o−$[(CH_3)_3NH]SbF_6$ viewed down [010].

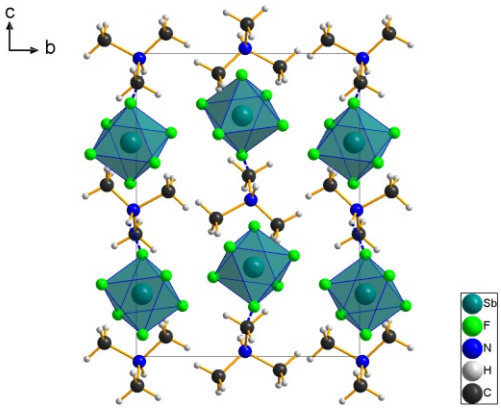

Figure 3.76: Crystal structure of o−$[(CH_3)_3NH]SbF_6$ viewed down [100].

In this symmetry descent from the cubic cell, the volume of the orthorhombic cell is doubled, still only one independent ion is present. The site symmetry of the $[SbF_6]^-$ anions is reduced from $m\bar{3}m$ to 1. The positions of the ions is modulated (Figure 3.73) resulting in a twofold superstructure in [001] directions. This is indicated by satellite reflections in the diffraction pattern (Figure 3.80).

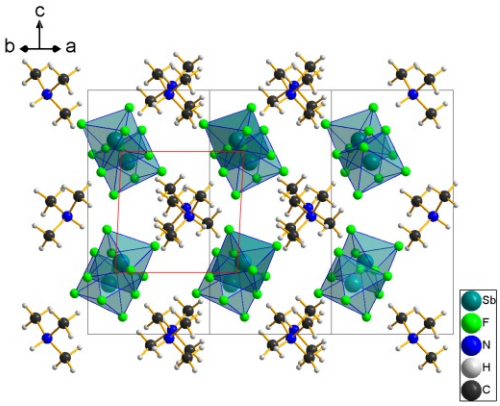

Figure 3.77: Crystal structure of o−$[(CH_3)_3NH]SbF_6$ viewed down [110] which corresponds to [100] in the cubic crystal structure.

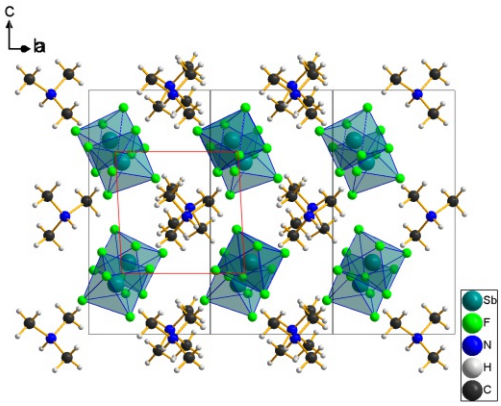

Figure 3.78: Crystal structure of o−$[(CH_3)_3NH]SbF_6$ viewed down [1$\bar{1}$0] which corresponds to [010] in the cubic crystal structure.

Table 3.28: Octahedron distances and angles in $[(CH_3)_3NH]SbF_6$.

Atoms	**distance (Å)**	**Atoms**	**∠ (°)**
Sb1—F4	1.84(2)	F1—Sb1—F4	92.7(10)
Sb1—F1	1.845(18)	F4—Sb1—F5	91.5(12)
Sb1—F5	1.864(18)	F5—Sb1—F1	93.6(10)
Sb1—F3	1.87(2)	F2—Sb1—F3	90.1(10)
Sb1—F2	1.878(16)	F3—Sb1—F6	90.0(11)
Sb1—F6	1.880(19)	F6—Sb1—F2	89.9(10)

Hydrogen bonds: Each $[(CH_3)_3NH]^+$ cation has only one H that can connect to one $[SbF_6]^-$ anion, each forming simple dimers oriented in the [101] and [10$\bar{1}$] directions (Figure 3.75).

Table 3.29: Atomic parameters of o−$[(CH_3)_3NH]SbF_6$.

Atom	Wyck.	Site	x/a	y/b	z/c	U_{eq}/U_{iso} (Å^2)
Sb1	4a	1	0.7007(2)	0.4745(2)	0.79434(16)	0.0230(4)
F1	4a	1	0.584(2)	0.473(3)	0.6642(15)	0.048(4)
F2	4a	1	0.814(2)	0.472(3)	0.9287(13)	0.048(4)
F3	4a	1	0.532(2)	0.582(3)	0.8613(19)	0.047(4)
F4	4a	1	0.869(2)	0.367(3)	0.7334(18)	0.047(4)
F5	4a	1	0.803(3)	0.6554(19)	0.7621(19)	0.044(4)
F6	4a	1	0.599(3)	0.294(2)	0.8328(18)	0.044(4)
N1	4a	1	0.820(3)	0.987(3)	0.483(2)	0.029(6)
H1	4a	1	0.92000	0.96570	0.44100	0.0350
C1	4a	1	0.680(5)	0.996(6)	0.404(3)	0.056(13)
H1A	4a	1	0.69870	1.07690	0.35230	0.0840
H1B	4a	1	0.58130	1.01510	0.44520	0.0840
H1C	4a	1	0.67070	0.90230	0.36480	0.0840
C2	4a	1	0.841(4)	1.143(4)	0.545(4)	0.040(10)
H2A	4a	1	0.85850	1.22150	0.49160	0.0600
H2B	4a	1	0.93340	1.13690	0.59460	0.0600
H2C	4a	1	0.74390	1.16400	0.58770	0.0600
C3	4a	1	0.795(4)	0.868(3)	0.566(3)	0.025(6)
H3A	4a	1	0.69420	0.88610	0.60490	0.0380
H3B	4a	1	0.88430	0.86890	0.61790	0.0380
H3C	4a	1	0.79030	0.77200	0.52900	0.0380

Deviation from the cubic metrics: The pseudo cubic cell of the basic structure of $[(CH_3)NH_3]SbF_6$ shows a small distortion mainly in the [001]-direction with respect to the cubic structure due to the orientation and modulation of the position of the cations (Table 3.30). The c axis is the shortest because the flat cations arrange themselves with their short site in this direction. Likewise, the influence of the elongated cation results in a widening of the γ angle. The transformation matrix relating the cells of the HT- and LT-phases is $\begin{pmatrix} 1/2 & -1/2 & 0 \\ 1/2 & 1/2 & 0 \\ 0 & 0 & 1/2 \end{pmatrix}$.

Table 3.30: Pseudo-cubic metrics of o-$[(CH_3)_3NH]SbF_6$ after transformation into the pseudo-cubic primitive cell.

Compound **pseudo-cubic metrics:**	**a** **(Å)**	**b** **(Å)**	**c** **(Å)**	α (°)	β (°)	γ (°)
$[(CH_3)_3NH]SbF_6$	6.0786(10)	6.0786(10)	6.054(15)	90	90	94.5234(180)

Twinning of $[(CH_3)_3NH]SbF_6$ During the phase transition upon cooling, a strong twinning occurred. The fourfold and threefold axes as well as the centres of inversion are lost, when the symmetry is reduced from $Pm\bar{3}m$ to $P2_12_12_1$. In total, this corresponds to a loss of point symmetry of index 12. This means that the crystal has twelve possibilities to align itself after the loss of symmetry. Of these twelve orientations, six are related by inversion to the other six, which is not necessarily noticeable in such a complex data set. Indeed, the crystals were processed and refined as sixfold twins.

Reciprocal space sections of $[(CH_3)_3NH]SbF_6$ Owing to the deviation from cubic metrics (see previous sections) the spots were separated enough, to warrant separate integration

of the six domains (with overlap information). The splitting of the reflections is clearly observed in the diffraction images (Figure 3.80).
In the high-temperature phase of $[(CH_3)_3NH]SbF_6$, the dynamic disorder of anions and cations is indicated by intense three-dimensional diffuse scattering visible in $\langle 100 \rangle$ directions (Figure 3.79). Also, the high-temperature phase scatters only to distinctly smaller angles, when compared to the reciprocal space sections of the low-temperatue phase (Figure 3.80).

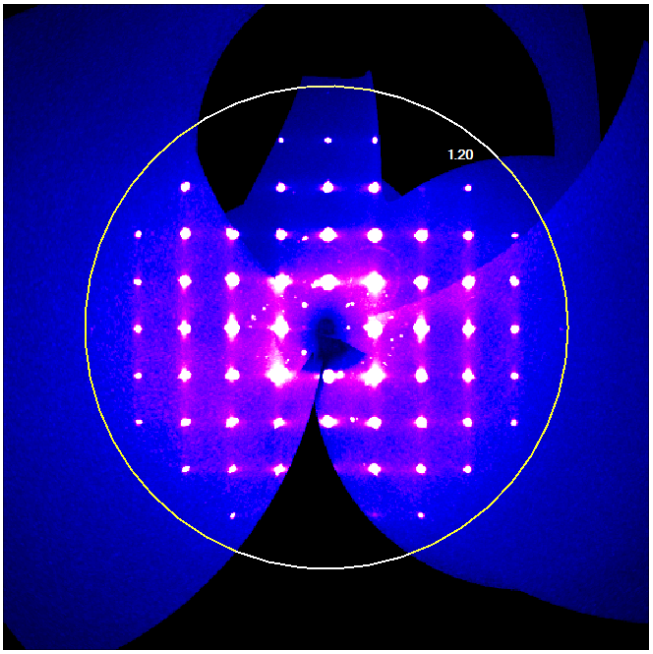

Figure 3.79: $(h0l)^*$ plane of reciprocal space of cub-$[(CH_3)_3NH]SbF_6$ reconstructed from CCD data collected at K.

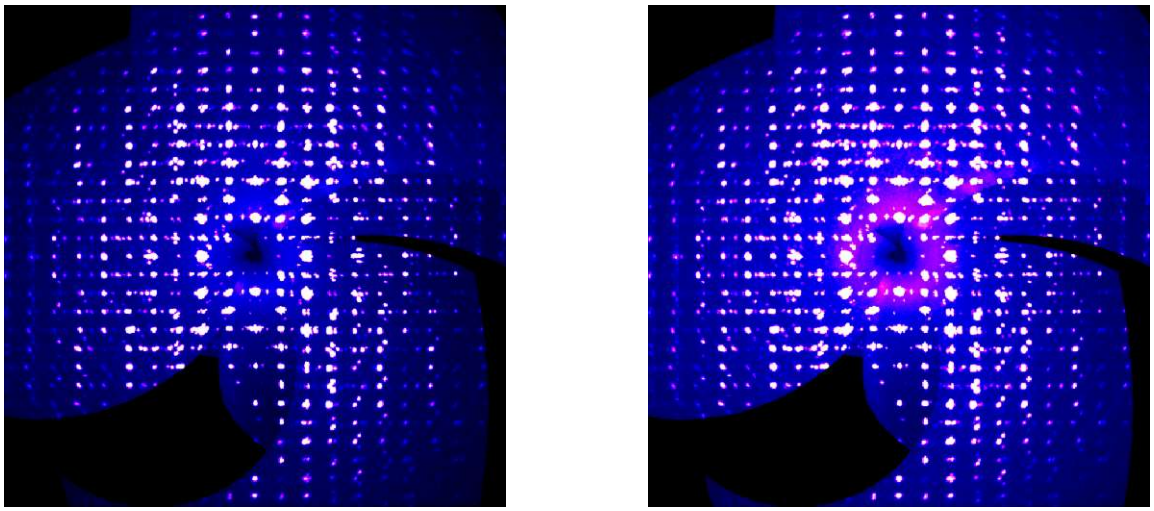

(a) 150 K (a) 100 K

Figure 3.80: $(0kl)^*$ plane of reciprocal space of o-$[(CH_3)_3NH]SbF_6$ reconstructed from CCD data collected at 250, 150 and 100 K.

3.8.2.1 PXRD analysis $[(CH_3)_3NH]SbF_6$

The results of the study of the temperature dependence are shown in Figure 3.81. The phase transition at 245 K is clearly visible as the appearance of intense superstructure reflections.

Since some reflections of the cubic phase disappear during the transition, not only the cell size but also at least one of the directions probably changes. Owing to the simultaneous existence of both phases, a phase transition with first order character can be assumed.

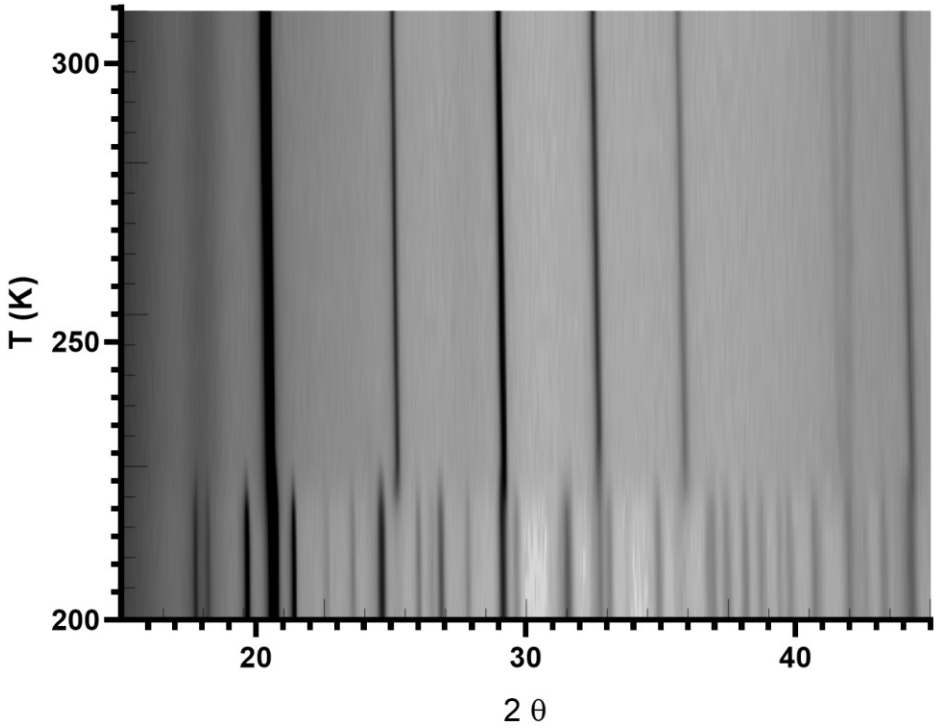

Figure 3.81: Temperature dependent PXRD of $[(CH_3)_3NH]SbF_6$ from 200 K to 315 K in 5 K steps.

3.8.3 Dimethylammonium hexafluoroantimonate ($[(CH_3)_2NH_2]SbF_6$)

For $[(CH_3)_2NH_2]SbF_6$, no crystal structure could be determined up to now. The crystal growth was initially carried out analogously to the other hexafluoroantimonates. However, this yielded the cubic phase at room temperature. On cooling, owing to the loss of point symmetry, the crystals fracture into multiple domains, which made it impossible to determine the symmetry.
To overcome this problem, crystallisation at -20 °C was attempted, which was successful for $[(CH_3)NH_3]SbF_6$. However, here this invariably gave the monohydrate $[(CH_3)_2NH_2]SbF_6 \cdot H_2O$ as a crystalline product. Above 280 K $[(CH_3)_2NH_2]SbF_6 \cdot H_2O$ decomposes under amorphisation, presumably losing the water of crystallisation.

Reciprocal space sections of $[(CH_3)_2NH_2]SbF_6$ As already mentioned, no structural solution could be obtained for single crystals of $[(CH_3)_2NH_2]SbF_6$ (without water of crystallization). However, when looking at the reciprocal space sections reconstructed from CCD data, the same effects of disordering can be observed as three-dimensional diffuse scattering in analogue to the corresponding monomethyl and trimethylammonium salts at high temperatures (Figure 3.82 a).
In the reciprocal space section at 100 K (Figure 3.82 b), no diffuse scattering is visible any more. The crystal visible here is a polycrystal, which was formed due to the fracturing during the phase transition.

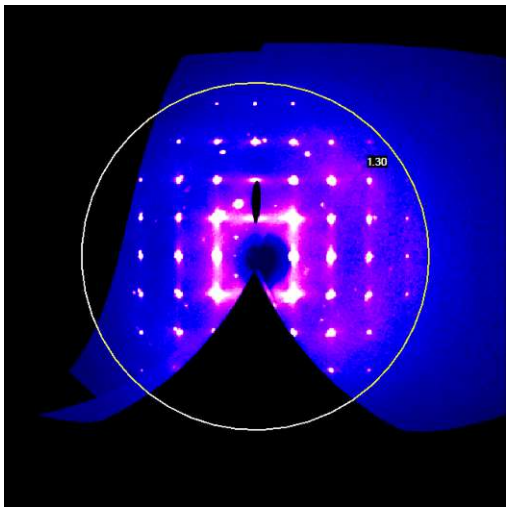

(a) 300 K

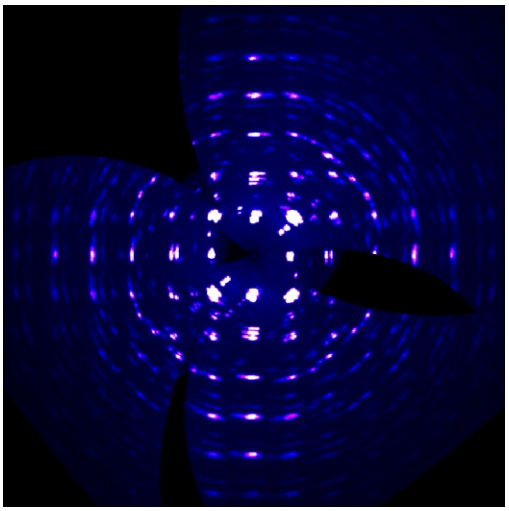

(a) 100 K

Figure 3.82: $(0kl)^*$ plane of reciprocal space of $[(CH_3)_2NH_2]SbF_6$ reconstructed from CCD data collected at (a) 300 and (b) 100 K.

3.8.3.1 PXRD analysis $[(CH_3)_2NH_2]SbF_6$

The results of the study of the temperature dependence are shown in Figure 3.83 for a powdered anhydrous sample. The phase transition at 275 K, just below room temperature is clearly visible. Temperature-dependent PXRD measurement of the hydrate was not possible owing to the decomposition at ca. 280 K.

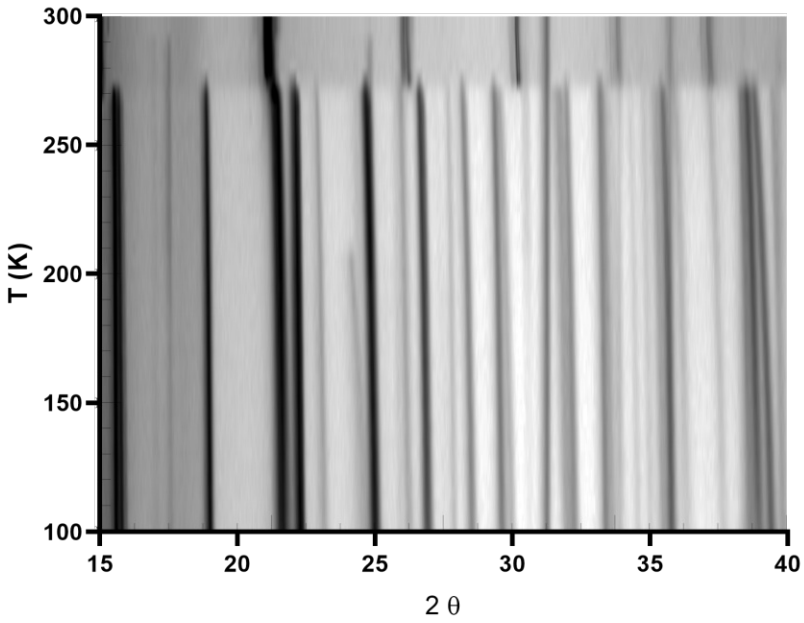

Figure 3.83: Temperature dependent PXRD of $[(CH_3)_3NH]SbF_6$ from 100 K to 300 K in 5 K steps.

3.8.3.2 Dimethylammonium hexafluoroantimonate monohydrate ($[(CH_3)_2NH_2]SbF_6 \cdot H_2O$)

Above about 130 K the high-temperature phase of the hydrate, for short HT-$[(CH_3)_2NH_2]SbF_6 \cdot H_2O$, is present with disordered hydrogens. Below the transition temperature, all hydrogens become ordered, resulting in the low-temperature phase, for short LT-$[(CH_3)_2NH_2]SbF_6 \cdot H_2O$. The hydrate can be described as a CsCl-like structure, just like the anhydrous compound. Starting from the cubic symmetry of $[(CH_3)_2NH_2]SbF_6$, there are numerous possible series of maximal group-/subgroup relations describing the symmetry descent. Here, only one possibility is listed in Figure 3.84.

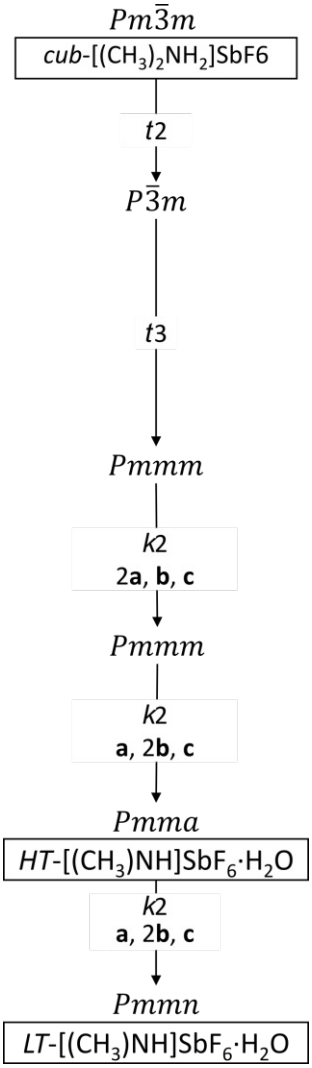

Figure 3.84: Bärnighausen family tree of $[(CH_3)_2NH_2]SbF_6 \cdot H_2O$.

Single crystal structure analysis HT-$[(CH_3)_2NH_2]SbF_6 \cdot H_2O$ The hydrate $[(CH_3)_2NH_2]SbF_6 \cdot H_2O$ crystallises with orthorhombic symmetry in the space group *Pmma* (No. 51).

Cell (240 K): 13.2972(11) Å, $b = 10.9348(10)$ Å, 6.6316(6) Å, $V = 964.25(15)$ Å^3, $Z = 4$

One water molecule per $[(CH_3)_2NH_2]^+$ cation incorporates into the crystal structure. This water molecule substitutes for the missing methyl groups of the $[(CH_3)_2NH_2]^+$ cation with respect to the highly symmetric $[(CH_3)_4N]^+$. The structure is stabilised owing to hydrogen bonds formed between N—H$\cdots$OH$_2$. The resulting crystal structure (Figure 3.85) resembles that of tet-$[(CH_3)_4N]SbF_6$. Owing to the H-bonds formed, some $[SbF_6]^-$ anions are disordered. Moreover, the water molecules form among each other tetramers via hydrogen bonding, which leads to a further symmetry descent from *Pmmm* to *Pmma*, as the mirror plane in [001] is reduced to a glide reflection plane. This is visible as modulation of the $[SbF_6]^-$ anion in [100] (Figure 3.89).

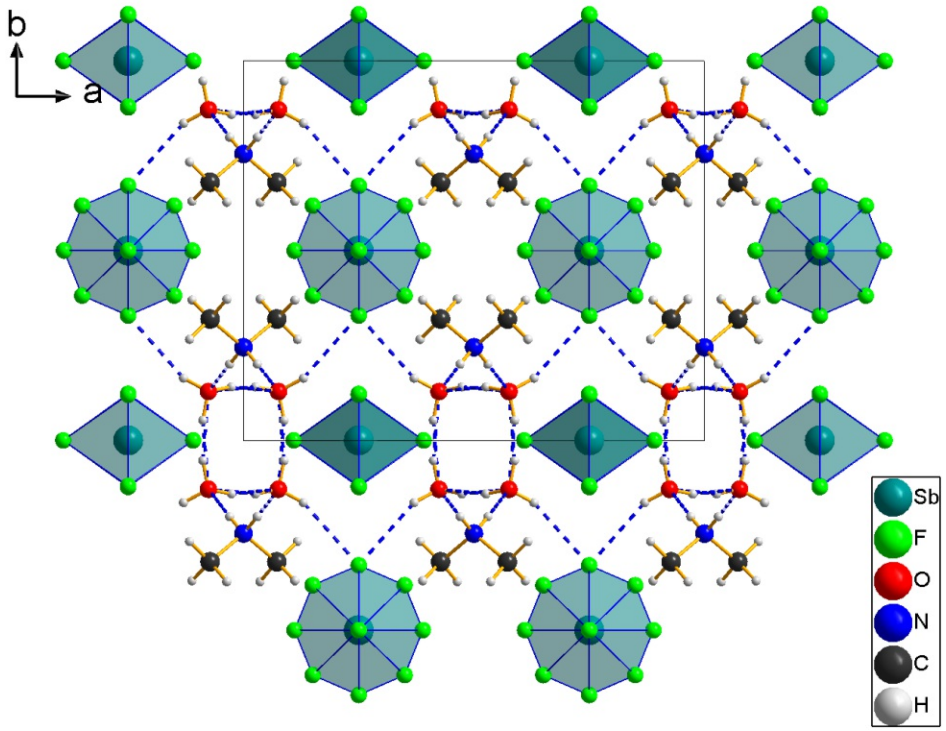

Figure 3.85: Crystal structure of HT-$[(CH_3)_2NH_2]SbF_6 \cdot H_2O$ viewed down [001].

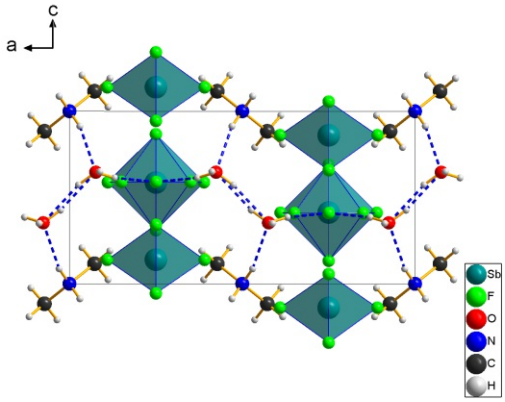

Figure 3.86: Crystal structure of HT-$[(CH_3)_2NH_2]SbF_6 \cdot H_2O$ viewed down [010].

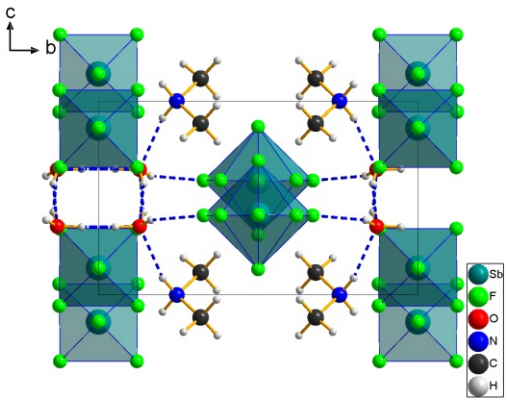

Figure 3.87: Crystal structure of HT-$[(CH_3)_2NH_2]SbF_6 \cdot H_2O$ viewed down [100].

Single crystal structure analysis LT-$[(CH_3)_2NH_2]SbF_6 \cdot H_2O$ Below 130 K, the hydrate $[(CH_3)_2NH_2]SbF_6 \cdot H_2O$ has orthorhombic symmetry and the space group *Pmmn* (No. 59).

Cell (100 K): 13.1647(13) Å, $b = 21.538(2)$ Å, 6.5963(6) Å, $V = 1870.32(31)$ Å^3, $Z = 8$

When $[(CH_3)_2NH_2]SbF_6 \cdot H_2O$ is cooled, the hydrogen atoms in the water-tetramers become ordered. This transition leads to a decrease in symmetry and accordingly an increase in the size of the unit cell, while other features of the crystal structure remain intact, resulting in the space group *Pmmn*. The symmetry relationship in the HT and LT phases is of the *klassengleiche* type. The point symmetry remains, whereas the half of the translations are lost in

[010] direction. The two phases are in a group/subgroup relationship of index 2.

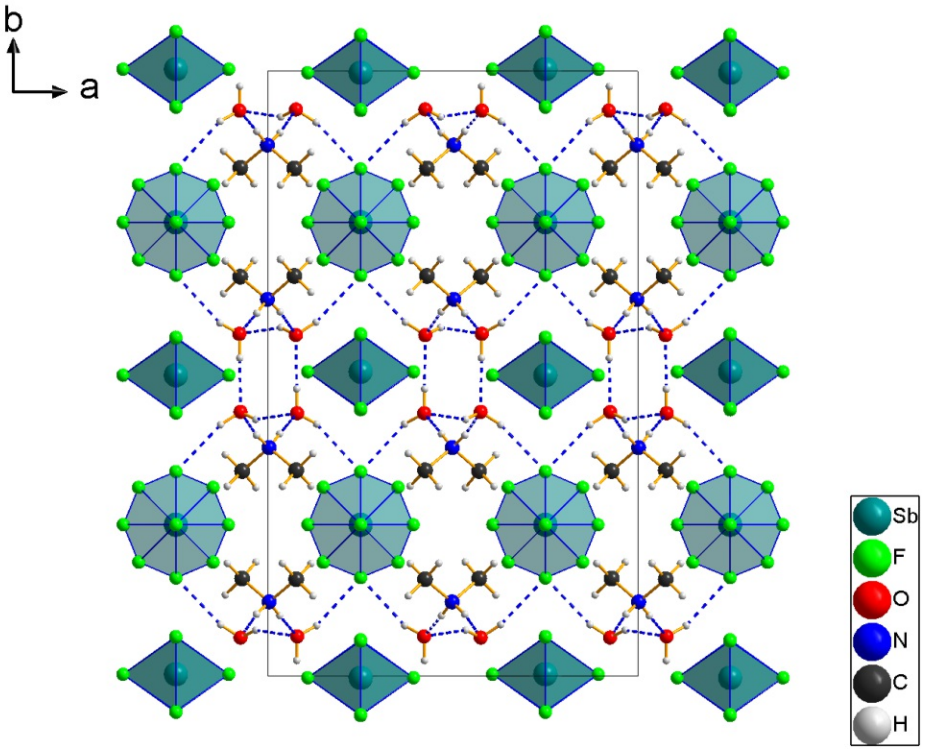

Figure 3.88: Crystal structure of LT-$[(CH_3)_2NH_2]SbF_6 \cdot H_2O$ viewed down [001].

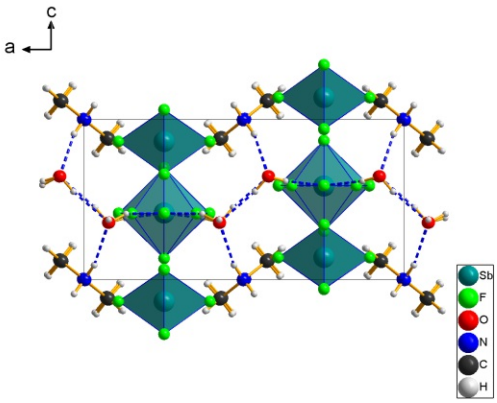

Figure 3.89: Crystal structure of LT-$[(CH_3)_2NH_2]SbF_6 \cdot H_2O$ viewed down [010].

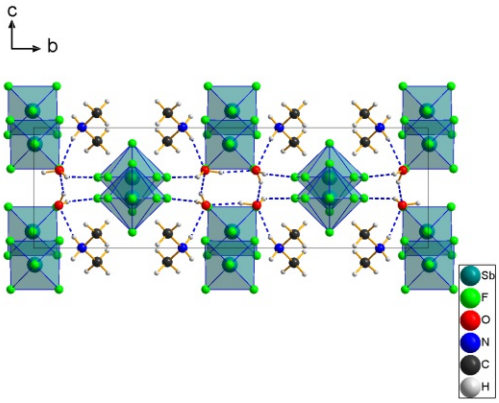

Figure 3.90: Crystal structure of LT-$[(CH_3)_2NH_2]SbF_6 \cdot H_2O$ viewed down [100].

Hydrogen bond network of $[(CH_3)_2NH_2]SbF_6 \cdot H_2O$ $[(CH_3)_2NH_2]SbF_6$ forms a complex two-dimensional hydrogen bonding network, due to the water of crystallisation. The hydrogen bond network can be described as sheets in the (001) plane (Figure 3.88). Each water molecule (e.g. short "$W1$": water formed by $O1$) is connected to four other units. The LT and HT structures only differ by the ordering of the hydrogen bonding between the $W1$ and $W2$ molecules. In the HT structure, all $W \cdots W$ H-bonds are disordered.
In the LT-structure, all $W \cdots W$ H-bonds are ordered, and the two water molecules are no longer symmetrical equivalent. In [100] direction $W1$ is always hydrogen bond acceptor when connected to W2 and the other way around in [010] direction. Only the disordered $[SbF_6]^-$

anions with *Sb*1 and *Sb*2 as central atom are interconnected with the hydrogen bond network. The resulting connectivity graph (Figure 3.92) shows that the resulting net is neither a Platonic nor an Archimedean net.

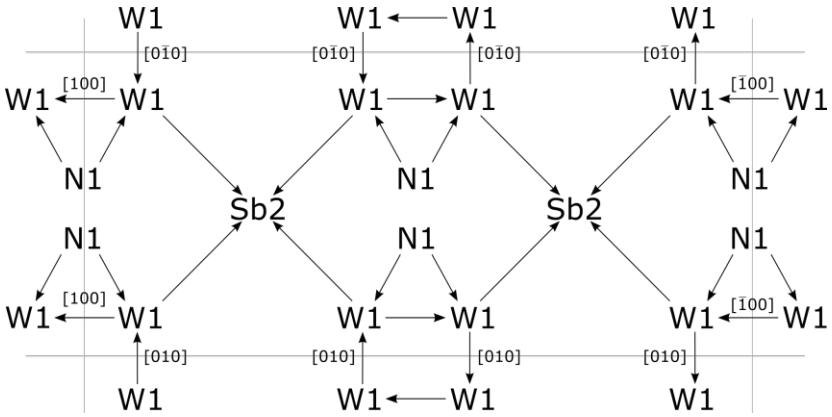

Figure 3.91: Connectivity graph of hydrogen bond network of HT-$[(CH_3)_2NH_2]SbF_6 \cdot H_2O$ viewed down [001] with unit cell boundaries. Double arrows represent disordered hydrogen bonds.

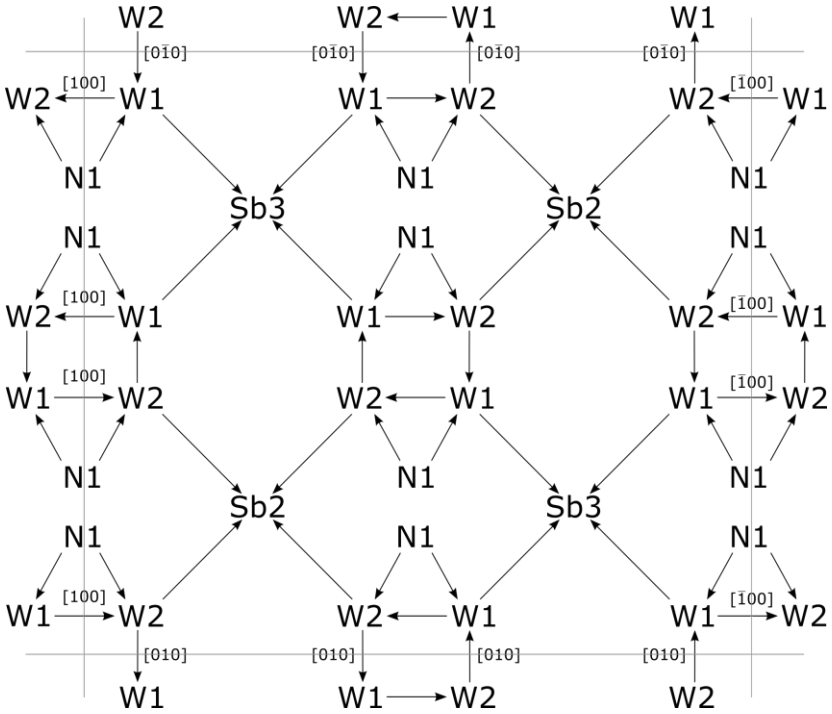

Figure 3.92: Connectivity graph of hydrogen bond network of LT-$[(CH_3)_2NH_2]SbF_6 \cdot H_2O$ viewed down [001] with unit cell boundaries.

Table 3.31: Atomic parameters of HT-$[(CH_3)_2NH_2]SbF_6 \cdot H_2O$.

Atom	**Wyck.**	**Site**	**occ.**	x/a	y/b	z/c	U_{eq}/U_{iso} (Å^2)
Sb1	2e	$mm2$	1	3/4	1	0.13935(4)	0.03182(7)
Sb2	2f	$mm2$	1	3/4	1/2	0.58690(4)	0.03081(7)
F1	4k	$m..$	1	3/4	0.8798(2)	0.3417(4)	0.0517(5)
F2	4k	$m..$	1	3/4	0.8773(3)	-0.0562(4)	0.0598(7)
F3	4i	$.m.$	1	0.8908(2)	1	0.1384(4)	0.0504(6)
F4	2f	$mm2$	1	3/4	1/2	0.8671(5)	0.0732(12)
F5	2f	$mm2$	1	3/4	1/2	0.3100(5)	0.0826(14)
F6	4k	$m..$	0.575(14)	3/4	0.6709(4)	0.5901(10)	0.081(3)
F6'	8l	1	0.425(14)	0.6503(6)	0.6184(8)	0.5906(10)	0.084(3)
F7	4j	$.m.$	0.575(14)	0.6108(4)	1/2	0.5881(11)	0.117(7)
O1	8l	1	1	0.5760(2)	0.8712(2)	0.6467(3)	0.0459(4)
N1	4g	.2.	1	1/2	0.7545(3)	1	0.0395(6)
C1	8l	1	1	0.4276(3)	0.6801(3)	0.8840(5)	0.0512(6)
H1A	8l	1	1	0.38307	0.73362	0.80902	0.0770
H1B	8l	1	1	0.38846	0.63014	0.97582	0.0770
H1C	8l	1	1	0.46386	0.62773	0.79094	0.0770
HN1	8l	1	1	0.530(2)	0.799(3)	0.913(4)	0.046(9)
H1	8l	1	1	0.630(2)	0.836(4)	0.614(6)	0.066(12)
H2	8l	1	1	0.526(3)	0.859(6)	0.573(7)	0.039(16)
H3	8l	1	1	0.588(4)	0.947(2)	0.650(8)	0.030(14)

Table 3.32: Atomic parameters of LT-$[(CH_3)_2NH_2]SbF_6 \cdot H_2O$.

Atom	Wyck.	Site	occ.	x/a	y/b	z/c	U_{eq}/U_{iso} (Å^2)
Sb1	2a	$mm2$	1	3/4	3/4	0.41594(6)	0.01108(8)
Sb2	2b	$mm2$	1	3/4	1/4	0.41544(6)	0.01155(8)
Sb3	4e	$m..$	1	3/4	0.49705(2)	0.86260(4)	0.01477(6)
F1	4e	$m..$	1	3/4	0.43481(14)	1.0616(5)	0.0272(7)
F2	4e	$m..$	1	3/4	0.43589(13)	0.6581(5)	0.0240(6)
F3	8g	1	1	0.60703(13)	0.49715(9)	0.8628(3)	0.0230(4)
F4	4e	$m..$	1	3/4	0.55802(13)	0.6577(5)	0.0232(6)
F5	4e	$m..$	1	3/4	0.55985(15)	1.0585(5)	0.0275(7)
F6	4e	$m..$	0.801(5)	3/4	0.66264(15)	0.4136(7)	0.0318(8)
F6'	8g	1	0.199(5)	0.8510(9)	0.6881(5)	0.4120(19)	0.0322(10)
F7	4f	$.m.$	0.801(5)	0.8922(3)	3/4	0.4140(7)	0.0323(8)
F8	2a	$mm2$	1	3/4	3/4	0.6981(7)	0.0307(10)
F9	2a	$mm2$	1	3/4	3/4	0.1324(7)	0.0288(9)
F10	2b	$mm2$	1	3/4	1/4	0.6979(7)	0.0313(10)
F11	2b	$mm2$	1	3/4	1/4	0.1322(6)	0.0248(8)
F12	4e	$m..$	0.405(5)	3/4	0.3379(3)	0.4126(14)	0.0318(8)
F12'	8g	1	0.595(5)	0.6494(3)	0.31171(17)	0.4125(6)	0.0322(10)
F13	4f	$.m.$	0.405(5)	0.6081(6)	1/4	0.4109(14)	0.0323(8)
O1	8g	1	1	0.57510(15)	0.43644(10)	0.3550(3)	0.0211(4)
H1	8g	1	1	0.5341(4)	0.4241(5)	0.4503(7)	0.16(4)
H2	8g	1	1	0.6292(3)	0.4151(3)	0.385(2)	0.053(16)
O2	8g	1	1	0.42188(16)	0.43442(8)	0.6446(4)	0.0203(4)
H3	8g	1	1	0.3692(3)	0.4166(3)	0.5903(12)	0.048(16)
H4	8g	1	1	0.423(6)	0.47445(13)	0.627(3)	0.11(3)
N1	8g	1	1	0.4976(2)	0.37749(11)	0.0018(5)	0.0179(4)
C1	8g	1	1	0.5706(3)	0.33880(14)	-0.1143(5)	0.0210(6)
H1A	8g	1	1	0.53330	0.31150	-0.20690	0.0320
H1B	8g	1	1	0.61080	0.31360	-0.02010	0.0320
H1C	8g	1	1	0.61600	0.36580	-0.19250	0.0320
C2	8g	1	1	0.4244(3)	0.34000(14)	0.1210(6)	0.0234(7)
H2A	8g	1	1	0.38420	0.31400	0.02910	0.0350
H2B	8g	1	1	0.37910	0.36770	0.19650	0.0350
H2C	8g	1	1	0.46150	0.31350	0.21630	0.0350
HN1	8g	1	1	0.532(3)	0.3980(19)	0.091(6)	0.033(13)
HN2	8g	1	1	0.469(3)	0.4003(16)	-0.089(5)	0.021(10)

Deviation from the cubic metrics: $[(CH_3)_2NH_2]SbF_6 \cdot H_2O$ shows a structure very similar to the cubic CsCl-like aristotype. As already mentioned, the cavities of the two missing methyl groups to achieve tetrahedral symmetry with respect to the $[(CH_3)_2NH_2]^+$ cation are compensated by the incorporation of water. The pseudo-cubic cell can be obtained by the following transformation matrix for HT-$[(CH_3)_2NH_2]SbF_6 \cdot H_2O$: $\begin{pmatrix} 1/2 & 0 & 0 \\ 0 & 1/2 & 0 \\ 0 & 0 & 1 \end{pmatrix}$, the parameters obtained are given in Table 3.33. The values obtained show that especially in the [010] direction, the pseudo-cubic cell obtained is already very far away from a cubic cell.
In addition, as already described, the structure is further distorted by the hydrogen bonds. Due to their orientation in the [010] and [001] directions, these cell parameters are also shortened.

Table 3.33: Pseudo-cubic metrics of $[(CH_3)_2NH_2]SbF_6 \cdot H_2O$ after transformation into the pseudo-cubic primitive cell.

Compound **pseudo-cubic metrics:**	**a** **(Å)**	**b** **(Å)**	**c** **(Å)**	α (°)	β (°)	γ (°)
$\mathbf{[(CH_3)_2NH_2]SbF_6 \cdot H_2O}$	6.5823(7)	5.3845(5)	6.5963(6)	90	90	90

Reciprocal space sections of $[(CH_3)_2NH_2]SbF_6 \cdot H_2O$ The simple phase transition can be observed in the diffraction pattern. On cooling between 130 and 110 K, additional superstructure reflections appear at half-integer values in the $\mathbf{b}^*$-direction, which corresponds to a loss of translation symmetry and to a doubling of the length of the b axis (Figure 3.93).

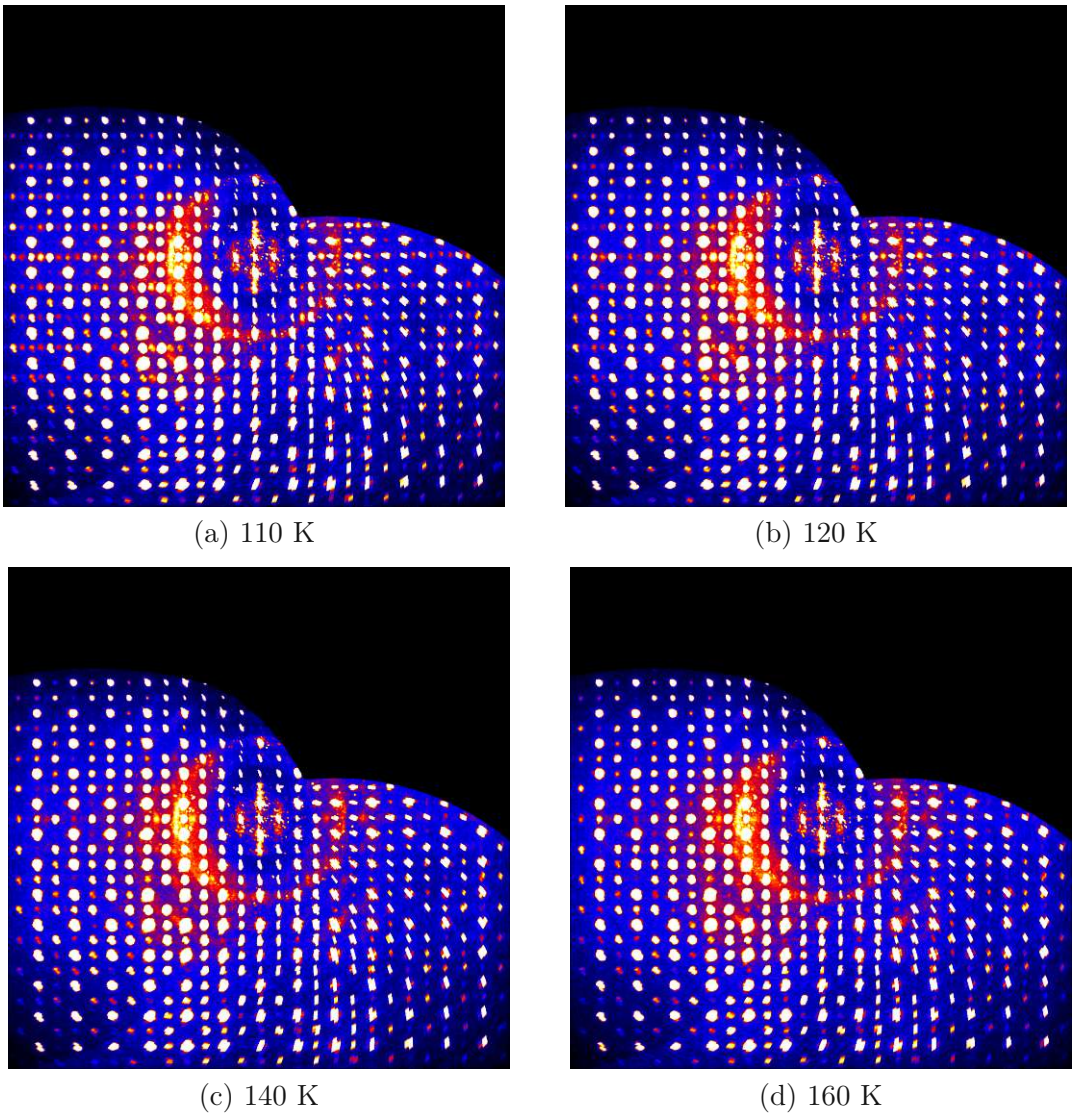

(a) 110 K (b) 120 K

(c) 140 K (d) 160 K

Figure 3.93: $(h0l)^*$ plane of reciprocal space of $[(CH_3)_2NH_2]SbF_6 \cdot H_2O$ reconstructed from CCD data collected at 110, 120, 140 and 160 K.

3.8.4 Monomethylammonium hexafluoroantimonate ($[(CH_3)NH_3]SbF_6$)

$[(CH_3)NH_3]SbF_6$ has a minimum of three polymorphs between 410 and 100 K with transition temperatures at ca. 275 and 385 K. The symmetry relationships are schematised in Figure 3.94. Surprisingly, as in the case of $[(CH_3)_4N]SbF_6$, the symmetry groups of all three phases are not in group/subgroup relations. The reason for this complex symmetry descent is a rearrangement of the existing hydrogen bond network. In the non-ambient XRPD, it appeared as if there were also an additional phase transition at 155 K. However, this phase transition could not yet be clearly proven with the help of single crystal measurements. For this reason, it is not yet certain whether there really is a fourth phase below 155 K.
For single crystal diffraction of the LT phases, the crystals had to be crystallised below the transformation temperature of ca. 0°C. Otherwise, massive twinning occurred during the phase transitions, as was the case for the dimethylammonium analogue. This is due to the transition of the symmetry from $Cmcm$ to $P\bar{1}$. The reduction of the point symmetry from mmm to $\bar{1}$ by an index of 4 suggests the formation of fourfold twins. However, note that the space group symmetries are not in a group/subgroup relation and the metrics of the pseudo-cubic basic structures differ significantly in both cases. Therefore, the crystals fracture on phase transition and could not be simply indexed as fourfold twins. Ultimately, reasonable data quality could only be obtained by growing the single crystals at low temperatures. This is due to the high reduction of point symmetry from $Cmcm$ to $P\bar{1}$.

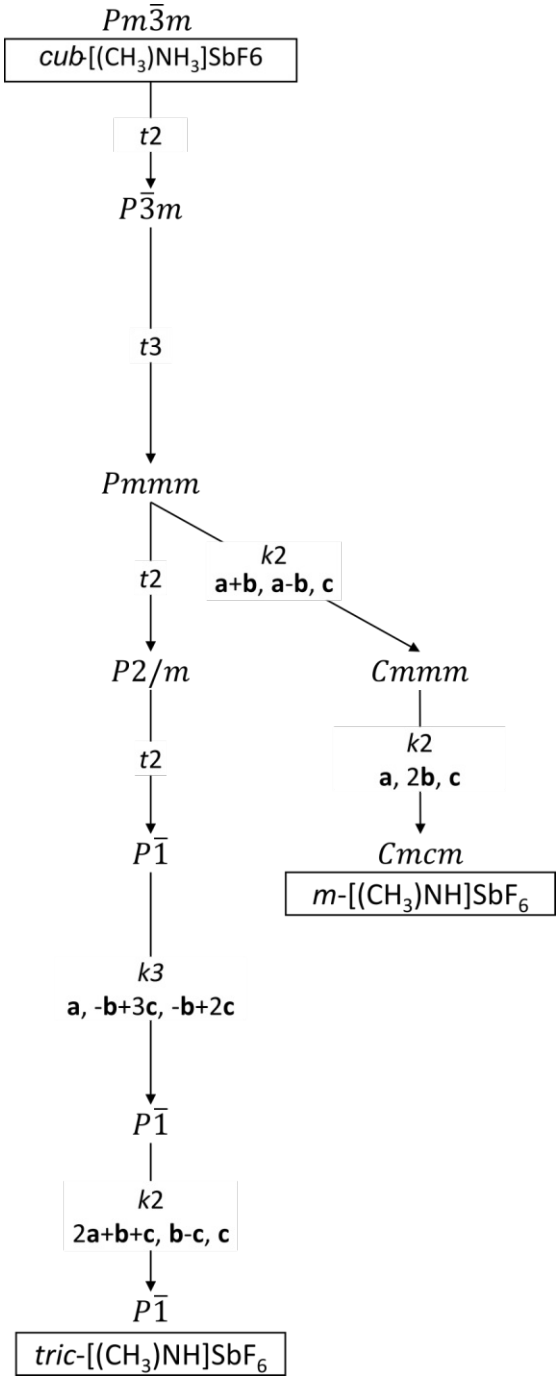

Figure 3.94: Bärnighausen family tree of $[(CH_3)NH_3]SbF_6$.

Single crystal structure analysis o–$[(CH_3)NH_3]SbF_6$ The orthorhombic phase of $[(CH_3)NH_3]SbF_6$ crystallises between 385 and 250 K in the space group $Cmcm$ (No. 63).

Cell (350 K): $a = 7.164(4)$ Å, $b = 8.947(4)$ Å, $c = 11.024(5)$ Å, $V = 706.6(6)$ Å^3, $Z = 4$
In the orthorhombic crystal structure, the $[CH_3{-}NH_3]^+$ cations appear aligned in [010] direction. As indicated by the full point group designation: $C\frac{2}{m}\frac{2}{c}\frac{2_1}{m}$, they are located on a twofold axis. That implies that the H atoms are disordered (Figure 3.95). Along the [100] direction the cations are translation-equivalent, in the [010] direction they are connected via a 2_1 screw axis (Figure 3.97).
As with all fluoroantimonates, the anions are nearly regular octahedra, however here stretched in the [010] direction. The two F atoms most affected in this direction have a Sb1—F1 distance of 1.859(4) Å, compared to Sb1—F2 1.830(3) Å. This distortion is most likely due to the packing of the non-spherical cations, as they also align along the [010] direction.

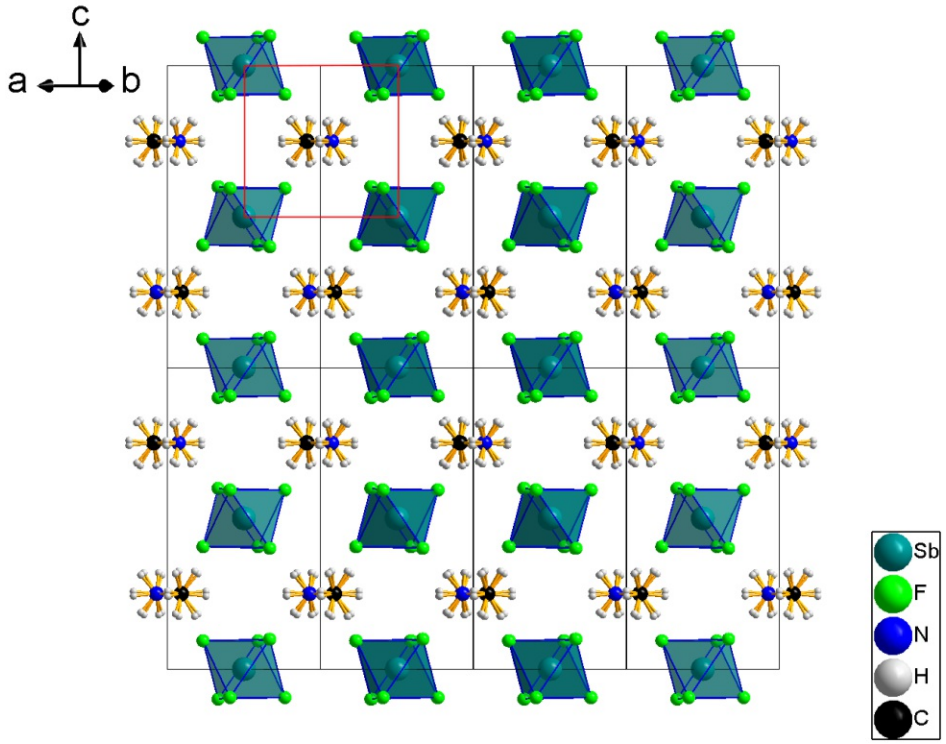

Figure 3.95: Pseudo-cubic distorted crystal structure of $[(CH_3)NH_3]SbF_6$ viewed down [110] with the primitive pseudo-cubic cell highlighted in red.

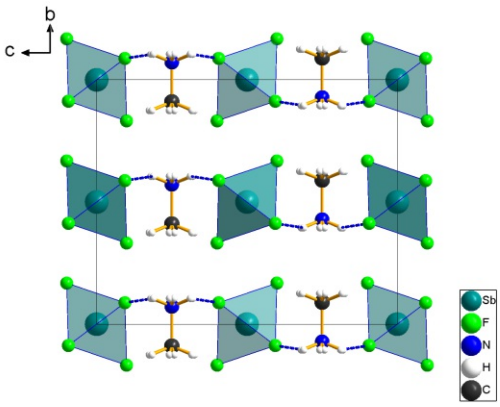

Figure 3.96: Crystal structure of o−$[(CH_3)NH_3]SbF_6$ viewed down [100].

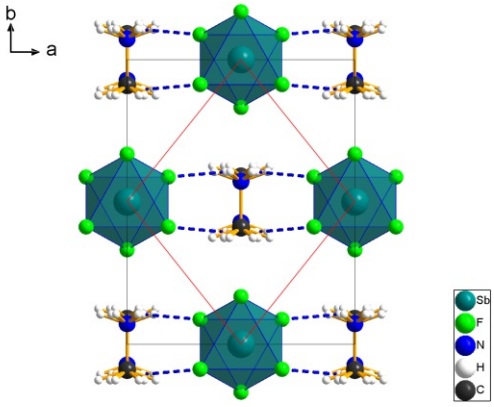

Figure 3.97: Crystal structure of o−$[(CH_3)NH_3]SbF_6$ viewed down [001].

Hydrogen bond network of o-$[(CH_3)NH_3]SbF_6$ o-$[(CH_3)_2NH_2]SbF_6$ forms a two-dimensional hydrogen bond network topology. The hydrogen bond network can be described as sheets in the sheets parallel to (010) planes (Figure 3.96). The $[(CH_3)NH_3]^+$ cation is disordered in a 1:1 manner, with only two of the three N—H acting as donor in each occupation. The resulting voltage graph can be considered as describing a square net (Figure 3.99).

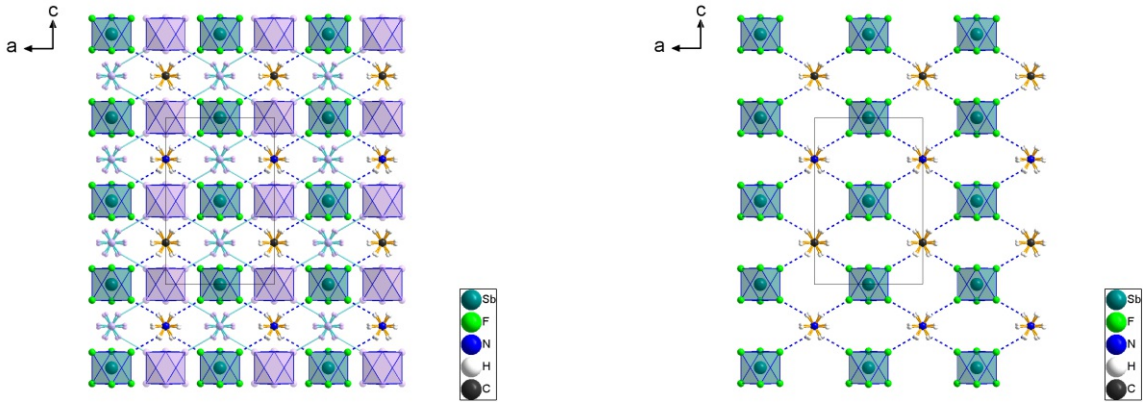

Figure 3.98: hydrogen bond network of o-$[(CH_3)NH_3]SbF_6$ viewed down [010] with second layer (centred at $y = \frac{1}{2}$) with different colors (left) and first layer only (centred at $y = 0$, right.

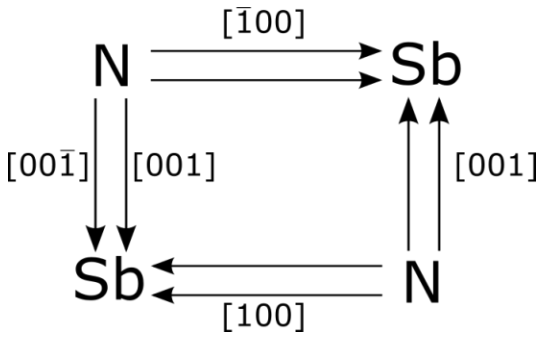

Figure 3.99: Voltage graph of the hydrogen bond network of o-$[(CH_3)NH_3]SbF_6$ of one sheet parallel to (010).

Table 3.34: Atomic parameters of o−$[(CH_3)NH_3]SbF_6$.

Atom	Wyck.	Site	occ.	x/a	y/b	z/c	U_{eq}/U_{iso} (Å^2)
Sb1	4b	$2/m..$	1	1/2	1	1/2	0.04728(17)
F1	8f	$m..$	1	1/2	0.8321(4)	0.5994(4)	0.1168(15)
F2	16h	1	1	0.6799(6)	1.0876(5)	0.5940(3)	0.174(2)
N1	4c	$m2m$	1	1/2	0.5724(7)	3/4	0.0579(15)
HN1	16h	1	0.25	0.43170	0.60550	0.81180	0.0870
HN2	16h	1	0.25	0.45180	0.60550	0.68060	0.0870
HN3	16h	1	0.25	0.61650	0.60550	0.75760	0.0870
C1	4c	$m2m$	1	1/2	0.4101(9)	3/4	0.098(3)
H1	16h	1	0.25	0.57390	0.37440	0.81660	0.1470
H2	16h	1	0.25	0.55180	0.37440	0.67510	0.1470
H3	16h	1	0.25	0.37430	0.37440	0.75830	0.1470

Deviation from the cubic metrics: o-$[(CH_3)NH_3]SbF_6$ shows a significant to the cubic structure with respect to the arrangement and form of the ions. The c axis is the shortest because the plane formed by three F atoms coincides with the long side of the cation (Figure 3.95). Likewise, the influence of the elongated cation results in a strong widening of the γ angle in the cubic metrics (Table 3.35). The matrix transforming the actual cell into the pseudo-cubic basic cell is: $\begin{pmatrix} 1/2 & -1/2 & 0 \\ 1/2 & 1/2 & 0 \\ 0 & 0 & 1/2 \end{pmatrix}$.

Table 3.35: Pseudo-cubic metrics of o−$[(CH_3)NH_3]SbF_6$ after transformation into the pseudo-cubic primitive cell.

Compound pseudo-cubic metrics:	**a** (Å)	**b** (Å)	**c** (Å)	α (°)	β (°)	γ (°)
o-$[(CH_3)NH_3]SbF_6$	5.7309(20)	5.7309(20)	5.5120(25)	90	90	102.6304(405)

Single crystal structure analysis *tric*−**[(CH$_3$)NH$_3$]SbF$_6$** The low-temperature phase of the compound possesses triclinic symmetry with the space group $P\bar{1}$ (No. 2).

Cell (220 K): $a = 11.3103$ Å, $b = 14.6740$ Å, $c = 12.2234$ Å, $\alpha = 74.2349°$, $\beta = 87.4170°$, $\gamma = 91.6732°$, $V = 1948.58$ Å^3, $Z = 4$ When the symmetry decreases as a result of the phase transition, the number of independent ions inside the unit cell is tripled. The $[CH_3{-}NH_3]^+$ cations line up in chains of six, which are then repeated after a small positional modulation (Figure 3.100). In the chains of six ions, the first three and last three possess the same orientation of the $[H_3C{-}NH_3]^+$ cations.

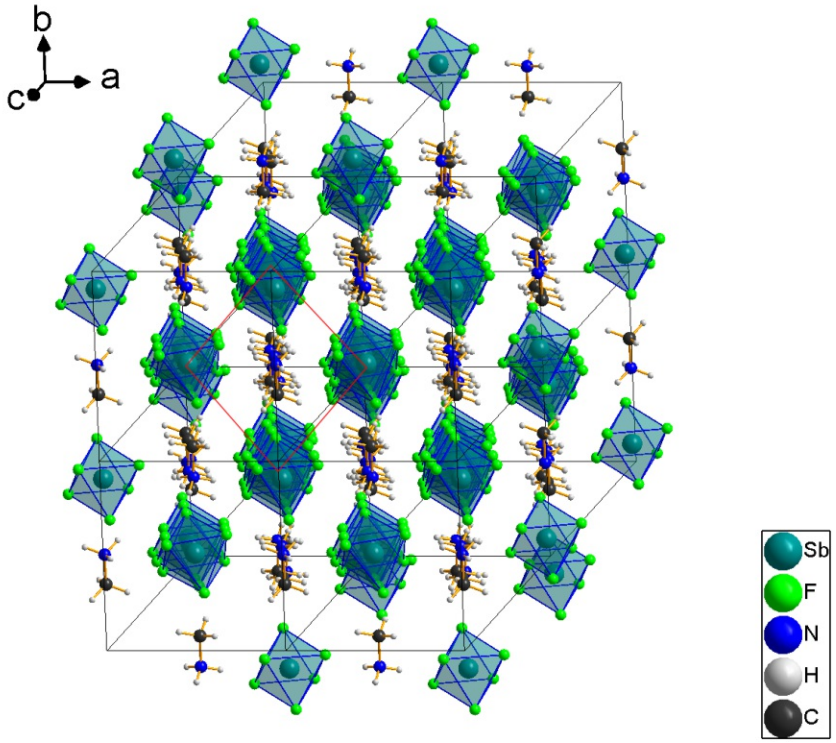

Figure 3.100: Pseudo-cubic distorted crystal structure of *tric*−[(CH$_3$)NH$_3$]SbF$_6$ viewed down [112] with the primitive pseudo-cubic cell highlighted in red.

Hydrogen bond network of *tric*-**[(CH$_3$)NH$_3$]SbF$_6$** After the phase transition, the hydrogen network becomes distinctly more complicated. In the orthorhombic phase, in the disordered state, only two of the three hydrogens on the $[(CH_3)NH_3]^+$ cation were connected to $[SbF_6]^-$ anions. Immediately after a ordering, only two of the hydrogens are involved in hydrogen bonding. Owing to the new connection formed by the third H and the two connections lost due to ordering, a completely unrelated two-dimensional network is formed. The voltage graph is shown in Figure 3.101. The net in this case is neither a Platonic nor an Archimedean net.

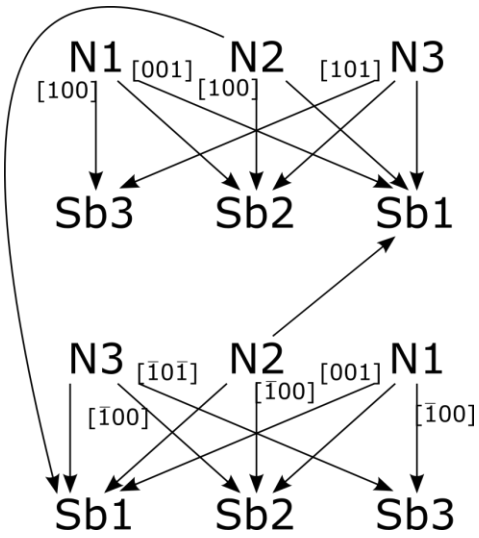

Figure 3.101: Voltage graph of the hydrogen bond network of *tric*-[$(CH_3)NH_3$]SbF_6 of one sheet parallel (010).

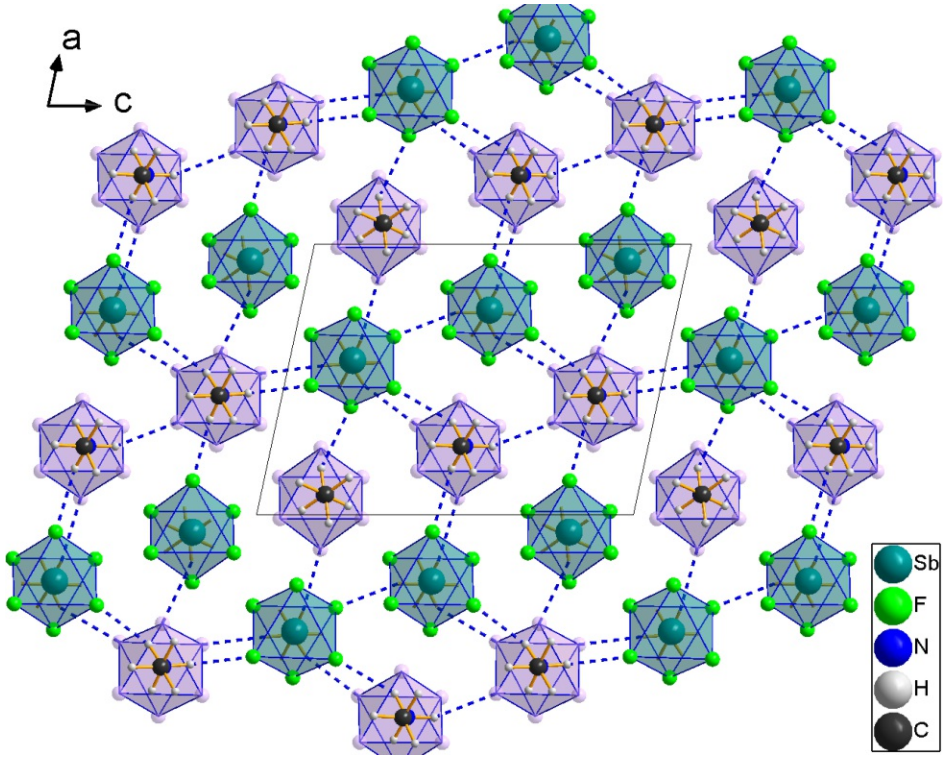

Figure 3.102: Hydrogen bond network of *tric*-[$(CH_3)NH_3$]SbF_6 viewed down [010] with lower part of the layer in different colours.

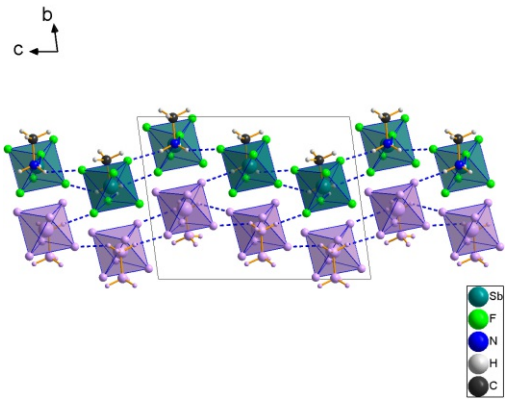

Figure 3.103: Hydrogen bond network of *tric*-$[(CH_3)NH_3]SbF_6$ viewed down [100] with lower part of the layer in different colours.

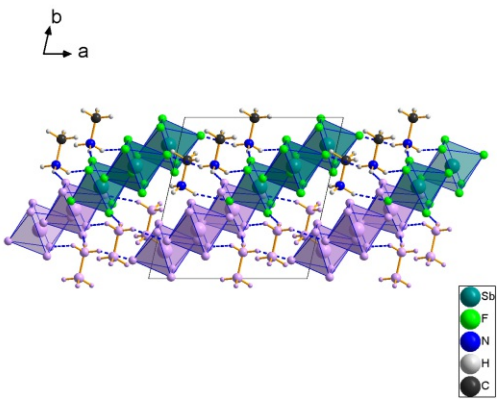

Figure 3.104: Hydrogen bond network of *tric*-$[(CH_3)NH_3]SbF_6$ viewed down [001] with lower part of the layer in different colours.

Table 3.36: Atomic parameters of *tric*–$[(CH_3)NH_3]SbF_6$.

Atom	Wyck.	Site	x/a	y/b	z/c	U_{eq}/U_{iso} (Å^2)
Sb1	2i	1	0.42968(2)	0.43060(2)	-0.16698(2)	0.01891(3)
Sb2	2i	1	0.24394(2)	0.30351(2)	0.49810(2)	0.02056(3)
Sb3	2i	1	0.06287(2)	0.17299(2)	0.16083(2)	0.02139(3)
F1	2i	1	0.59983(13)	0.51857(13)	-0.18836(10)	0.0316(2)
F2	2i	1	0.34192(14)	0.59368(13)	-0.2627(1)	0.0339(3)
F3	2i	1	0.53150(15)	0.32757(13)	-0.29155(10)	0.0365(3)
F4	2i	1	0.25828(13)	0.34674(14)	-0.14626(11)	0.0356(3)
F5	2i	1	0.52233(13)	0.27062(12)	-0.07124(10)	0.0320(2)
F6	2i	1	0.33495(14)	0.53599(14)	-0.04264(10)	0.0334(2)
F7	2i	1	0.24723(13)	0.23970(14)	0.13260(11)	0.0388(3)
F8	2i	1	-0.01335(14)	0.34070(13)	0.06424(10)	0.0376(3)
F9	2i	1	0.13939(17)	0.06294(15)	0.03902(11)	0.0472(3)
F10	2i	1	-0.12606(13)	0.11393(14)	0.18886(12)	0.0432(3)
F11	2i	1	0.13929(16)	0.00917(13)	0.25868(12)	0.0462(3)
F12	2i	1	-0.01389(14)	0.28629(13)	0.2820(1)	0.0357(3)
F13	2i	1	0.42287(13)	0.37890(14)	0.47367(11)	0.0382(3)
F14	2i	1	0.16201(14)	0.46958(13)	0.40288(10)	0.0363(3)
F15	2i	1	0.33242(16)	0.19801(14)	0.37315(11)	0.0418(3)
F16	2i	1	0.06208(14)	0.23303(14)	0.52366(11)	0.0375(3)
F17	2i	1	0.32708(16)	0.13933(14)	0.59300(12)	0.0439(3)
F18	2i	1	0.16067(14)	0.41243(14)	0.62172(10)	0.0360(3)
N1	2i	1	0.55814(17)	0.16369(17)	0.16209(14)	0.0285(3)
H1A	2i	1	0.64630	0.17240	0.17810	0.0430
H1B	2i	1	0.47660	0.20530	0.21310	0.0430
H1C	2i	1	0.55080	0.21010	0.09170	0.0430
N2	2i	1	0.74503(17)	0.29615(16)	0.48674(13)	0.0253(3)
H2A	2i	1	0.74690	0.33790	0.41410	0.0380
H2B	2i	1	0.82850	0.30670	0.50850	0.0380
H2C	2i	1	0.65840	0.34110	0.53190	0.0380
N3	2i	1	-0.07496(16)	0.42401(14)	0.83258(12)	0.0250(3)
H3A	2i	1	-0.03370	0.46490	0.76290	0.0380
H3B	2i	1	-0.01810	0.42750	0.88230	0.0380
H3C	2i	1	-0.17270	0.47480	0.85490	0.0380
C1	2i	1	0.5594(3)	0.0046(2)	0.1677(2)	0.0397(5)
H1D	2i	1	0.46700	-0.00470	0.14650	0.0600
H1E	2i	1	0.56180	-0.04440	0.24460	0.0600
H1F	2i	1	0.65040	-0.04150	0.11560	0.0600
C2	2i	1	0.7470(3)	0.1359(2)	0.4963(2)	0.0394(5)
H2D	2i	1	0.84230	0.08670	0.44990	0.0590
H2E	2i	1	0.65920	0.12440	0.47000	0.0590
H2F	2i	1	0.74090	0.09180	0.57510	0.0590
C3	2i	1	-0.0755(3)	0.2669(2)	0.8289(2)	0.0381(5)
H3D	2i	1	-0.13790	0.26330	0.77610	0.0570
H3E	2i	1	-0.11870	0.22240	0.90420	0.0570
H3F	2i	1	0.02970	0.21250	0.80380	0.0570

Cell (100 K): $a = 9.0717(17)$ Å, $b = 9.3186(17)$ Å, $c = 12.100(2)$ Å, $\alpha = 79.694(3)°$, $\beta = 75.804(3)°$, $\gamma = 75.744(3)°$, $V = 953.43(30)$ Å^3, $Z = 6$

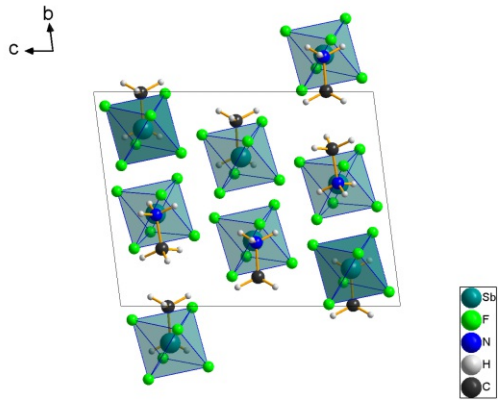

Figure 3.105: Crystal structure of *tric*-$[(CH_3)NH_3]SbF_6$ viewed down [100].

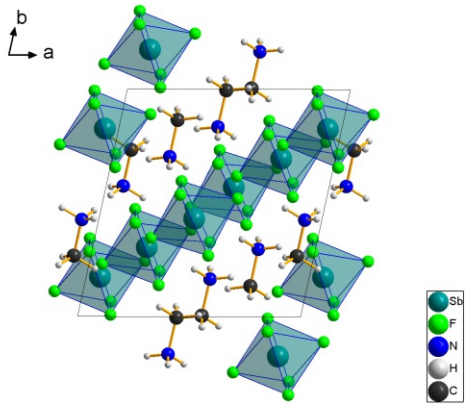

Figure 3.106: Crystal structure of *tric*-$[(CH_3)NH_3]SbF_6$ viewed down [001].

Deviation from the cubic metrics: *tri*−$[(CH_3)NH_3]SbF_6$ shows a large distortion with respect to the cubic structure due to the modulated arrangement of the $[(CH_3)NH_3]^+$ cations. The high positional modulation is especially evident in the pseudo-cubic arrangement, when viewed down [112] (Figure 3.100). This leads to a strong distortion, which is also reflected in the parameters of the pseudo-cubic metrics (Table 3.37). The transformation matrix relating the cells of the cubic and the triclinic structures is $\begin{pmatrix} 1/2 & 1/3 & 1/6 \\ -1/2 & 1/3 & 1/6 \\ 0 & -1/3 & 1/3 \end{pmatrix}$.

Table 3.37: Pseudo-cubic metrics of *tric*−$[(CH_3)NH_3]SbF_6$ after transformation into the pseudo-cubic primitive cell.

Compound	**a**	**b**	**c**	α	β	γ
pseudo-cubic metrics:	**(Å)**	**(Å)**	**(Å)**	**(°)**	**(°)**	**(°)**
tric−**$[(CH_3)NH_3]SbF_6$**	5.4495(5)	5.6551(4)	5.2912(10)	88.785(2)	86.160(1)	86.566(2)

Reciprocal space sections of $[(CH_3)NH_3]SbF_6$ In the reciprocal space sections reconstructed from CCD data, the same effects of disordering $[(CH_3)NH_3]^+$ cations can be observed as three-dimensional diffuse scattering in analogue to the corresponding dimethyl and trimethylammonium salts at high temperatures (Figure 3.107 a).
After ordering at 350 K (Figure 3.107 b), no diffuse scattering is visible any more. From the high temperature to the low temperature, the crystals scatter to larger and larger angles.

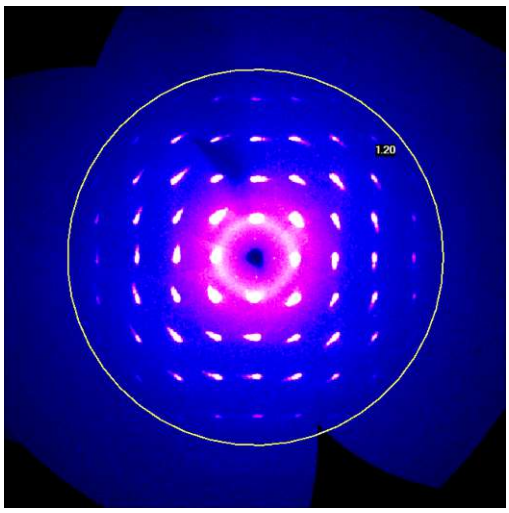

(a) $(0kl)^*$ plane at 410 K

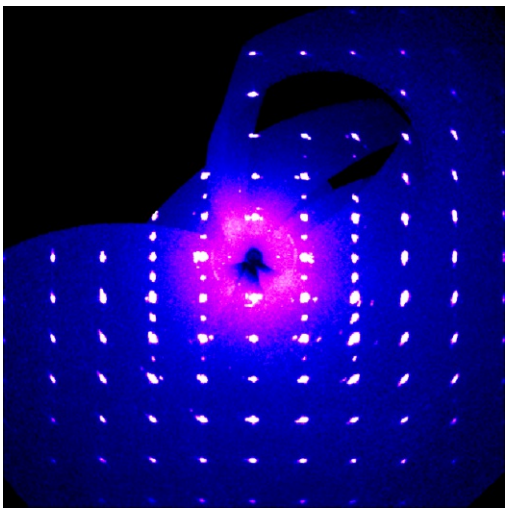

(b) $(0kl)^*$ plane at 350 K

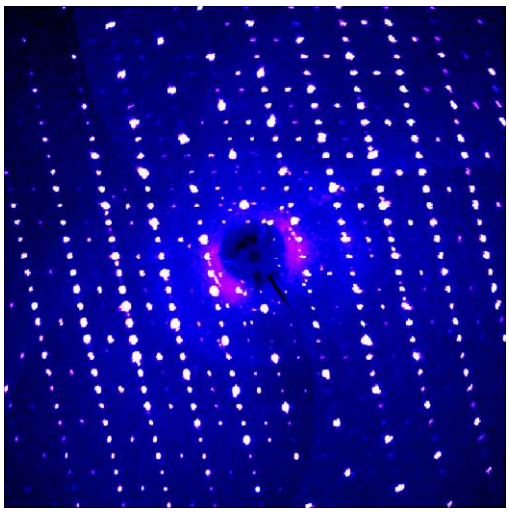

(c) $(h0l)^*$ plane at 220 K

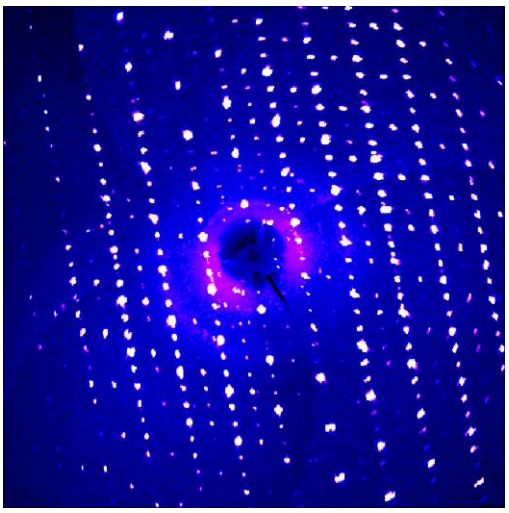

(d) $(h0l)^*$ plane at 100 K

Figure 3.107: Planes of reciprocal space of $[(CH_3)NH_3]SbF_6$ reconstructed from CCD data collected at 410, 350, 220 and 100 K.

3.8.4.1 PXRD analysis $[(CH_3)NH_3]SbF_6$

The non-ambient measurements below room temperature (Figure 3.108) and above room temperature (Figure 3.109) show very clearly the phase transitions at about 385 K. At 155 K the disappearing and appearing of a peak can be observed, which could indicate a phase transition, which was however not evidenced by single-crystal diffraction.

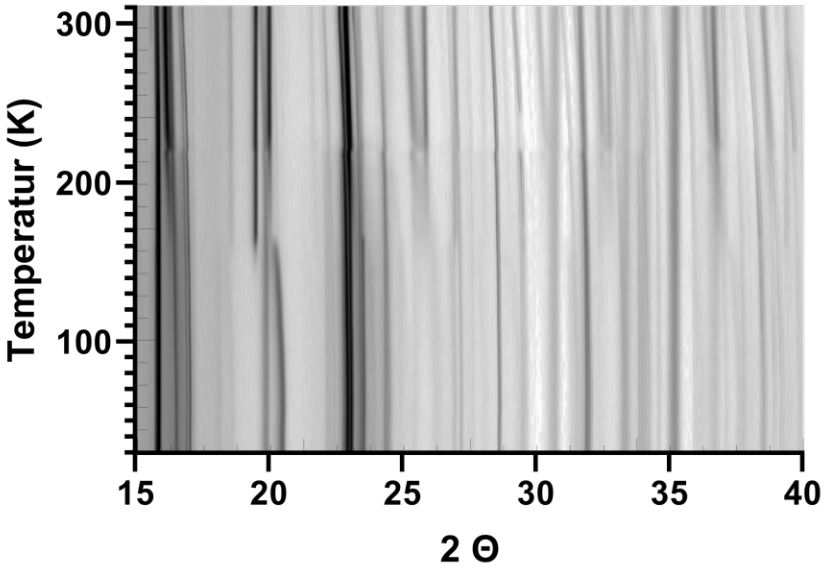

Figure 3.108: Temperature dependent PXRD of $[(CH_3)NH_3]SbF_6$ from 30K to 310K in 10K steps.

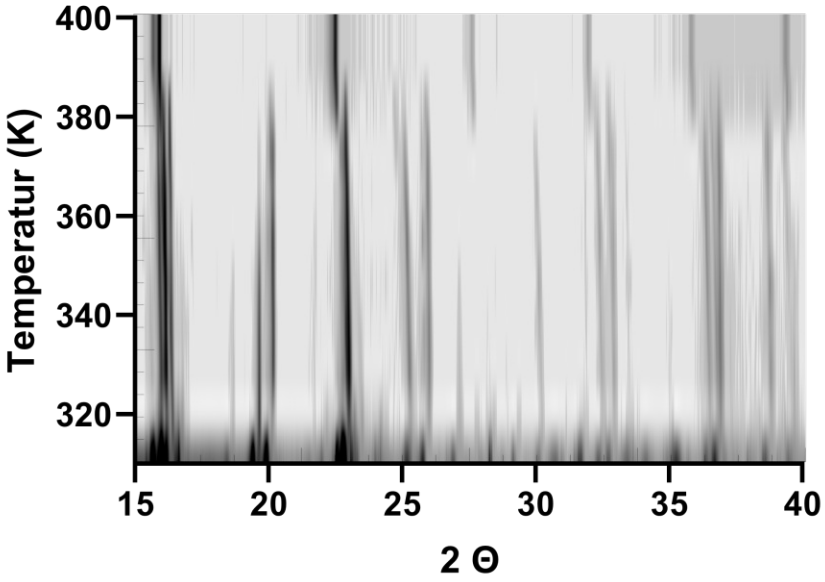

Figure 3.109: Temperature dependent PXRD of $[(CH_3)NH_3]SbF_6$ from 300K to 400K in 10K steps.

3.9 Hypophosphorous acid (H_3PO_2)

H_3PO_2 was originally only required for the synthesis of the salts (see section 3.10). After a literature search, contradictory data concerning the nature of the hydrogen bond were noticed [70], which is why the structure was reexamined more closely again.

Since the H_3PO_2 molecule has only one hydrogen bond donor, the hydrogen bond network is particularly simple. The hydridic H atoms are not able to form hydrogen bonds. When crystallising, H_3PO_2 forms a one-dimensional hydrogen-bonding network, consisting of rods. The HT structure has already been derived using X-ray and neutron diffraction methods [71], but the exact nature of the hydrogen bonds was not fully resolved. There was evidence of asymmetric H-bonds (difference Fourier synthesis), but refinements were only possible with the hydrogen located on the twofold axis. This would correspond to a symmetric hydrogen bond. In this work, all H-bonds were determined as being asymmetric, according to difference Fourier syntheses. Refinements were also possible using asymmetric hydrogen bonds with half-occupancy. Part of this discussion has already been published [72].
Above the phase transition temperature range (225–200 K), the hydrogen bonds become disordered as shown in Figure 3.110. After cooling, these hydrogens are ordered. Note, that in Figure 3.111 the H-bonds look disordered due to the superimposition of two opposite orientated rods.

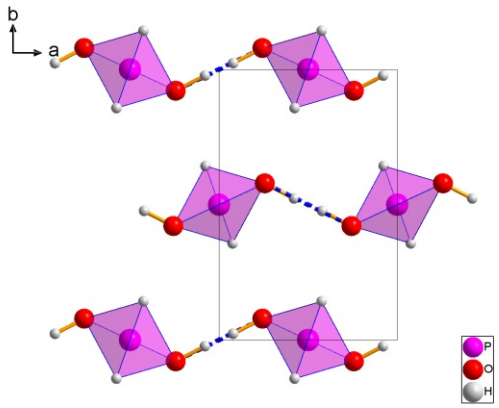

Crystal structure of H_3PO_2 at 290 K viewed down [001]

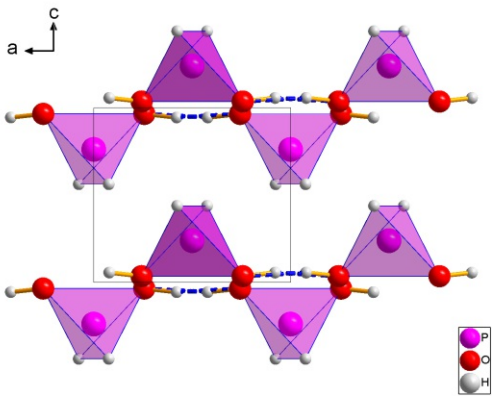

Crystal structure of H_3PO_2 at 290 K viewed down [010]

Figure 3.110: Rods of hydrogen-bonded H_3PO_2 molecules (above the phase transition temperature).

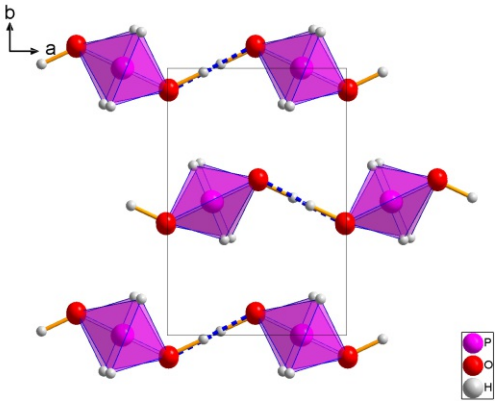

Crystal structure of H_3PO_2 viewed down [001]

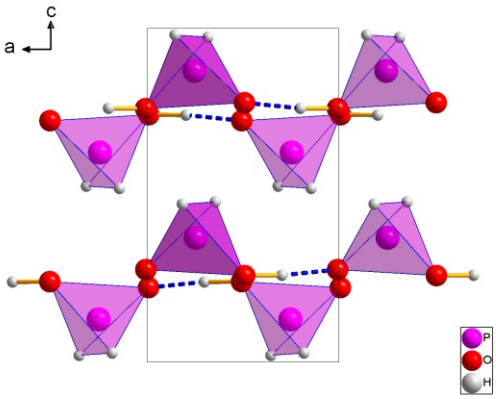

Crystal structure of H_3PO_2 viewed down [010]

Figure 3.111: Rods of hydrogen-bonded H_3PO_2 molecules at 100 K (below the phase transition temperature).

Single crystal structure analysis HT−H_3PO_2 The high-temperature phase of the compound crystallises with orthorhombic symmetry in the space group $P2_12_12$ (No. 18).

Cell (290 K): 4.5133(8) Å, 6.8475(11) Å, 4.0008(7) Å, 123.64(4) Å^3, $Z = 2$

In the HT phase, the hydrogen bond is located on a twofold axis. In such a case, the hydrogen bond might either be symmetric with the H atom located on the rotation axis or asymmetric, but with the H atom being disordered in a 1:1 manner. While previous investigations of the nature of the hydrogen bond only indicated a splitting of the hydrogen position [71], in our case, refinements with a disorder model (H-occupation of 0.5 on each of the two possible positions) converged satisfactorily with and without distance constraints identifying the hydrogen position as split and disordered.

Single crystal structure analysis LT−H_3PO_2 The low-temperature phase of the compound crystallises with orthorhombic symmetry in the space group $P2_12_12_1$ (No. 19).

Cell (100 K): 4.5149(7) Å, 6.7238(10) Å, 7.8515(12) Å, 238.35(6) Å^3, $Z = 4$
On cooling, the hydrogen atoms become ordered. This transition leads to an increase in the size of the unit cell, while other symmetry features of the crystal structure remain unchanged. This transition is a particularly simple example of an order-disorder phase transition. The symmetry relation of the infinite chains in the HT and LT phases is of the *translationengleiche* type (in contrast to the structure). The translation symmetry remains, whereas the point groups of the rods are in a group/subgroup relationship of index 2.

Reciprocal space sections of H_3PO_2 This simple transition can be observed in the diffraction pattern. On cooling between 225 and 200 K, additional superstructure reflections appear at half-integer values in the $\mathbf{c}^*$-direction, which corresponds to a loss of translation symmetry and to a doubling of the length of the c axis (Figure 3.112).

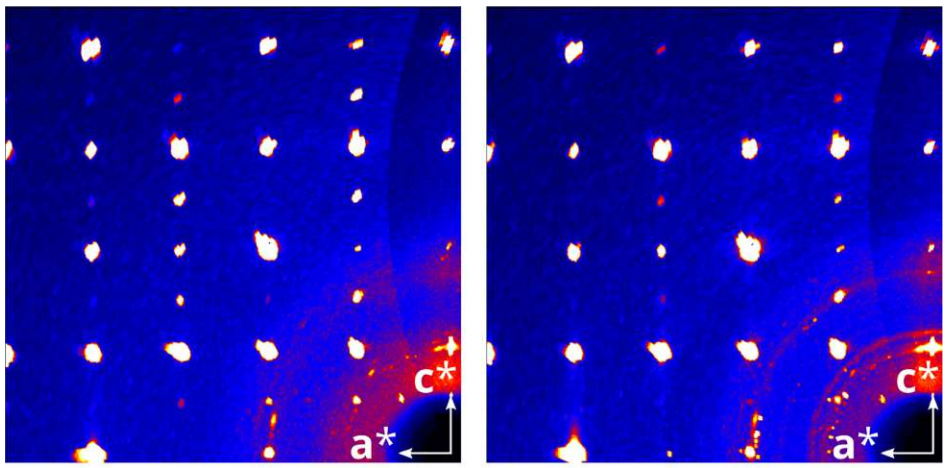

(a) 100 K (b) 200 K

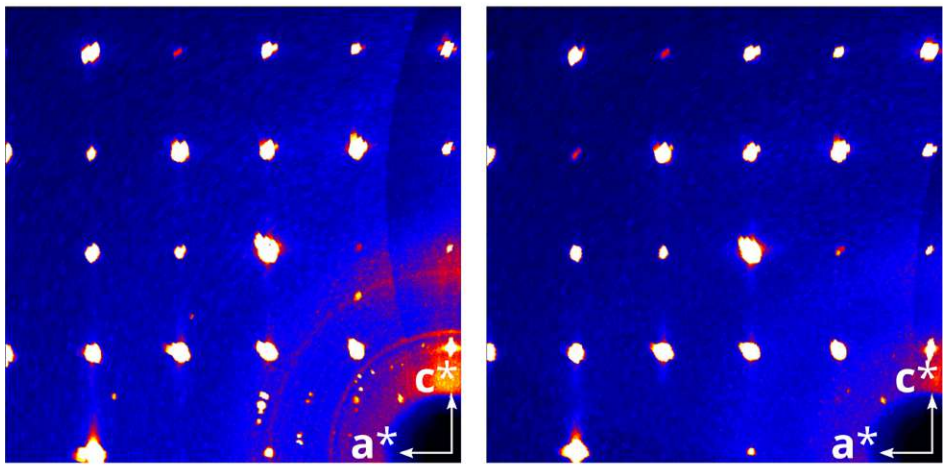

(c) 225 K (d) 290 K

Figure 3.112: $(h0l)^*$ plane of reciprocal space of H_3PO_2 reconstructed from CCD data collected at 100, 200, 225 and 290 K.

Hydrogen bond topology: The hydrogen-bonding topology of the phases of H_3PO_2 can be represented by the infinite graphs. The high-temperature phase is represented in Equation 3.11 and for the LT phase in Equation 3.12, where P stands for a H_3PO_2 molecule:

$$\cdots\cdots \text{P} \longleftrightarrow \text{P} \cdots\cdots \tag{3.11}$$

$$\cdots\cdots \text{P} \longrightarrow \text{P} \cdots\cdots \tag{3.12}$$

The particular graph above is the double-infinite linear graph. Thus, from a topological point of view, the symmetry increase of the phase transition corresponds to the mapping of a directed graph onto the corresponding undirected graph. Note that the mapping is surjective (onto), but not injective (one-to-one), because each edge in the undirected graph may possess one of two orientations in the directed graph. When the connectivity graphs are reduced to voltage graphs, single-node graphs are obtained (Figure 3.113), since all molecules in the chains are translationally equivalent.

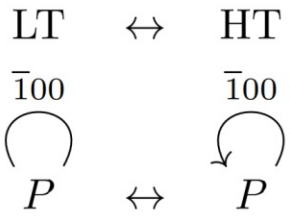

Figure 3.113: Voltage graphs of HT and LT H_3PO_2.

3.10 Phosphinates

All methyl-substituted ammonium phosphinates form H-bond networks. The $[H_2PO_2]^-$ anion can only act as a hydrogen-bond acceptor, as hydridic H cannot form H-bonds. The methyl-substituted ammonium cations act as a hydrogen bond donors. With each additional methyl group less hydrogen bonds can form. This means that $[(CH_3)NH_3]^+$, for example, can act as a triple hydrogen bond donor while $[(CH_3)_4N]^+$ does not participate in the hydrogen bonding network at all.

3.10.1 Methylammonium phosphinate ($[(CH_3)NH_3]H_2PO_2$)

Single crystal structure analysis $[(CH_3)NH_3]H_2PO_2$ The compound crystallises with monoclinic symmetry in the space group $C2/c$ (No. 15).

Cell (100 K): $a = 8.8481(10)$ Å, $b = 10.0438(11)$ Å, $c = 10.6507(12)$ Å, $\beta = 90.771(2)°$, $V = 946.43(18)$ Å^3, $Z = 8$

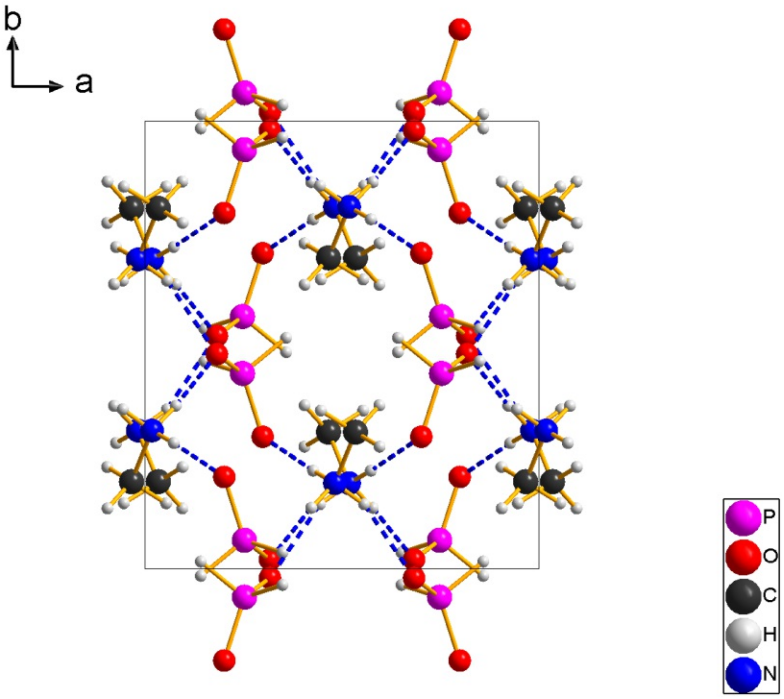

Figure 3.114: Crystal structure of $[(CH_3)NH_3]H_2PO_2$ viewed down [001].

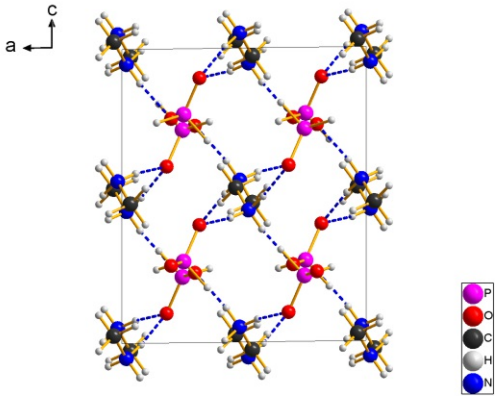

Figure 3.115: Crystal structure of $[(CH_3)NH_3]H_2PO_2$ viewed down [010].

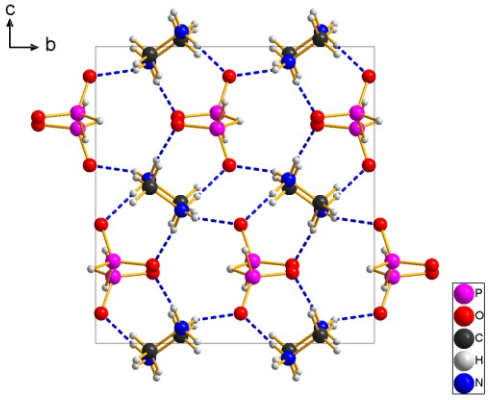

Figure 3.116: Crystal structure of $[(CH_3)NH_3]H_2PO_2$ viewed down [100].

Hydrogen bond topology: Of the methyl-substituted ammonium phosphinates, the methylammonium cation has the highest number of H atoms that can act as a H-bond donor. Nevertheless, $[(CH_3)NH_3]H_2PO_2$ forms a relatively simple hydrogen bond network of infinite chains. This is due to the fact that tetramers are formed from two cations and two anions. They are then connected by two hydrogen bonds to the next one. These chains run in parallel layers

stacked along [001], alternating in the [110] (Figure 3.117) and [$\bar{1}$10] directions (Figure 3.118) respectively. One chain along [110] (centred at $z = \frac{1}{2}$) is highlighted yellow and a chain parallel [$\bar{1}$10] (centred at $z = 1$) is highlighted green.

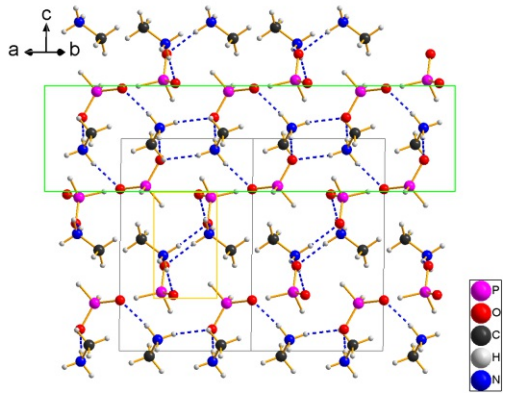

Figure 3.117: Crystal structure of $[(CH_3)NH_3]H_2PO_2$ viewed down [110].

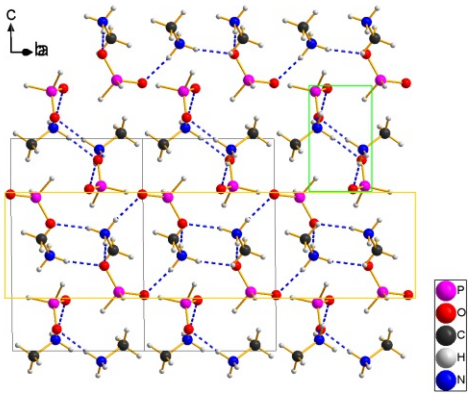

Figure 3.118: Crystal structure of $[(CH_3)NH_3]H_2PO_2$ viewed down [1$\bar{1}$0].

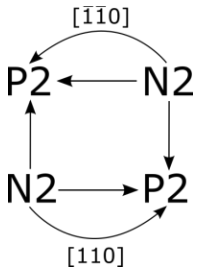

Figure 3.119: Voltage graph of $[(CH_3)NH_3]H_2PO_2$ of chains parallel to [110].

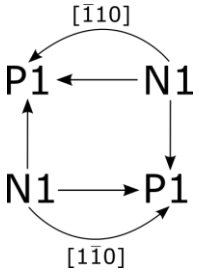

Figure 3.120: Voltage graph of $[(CH_3)NH_3]H_2PO_2$ of chains parallel to [1$\bar{1}$0].

Table 3.38: Atomic parameters of $[(CH_3)NH_3]H_2PO_2$.

Atom	Wyck.	Site	x/a	y/b	z/c	U_{eq}/U_{iso} (Å^2)
P1	8f	1	0.75249(2)	0.43641(2)	0.72367(2)	0.01417(6)
O1	8f	1	0.81726(6)	0.47957(5)	0.60015(5)	0.01741(10)
O2	8f	1	0.70131(7)	0.29494(6)	0.73760(5)	0.02067(11)
C1	8f	1	0.46592(9)	0.30537(7)	0.47386(6)	0.01839(12)
H1A	8f	1	0.40450	0.27268	0.40308	0.0280
H1B	8f	1	0.55371	0.35362	0.44201	0.0280
H1C	8f	1	0.40513	0.36533	0.52533	0.0280
N1	8f	1	0.51797(7)	0.19117(6)	0.55123(5)	0.01358(10)
HP1	8f	1	0.6417(14)	0.5160(14)	0.7509(13)	0.036(3)
HP2	8f	1	0.8490(14)	0.4638(12)	0.8132(12)	0.028(3)
HN1	8f	1	0.5731(13)	0.2190(12)	0.6168(11)	0.025(3)
HN2	8f	1	0.4439(13)	0.1439(11)	0.5776(11)	0.021(3)
HN3	8f	1	0.5781(13)	0.1360(11)	0.5052(11)	0.020(3)

3.10.2 Dimethylammonium phosphinate ($[(CH_3)_2NH_2]H_2PO_2$)

Single crystal structure analysis $[(CH_3)_2NH_2]H_2PO_2$ The compound crystallises with monoclinic symmetry in the space group $Pca2_1$ (No. 29).

Cell (100 K): $a = 11.6518(9)$ Å, $b = 5.4894(4)$ Å, $c = 9.2090(8)$ Å, $V = 589.02(8)$ Å^3, $Z = 4$

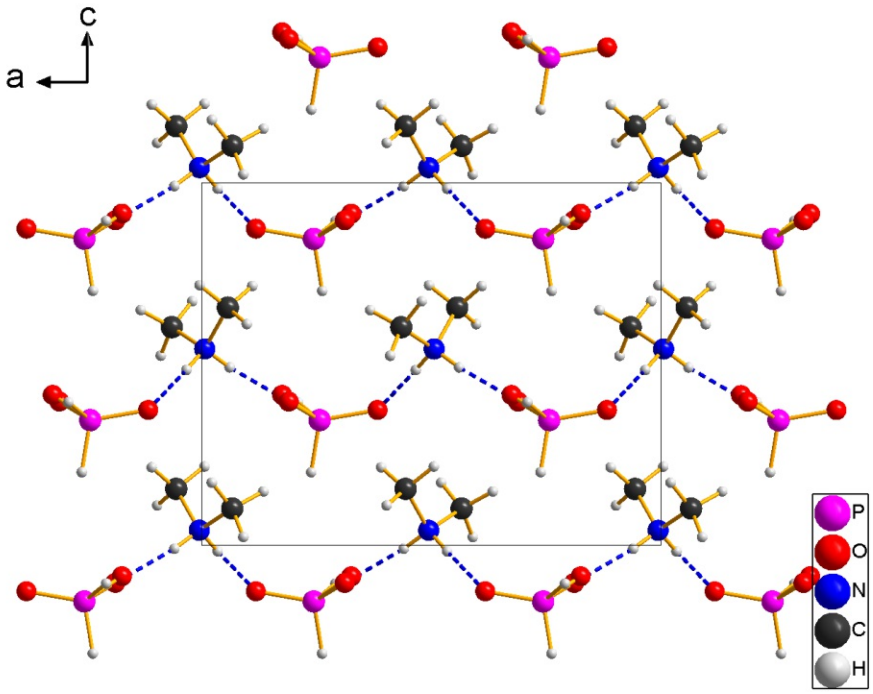

Figure 3.121: Crystal structure of $[(CH_3)_2NH_2]H_2PO_2$ viewed down [010].

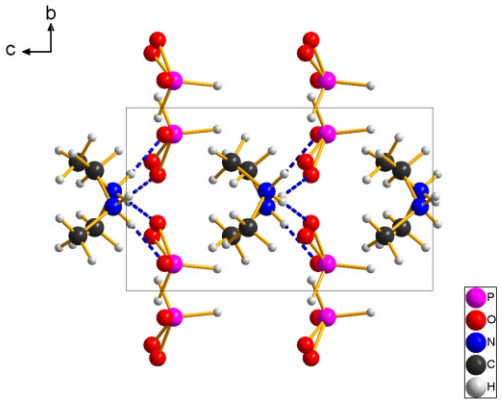

Figure 3.122: Crystal structure of $[(CH_3)_2NH_2]H_2PO_2$ viewed down [100].

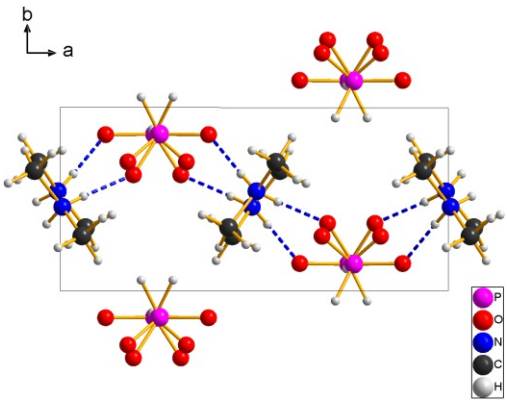

Figure 3.123: Crystal structure of $[(CH_3)_2NH_2]H_2PO_2$ viewed down [001].

Hydrogen bond topology: Each $[(CH_3)_2NH_2]^+$ cation has two hydrogens that can connect to two different $[H_2PO_2]^-$ anions. $[(CH_3)_2NH_2]H_2PO_2$ forms a simple one-dimensional hydrogen network in the form of infinite rods. Each rod extends parallel to the [100] direction (Figure 3.121) resulting in the simple voltage graph depicted in Figure 3.124.

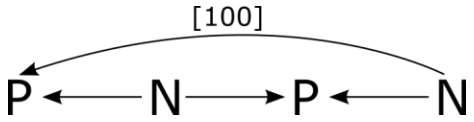

Figure 3.124: Voltage graph of $[(CH_3)_2NH_2]H_2PO_2$ of one chain parallel in [100].

Table 3.39: Atomic parameters of $[(CH_3)_2NH_2]H_2PO_2$.

Atom	**Wyck.**	**Site**	**occ.**	x/a	y/b	z/c	U_{eq}/U_{iso} (Å^2)
P1	4a	1	1	0.24359(3)	0.85455(7)	0.34561(8)	0.01895(11)
O1	4a	1	0.74(2)	0.3110(4)	0.6325(16)	0.3968(6)	0.0315(11)
O1'	4a	1	0.26(2)	0.3253(12)	0.703(3)	0.4151(16)	0.0315(11)
O2	4a	1	1	0.11739(10)	0.8519(2)	0.37363(14)	0.0215(3)
N1	4a	1	1	0.49410(13)	0.4574(3)	0.54193(18)	0.0187(3)
C1	4a	1	1	0.44377(17)	0.2991(4)	0.6561(2)	0.0219(3)
H1B	4a	1	1	0.39047	0.39452	0.71560	0.0330
H1C	4a	1	1	0.50522	0.23434	0.71767	0.0330
H1D	4a	1	1	0.40240	0.16387	0.61039	0.0330
C2	4a	1	1	0.56583(18)	0.6557(3)	0.6020(3)	0.0256(4)
H2A	4a	1	1	0.63371	0.58591	0.64907	0.0380
H2B	4a	1	1	0.52128	0.74828	0.67347	0.0380
H2C	4a	1	1	0.58999	0.76438	0.52329	0.0380
HN1	4a	1	1	0.534(2)	0.363(4)	0.484(3)	0.028(7)
HN2	4a	1	1	0.4397(18)	0.515(4)	0.491(3)	0.027(6)
HP1	4a	1	1	0.262(3)	0.881(6)	0.202(2)	0.049(10)
HP2	4a	1	1	0.291(2)	1.057(5)	0.395(3)	0.051(8)

3.10.3 Tetramethylammonium phosphinate dihydrate ($[(CH_3)_4N]H_2PO_2 \cdot 2\,H_2O$)

Single crystal structure analysis $[(CH_3)_4N]H_2PO_2 \cdot 2\,H_2O$ The compound crystallises with monoclinic symmetry in the space group $C2/c$ (No. 15).

Cell (100 K): $a = 6.7780(2)$ Å, $b = 15.1614(4)$ Å, $c = 8.9582(3)$ Å, $\beta = 92.676(1)°$, $V = 919.58(5)$ Å^3, $Z = 4$
As expected, the $[(CH_3)_4N]^+$ cation does not participate in any hydrogen networks. Instead, two water molecules per ion pair are incorporated, forming a two-dimensional hydrogen bonding network. Drying at 10^{-4} mbar for one day could not remove the water of crystallisation.

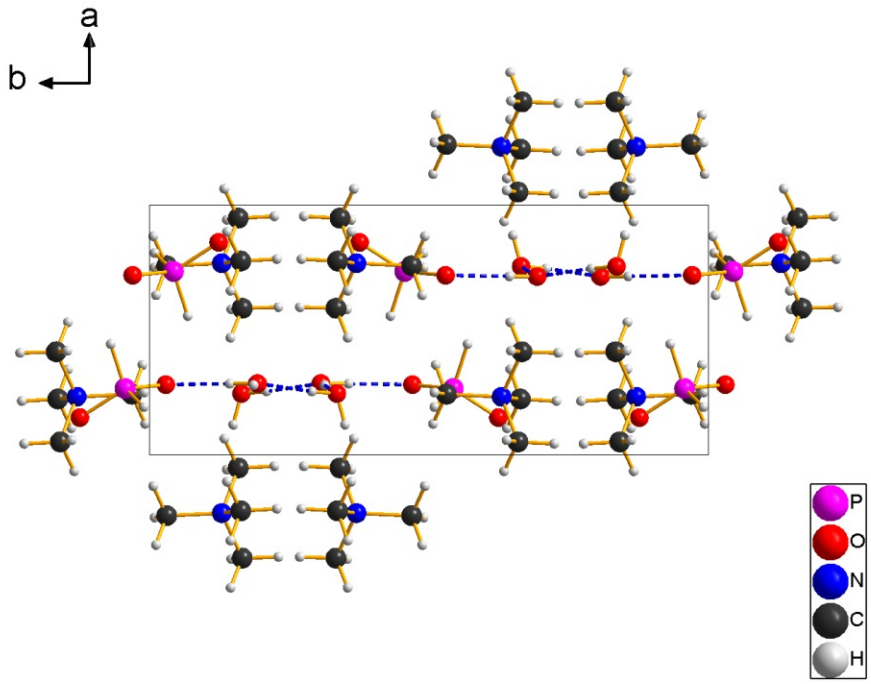

Figure 3.125: Crystal structure of $[(CH_3)_4N]H_2PO_2 \cdot 2\,H_2O$ viewed down [001].

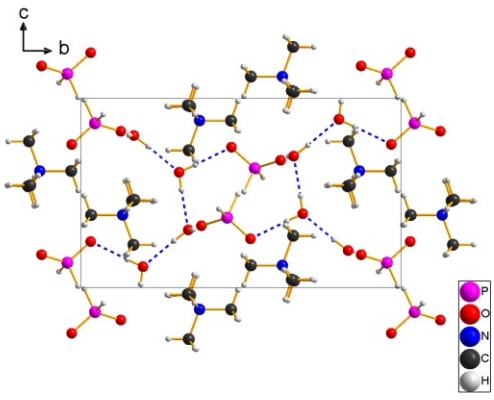

Figure 3.126: Crystal structure of $[(CH_3)_4N]H_2PO_2 \cdot 2\,H_2O$ viewed down [100].

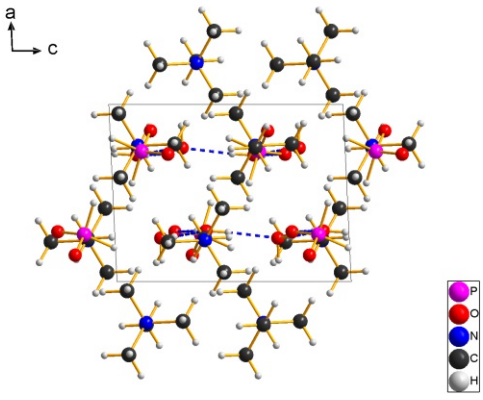

Figure 3.127: Crystal structure of $[(CH_3)_4N]H_2PO_2 \cdot 2\,H_2O$ viewed down [010].

Hydrogen bond topology: $[(CH_3)_4N]H_2PO_2 \cdot 2\,H_2O$ forms a complex two-dimensional hydrogen bond network, owing to the water of crystallisation. The hydrogen bonding network consists of sheets in the [011] plane (Figure 3.128). Each water molecule (short "W") is connected to three molecules: one $[H_2PO_2]^-$ anion and two different water molecules, with one as H-bond acceptor and one as donor. Therefore, each $[H_2PO_2]^-$ anion is connected to two water molecules. The voltage graph is shown in Figure 3.129. The net in this case is neither a Platonic nor an Archimedean net.

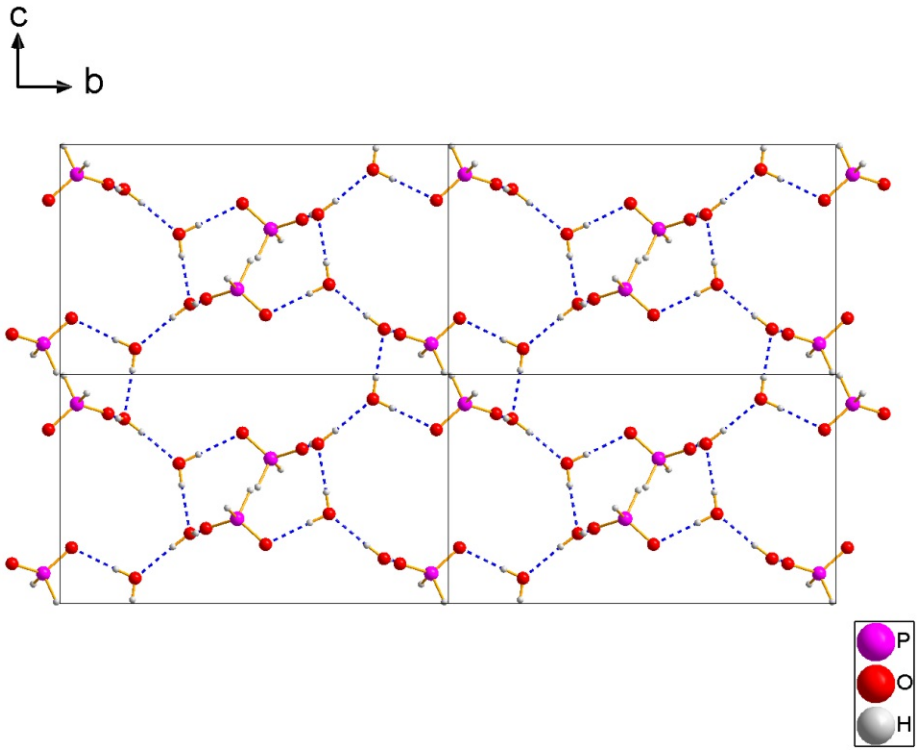

Figure 3.128: Crystal structure of $[(CH_3)_4N]H_2PO_2 \cdot 2\,H_2O$ (without cations) viewed down [100] showing one layer of the hydrogen bond network.

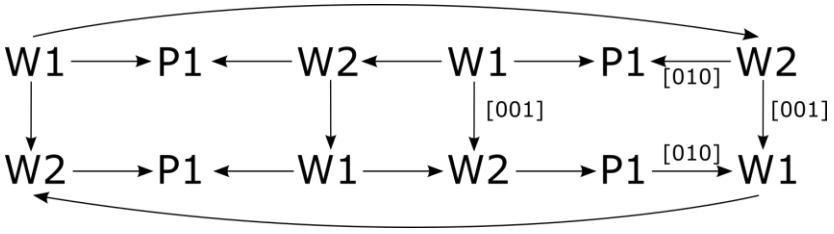

Figure 3.129: Voltage graph of the hydrogen bond network of $[(CH_3)_4N]H_2PO_2 \cdot 2\,H_2O$ of one sheet parallel (100).

Table 3.40: Atomic parameters of $[(CH_3)_3NH]H_2PO_2 \cdot 2\,H_2O$.

Atom	**Wyck.**	**Site**	x/a	y/b	z/c	U_{eq}/U_{iso} (Å^2)
P1	4e	1	0.73431(4)	0.54330(2)	0.63070(3)	0.01377(9)
OW2	4e	1	1.24549(15)	0.66474(6)	0.69541(10)	0.0215(2)
OW1	4e	1	0.71381(15)	0.30658(6)	0.60982(10)	0.0219(2)
O1	4e	1	0.71878(15)	0.47030(6)	0.74279(9)	0.0219(2)
O2	4e	1	0.85071(14)	0.62390(6)	0.67315(10)	0.0240(2)
N1	4e	1	0.23296(14)	0.12959(6)	0.38338(9)	0.01163(19)
C1	4e	1	0.41288(18)	0.16624(8)	0.46409(13)	0.0194(3)
H1A	4e	1	0.53119	0.14536	0.41608	0.0290
H1B	4e	1	0.41687	0.14655	0.56838	0.0290
H1C	4e	1	0.40850	0.23082	0.46069	0.0290
C2	4e	1	0.22384(19)	0.16342(8)	0.22610(12)	0.0178(2)
H2A	4e	1	0.34295	0.14525	0.17628	0.0270
H2B	4e	1	0.21557	0.22795	0.22706	0.0270
H2C	4e	1	0.10704	0.13919	0.17204	0.0270
C3	4e	1	0.05220(17)	0.15911(8)	0.45902(12)	0.0166(2)
H3A	4e	1	0.04464	0.22365	0.45695	0.0250
H3B	4e	1	0.05886	0.13870	0.56293	0.0250
H3C	4e	1	-0.06532	0.13432	0.40672	0.0250
C4	4e	1	0.24298(19)	0.03114(7)	0.38314(13)	0.0183(2)
H4A	4e	1	0.12462	0.00727	0.33066	0.0280
H4B	4e	1	0.25034	0.00950	0.48634	0.0280
H4C	4e	1	0.36057	0.01207	0.33226	0.0280
HP1	4e	1	0.808(2)	0.5097(9)	0.5070(13)	0.018(4)
HP2	4e	1	0.5563(18)	0.5689(9)	0.5841(16)	0.022(4)
HW1A	4e	1	0.715(3)	0.3563(9)	0.6488(18)	0.035(5)
HW1B	4e	1	0.721(3)	0.3137(12)	0.5162(16)	0.045(5)
HW2A	4e	1	1.121(2)	0.6501(12)	0.694(2)	0.057(6)
HW2B	4e	1	1.254(3)	0.7095(11)	0.753(2)	0.052(6)

3.11 *trans* - Dihydridotetrafluorophosphate ($[H_2PF_4]^-$)

As described above, only $[(CH_3)_3NH]H_2PO_2$ yielded a crystalline product after fluorination. Depending on ratio of cocrystallised of $[H_2PO_2]^-$ with respect to $[H_2PF_4]^-$, different crystal structures are obtained. So far, two crystal structures of incompletely fluorinated products could be identified. The crystal structure with a higher proportion of the unfluorinated phosphinate crystallises in an orthorhombic crystal structure (Figure 3.130) and the more fluorinated product yielded a monoclinic crystal structure (Figure 3.131). Both crystal structures have two crystallographically independent anion positions. In each case, only one of the positions is occupied partly by the $[H_2PF_4]^-$ and partly by the $[H_2PO_2]^-$ anion, whereas the other is fully occupied by $[H_2PF_4]^-$.

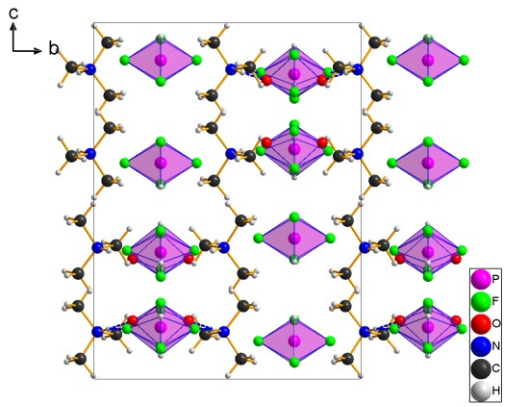

Figure 3.130: Crystal structure of $o-[(CH_3)_3NH][H_2PF_4]_{0.58} \cdot [H_2PO_2]_{0.42}$ viewed down [100].

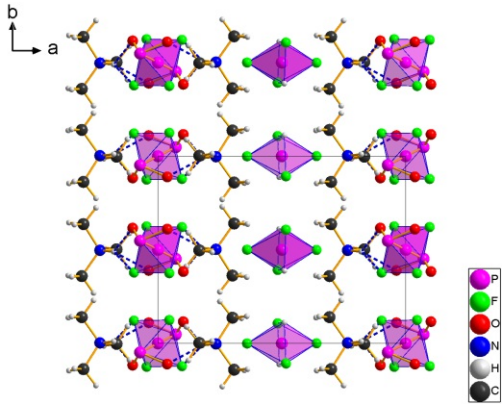

Figure 3.131: Crystal structure of $m-[(CH_3)_3NH][H_2PF_4]_{0.9} \cdot [H_2PO_2]_{0.1}$ viewed down [001].

3.11.1 Single crystal structure analysis of $o-[(CH_3)_3NH][H_2PF_4]_{0.58}\cdot[H_2PO_2]_{0.42}$

The compound crystallises with orthorhombic symmetry in the space group *Pnma* (No. 62).

Cell (100 K): $a = 7.1974(7)$ Å, $b = 12.2773(11)$ Å, $c = 16.3462(15)$ Å, $V = 1444.43(23)$ Å^3, $Z = 8$

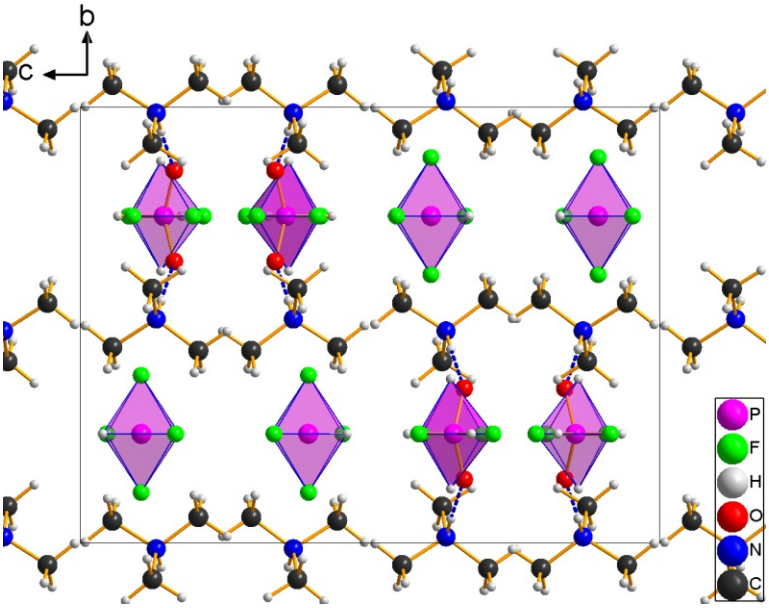

Figure 3.132: Crystal structure of $o-[(CH_3)_3NH][H_2PF_4]_{0.58}\cdot[H_2PO_2]_{0.42}$ viewed down [100].

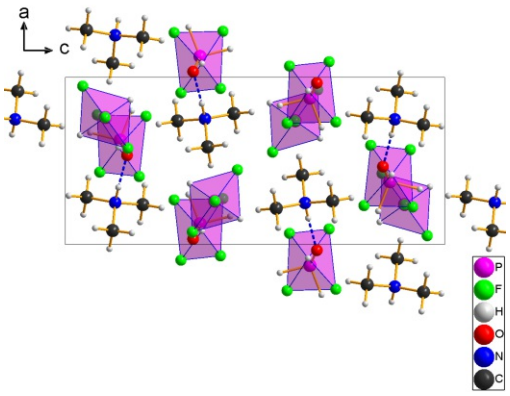

Figure 3.133: Crystal structure of $o-[(CH_3)_3NH][H_2PF_4]_{0.58}\cdot[H_2PO_2]_{0.42}$ viewed down [010].

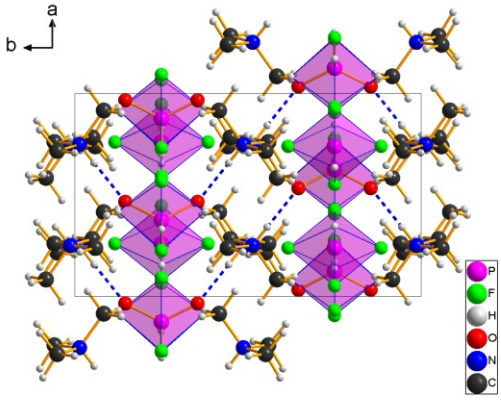

Figure 3.134: Crystal structure of $o-[(CH_3)_3NH][H_2PF_4]_{0.58}\cdot[H_2PO_2]_{0.42}$ viewed down [001].

The crystal structure of $o-[(CH_3)_3NH][H_2PF_4]_{0.58}\cdot[H_2PO_2]_{0.42}$ posses two independent $[H_2PF_4]^-$ anions. *P*1 and *P*2 are located on a reflection plane parallel to (101). The *P*1 position is fully occupied by $[H_2PF_4]^-$, whereas the *P*2 position is occupied by about 26 % $[H_2PF_4]^-$ and about 84 % $[H_2PO_2]^-$.
The $[(CH_3)_3NH]^+$ cations are located between the anions in such a way that the fully occupied $[H_2PF_4]^-$ anion positions are shielded by the methyl groups. The $[(CH_3)_3NH]^+$ cations only form H-bonds with the $[H_2PO_2]^-$ anions. The N-H-bonds are directed towards the $[H_2PO_2]^-$ anions and thereby form hydrogen bonds to the O. Two $[(CH_3)_3NH]^+$ cations and one $[H_2PO_2]^-$ anion form trimers, which are oriented in the [110] direction.

Table 3.41: Atomic parameters of $o-[(CH_3)_3NH][H_2PF_4]_{0.58} \cdot [H_2PO_2]_{0.42}$.

Atom	Wyck.	Site	occ.	x/a	y/b	z/c	U_{eq}/U_{iso} (Å^2)
P1	4c	.*m*.	1	0.74008(6)	1/4	0.60597(3)	0.01636(12)
F1	8d	1	1	0.73962(13)	0.38434(6)	0.60565(5)	0.0347(2)
F2	4c	.*m*.	1	0.55303(19)	1/4	0.54630(8)	0.0364(3)
F3	4c	.*m*.	1	0.92481(18)	1/4	0.66508(8)	0.0365(3)
F4	4c	.*m*.	0.124(3)	0.225(2)	3/4	0.9156(9)	0.050(4)
P2	4c	.*m*.	1	0.37528(8)	3/4	0.85524(3)	0.02343(14)
F5	4c	.*m*.	0.124(3)	0.593(2)	3/4	0.8049(13)	0.102(7)
F4'	4c	.*m*.	0.036(3)	0.233(8)	3/4	0.787(4)	0.072(13)
F5'	4c	.*m*.	0.036(3)	0.567(8)	3/4	0.909(3)	0.072(13)
F6	8d	1	0.160(3)	0.4180(14)	0.6241(8)	0.8601(6)	0.046(3)
O1	8d	1	0.840(3)	0.4662(3)	0.64561(16)	0.83709(14)	0.0477(6)
N1	8d	1	1	0.74861(16)	0.51358(9)	0.86826(7)	0.0193(2)
C1	8d	1	1	0.9159(2)	0.58336(12)	0.87496(9)	0.0279(3)
H1A	8d	1	1	1.02562	0.53751	0.88362	0.0420
H1B	8d	1	1	0.90153	0.63335	0.92127	0.0420
H1C	8d	1	1	0.93123	0.62536	0.82443	0.0420
C2	8d	1	1	0.76085(19)	0.44092(11)	0.79561(8)	0.0246(3)
H2A	8d	1	1	0.77989	0.48499	0.74633	0.0370
H2B	8d	1	1	0.64529	0.39931	0.79028	0.0370
H2C	8d	1	1	0.86543	0.39061	0.80238	0.0370
C3	8d	1	1	0.7167(2)	0.44915(12)	0.94397(8)	0.0258(3)
H3A	8d	1	1	0.60075	0.40786	0.93867	0.0390
H3B	8d	1	1	0.70776	0.49849	0.99094	0.0390
H3C	8d	1	1	0.82039	0.39862	0.95221	0.0390
HN1	8d	1	1	0.658(2)	0.5555(12)	0.8600(9)	0.030(4)
HP1A	4c	.*m*.	1	0.635(3)	1/4	0.6716(10)	0.014(5)
HP1B	4c	.*m*.	1	0.846(3)	1/4	0.5391(10)	0.019(5)
HP2A	4c	.*m*.	0.840(3)	0.200(3)	3/4	0.8248(19)	0.034(9)
HP2B	4c	.*m*.	0.840(3)	0.331(5)	3/4	0.9345(12)	0.054(12)

3.11.2 Single crystal structure analysis of $m-[(CH_3)_3NH][H_2PF_4]_{0.9}\cdot[H_2PO_2]_{0.1}$

The compound crystallises with monoclinic symmetry in the space group $P2_1/c$ (No. 14).

Cell (250 K): $a = 11.8454(15)$ Å, $b = 8.7965(11)$ Å, $c = 7.5452(9)$ Å, $\beta = 100.418(4)$, $V = 773.23(17)$ Å^3, $Z = 4$

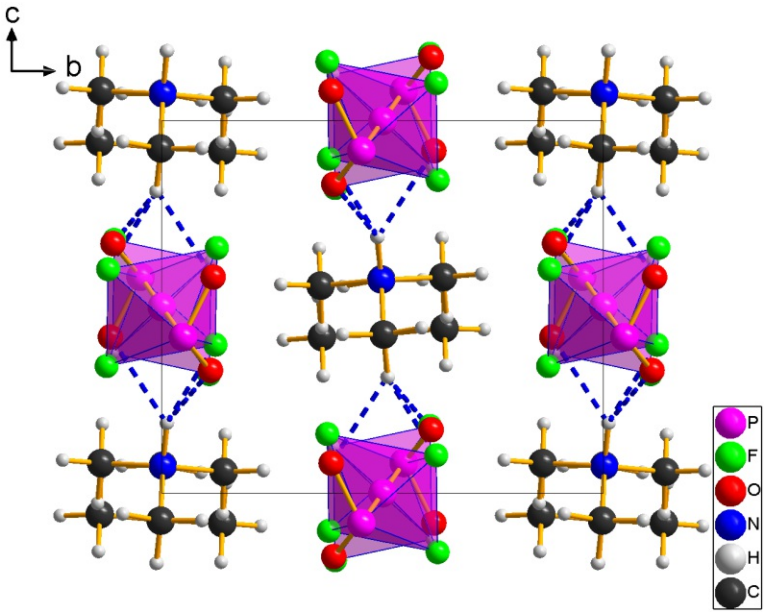

Figure 3.135: Crystal structure of $m-[(CH_3)_3NH][H_2PF_4]_{0.9}\cdot[H_2PO_2]_{0.1}$ viewed down [100].

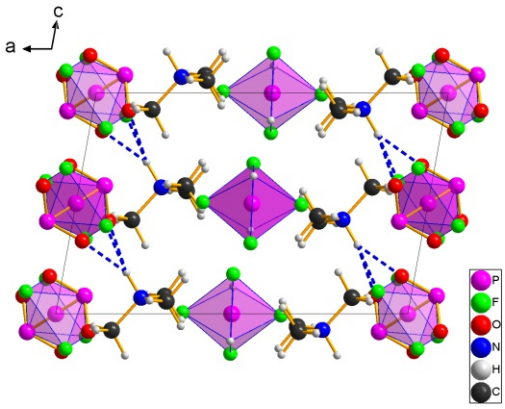

Figure 3.136: Crystal structure of $m-[(CH_3)_3NH][H_2PF_4]_{0.9}\cdot[H_2PO_2]_{0.1}$ viewed down [010].

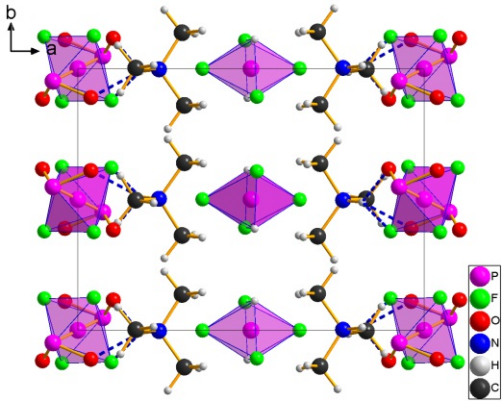

Figure 3.137: Crystal structure of $m-[(CH_3)_3NH][H_2PF_4]_{0.9}\cdot[H_2PO_2]_{0.1}$ viewed down [001].

Like previously, possesses the crystal structure of $m-[(CH_3)_3NH][H_2PF_4]_{0.58}\cdot[H_2PO_2]_{0.42}$ two independent $[H_2PF_4]^-$ anions. In contrast to the orthorhombic crystal structure, the ions on both positions are located on alternating sheets in parallel to the (100) plane. The $P1$ position is fully occupied by $[H_2PF_4]^-$, whereas the $P2$ position is occupied by about 96.5 % $[H_2PF_4]^-$. The $[H_2PF_4]^-$ anions are always localised on inversion centres. The $[H_2PO_2]^-$ anions are disordered around the inversion centre located at the $P2$ position. In this structure, the cations are also connected to the $[H_2PF_4]^-$ via hydrogen bonds. Like in the orthorhombic structure, the ions connected by H-bonds form short trimers.

Table 3.42: Atomic parameters of $m-[(CH_3)_3NH][H_2PF_4]_{0.9} \cdot [H_2PO_2]_{0.1}$.

Atom	Wyck.	Site	occ.	x/a	y/b	z/c	U_{eq}/U_{iso} (Å^2)
P1	2d	$\bar{1}$	1	1/2	0	1/2	0.0405(4)
F1	4e	1	1	0.5167(2)	-0.1074(3)	0.6803(3)	0.0952(9)
F2	4e	1	1	0.64016(15)	0.00052(18)	0.5065(3)	0.0773(7)
P2	2c	$\bar{1}$	0.965(3)	0	1/2	0	0.0422(4)
F3	4e	1	0.864(4)	0.9032(3)	0.3785(3)	0.8985(4)	0.1029(14)
F4	4e	1	0.864(4)	0.9541(3)	0.6249(3)	0.8413(4)	0.0954(13)
P3	4e	1	0.0176(14)	0.928(3)	0.548(5)	0.081(5)	0.0422(4)
O1	4e	1	0.136(4)	0.0373(13)	0.6104(18)	0.1704(18)	0.0422(4)
O2	4e	1	0.136(4)	0.8978(11)	0.6163(17)	0.9196(19)	0.0422(4)
N1	4e	1	1	0.7658(2)	0.4973(2)	0.5729(3)	0.0456(6)
HN1	4e	1	1	0.82106	0.48954	0.68783	0.0550
C1	4e	1	1	0.8330(3)	0.5025(3)	0.4260(5)	0.0692(10)
H1A	4e	1	1	0.78130	0.51301	0.31133	0.1040
H1B	4e	1	1	0.87685	0.40939	0.42627	0.1040
H1C	4e	1	1	0.88495	0.58865	0.44410	0.1040
C2	4e	1	1	0.6991(3)	0.6373(4)	0.5805(5)	0.0683(9)
H2A	4e	1	1	0.74997	0.72444	0.58863	0.1020
H2B	4e	1	1	0.66245	0.63442	0.68542	0.1020
H2C	4e	1	1	0.64102	0.64535	0.47242	0.1020
C3	4e	1	1	0.6925(3)	0.3596(4)	0.5573(5)	0.0691(9)
H3A	4e	1	1	0.63835	0.36246	0.44434	0.1040
H3B	4e	1	1	0.65096	0.35649	0.65683	0.1040
H3C	4e	1	1	0.74030	0.26973	0.56049	0.1040
HP1	4e	1	1	0.490(2)	-0.112(3)	0.376(3)	0.057(9)
HP2	4e	1	0.965(3)	0.929(3)	0.549(5)	0.079(5)	0.057(9)

3.12 NMR-Measurements

Since, as already mentioned, OH^- and F^- hardly differ from each other in X-ray diffraction, NMR measurements were carried out as a complimentary method. Despite favourable receptivities and a large chemical shift range, the two antimony nuclei both possess moderate nuclear quadrupole moments (Table 3.43), and relaxation is invariably dominated by the efficient quadrupolar mechanism [73]. Thus when the antimony nucleus is at a site of low electronic symmetry the resonance becomes rather complicated. The approach using ^{19}F-NMR is useful in case of highly symmetrical compounds [74, 75] such as all octahedral hexafluoroantimonates. However, less symmetric antimonates (such as salts of $[SbF_5(OH)]^-$ and $[SbF_4(OH)_2]^-$) are more difficult to analyze.

Table 3.43: NMR characteristics of antimony nuclei [76].

	^{121}Sb	**^{123}Sb**
Nuclear spin quantum number I	$\frac{5}{2}$	$\frac{7}{2}$
Natural abundance (%)	57.25	42.75
Magnetogyric ratio (10^7 **rad** $T^{-1}s^{-1}$)	6.4355	3.4848
Quadrupole moment, Q ($10^{-28}m^2$)	-0.28	-0.36
Resonance frequency (MHz at 2.349 T)	24.056	13.026
Line width factor ($10^{-54}m^4$)	$2.5 * 10^{-2}$	$1.8 * 10^{-2}$
Receptivity relative to ^{13}C	527	113

3.12.1 identification of $[SbF_6]^-$

Intense investigation on antimonate compounds have already been carried out in the past. However, little work has been performed on asymmetric fluorohydroxoantimonates.
Moreover, the nature of the $[SbF_6]^-$ anion depends on the employed solvent. For example, the $[SbF_6]^-$ anion, is present as $[SbF_5(OH)]^-$ in H_2O/ D_2O [26] as solvent or as corner linked dimers ($[Sb_2F_{11}]^-$) in SO_2 [77]. Since this quickly reduces the symmetry of the anions and thus increases the complexity of the spectra obtained, d_6−DMSO was chosen as the solvent, which gave good results and, as desired, easy discrimination of the different fluoroantimonates. It also has sufficient solubility for the compounds under investigation, and there is no risk of unwanted hydrolysis. The use of standard NMR sample tubes was not a problem here, no fluorosilicates could be detected in the respective spectra and there was no visible etching off the glass.

The $[SbF_6]^-$-ion could be clearly identified by the characteristic ^{19}F spectra. The six fluoride-signals are identical in the octahedral anion, and they split into 6+8 signals owing to the coupling with the two predominant antimony isotopes. The corresponding range of the measurement is shown in Figure 3.138, the corresponding parameters are listed in Table 3.44.

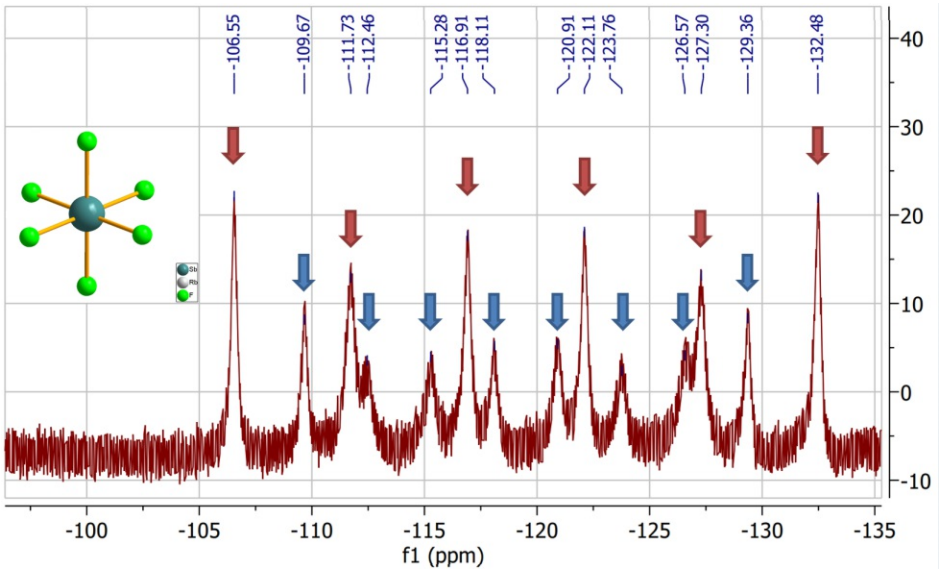

Figure 3.138: $^{19}F\{^{1}H\}$-NMR (235 MHz, d_6−DMSO, 20° C) of $RbSbF_6$.

Table 3.44: Fluorine-^{19}NMR parameters observed for $[SbF_6]^-$ anions in d_6−DMSO at 295K.

	$\delta(^{19}F)$	Multiplicity	
	obs.	J(^{19}F-^{121}Sb)	J(^{19}F-^{123}Sb)
$[SbF_6]^-$	-119,5	→ sxt, 1954 Hz	→ oct, 1060 Hz

3.12.2 Identification of $[SbF_{6-x}(OH)_x]^-$

Since no NMR studies have yet been performed on the hydrolysed products, similar compounds were used for reference. Here, the chlorofluoroantimonates [73] were chosen due to similar electronegativity distribution. At first, it was assumed that $[SbF_5(OH)]^-$ would exhibit similar behaviour to $[SbClF_5]^-$ and likewise $[SbF_4(OH)_2]^-$ would exhibit similar behaviour to $[SbCl_2F_4]^-$. However, this turned out to be incorrect. In contrast to the chlorofluoroantimonates, the $[SbF_{6-x}(OH)_x]^-$ form adducts, resulting in complex NMR spectra (Figure 3.139 and 3.141).

However, the hydrolysed products were easily identified using the ^{1}H NMR (Figure 3.140 and 3.142). Identification based on the ^{19}F and possibly subsequently on measurements of the ^{121}Sb spectrum was not pursued. This would have been beyond the scope of the work and also would not have fulfilled the goal of a fast and simple characterisation method.
All fluorohydroxoantimonates show one common signal in the ^{1}HNMR: $[SbF_5(OH)]^-$ $\delta(^{1}H)$=6.20(1) ppm) and $[SbF_4(OH)_2]^-$ $\delta(^{1}H)$=4.98(2) ppm, corresponding to the (OH) groups.

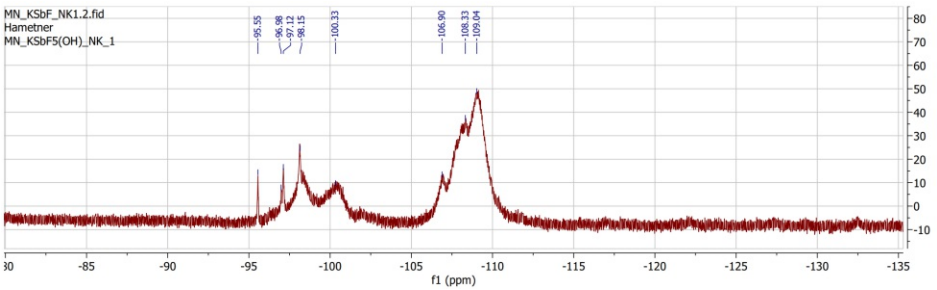

Figure 3.139: $^{19}F\{^{1}H\}$-NMR (235 MHz, d_6−DMSO, 20° C) of $KSbF_5(OH)$.

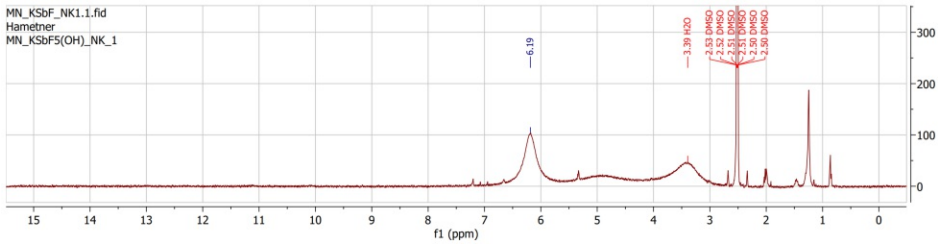

Figure 3.140: ^{1}H-NMR (235 MHz, d_6−DMSO, 20° C) of $KSbF_5(OH)$.

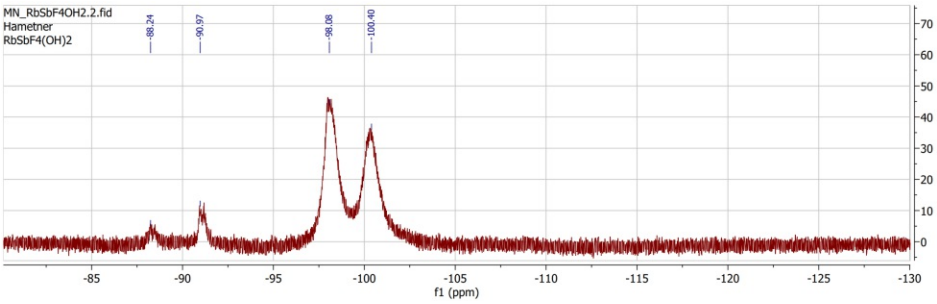

Figure 3.141: $^{19}F\{^{1}H\}$-NMR (235 MHz, d_6−DMSO, 20° C) of $RbSbF_4(OH)_2$.

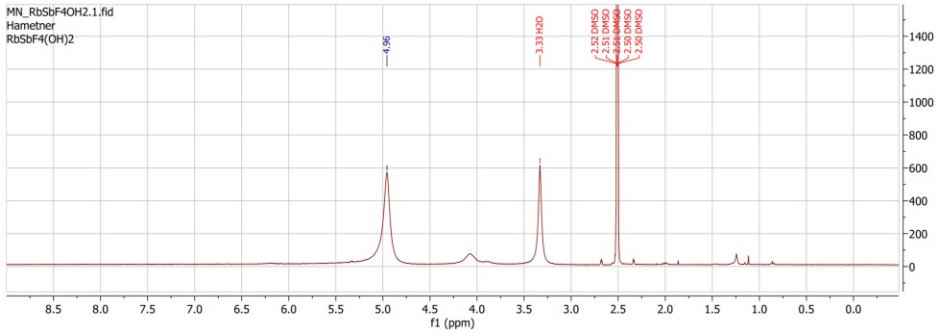

Figure 3.142: ^{1}H-NMR (235 MHz, d_6−DMSO, 20° C) of $RbSbF_4(OH)_2$.

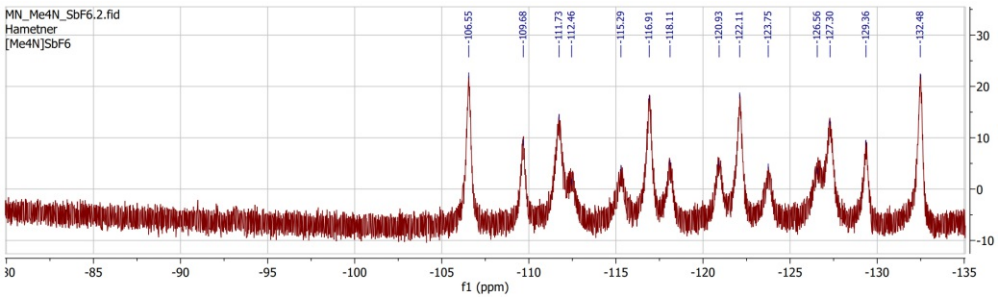

Figure 3.143: $^{19}F\{^{1}H\}$-NMR (235 MHz, d_6−DMSO, 20° C) of $[(CH_3)_4N]SbF_6$.

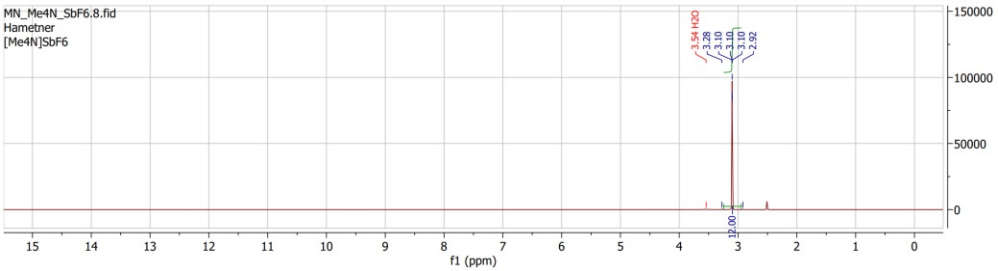

Figure 3.144: ^{1}H-NMR (d_6−DMSO, 20° C) of $[(CH_3)_4N]SbF_6$.

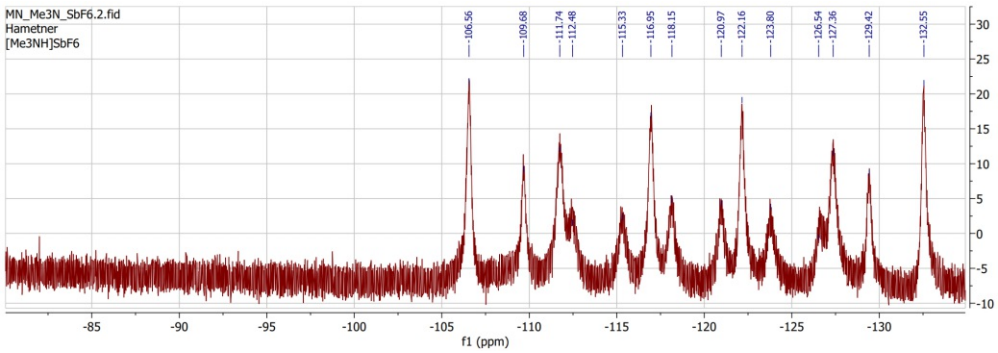

Figure 3.145: $^{19}F\{^{1}H\}$-NMR (235 MHz, d_6−DMSO, 20° C) of $[(CH_3)_3NH]SbF_6$.

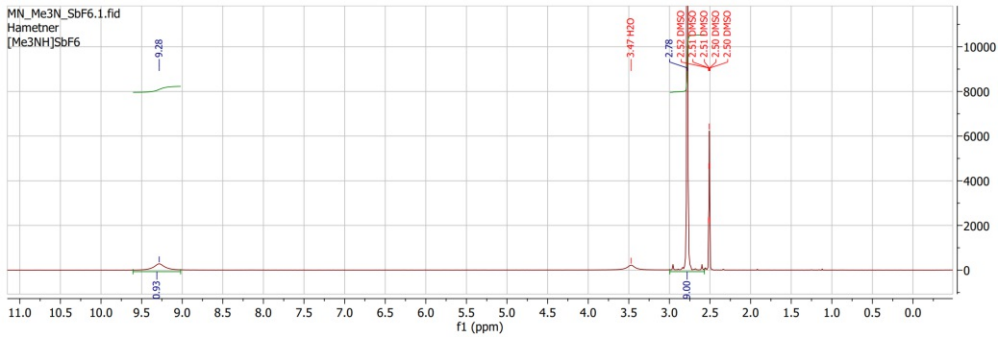

Figure 3.146: ^{1}H-NMR (d_6−DMSO, 20° C) of $[(CH_3)_3NH]SbF_6$.

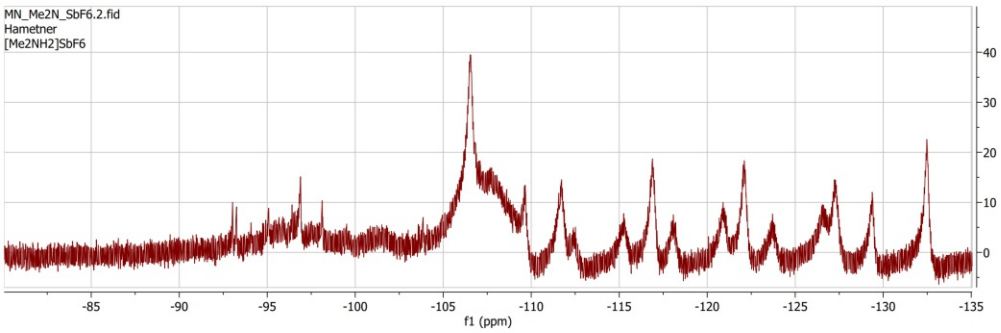

Figure 3.147: $^{19}F\{^{1}H\}$-NMR (235 MHz, d_6−DMSO, 20° C) of $[(CH_3)_2NH_2]SbF_6$.

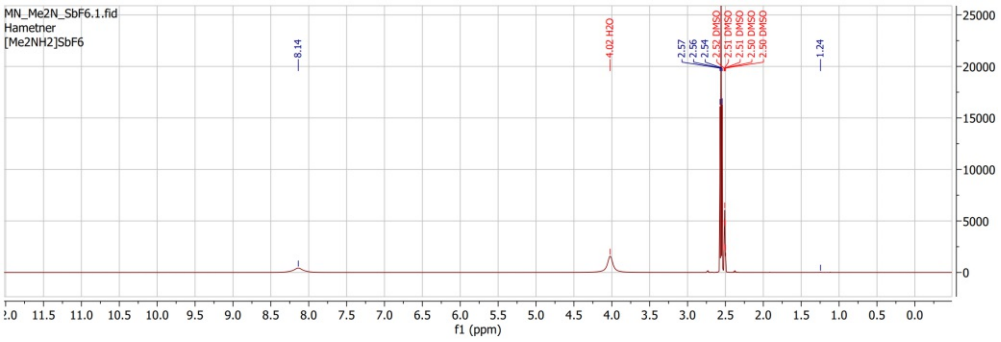

Figure 3.148: ^{1}H-NMR (d_6−DMSO, 20° C) of $[(CH_3)_2NH_2]SbF_6$.

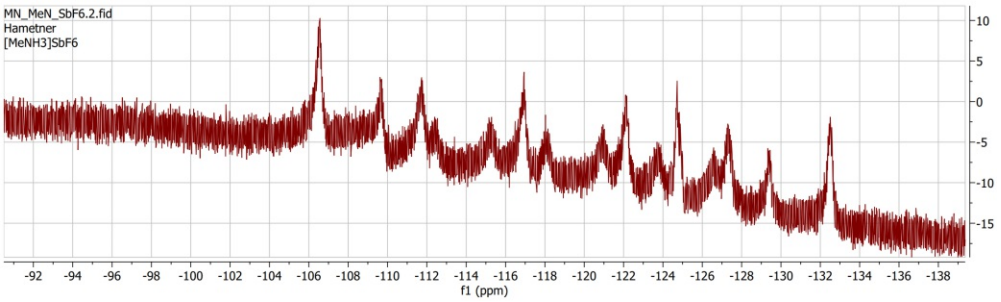

Figure 3.149: $^{19}F\{^{1}H\}$-NMR (235 MHz, d_6−DMSO, 20° C) of $[(CH_3)NH_3]SbF_6$.

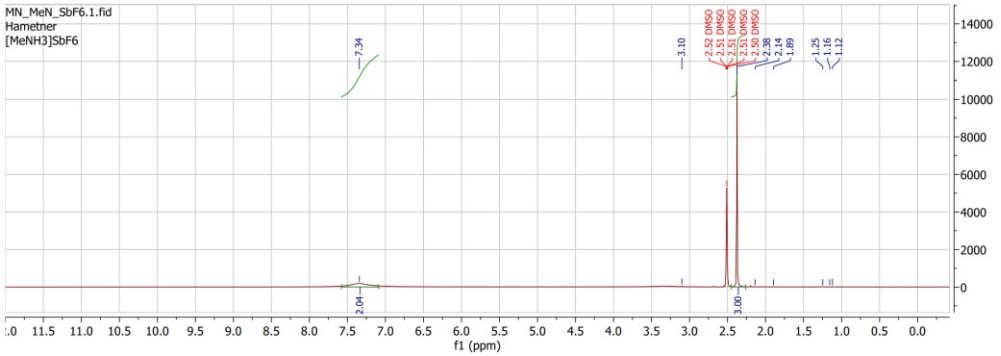

Figure 3.150: ^{1}H-NMR (d_6−DMSO, 20° C) of $[(CH_3)NH_3]SbF_6$.

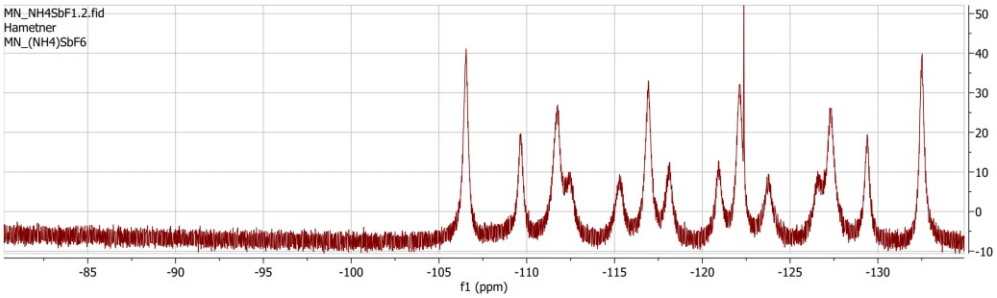

Figure 3.151: $^{19}F\{^{1}H\}$-NMR (235 MHz, d_6−DMSO, 20° C) of $[NH_4]SbF_6$.

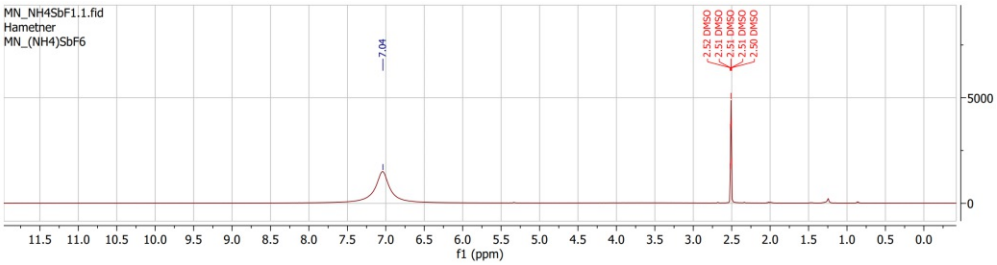

Figure 3.152: ^{1}H-NMR (d_6−DMSO, 20° C) of $[NH_4]SbF_6$.

3.12.3 trans-$[(CH_3)_3NH]H_2PF_4$

The ^{1}H-NMR spectroscopy is a useful tool to characterise the bulk and to determine the conversion rate (Figure 3.153). In this case, the incomplete conversion of the $[H_2PO_2]^-$ ion is quickly apparent, as it gives a doublet (δ 7.01, d, J = 485.9 Hz), due to the H-P-coupling. The desired product yields a doublet-on-quintuplet, by the coupling of the two equivalent H with the four F (δ 5.64, dq, J = 919.3, 120.8 Hz,).
An estimation of the degree of conversion can be derived from the integrals of the signals. The sum of the signals caused by the P-H couplings is logically normalised to 2, since this involves a total sum of exactly two H in $[H_2PO_2]^-$ plus $[H_2PF_4]^-$. The value of the integral of the non-overlapped quintet, represents only one H-coupling from the $[H_2PF_4]^-$. This provides a rough estimate for the proportion $[H_2PF_4]^-$ directly from the area under the right quintet. Also, residual water in the solvent for the NMR measurement leads to a hydrolysis, resulting in a ratio shifted to the $[H_2PO_2]^-$. In the example below (Figure 3.153), this yields a ratio $[H_2PO_2]^-$:$[H_2PF_4]^-$ of about 0.6:0.4.
Also visible are the signal of the cation ($\delta(^1H)$ 2.72, s), as well as an excess of HF, which leads to a broad signal on the far left of the spectrum ($\delta(^1H)$ 11.09, s).

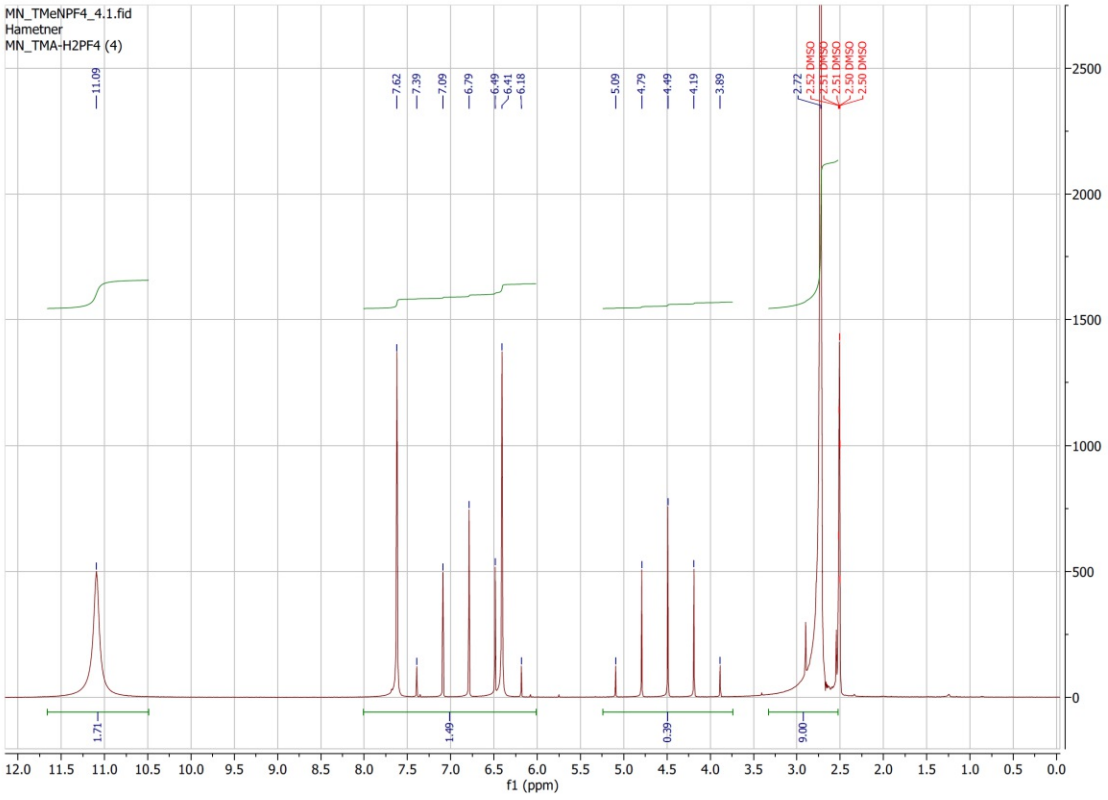

Figure 3.153: ^{1}H-NMR (400 MHz, DMSO−d_6, 20° C) of $[(CH_3)_3NH]H_2PF_4$.

4. Conclusion

As expected, Sb(V) was found to have similar chemical properties to As(V) and P(V). The refined synthesis strategies that were worked out demonstrated this vividly. When Sb(V) oxides or hydroxides are treated with aqueous hydrofluoric acid, the surprisingly stable $[SbF_6]^-$ anion is obtained. The alkali salts show a symmetry of $R\bar{3}$, as has been shown before. Surprisingly, this symmetry is preserved when substituting one F by an OH group, due to disordering. An unexpected exception here was $KSbF_5(OH)$.
As planned, further hydrolysis led to $[SbF_4(OH)_2]^-$ compounds and complex polytypes were formed. $KSbF_4(OH)_2$ forms one commensurately modulated crystal structure in contrast to the incommensurate arsenate. Surprisingly, $RbSbF_4(OH)_2$ forms a wide variety of polytypes, some of which are stable at the same temperature, leading to phenomena such as allotwinning. Since F and OH are not always easy to distinguish by X-ray diffraction methods, NMR spectroscopy was successfully applied as a reliable complementary characterisation method.
All four $[(CH_3)_xNH_{4-x}]SbF_6$ salts exist at or a little above room temperature in a cubic modification, as can be observed with a polarized light microscope. It is interesting that at these temperatures, both the $[SbF_6]^-$ anions and the ammonium cation behave like spheres. On cooling, the symmetry changes in entirely different ways. The reason for this are the highly complex hydrogen networks that are formed. A remarkable example of unexpected crystallographic properties is provided by $[(CH_3)NH_3]SbF_6$. Due to the formation of hydrogen bond network between cations and anions, the symmetry first decreases from $Pm\bar{3}m$ to $Cmcm$ and finally to $P\bar{1}$. Including the lost translation, this corresponds to a total symmetry decrease of index 144. Crystallochemically interesting crystals also resulted from the crystallisation of $[(CH_3)_2NH_2]SbF_6$ below the freezing point.
In addition to all the planned new crystal structures, methyl-substituted ammonium phosphinates were also prepared and most of them were successful crystallised and subsequently characterised. After experiments, $[(CH_3)_3NH]H_2PO_2$ was found as reactant, that can be reacted with hydrofluoric acid to obtain the $[H_2PF_4]^-$ anion, that was previously extremely difficult to synthesise. But, only the first step has been taken so far. Although there is now a simpler synthesis, it still needs to be optimised. The main problem has been identified, namely the cocrystallisation of the reactant, which is caused by hydrogen bonds to the cation. If this can be solved, it will allow many new salts with this anion to be studied in the future.
To combine the interesting features of the hydrolysed anions and ammonium cations, a hydrolysis of the methyl-substituted ammonium salts would be the next logical step. Since the cations of these are also able to form hydrogen bonds, particularly intricate structures are expected. In order to identify the nature of the hydrogen bonds in the $[SbF_4(OH)_2]^-$ compounds with certainty, neutron diffraction experiments have to be carried out. For this, however, the crystal growth must first be optimised.
In addition, successful crystallisation and characterisation of the anhydrous $[(CH_3)_2NH_2]SbF_6$ salt is still pending. With regard to $[H_2PF_4]^-$, unfortunately only the first step has been taken so far, the synthesis still needs to be tweaked.
The interesting results show how unpredictable crystallisation behaviour is in some simple systems, and that further work is needed in both the practical and theoretical fields. Only if enough phenomenological observations are documented can (diffraction) patterns be recog-

nised and lessons learned.

Bibliography

[1] G. R. Desiraju and R. Gautam. Crystal Engineering: A Holistic View. *Angewandte Chemie International Edition*, 46(44):8342–8356, 2007.

[2] Katharina Ehrmann, Stefan Baudis, and Berthold Stöger. From space group to space groupoid: the partial symmetry of low-temperature E-vanillyl oxime. *Acta Crystallographica Section B: Structural Science, Crystal Engineering and Materials*, 75(4):733–741, 2019.

[3] R. Sadanaga and K. Ohsumi. Basic theorems of vector symmetry in crystallography. *Acta Crystallographica Section A*, 35(1):115–122, Jan 1979.

[4] J. F. Nye, John Frederick, et al. *Physical properties of crystals: their representation by tensors and matrices*. Oxford university press, 1985.

[5] S. Parveen, R. J. Davey, G. Dent, and R. G. Pritchard. Linking solution chemistry to crystal nucleation: the case of tetrolic acid. *Chem. Commun.*, pages 1531–1533, 2005.

[6] Carolyn Pratt Brock, T. Hahn, H. Wondratschek, U. Müller, U. Shmueli, E. Prince, A. Authier, V. Kopskỳ, D. B. Litvin, E. Arnold, et al. *International tables for crystallography volume A: Space-group symmetry*. Wiley Online Library, 2016.

[7] Kopsky Vojtěčch, Litvin, and B. Daniel. *International Tables for Crystallography Volume E: Subperiodic groups*. John Wiley, 2010.

[8] C. Hermann. XXXV. Zur systematischen Strukturtheorie.: IV. Untergruppen. *Zeitschrift für Kristallographie - Crystalline Materials*, 69(1-6):533–555, 1929.

[9] H. Wondratschek and W. Jeitschko. Twin domains and antiphase domains. *Acta Crystallographica Section A: Crystal Physics, Diffraction, Theoretical and General Crystallography*, 32(4):664–666, 1976.

[10] Ludwig Bieberbach. Über die Bewegungsgruppen der euklidischen Räume. *Mathematische Annalen*, 70(3):297–336, 1911.

[11] Ulrich Müller. *Relating crystal structures by group–subgroup relations*, chapter 1.6, pages 44–56. Wiley Online Library, 2011.

[12] Ulrich Müller. *Symmetry relationships between crystal structures: applications of crystallographic group theory in crystal chemistry*, volume 18. OUP Oxford, 2013.

[13] B. B. Zvyagin. A contribution to polytype systematics. *Phase transitions*, 43(1-4):21–25, 1993.

[14] A. Guinier, G. B. Bokij, K. Boll-Dornberger, J. M. Cowley, S. Ďurovič, H. Jagodzinski, P. Krishna, P. M. de Wolff, B. B. Zvyagin, D. E. Cox, P. Goodman, Th. Hahn, K. Kuchitsu, and S. C. Abrahams. Nomenclature of polytype structures. Report of the International Union of Crystallography *Ad hoc* Committee on the Nomenclature of Disordered,

Modulated and Polytype Structures. *Acta Crystallographica Section A*, 40(4):399–404, Jul 1984.

[15] Massimo Nespolo, Giovanni Ferraris, and Slavomil Ďurovič. OD character and twinning–Selective merohedry in class II merohedric twins of OD polytypes. *Zeitschrift für Kristallographie-Crystalline Materials*, 214(12):776–779, 1999.

[16] Massimo Nespolo, Toshihiro Kogure, and G. Ferraris. Allotwinning: oriented crystal association of polytypes–Some warnings on consequences. *Zeitschrift für Kristallographie-Crystalline Materials*, 214(1):5–8, 1999.

[17] Martina Schroffenegger, Felix Eder, Matthias Weil, Berthold Stöger, Karolina Schwendtner, and Uwe Kolitsch. News about thallium arsenates(V). *Journal of Alloys and Compounds*, 820:153369, 2020.

[18] J. Peterková, M. Dušek, V. Petříček, and J. Loub. Structures of Fluoroarsenates $KAsF_{6n}(OH)_n$ $n = 0$, 1, 2: Application of the Heavy-Atom Method for Modulated Structures. *Acta Crystallographica Section B: Structural Science*, 54(6):809–818, Dec 1998.

[19] H. Sowa and H. Ahsbahs. Single-crystal study of the pressure-induced NaCl to CsCl type phase transition in KPF_6 and the crystal structure of the high-pressure phase: . *Zeitschrift für Kristallographie - Crystalline Materials*, 214(11):751–757, 1999.

[20] Kouichi Kitashita, Rika Hagiwara, Yasuhiko Ito, and Osamu Tamada. Crystal structures of some cubic hexafluorophosphates at ambient temperatures. *Journal of Fluorine Chemistry*, 101(2):173–179, 2000.

[21] Hans Bode and Heinrich Clausen. Die Kristallstruktur des Kalium-, Ammonium- und Cäsiumhexafluorophosphats. *Zeitschrift für anorganische und allgemeine Chemie*, 265(4-6):229–243, 1951.

[22] Karolina Schwendtner and Uwe Kolitsch. Octahedral As in M^+ arsenates–architecture and seven new members. *Acta Crystallographica Section B: Structural Science*, 63(2):205–215, 2007.

[23] Chemical Abstracts Service. Antimonate(1-), pentafluorohydroxy- , cesium, (OC-6-21) - (9CI). (CAS RN: 70709-17-0).

[24] Alexey A. Mikhaylov, Elena A. Mel'nik, Andrei V. Churakov, Vladimir M. Novotortsev, Judith A.K. Howard, Sergey Sladkevich, Jenny Gun, Subramanian Bharathi, Ovadia Lev, and Petr V. Prikhodchenko. Synthesis, crystal structure and characterization of alkali metal hydroxoantimonates. *Inorganica Chimica Acta*, 378(1):24–29, 2011.

[25] M. J. Nolte and W. H. J. de Beer. Caesium pentafluorohydroxoantimonate. *Acta Crystallographica Section B: Structural Crystallography and Crystal Chemistry*, 35(5):1208–1210, May 1979.

[26] A. William W. A. Mazeika and H.M. Neumann. Stepwise Hydrolysis of Hexafluoroantimonate (V). *Inorganic Chemistry*, 5(2):309–311, 1966.

[27] Karl O. Christe, Carl J. Schack, and E. C. Curtis. trans-Dihydridotetrafluorophosphate (V) anion, trans$-H_2PF_4$. *Inorganic Chemistry*, 15(4):843–848, 1976.

[28] S. S. Chan and C. J. Willis. Trifluoromethyl-substituted fluorophosphates and fluoroarsenates. *Canadian Journal of Chemistry*, 46(8):1237–1248, 1968.

[29] Rolf Minkwitz, Frank Neikes, and Dirk Rüttershoff. Reaktionen von Ameisensäuremethylester in den supersauren Systemen XF/MF_5(X=H,D;M=As,Sb) und die Kristallstruktur von $HC(OH)(OCH_3)^+$ AsF_6^-. *Zeitschrift für anorganische und allgemeine Chemie*, 626(10):2203–2207, 2000.

[30] K. O. Christe, P. Charpin, E. Soulie, R. Bougon, J. Fawcett, and D. R. Russell. Structure and vibrational spectra of oxonium hexafluoroarsenates (V) and-antimonates (V). *Inorganic Chemistry*, 23(23):3756–3766, 1984.

[31] Caroline Röhr and Sandra Loss. $RbAsF_6$, $CsAsF_6$ und $RbSbF_6$: Kristallstrukturen, Thermische Phasenumwandlungen und Schwingungsspektren/ $RbAsF_6$, $CsAsF_6$ and $RbSbF_6$: Crystal Structures, Thermal Phase Transitions, and Vibrational Spectra. *Zeitschrift für Naturforschung B*, 53(1):75–80, 1998.

[32] Nils Schrewelius. Röntgenuntersuchung der Verbindungen $NaSb(OH)_6$, $NaSbF_6$, $NaSbO_3$ und gleichartiger Stoffe. *Zeitschrift für anorganische und allgemeine Chemie*, 238(2-3):241–254, 1938.

[33] Hans Bode and Ernst Voss. Die Kristallstruktur des Kaliumhexafluoroantimonats (V). *Zeitschrift für anorganische und allgemeine Chemie*, 264(2-4):144–150, 1951.

[34] G.E. Griffiths, J. E. Walrafen, and E. George. Raman study of the hydrolysis of the hexafluoroantimonate (1-) ion. *Inorganic Chemistry*, 11(2):427–429, 1972.

[35] Rolf Minkwitz, Andreas Liedtke, and Rüdiger Nass. Synthese der Monofluorammoniumsalze $NH_3F{\equiv}HF_2{-}{\cdot}$nHF, -$SbF_6^-$, -$AsF_6^-$, -$BF_4^-$. *Journal of Fluorine Chemistry*, 35(2):307–315, 1987.

[36] W. H. J. de Beer and A. M. Heyns. The infrared and raman spectra of solid $CsSbF_5OH$ and $CsSbF_4(OH)_2$. *Solid state commun.; USA; DA. 1980; BIBL. 13 REF.*, 33(1):31–34, 1980.

[37] Markus Rotter. Symmetriebeziehungen in Fluorophosphaten, -arsenaten und -antimonaten. Master's thesis, TU Wien, 2020.

[38] Karl O. Christe, William W. Wilson, and Carl J. Schack. On the syntheses and properties of some hexafluorobismuthate (V) salts and their in the metathetical synthesis of NF+4 salts. *Journal of Fluorine Chemistry*, 11(1):71–85, 1978.

[39] M. Ponikvar, B. Žemva, and Joel F. Liebman. The analytical and descriptive inorganic chemistry of the hydrolysis of hexafluoropnictate ions, PnF_6^- (Pn= P, As, Sb, Bi). *Journal of Fluorine Chemistry*, 123(2):217–220, 2003.

[40] Jean-Guillaume Eon. Euclidian embeddings of periodic nets: definition of a topologically induced complete set of geometric descriptors for crystal structures. *Acta Crystallographica Section A*, 67(1):68–86, Jan 2011.

[41] Reinhard Diestel. *The Basics. In: Graph Theory. Graduate Texts in Mathematics*, pages 1–34. Springer Berlin Heidelberg, Berlin, Heidelberg, 2017.

[42] M. P. Qin, Q. N. Chen, Z. Y. Xie, J. Chen, J. F. Yu, H. H. Zhao, B. Normand, and T. Xiang. Partial long-range order in antiferromagnetic Potts models. *Phys. Rev. B*, 90:144424, Oct 2014.

[43] Alessandro Codello. Exact Curie temperature for the Ising model on Archimedean and Laves lattices. *Journal of Physics A: Mathematical and Theoretical*, 43(38):385002, Aug 2010.

[44] Thomas Degen, Mustapha Sadki, Egbert Bron, Uwe König, and Gwilherm Nénert. The highscore suite, 2014.

[45] Bruker APEX. SAINT and SADABS. Bruker AXS Inc. *Madison, WI, USA*, 2009.

[46] George M. Sheldrick. SHELXT–Integrated space-group and crystal-structure determination. *Acta Crystallographica Section A: Foundations and Advances*, 71(1):3–8, 2015.

[47] George M. Sheldrick. Crystal structure refinement with SHELXL. *Acta Crystallographica Section C: Structural Chemistry*, 71(1):3–8, 2015.

[48] A. L. Spek. Single-crystal structure validation with the program *PLATON*. *Journal of Applied Crystallography*, 36(1):7–13, Feb 2003.

[49] H. Putz and K. Brandenburg GbR. Diamond - Crystal and Molecular Structure Visualization, 2009.

[50] Václav Petříček, Michal Dušek, and Lukáš Palatinus. Crystallographic Computing System JANA2006: General features. *Zeitschrift für Kristallographie - Crystalline Materials*, 229(5):345–352, 2014.

[51] John F. Lehmann, Sebastian Riedel, and Gary J. Schrobilgen. Behavior of BrO_3F and ClO_3F toward strong Lewis acids and the characterization of $[XO_2][SbF_6](X=Cl,Br)$ by single crystal X-ray diffraction, Raman spectroscopy, and computational methods. *Inorganic Chemistry*, 47(18):8343–8356, 2008.

[52] F. A. Josien and G. Duquenoy. Synthesis in solid-state *M*-Sb-O (*M*= K, Rb or Cs) compounds. *REVUE DE CHIMIE MINERALE*, 17(1):40–45, 1980.

[53] Lothar Kolditz and Walter Rehak. Über fluorhaltige Verbindungen der Elemente der V. hauptgruppe. IX. über monomere und kondensierte Fluoroantimonate. *Zeitschrift für anorganische und allgemeine Chemie*, 300(5-6):322–336, 1959.

[54] G. Zundel and H. Metzger. Energiebänder der tunnelnden überschuß-protonen in flüssigen säuren. Eine IR-Spektroskopische Untersuchung der Natur der Gruppierungen $H_5O_2^+$. *Zeitschrift für Physikalische Chemie*, 58(5_6):225–245, 1968.

[55] Rolf Minkwitz, Stefan Schneider, and Andreas Kornath. On the reaction of phosphorous acid with superacids and the crystal structure of $H_5O_2^+SbF_6^-$ and $Me_4N^+HPF_5^-$. *Inorganic chemistry*, 37(18):4662–4665, 1998.

[56] George A. Olah, John T. Welch, Yashwant D. Vankar, Mosatomo Nojima, Istvan Kerekes, and Judith A. Olah. Synthetic methods and reactions. 63. Pyridinium poly (hydrogen fluoride)(30% pyridine-70% hydrogen fluoride): a convenient reagent for organic fluorination reactions. *The Journal of Organic Chemistry*, 44(22):3872–3881, 1979.

[57] K. Syed Mohamed, D.K. Padma, R.G. Kalbandkeri, and A.R. Vasudeva Murthy. Pyridinium poly(hydrogen fluoride) — a reagent for the preparation of hexafluorophosphates. *Journal of Fluorine Chemistry*, 23(6):509 – 514, 1983.

[58] Zoran Mazej and Evgeny Goreshnik. Crystal structures of $[SbF_6]^-$ salts of di-and tetrahydrated Ag^+, tetrahydrated Pd_2^+ and hexahydrated Cd_2^+ cations. *Zeitschrift für Kristallographie-Crystalline Materials*, 232(5):339–347, 2017.

[59] Takeshi Asai. Refinement of the crystal structure of sodium hexahydroxoantimonate (V), $NaSb(OH)_6$. *Bulletin of the Chemical Society of Japan*, 48(10):2677–2679, 1975.

[60] Hans Beyer et al. Lehrbuch der organischen Chemie, 1955.

[61] G. J. Kruger, C. W. F. T. Pistorius, and A. M. Heyns. Potassium hexafluoroantimonate (I). *Acta Crystallographica Section B: Structural Crystallography and Crystal Chemistry*, 32(10):2916–2918, 1976.

[62] Anton M. Heyns and Carl W. F. T. Pistorius. Polymorphism, high-pressure phase diagram and vibrational spectra of $KSbF_6$. *Spectrochimica Acta Part A: Molecular Spectroscopy*, 32(3):535–545, 1976.

[63] Ivar Olovsson. Hydrogen-Bond Studies. XXIX. Crystal Structure of Perchloric Acid Dihydrate, $H_5O_2^+ClO_4^-$. *The Journal of Chemical Physics*, 49(3):1063–1067, 1968.

[64] Michael Wiebcke and Dietrich Mootz. Clathrathydrate starker Säuren: Isostrukturelle Hexahydrate der Hexafluoroarsen(V)-säure und Hexafluoroantimon(V)-säure. *Zeitschrift für Kristallographie - Crystalline Materials*, 183(1-4):1–14, 1988.

[65] Hugh M. Matheson and W. Alex Whitla. Crystal structure of aquohydronium hexachloroantimonate (V). *Canadian Journal of Chemistry*, 56(7):957–958, 1978.

[66] Darja Gantar and Ana Rahten. Thermal analysis of new hydrazinium (2+) hexafluoroantimonate. *Journal of thermal analysis*, 36(2):553–558, 1990.

[67] Zoran Mazej and Evgeny A. Goreshnik. Crystal Structures of Hydrazinium (II) Salts of $[SbF_6]^-$ and $[Sb_2F_{11}]^-$. *Zeitschrift für anorganische und allgemeine Chemie*, 641(7):1216–1219, 2015.

[68] Michal Dušek, Institute of Physics of the Czech Academy of Sciences. private communication, 2021.

[69] Y. Wang, L. D. Calvert, and S. K. Brownstein. The structure of tetramethylammonium hexafluorophosphate. *Acta Crystallographica Section B*, 36(6):1523, Jun 1980.

[70] S. Detoni, D. Hadži, and B. Orel. Vibrational spectra of crystalline hypophosphorous acid. *Journal of Molecular Structure*, 33(2):279–288, 1976.

[71] Jack M. Williams and S.W. Peterson. Molecular structure determination by neutron and X-ray diffraction ** based on work performed under the auspices of the U.S. atomic energy commission. In C.N.R. Rao and John R. Ferraro, editors, *Spectroscopy in Inorganic Chemistry*, pages 1–56. Academic Press, 1971.

[72] Martin Nastran and Berthold Stöger. The order/disorder phase transition of hypophosphorous acid H_3PO_2. *Zeitschrift für Kristallographie - Crystalline Materials*, 236(5-7):163–172, 2021.

[73] Michael F. A. Dove and Jeremy C. P. Sanders. Synthesis and characterisation of chlorofluoroantimonates (V). *Journal of the Chemical Society, Dalton Transactions*, pages 3311–3316, 1992.

[74] R. G. Kidd and R. W. Matthews. Antimony-121 nuclear magnetic resonance in some antimony (V) compounds. *Journal of Inorganic and Nuclear Chemistry*, 37(3):661–663, 1975.

[75] Paul N. Billinger, Preet P. K. Claire, Helen Collins, and Gerald R. Willey. Halide abstraction reactions of Sb (V) chloride: Synthesis and characterisation of hexachloroantimonate salts of *M* (II) *M*= Zn, Mg; *M* (III) *M*= Cr; and *M* (IV) M= Ti, Sn and related Cp2*M* (IV) *M*= Ti, Zr and Hf. *Inorganica chimica acta*, 149(1):63–67, 1988.

[76] R. K. Harris. *NMR and the Periodic Table*, volume 5. The Royal Society of Chemistry, 1976.

[77] J. Bacon, P. A. W. Dean, and R. J. Gillespie. A 19F nuclear magnetic resonance investigation of the formation of $Sb_2F_{11}^-$ and $Sb_nF_{5n+1}{}^-$ in the CsF−SbF_5, t-butyl halide-SbF_5, and tetraalkylammonium hexafluoroantimonate-SbF_5 systems. *Canadian Journal of Chemistry*, 47(10):1655–1659, 1969.

5. Glossary and Appendix

Abbreviation

PMMA	Polymethylmethacrylat polymer
BBHD	Bragg-Brentano High Definition (divergent incident beam module)
PTFE	Polytetrafluorethylen polymer
Me	methyl-group ($-CH_3$)
MeOH	methanol
HM symbol	Hermann-Mauguin symbol
Gu	guanidine
HT	high-temperature
LT	low-temperature
M^+	cation (eg. K^+, Rb^+, Cs^+, $[NH_4]^+$, $[H_5O_2]^+$, ...)
SG	space group
SC	single crystal
XRD	X-ray diffraction
PXRD	powder X-ray diffraction
XRPD	X-ray powder diffractogram
SC-XRD	single crystal X-Ray diffraction
Wyck.	multiplicity and Wyckoff letter
occ.	site occupancy
U_{eq}	isotropic thermal parameters (in $Å^2$)

Table 5.1: Overview of crystal structures: cell parameters obtained from SC-XRD data.

Compound	Space Group	a (Å)	b (Å)	c (Å)	α (°)	β (°)	γ (°)	V (Å^3)	T (K)	Z
$[H_5O_2]SbF_6$	$P\bar{1}$ (2)	6.5088(6)	7.4912(6)	8.1258(7)	116.384(2)	93.548(2)	112.078(2)	316.16(5)	100	2
$RbSbF_6$	$R\bar{3}$ (148)	7.640(2)		7.758(2)				392.16(23)	100	3
$CsSbF_6$	$R\bar{3}$ (148)	7.8692(11)		8.126(2)				435.75(15)	100	3
$[NH_4]SbF_6$	$R\bar{3}$ (148)	7.6330(11)		7.759(2)				391.50(14)	100	3
$RbSbF_5(OH)$	$R\bar{3}$ (148)	7.6421(10)		7.7335(11)				391.14(12)	100	3
$CsSbF_5(OH)$	$R\bar{3}$ (148)	7.8626(5)		8.1138(5)				434.40(6)	100	3
$[NH_4]SbF_5(OH)$	$R\bar{3}$ (148)	7.6128(8)		7.7282(9)				387.88(9)	100	3
$KSbF_5(OH)$	$Pbca$ (61)	10.189(2)	10.372(2)	19.985(4)				2112.0(7)	100	16
$KSbF_4(OH)_2$	$P2_1/c$ (14)	4.9806(4)	16.0927(12)	6.6138(4)		96.533(3)		526.66(7)	100	4
$CsSbF_4(OH)_2$	$P2_1/n$ (14)	5.1208(10)	16.938(3)	7.1356(14)		98.612(4)		611.94(20)	100	4
s-$RbSbF_4(OH)_2$	$C\bar{1}$ (2)	4.9994(5)	16.4436(15)	6.8666(6)	87.806(3)	96.842(3)	94.537(5)	558.48(9)	100	4
l-$RbSbF_4(OH)_2$	$C\bar{1}$ (2)	5.0389(4)	49.472(4)	6.8273(5)	89.729(3)	98.319(3)	90.393(3)	1683.98(20)	150	12
l-m-$RbSbF_4(OH)_2$	Cc (9)	5.1075(10)	50.19(1)	6.9095(14)		97.87(3)		1754.5(6)	300	12
m-$RbSbF_4(OH)_2$	$P2_1/c$ (14)	5.0697(3)	16.5935(9)	6.8649(4)		97.961(1)		571.94(6)	300	4
$[(CH_3)_4N]SbF_6$	$P\bar{4}3m$ (215)	6.4490(13)						268.21(16)	430	1
$[(CH_3)_4N]SbF_6$	$P4/n$ (85)	8.8924(9)		6.5118(6)				514.92(11)	300	4
$[(CH_3)_3NH]SbF_6$	$P2_12_12_1$ (19)	8.2505(18)	8.929(2)	12.108(3)				892.0(3)	100	4
$[(CH_3)_3NH]SbF_6$	$P432$ (207)	6.144(6)						232.0(7)	250	1
$[(CH_3)_2NH_2]SbF_6 \cdot H_2O$	$Pmmn$ (59)	13.1647(13)	21.538(2)	6.5963(6)				1870.3(3)	100	8
$[(CH_3)_2NH_2]SbF_6 \cdot H_2O$	$Pmmn$ (59)	13.2972(11)	10.9348(10)	6.6316(6)				964.25(15)	100	8
$[(CH_3)_2NH_2]SbF_6$	$P\bar{4}3m$ (215)	5.916(3)						207.1(3)	300	1
$[(CH_3)NH_3]SbF_6$	$P\bar{1}$ (2)	9.0717(17)	9.3186(17)	12.100(2)	79.694(3)	79.694(3)	75.804(3)	953.43(30)	100	6
$[(CH_3)NH_3]SbF_6$	$P\bar{1}$ (2)	9.1318(4)	9.3934(4)	12.2234(5)	79.334(1)	75.747(1)	75.242(1)	974.29(7)	220	6
$[(CH_3)NH_3]SbF_6$	$Cmcm$ (63)	7.164(4)	8.947(4)	11.024(5)				706.6(6)	350	4
$[(CH_3)NH_3]SbF_6$	$Pm\bar{3}m$ (221)	5.658(9)						181.2(8)	410	1
$[(CH_3)_4N]H_2PO_2 \cdot H_2O$	$P2_1/c$ (14)	6.7780(2)	15.1614(4)	8.9582(3)		92.676(1)		919.58(5)	100	4
$[(CH_3)_2NH_2]H_2PO_2$	$Pca2_1$ (29)	11.6518(9)	5.4894(4)	9.2090(8)				589.02(8)	100	4
$[(CH_3)NH_3]H_2PO_2$	$C2/c$ (15)	8.8481(10)	10.0438(11)	10.6507(12)		90.771(2)		946.43(18)	100	8
m-$[(CH_3)_3NH]H_2P_4$	$P2_1/c$ (14)	11.8454(15)	8.7965(11)	7.5452(9)		100.418(4)		773.23(17)	100	4
o-$[(CH_3)_3NH]H_2P_4$	$Pnma$ (62)	7.1974(7)	12.2773(11)	16.3462(15)				1444.4(2)	250	8

Table 5.2: Comparison of the unit cells with their distorted pseudo-cubic parameters.

Compound	**a** (Å)	**b** (Å)	**c** (Å)	α (°)	β (°)	γ (°)	**V** (Å^3)	**T** (K)
$[H_5O_2]SbF_6$	6.0168(5)	5.0460(3)	5.3605(4)	102.634(1)	87.238(1)	84.760(1)	157.755	**100**
$RbSbF_6$	5.1131(14)	5.1131(6)	5.1131(14)	96.6794(192)	96.6793(249)	96.6794(192)	130.720	**100**
$CsSbF_6$	5.2894(8)	5.2894(4)	5.2894(8)	96.1242(111)	96.1242(139)	96.1242(111)	145.254	**100**
$[NH_4]SbF_6$	5.1098(8)	5.1098(4)	5.1098(8)	96.6449(115)	96.6449(144)	96.6449(115)	130.499	**100**
$KSbF_5(OH)$	5.0945(10)	5.1860(10)	4.9962(10)	90	90	90	132.000	**100**
$[(CH_3)_4N]SbF_6$	6.2879(4)	6.2879(4)	6.5118(6)	90	90	90	257.462	**300**
$[(CH_3)_3NH]SbF_6$	6.0786(10)	6.0786(10)	6.054(15)	90	90	94.5234(180)	222.995	**100**
$[(CH_3)_2NH_2]SbF_6 \cdot H_2O$	6.5823(7)	5.3845(5)	6.5963(6)	90	90	90	233.789	**100**
$[(CH_3)NH_3]SbF_6$	5.7309(20)	5.7309(20)	5.5120(25)	90	90	102.6304(405)	176.651	**350**
$[(CH_3)NH_3]SbF_6$	5.4495(5)	5.6551(4)	5.2912(10)	88.785(2)	86.160(1)	86.566(2)	162.379	**220**
$[(CH_3)NH_3]SbF_6$	5.4056(35)	5.6457(31)	5.2301(39)	88.552(1)	86.061(1)	86.466(2)	158.899	**100**

List of Figures

List of Tables